Three-dimensional analysis of bone cellular tissue from SR CT Imaging

Pei Dong

N° d'ordre : 2014-ISAL-0022 Année 2014

THÈSE

présentée devant

L'Institut National des Sciences Appliquées de Lyon

pour obtenir

LE GRADE DE DOCTEUR

ÉCOLE DOCTORALE: ÉLECTRONIQUE, ÉLECTROTECHNIQUE, AUTOMATIQUE

par

Pei DONG

Three-dimensional analysis of bone cellular tissue from SR CT Imaging

Soutenue le 21 Février 2014 devant la commission d'examen

Jury

Rapporteurs :

Valérie BOUSSON	Professeur des Universités - Praticien Hospitalier, Université Paris Diderot
Jean Marc CHASSERY	Directeur de recherche CNRS

Examinateurs:

Joachim OHSER	Professeur des Universités, Université de sciences appliquées de Darmstadt
Maciej ORKISZ	Professeur des Universités, Université Claude Bernard Lyon 1

Directeur de thèse:

Françoise PEYRIN	Directeur de recherche INSERM

INSA Direction de la Recherche - Ecoles Doctorales – Quinquennal 2011-2015

SIGLE	ECOLE DOCTORALE	NOM ET COORDONNEES DU RESPONSABLE
CHIMIE	**CHIMIE DE LYON** **http://www.edchimie-lyon.fr** Insa : R. GOURDON	M. Jean Marc LANCELIN Université de Lyon – Collège Doctoral Bât ESCPE 43 bd du 11 novembre 1918 69622 VILLEURBANNE Cedex Tél : 04.72.43 13 95 directeur@edchimie-lyon.fr
E.E.A.	**ELECTRONIQUE, ELECTROTECHNIQUE, AUTOMATIQUE** **http://edeea.ec-lyon.fr** Secrétariat : M.C. HAVGOUDOUKIAN eea@ec-lyon.fr	M. Gérard SCORLETTI Ecole Centrale de Lyon 36 avenue Guy de Collongue 69134 ECULLY Tél : 04.72.18 65 55 Fax : 04 78 43 37 17 Gerard.scorletti@ec-lyon.fr
E2M2	**EVOLUTION, ECOSYSTEME, MICROBIOLOGIE, MODELISATION** **http://e2m2.universite-lyon.fr** Insa : H. CHARLES	Mme Gudrun BORNETTE CNRS UMR 5023 LEHNA Université Claude Bernard Lyon 1 Bât Forel 43 bd du 11 novembre 1918 69622 VILLEURBANNE Cédex Tél : 06.07.53.89.13 e2m2@ univ-lyon1.fr
EDISS	**INTERDISCIPLINAIRE SCIENCES-SANTE** **http://www.ediss-lyon.fr** Sec : Samia VUILLERMOZ Insa : M. LAGARDE	M. Didier REVEL Hôpital Louis Pradel Bâtiment Central 28 Avenue Doyen Lépine 69677 BRON Tél : 04.72.68.49.09 Fax :04 72 68 49 16 Didier.revel@creatis.uni-lyon1.fr
INFOMATHS	**INFORMATIQUE ET MATHEMATIQUES** **http://infomaths.univ-lyon1.fr** Sec :Renée EL MELHEM	Mme Sylvie CALABRETTO Université Claude Bernard Lyon 1 INFOMATHS Bâtiment Braconnier 43 bd du 11 novembre 1918 69622 VILLEURBANNE Cedex Tél : 04.72. 44.82.94 Fax 04 72 43 16 87 infomaths@univ-lyon1.fr
Matériaux	**MATERIAUX DE LYON** **http://ed34.universite-lyon.fr** Secrétariat : M. LABOUNE PM : 71.70 –Fax : 87.12 Bat. Saint Exupéry Ed.materiaux@insa-lyon.fr	M. Jean-Yves BUFFIERE INSA de Lyon MATEIS Bâtiment Saint Exupéry 7 avenue Jean Capelle 69621 VILLEURBANNE Cedex Tél : 04.72.43 83 18 Fax 04 72 43 85 28 Jean-yves.buffiere@insa-lyon.fr
MEGA	**MECANIQUE, ENERGETIQUE, GENIE CIVIL, ACOUSTIQUE** **http://mega.ec-lyon.fr** Secrétariat : M. LABOUNE PM : 71.70 –Fax : 87.12 Bat. Saint Exupéry mega@insa-lyon.fr	M. Philippe BOISSE INSA de Lyon Laboratoire LAMCOS Bâtiment Jacquard 25 bis avenue Jean Capelle 69621 VILLEURBANNE Cedex Tél :04.72 .43.71.70 Fax : 04 72 43 72 37 Philippe.boisse@insa-lyon.fr
ScSo	**ScSo*** **http://recherche.univ-lyon2.fr/scso/** Sec : Viviane POLSINELLI Brigitte DUBOIS Insa : J.Y. TOUSSAINT	M. OBADIA Lionel Université Lyon 2 86 rue Pasteur 69365 LYON Cedex 07 Tél : 04.78.77.23.86 Fax : 04.37.28.04.48 Lionel.Obadia@univ-lyon2.fr

*ScSo : Histoire, Géographie, Aménagement, Urbanisme, Archéologie, Science politique, Sociologie, Anthropologie

ACKNOWLEDGMENT

I would like to thank everyone who gave me their help and support during my thesis writing.

First and foremost, I would like to thank my supervisor Dr. Françoise Peyrin for giving me this excellent opportunity to work on this exciting project and for her meticulous guidance throughout my PhD study. Her passion and enthusiasm to the work really inspired me to keep moving forward when I faced many difficulties.

I express my thanks to the jury members of this thesis, Dr. Valérie Bousson, Dr. Jean Marc Chassery, Dr. Joachim Ohser, Dr. Maciej Orkisz, Dr. Françoise Peyrin, for conscientiously reading this thesis, providing their valuable comments and being present at my defense. Particularly, I thank the two referees Dr. Valérie Bousson and Dr. Jean Marc Chassery for writing the constructive reports. Also, deep gratitude goes to Dr. Valérie Bousson for her insightful suggestions on the sample biological interpretation.

I acknowledge everyone in the bone team for giving me help and for the wonderful discussion and collaboration. Especially, I thank Pierre-jean Gouttenoire for his support on the program code. I thank Dr. Maria A. Zuluaga for the great scientific discussion and for giving me lots of encouragement. My thanks also go to Cécile Olivier for the sample preparation and data acquisition. I also acknowledge Dr. Bernard Hesse, Dr. Max Langer and Dr. Alexandra Pacureanu for their help on the publication correction and many of insightful discussion and suggestion.

Many thanks to the group of Dr. Sharmila Majumdar from UCSF and group of LIP (Laboratoire d'Imagerie Paramétrique), for providing and preparing the valuable samples. Special thanks to Dr. Sylvain Haupert for fruitful suggestion and discussions on the bone sample analysis. I also give my regards to the sample donors for their contributions of scientific research.

I would also like to sincerely thank to the team of ID19 and ID22 of ESRF, particularly to Dr. Paul Tafforeau, Dr. Elodie Boller, Dr. Alexander Rack and Dr. Lukas Helfen from ID19 and Dr. Peter Clotens and Dr. Heikki Suhonen form ID22. The image analysis presented in the thesis would not have been possible without their support of data acquisition and image reconstruction. Especially, I would like to thank Dr. Paul Tafforeau for his help during the image acquisition in BM05 and also for his great tools of ring artifacts elimination. Besides, the wonderful art like 3D rending skills using the software VGStudioMax really opens my mind and motivated me for making better images for the scientific illustration.

My gratitude goes to the ID19 team for creating such a nice and friendly working atmosphere, particularly, to Adeline, Anne, Carmen, Irene, Jean-david, Jean Paul, Julio, Maite, Vincent, and Zongjun Yin.

Last but not least, my sincere thanks go to my parents, who have always actively supported me during my PhD study. I also would like to express my deepest gratitude to my beloved wife Fanglue for her support and encouragement during the most difficult time of thesis writing.

CONTENTS

ACKNOWLEDGMENT ..... **I**
CONTENTS ..... **II**
ABSTRACT ..... **VI**
RESUME ETENDU ..... **IX**
SYMBOL LIST ..... **XXXIV**
I. BACKGROUND **1**
1. Introduction **2**
1.1 Background 3
1.2 Thesis objective 3
1.3 Layout of the thesis 3
2. Bone tissue and embedded osteocytes **5**
2.1 Introduction 6
2.2 Hierarchical structure of bone 6
2.3 Bone dynamics 11
2.4 The osteocytes 13
2.4.1 Structure of the osteocyte network 13
2.4.2 Functions of the osteocyte network 14
2.4.3 Relation between LCN morphology and the osteocytes functions 15
2.5 Conclusion 15
3. Imaging the lacuno-canalicular network **16**
3.1 Introduction 17
3.2 2D imaging techniques 18
3.2.1 Optical microscopy 18
3.2.2 Electron Microscopy 19
3.2.3 Atomic Force Microscopy 23
3.3 3D imaging technique 23
3.3.1 Confocal laser scanning microscopy 23
3.3.2 X-ray computed tomography 24
3.3.3 Focused ion beam - scanning electron microscopy (FIB/SEM) 30
3.4 Conclusion 31
4. Parameters of the osteocyte network and the lacuno-canalicular network – state of art **32**
4.1 Introduction 33
4.2 Characterization of osteocyte or lacunae 34
4.2.1 Lacunar properties at tissue level 34
4.2.2 Lacunar properties at cellular level 37

4.3 Characterization of osteocyte processes or canaliculi 41
4.3.1 Canalicular properties at tissue level 41
4.3.2 Morphological parameters of canaliculi and processes 43
4.4 Conclusion 46
II. CONTRIBUTION 47
5. Image acquisition from synchrotron radiation CT from micro to nanoscale 48
5.1 Introduction 49
5.2 European synchrotron radiation facility 50
5.3 Synchrotron radiation micro and nano CT 51
5.3.1 SR micro-CT setup at beamline ID19 51
5.3.2 X-ray magnified phase tomography setup at ID22 52
5.4 Data reconstruction 53
5.4.1 Absorption CT 53
5.4.2 Phase nano CT 54
5.5 Experiments and image acquisition 56
5.5.1 SR CT at the submicrometer scale (300 nm voxel size) 58
5.5.2 Magnified SR phase CT at the nanometer scale (50 nm voxel size) 62
5.6 Conclusion 64
6. Development of a 3D quantification method of Lacunae from Synchrotron CT images at micrometer scale 66
6.1 Introduction 68
6.2 Material and methods 70
6.2.1 Sample Description 70
6.2.2 Synchrotron radiation microtomography (SR-μCT) 70
6.2.3 Image Processing 71
6.2.4 Segmentation of osteocyte lacunae 71
6.2.5 Labeling, number of lacunae (N.Lc) 72
6.2.6 Calculation of 3D individual osteocyte lacunae descriptors 72
6.2.7 Calculation of tissue indices 74
6.2.8 Artifact elimination 75
6.2.9 Local analysis 76
6.2.10 Statistics analysis 77
6.3 Results 77
6.3.1 Evaluation of the segmentation method 77
6.3.2 Histomorphometry parameters of the bone tissue 79
6.3.3 3D shape descriptors of osteocyte lacunae 80
6.3.4 Osteocyte lacunar density distribution 84
6.3.5 Correlations between bone porosity and osteocyte lacunae features 86
6.4 Discussion 88
7. Development of a 3D Quantification method of Canaliculi from Synchrotron CT images at sub-micrometer scale 94

7.1 Introduction 95
7.2 Material and method 96
7.2.1 Sample preparation 96
7.2.2 Synchrotron radiation micro-CT imaging 97
7.2.3 Segmentation 97
7.2.4 Quantification Method 98
7.3 Results 100
7.3.1 Validation of the canaliculi counting method 100
7.3.2 Application to SR micro-CT image 102
7.4 Discussion 105
8. Segmentation and quantification of the LCN in a series of human tibial samples 107
8.1 Introduction 109
8.2 Samples and image acquisition 110
8.2.1 Sample description and preparation 110
8.2.2 Synchrotron radiation microtomography (SR-µCT) at 3.5 µm 111
8.2.3 Synchrotron radiation microtomography (SR-µCT) at 300 nm 113
8.3 Segmentation and quantification method 113
8.3.1 Background on minimal path extraction through geodesic voting 113
8.3.2 Workflow of the segmentation method 114
8.3.3 Input volume 115
8.3.4 Bone volume and lacunae segmentation 115
8.3.5 Lacunae tessellation 116
8.3.6 Candidate paths extraction via minimal path extraction and geodesic voting 116
8.3.7 Acceleration of the algorithm 117
8.3.8 Post processing: maximum rank filter 119
8.3.9 Enhancement of canaliculi pathways 119
8.3.10 Normalization and thresholding 120
8.3.11 Quantification 120
8.4 Selection of the parameters in the segmentation method 121
8.4.1 Comparison between the reconstructed SR micro-CT images 121
8.4.2 Manual Segmentation 123
8.4.3 Automatic segmentation 125
8.5 Application to human tibial SR micro-CT images 130
8.5.1 Selection of regions of interest 130
8.5.2 Parameters of the lacunae segmentation method 130
8.5.3 Histomorphometry parameters of the tibial tissues 131
8.5.4 Morphological descriptors of the osteocyte lacunae 133
8.5.5 Ramification of the canaliculi 136
8.6 Discussion and conclusion 139
9. Conclusion and perspective 143

10. Annex 1 146
11. Annex 2 152
12. Annex 3 184
PUBLICATIONS 185
BIBLIOGRAPHY 187

ABSTRACT

Bone diseases severely affect the quality of life around the world. Unfortunately, bone fragility remains only partially understood despite decades of research in this area.

Bone is a complex structured material with a hierarchical arrangement from the macroscale to the sub-nanoscale, constantly changing its mass and structure throughout the lifespan. At the cellular scale, the osteocyte system has raised increasing interest in the recent years, since it is hypothesized to play an important role in orchestrating bone adaptation. The osteocytes are supposed to be essential cells in bone mechanosensation and bone mechanotransduction. These bones cells are deeply buried within the bone matrix, where their bodies are encysted in cavities called lacunae and their stellular processes are enclosed in tunnels called canaliculi. Together they form a negative imprint of the osteocyte network, which is called lacuno-canalicular network (LCN). The geometry of the LCN is of important since it reflects the viability of the osteocyte and is supposed to be related to biomechanical constraints at the cell level. However, the study of the osteocyte and LCN is quite challenging, limited by the ideal imaging modality and the available quantitative analysis tools.

Imaging the LCN is quite challenging, due to its deep location within hard bone tissue and also the complexity of the LCN which form a dense network made of very thin structures (100-700nm in diameter). Up to now, the most common way for the investigation of the osteocyte system was conducted using two dimensional imaging techniques, such as light microscopy (LM) and scanning electron microscopy (SEM). In recent years, more attempts have been made to use three dimensional imaging modalities including confocal laser scanning microscopy (CLSM), serial 2D images taken at consecutive sectioned layers and computed tomography (CT). Among these imaging modalities, micro/nano-CT coupled with synchrotron radiation source (SR micro/nano-CT) has attractive properties but imaging the LCN has only been demonstrated very recently.

Various studies have been devoted to the assessment of morphological parameters on the osteocyte system. Most of the morphometric data were obtained from 2D images, most of the time by manual measurements. Although geometric models for the osteocytes have been established to extrapolate the 2D measurements to 3D, the results can be biased since they are based on model assumptions. With the development of 3D imaging, 3D morphometric data on osteocyte lacunae were reported in several recent studies. However, up to now, there has been no attempt to formalize and validate the methods that has been used and the numbers of samples and subjects analyzed so far, were quite limited.

In this work, we propose to quantify the LCN based on SR micro/nano-CT imaging at the European synchrotron radiation facility (ESRF). Taking the advantage of multiscale imaging on different beamlines, imaging was performed at spatial resolution between 3.5 µm down to 50 nm. A series of bone samples was imaged at a spatial resolution of 3.5 µm on beamline BM05. This experiment served as a pre-study in order to select a proper region of interest to

be scanned at high resolution. The higher resolution imaging at 1.4 µm and 300nm were performed on the parallel beam SR micro-CT setup, installed on the beamline ID19. This technique allows acquiring 3D data on both the morphology of the cell network and the composition of the bone matrix. To imaging the ultra-structure of the LCN, we used X-ray magnified phase tomography on beamline ID22. By using a focused beam, this method can reach the spatial resolution of 50 nm, providing about 120 μm^3 FOV. This imaging technique allows resolving the morphology of the canaliculi.

To quantify lacunae, we proposed an automatic and efficient 3D analysis method to extract 3D morphological descriptors on a large population of bone cells. To this aim, an image moment-based approach was used to calculate the volume, length, width, height and anisotropy of each osteocyte lacuna. We employed a fast algorithm based on intrinsic volumes to further efficiently calculate the surface area, the Euler number and the structure model index (SMI) of each lacuna. The segmentation was refined by eliminating artifacts according to some descriptors. Validation of segmentation and experimental results on thirteen bone samples are presented. We also introduced the 3D lacunar density map to directly visualize the lacunar density variation over a large field of view. The mean volume and surface were found to be $409.5 \pm 149.7\ \mu m^3$ and $336.2 \pm 94.5\ \mu m^2$. The average dimensions were of 18.9 ± 4.9 µm in length, 9.2 ± 2.1 µm in width and 4.8 ± 1.1 µm in depth. We found that the lacunar number density and six osteocyte lacunar descriptors, three axis lengths, two anisotropy ratios and SMI, were significantly correlated to bone porosity.

For the 3D assessment of canaliculi, we proposed an automatic method to quantify the number of canaliculi issued from each lacuna from SR micro-CT images at 300 nm. After segmentation, our method first separates and labels each lacuna of the LCN. Then, a signature of the numbers of canaliculi at different distances from the lacunar surface is estimated through the calculation of topological parameters. This method allows to evidence the ramification of canaliculi. It was applied to the 3D SR micro-CT image of a human femoral mid-diaphysis bone sample. Statistical results are reported on 399 lacunae, showing increasing mean values of the number canaliculi per lacunae at increasing distance from the surface of lacunae. The average number of canaliculi is in agreement with the previous literature and it is the first quantitative assessment of the ramification process.

The last contribution of the thesis was to improve the segmentation of the canaliculi network and to illustrate the feasibility of using the proposed method to conduct automated quantification on a series of bone specimens. Based on a previous work of the group, we investigated a segmentation approach based on minimum cost paths and geodesic voting. A fully automatic initialization scheme was proposed thanks to a Voronoi tessellation of the image domain. To overcome the prohibitive computing times, a parallel computation scheme was implemented. It allowed to speed up the process by about a factor 500. A post-processing scheme was proposed to improve the segmentation results. The final binary LCN was obtained by applying a local thresholding on each Voronoi cell. The quantification was performed by using the methods proposed in the two previous chapters in which we included Voronoi tessellation. Then for each lacunae, we calculated its Voronoi cell volume and the quantification of the canaliculi ramification was restricted for each lacuna to its Voronoi cells.

Statistical results are reported on 8 large 3D micro-CT images, including around a hundred lacunae with their connected canaliculi.

If the goal of this work was more oriented towards quantification, it has been necessary to handle the segmentation of experimental data set. The segmentation of canaliculi from images at 300 nm as well as its evaluation, remain challenging and will have to be pursued in future works. In terms of quantification, further works have also to be performed to extract additional descriptors from SR CT images at both 300 nm and 50 nm. Nevertheless, this work opens many perspectives for a better knowledge of the physiopathology of bone at the cellular scale.

RESUME ETENDU

Introduction

L'ostéoporose est une maladie de la fragilité osseuse, fréquente dans la population âgée, qui s'installe insidieusement et provoque à long terme des fractures handicapantes. Elle est définie par une perte osseuse et des altérations de microarchitecture osseuse. L'os pathologique contrairement à l'os sain n'arrive pas à s'adapter aux contraintes biomécaniques auxquelles il est soumis, d'ou l'apparition de fractures. Comprendre la fragilité osseuse est un enjeu important pour pouvoir agir à un stage précoce de la maladie et éviter les fractures. Cette compréhension nécessite de pouvoir caractériser les propriétés du tissu osseux à différentes échelles.

L'os est un matériau structuré complexe avec un agencement hiérarchique à partir de l'échelle macroscopique jusqu'à l'échelle nanométrique. Au niveau microscopique, on peut distinguer deux types d'os: l'os cortical correspondant à la partie périphérique de l'os et l'os trabéculaire constitué de fines travées osseuses organisées en un réseau complexe. Sous l'effet des phénomènes cellulaires, l'os subit des remaniements permanents ce qui conduit à des changements de sa masse et sa micro structure. A l'échelle cellulaire, les ostéocytes sont les cellules les plus nombreuses dans le tissu osseux. Le système ostéocytaire soulève un intérêt croissant depuis quelques années car il est joue un rôle important dans l'adaptation de l'os. Toutefois, l'observation du système ostéocytaire est difficile car les ostéocytes sont profondément enfouies dans la matrice osseuse et difficilement accessible par les techniques optiques. On manque donc de données quantitatives sur ce réseau en relation avec l'âge ou la maladie.

Le système ostéocytaire est inclus dans un réseau poreux dénommé le réseau lacuno-canaliculaire (LCN). Récemment l'équipe de Creatis a montré la faisabilité d'imager le LCN en 3D grâce à la micro tomographie par rayonnement synchrotron. Cette technique exploite les propriétés intéressantes du rayonnement synchrotron et permet d'acquérir des images jusqu'à des résolutions nanométriques en des temps d'acquisition limités avec des rapports signal sur bruit supérieurs à ceux des images issues de la micro tomographie standard. Toutefois, il n'existe actuellement pas de méthodes d'analyse permettant de quantifier, de façon automatique, le réseau lacuno-canaliculaire en 3D.

L'objectif de cette thèse était de développer des méthodes d'analyse d'images permettant d'extraire des paramètres quantitatifs sur le réseau lacuno-canaliculaire. Ceci nécessite de définir à la fois des paramètres pertinents au niveau biologique et de proposer des méthodes de calcul efficaces compte tenu de la grande taille des images à traiter. Ces méthodes seront appliquées à l'étude d'échantillons d'os cortical humain après avoir acquis des images expérimentales par micro-CT synchrotron 3D.

Ce manuscrit est organisé de la façon suivante :

La première partie, consacrée à l'état de l'art, inclut 3 chapitres. Le chapitre 1 présente les objectifs de ce travail. Le chapitre 2 rappelle les éléments de base sur le tissu osseux et

présente les caractéristiques du réseau lacuno-canaliculaire. Le chapitre 3 présente les différentes méthodes d'imagerie utilisées jusqu'à présent pour étudier le réseau lacuno-canaliculaire. Le chapitre 4 présente l'état de l'art sur les paramètres qui sont classiquement utilisés pour caractériser le réseau lacuno-canaliculaire. Il rapporte une étude très exhaustive des valeurs des différents paramètres mesurés en 2D ou en 3D dans la littérature sur les lacunes et les canalicules.

La seconde partie est consacrée aux contributions de ce travail. Le chapitre 5 présente les deux systèmes expérimentaux de l'ESRF sur lesquels des images d'échantillons osseux ont été acquises. Le chapitre 6 décrit la méthode développée pour la quantification des lacunes ostéocytaires à partir d'images à l'échelle micrométrique. Elle propose de calculer des paramètres issus des moments géométriques ainsi que des paramètres basés sur la notion de volumes intrinsèques. Les méthodes sont appliquées à une série de 13 échantillons acquis en collaboration avec le Laboratoire d'Imagerie Paramétrique, Paris. Les résultats obtenus sont comparés et discutés par rapport à ceux de la littérature. Le chapitre 7 décrit la quantification des canalicules reliant les ostéocytes à partir d'images à l'échelle sous-micrométrique. En particulier, nous nous sommes intéressées à estimer le nombre de canalicules issues d'une lacune ostéocytaire, paramètre encore jamais mesuré en 3D. L'évolution de ce paramètre en fonction de la distance au centre de la lacune a permis de mettre en évidence et de quantifier la ramification des canalicules. Le chapitre 8 propose l'application des méthodes développées à une série d'échantillons acquis en collaboration le groupe de Sharmila Majumdar à l'université de San Francisco. Dans ce chapitre, nous avons travaillé sur une nouvelle méthode de segmentation du réseau lacuno-canaliculaire basée sur une méthode de chemins géodésiques. Les premiers résultats acquis sur 7 échantillons humains d'âges différents sont présentés.

Finalement, le chapitre 9 conclut ce travail et présente des perspectives.

Ce travail a fait l'objet de 4 publications dans des journaux (2 acceptées et 2 soumises), de 8 conférences internationales dont 6 avec actes longs (type IEEE ou SPIE) et 1 présentation orale dans une conférence nationale.

La partie suivante donne un résumé plus étendu de ces différents chapitres.

Partie I : Etat de l'art

Chapitre 2 Tissu osseux et ostéocytes

L'os est un tissu vivant avec différentes échelles d'organisation et assurant plusieurs fonctions dans l'organisme. Sa capacité à s'adapter aux contraintes mécaniques est bien connue et est essentielle dans la prévention des fractures. Comprendre le risque de fracture est un objectif majeur de la recherche sur l'ostéoporose, car on estime que cette maladie affecte plus de 200 millions de femmes dans le monde. Les fractures ostéoporotiques du col du fémur sont les plus graves et ont un fort impact sur la qualité de vie. On estime qu'elles ont augmenté de 25% en dix ans. Ainsi, l'ostéoporose et ses conséquences constituent un problème de santé publique et une meilleure compréhension du risque de fracture est nécessaire pour mieux prévenir cette maladie et ses complications.

Le diagnostic clinique de l'ostéoporose repose actuellement sur un examen en DXA (Dual X-Ray Absorptionmetry) qui permet de mesurer la densité minérale osseuse surfacique. Toutefois, il a été montré ce paramètre n'est pas suffisamment prédictif des fractures au niveau individuel. On observe en effet un nombre important de sujets chez qui une fracture apparaît malgré une densité minérale osseuse normale. Ceci est lié au fait que la densité minérale osseuse est une mesure globale qui reflète principalement la masse osseuse. Si la masse osseuse est un déterminant important de la fragilité osseuse, elle n'est pas le seul facteur expliquant le risque de fracture. Le concept de qualité osseuse, incluant la micro structure osseuse et les propriétés du tissu osseux jusqu'à l'échelle nanométrique, est de plus en plus discuté pour expliquer la fragilité osseuse.

Un phénomène fondamental dans l'étude du tissu osseux est sa capacité à s'auto-réparer grâce au phénomène de remodelage osseux. Le remodelage est un processus dynamique qui consiste en une séquence de résorption et de formation osseuse, suivi d'une minéralisation secondaire progressive pendant laquelle l'os gagne en concentration minérale. Le remodelage est un phénomène essentiel non seulement dans la réparation osseuse comme on le verra plus loin, mais également pour expliquer la perte osseuse apparaissant en particulier dans l'ostéoporose. En effet, idéalement, la formation osseuse devrait être équivalente à la résorption osseuse, c'est à dire qu'il devrait y avoir autant d'os nouvellement formé que d'os résorbé. Malheureusement sous l'effet de l'âge ou d'autres processus, la formation est souvent inférieure à la résorption, ce qui conduit à une perte osseuse. Le remodelage est réalisé grâce à l'action de différents types de cellules osseuses : les ostéoclastes sont responsables de la résorption osseuse tandis que les ostéoblastes participent à la formation osseuse. Toutefois un autre type de cellules soulève un intérêt croissant : les ostéocytes.

Les ostéocytes se trouvent en abondance dans le tissu osseux. Contrairement aux autres cellules, elles ne se trouvent pas sur les surfaces osseuses mais elles sont profondément enfouies dans la matrice osseuse. Elles communiquent entre elles par le biais de processus cellulaires formant ainsi un réseau. Si leur rôle a été pendant longtemps méconnu, de plus en plus de travaux s'intéressent au système ostéocytaire car il est supposé jouer un rôle important dans les mécanismes d'adaptation de l'os. En effet, les ostéocytes sont des cellules mécano sensibles et mécano transductrices qui seraient capables de contrôler et de déclencher le

remodelage osseux. Les informations seraient captées et transmises par l'intermédiaire de différences de pression dans les fluides circulant dans le système ostéocytaire. Les ostéocytes pourraient ainsi localement être sensibles aux défauts du tissu osseux tels que les micro fissures, déclencher le remodelage osseux, qui résorberait le tissu endommagé et procéderait à la formation d'un nouveau tissu minéral de bonne qualité. Cependant, les mécanismes exacts impliqués dans l'activité des ostéocytes ne sont pas précisément élucidés et restent controversés. Une analyse plus précise du système ostéocytaire est donc nécessaire pour mieux comprendre ces phénomènes cellulaires. Pour cela, nous allons décrire plus précisément les ostéocytes et donner leurs caractéristiques géométriques.

L'os cortical humain est organisé en ostéons autours des canaux de Havers. L'ostéon est composé de lamelles concentriques s'enroulant autour des canaux de Havers dans lesquelles sont réparties les ostéocytes. Les ostéocytes communiquent entre elles par le biais de longues dentrites pour former le réseau ostéocytaire. Les ostéocytes sont contenues dans des pores appelés lacunes ostéocytaires et leurs processus dentritiques, dans des petits canaux appelés canalicules. L'ensemble des lacunes et des canalicules forment le réseau lacuno-canaliculaire (LCN).

Les lacunes ostéocytaires sont décrites comme des ellipsoïdes aplatis de dimensions de quelques micromètres. Les canalicules ont un diamètre estimé entre 100 et 700nm. Le nombre de lacunes par mm^3 est de l'ordre de plusieurs milliers et celui des canalicules une centaine de fois supérieure. Le phénomène de mécano sensibilité repose sur les contraintes induites par la circulation de fluides à l'intérieur de cette structure. Des travaux récents font l'hypothèse qu'il y a une forte corrélation entre la fonction du tissu osseux et la morphologie du réseau ostéocytaire. De plus, une étude récente suggère que les ostéocytes aient un rôle dans la régulation du calcium, hypothèse qui reste controversée dans la littérature.

En conclusion, le réseau lacuno canaliculaire joue un rôle majeur dans le tissu osseux mais un certain nombre de mécanismes restent encore assez méconnus ou font l'objet d'hypothèses contradictoires. Il apparait donc important de disposer de moyens permettant de l'étudier dans l'os sain et pathologique.

Chapitre 3 Imagerie du réseau lacuno-canaliculaire

Le chapitre 3 présente les différentes méthodes d'imagerie utilisées jusque la pour étudier le du réseau lacuno-canaliculaire.

La caractérisation du réseau lacuno canaliculaire est difficile expliquant le nombre limité d'études. Les difficultés sont principalement liées à deux raisons : la localisation du réseau lacuno canaliculaire qui est profondément enfoui dans le tissu osseux, et la complexité de cette structure qui se présente sous la forme d'un réseau dense et ramifié à l'échelle nanométrique. La localisation du réseau lacuno canaliculaire le rend difficile d'accès pour les méthodes optiques du fait de la pénétration limitée de la lumière dans les tissus très absorbants comme l'os. La taille des structures, micro et nanométriques, nécessite d'utiliser des méthodes à très haute résolution spatiale. La complexité du réseau le rend difficile à analyser et à quantifier.

Jusqu'à présent, les méthodes les plus usuelles pour caractériser le réseau lacuno canaliculaire reposent sur des images bidimensionnelles (2D) effectuées sur des coupes fines. La microscopie optique a principalement été utilisée dans les études sur le réseau lacuno canaliculaire, en particulier par Marroti. Cette technique permet de compter les ostéocytes, d'identifier les lacunes ostéocytaires vides et d'estimer les dimensions des lacunes ou des ostéocytes. Notons que toutes ces mesures sont 2D, donc dépendent de la direction du plan de coupe. Toutefois, la forte anisotropie des lacunes ostéocytaires a pu être décrite en observant des coupes histologiques dans deux directions.

La microscopie électronique à balayage (MEB), la microscopie électronique à transmission (MET) et la microscopie à force atomique (AFM) peuvent également être utilisées. Ce sont des techniques à très haute résolution spatiale qui sont donc plus appropriées pour caractériser les processus dendritiques des ostéoctytes ainsi que les canalicules. Elles ont notamment permis d'estimer les diamètres des canaux et de compter le nombre de canaux par ostéocyte. Encore une fois, ces mesures sont 2D donc ne donnent qu'une vue partielle des structures.

Au cours des dernières années, plusieurs tentatives ont été faites pour quantifier le réseau lacuno canaliculaire en trois dimensions. Différentes techniques peuvent être employées. Parmi les méthodes optiques, on peut noter des coupes sériées d'images 2D prises sur des sections consécutives de l'échantillon ou la microscopie confocale à balayage laser (CLSM). La première technique est fastidieuse, souffre de distorsions, et il n'est généralement pas possible d'obtenir une aussi bonne résolution spatiale dans la direction de la coupe. La seconde technique souffre également de distorsions, reste limitée à de faibles épaisseurs et fournit des images dont la résolution spatiale généralement plus faible dans la direction de la coupe. Ces techniques sont donc difficilement utilisables pour une quantification 3D.

Plus récemment, l'imagerie tomographique (CT) par rayons X a pu être utilisée. L'avantage de cette technique est qu'elle fournit des images tridimensionnelles avec des résolutions spatiales isotropes. Toutefois, compte tenu de la taille des structures à étudier, il est nécessaire d'utiliser une version de la CT permettant d'atteindre une résolution spatiale très élevée (de l'ordre du micromètre pour l'étude des lacunes ostéocytaires et de l'ordre de quelques centaines de nanomètres pour l'étude des canalicules). Les CT cliniques sont loin d'atteindre des résolutions spatiales suffisantes. Les systèmes de micro-CT par rayons X qui se sont

largement développés pour l'étude de la micro architecture osseuse depuis 10 ans ont des résolutions spatiales de l'ordre de quelques dizaines de microns et restent limités pour aller quantifier le réseau lacuno canaliculaire. Toutefois de nouveaux systèmes permettant d'atteindre des échelles sous micrométriques sont apparus et ont été dénommés, un peu abusivement, nano-CT. Le système développé par SkyScan a notamment permis d'étudier la morphologie des lacunes ostéocytaires chez l'homme et la souris, sur des nombres très réduits d'échantillons. Il est à noter que la tomographie par rayons X ne permet pas d'observer directement les ostéocytes et leurs dendrites mais seulement le réseau poreux de la matrice osseuse, c'est à dire les lacunes et leurs canalicules. Jusqu'à présent, les nano-CT commercialisés ont été utilisés dans seulement deux études du même groupe, ceci pouvant être lié au faible rapport signal sur bruit des images ou aux distorsions inévitables avec ces appareils rendant difficile l'analyse quantitative des données.

De meilleures qualités d'images sont obtenues en micro-CT X lorsque des sources synchrotron sont utilisées à la place des sources standard de rayons X. En effet, on dispose alors d'un très haut flux de photons permettant d'extraire des rayonnements X monochromatiques. Il est alors possible d'atteindre des résolutions micrométriques ou sous micrométriques tout en conservant un bon rapport sur bruit, bien supérieur à ceux des images issus de micro ou de nano CT classiques. Divers systèmes de micro-CT par rayonnement synchrotron ont été construits sur différentes sources synchrotron dans le monde. Si ces systèmes ont dans un premier temps été conçus ou exploités pour étudier la micro architecture osseuse, des études sur l'analyse des lacunes ostéocytaires ont commencé à voir le jour. Dans ces études, les tailles de voxel utilisées sont comprises entre 0.7 et 1.4 micromètres, conduisant généralement à des champs de vue entre 1.4 et 2.8mm de coté. Toutefois, peu de méthodes adaptées ont été proposées pour l'analyse des lacunes ostéocytaires.

En revanche, une résolution spatiale supérieure est nécessaire pour observer les canalicules. A l'ESRF (Installation Européenne de Rayonnement Synchrotron), deux systèmes de nano-CT par rayonnement synchrotron permettent d'atteindre des résolutions spatiales entre quelques dizaines et quelques centaines de nanomètres. Dans des travaux antérieurs récents, notre équipe a pu obtenir les premières images du réseau lacuno canaliculaire en utilisant le système de micro-CT parallèle de la ligne ID19 avec une taille de voxel de 0.3 micromètre. Pour cela, il a été nécessaire d'optimiser le détecteur afin de minimiser la dose et d'éviter les problèmes liés au dommage d'irradiation sur l'échantillon. Un compromis dose versus rapport signal sur bruit a été trouvé et a permis de produire de premiers rendus du réseau lacuno-canaliculaire en 3D dans tout un ostéon, mais les analyses sont à ce stade restées assez qualitatives. Récemment également, nous avons également obtenu des images 3D du réseau lacuno-canaliculaire avec une taille de voxel de 60nm en utilisant le système de nano-CT de phase de la ligne ID22 de l'ESRF.

La ptychographie, technique de diffraction cohérente par rayonnement synchrotron, a également permis d'obtenir l'image d'une lacune entourée de ses canalicules à une taille de voxel de 50nm. Toutefois, les temps d'acquisition prohibitifs rendent difficile l'exploitation de cette technique sur des séries d'échantillon. Citons encore une étude récente par FIB/SEM (Focus Ion Beam/Scanning Electron Microscopy) qui a été proposée pour imager en 3D un échantillon de tissu osseux. Si cette technique est extrêmement précise, elle est longue et

destructive et n'a été démontrée que pour imager une partie d'une lacune. Elle reste donc difficile à envisager pour une étude sur une série d'échantillons.

En conclusion, parmi les différentes techniques proposées dans la littérature, la micro et nano CT par rayonnement sont attractives pour l'imagerie tridimensionnelle du réseau lacunao-canaliculaire à différentes échelles.

Chapitre 4 Paramètres du système ostéocytaire et du réseau lacuno-canaliculaire - Etat de l'art

Le chapitre 4 présente l'état de l'art sur les paramètres qui ont été classiquement utilisés dans la littérature pour caractériser le réseau lacuno-canaliculaire. On dénombre assez peu de publications sur ce sujet jusqu'aux années 2000 mais celles ci sont actuellement en expansion.

Nous avons classé ces paramètres selon qu'ils permettaient de quantifier les lacunes (ou les ostéocytes), puis les canalicules (ou les dendrites) et selon qu'ils étaient 2D ou 3D. Après avoir décrit quels paramètres sont utilisés, le chapitre rapporte une étude très exhaustive des valeurs des différents paramètres mesurés dans la littérature sous forme de tableaux. Ces valeurs nous serviront lors de la comparaison et de la discussion des résultats obtenues dans les chapitres suivants.

La plupart des données ont été obtenues à partir d'images 2D du fait du peu de modalités permettant d'obtenir des images 3D du réseau lacuno-canaliculaire. Si la microscopie confocale est une des rares techniques à avoir permis d'imager en 3D le réseau lacuno-canaliculaire, il faut noter que sa résolution spatiale anisotrope rend plus difficile une analyse quantitative. D'une façon générale, les analyses réalisées à partir d'images 2D, ont été faites le plus souvent manuellement ou avec des logiciels sommaires. Il en résulte que les données sont le plus souvent limitées à un petit nombre d'échantillons, et sur chaque échantillon à une nombre relativement réduit de cellules.

Il faut noter que les paramètres 2D peuvent être extrapolés en 3D en utilisant des méthodes stéréologiques qui nécessitent de faire des hypothèses de modèle. Ces résultats sont sujets à un certain nombre de limitations. D'une part, les hypothèses de modèles sont parfois simplistes ; par exemple une étude a utilisé l'hypothèse que les lacunes sont des sphères, ce qui n'est visiblement pas le cas. D'autre part, il est difficile de contrôler la direction de coupe des lacunes dans la mesure ou bien qu'elles aient une orientation privilégiée, des fluctuations autour de ces orientations peuvent être présentes. Enfin, il peut exister des variations de modèles entre les lacunes, qui n'étant pas prises en compte, vont introduire des erreurs dans l'estimation des paramètres. Si les méthodes stéréologiques permettent d'avoir un ordre de grandeur sur les mesures, elles sont donc toutefois généralement biaisées.

Nous décrivons les paramètres mesurés sur les lacunes, puis sur les canalicules.

Densité lacunaire

La densité de lacunes ou d'ostéocytes est le paramètre le plus souvent rapporté dans la littérature. En 2D, le nombre des lacunes, noté N.Lc, est ramené à la surface de tissu osseux (N.Lc/BA) ou à la surface de tissu (N.Lc/BA), donc exprimé par mm^{-2}. En 3D, il est ramené au volume de tissu osseux (N.Lc/BV) ou de tissu (N.Lc/TV) et exprimé en mm^{-3}. Les notations suivent les nomenclatures préconisées dans un article de Parfitt. Certaines études rapportent à la fois la densité de lacunes et celles des ostéocytes, qui sont généralement corrélées. Celles-ci varient selon le site anatomique, le type de tissu, l'espèce (homme ou animal), l'âge, ainsi que la méthode d'imagerie utilisée. Nous nous limiterons aux valeurs obtenues sur les lacunes et chez l'homme. Chez l'homme, des densités de lacunes rapportées dans différentes études à partir d'images 2D varient entre 120 et 850 mm^{-2}. En extrapolant des

mesures 2D en 3D, Mullender rapporte des valeurs de densité sur des sujets contrôle et ostéoporotiques, entre 12000 et 17000 mm^{-3} alors que Jordan les estime entre 35000 et 39000 mm^{-3}. Depuis 2012, quelques travaux ont rapporté des densités mesurées à partir d'images 3D, portant généralement sur un très petit nombre d'échantillons. Van Hove rapporte des densités de 8000, 15600 et 21800 mm^{-3} mesurées respectivement sur 1 seul échantillon ostéopénique, ostéopétrosique et ostéoartritique de tibia proximal, étude faite à partir d'un système de nano-CT standard. Dans un travail de 2013 utilisant des images de micro-CT synchrotron, Carter mesure une densité moyenne de 24000 mm^{-3} sur 30 échantillons d'os fémoral.

Porosité

La porosité lacunaire n'a été rapportée que très récemment sur des images 3D. Elle s'exprime en pourcentage rapporté au volume de tissu osseux ou au volume total. Nous n'avons trouvé que des mesures chez l'animal avec des valeurs de l'ordre de 1 à 2%.

Paramètres morphologiques sur les lacunes

En 2D, les principaux paramètres morphologiques que l'on trouve dans la littérature sont la surface totale des lacunes (Lc.Ar, en μm^2), la surface des lacunes (Lc.S, en μm^2), le périmètre des lacunes (Lc.Pm, en µm), la distance moyenne entre lacune (Lc-Lc en µm). La longueur, la largeur et la profondeur des lacunes peuvent également être rapportées sans être très précisément définies. Les mêmes paramètres peuvent être calculés sur les ostéocytes. Nous ne donnerons en exemple que des paramètres mesurés sur les lacunes et chez l'homme. Wright rapporte une surface de lacunes moyenne de 65 μm^2 sur des sujets contrôles contre 81 μm^2 sur des sujets ostéoporotiques au niveau de la crête iliaque. Dans une étude similaire, Mullender trouve respectivement des valeurs de 39 μm^2 et de 44 μm^2. Jordan rapport des valeurs du même ordre de grandeur au niveau du fémur. Pour ce qui est des dimensions des lacunes, Marotti rapporte respectivement une longueur de 22 µm, une largeur de 9 µm et une profondeur de 4 µm en prenant des sections suivant différentes directions. Il s'agit quasiment de la seule étude 2D faite chez l'homme.

Depuis que les images 3D sont apparues, des études très récentes, publiées pendant que ce travail était réalisé, rapportent des paramètres 3D sur les lacunes. On trouve ainsi, le volume des lacunes (Lc.V en μm^3), la surface des lacunes (Lc.S en μm^2), les dimensions des lacunes, dont la méthode de calcul n'est pas toujours précisée, l'anisotropie des lacunes définie comme les rapports de dimensions, l'orientation des lacunes par rapport à un axeCarter a récemment introduit les 3 valeurs propres du tenseur d'anisotropie, sans préciser à quoi cette valeur correspond physiquement et a introduit des quantités calculées à partir des rapports de ces valeurs propres qu'il a appelé élongation, « equancy » et aplatissement. Si l'on note EV1, EV2 et EV3 les 3 valeurs propres, les 3 paramètres d'anisotropie sont définis comme :

$$Lc.Eq = EV3 : \mathrm{EV1}$$
$$Lc.El = 1 - EV2 : EV1$$
$$Lc.Fl = 1 - EV3 : EV2$$

Nous ne rappellerons que les résultats obtenus sur l'os humain. La première étude par microscopie confocale 3D chez l'humain rapporte un volume de lacunes de l'ordre de 455 μm^3 dans la tête fémorale. A partir d'images de nano-CT commercialisés, dont on a vu les limitations, Van Hove rapporte des valeurs de volume entre 50 et 180 μm^3. En utilisant la

micro-CT synchrotron, Carter donne des valeurs de volume lacunaire autour de 400 μm^3 sur du fémur.

Mc Creadie décrit un rapport d'anisotropie de 0.3 entre le plus grand et plus petit axe. Carter rapporte des valeurs d'élongation, d'« equancy » et d'aplatissement respectivement autour de 0.77, 0.2 et 0.6. Ces grandeurs n'ont ni une signification physique immédiate par rapport aux dimensions des lacunes et ne sont pas définies de manière cohérente dans les deux articles de Carter.

Paramètres des canalicules

D'une façon générale, les caractéristiques des canalicules sont bien moins documentées que celle des lacunes et la plupart des études existantes ont été faites à partir d'images 2D. Marotti a évalué le nombre de canalicules pour 10µm de longueur et rapporte des valeurs entre 2.3 et 6.3. Dans d'autres travaux, la densité canaliculaire est exprimée comme le nombre de canalicules par 100 μm^2 de surface. Ce nombre varie autour de 5 chez l'homme, mais très peu d'études rapportent ce paramètre. Le diamètre des canalicules ou des dentrites a été mesuré grâce à des images à très haute résolution par microscopie électronique par exemple. On estime qu'il se situe entre 100 et 700 nm chez l'homme. Un autre paramètre important est le nombre de canalicules émanant d'une lacune. Il traduit en quelque sorte la fonctionnalité de l'ostéocyte. En partant de mesures sur des coupes 2D et en utilisant des considérations stéréologiques, Beno a estimé le nombre moyen de canalicules émanant d'une lacune à 41 chez l'homme. La distance moyenne entre canalicules est estimée à 26 µm dans une étude sur la souris. La longueur totale des dendrites peut atteindre 1000 µm.

Conclusion

En conclusion, la plupart des connaissances obtenues sur les caractéristiques des lacunes et des canalicules ont été obtenues à partir d'images de microscopie optique ou électronique. Les quantifications sont réalisées le plus souvent par des comptages ou mesures manuelles. Seulement quelques rares travaux récents ont permis d'avoir des caractéristiques tridimensionnelles. Nous avons synthétisé dans ce chapitre, les ordres de grandeurs des paramètres qui ont été jusque la, rapportés sur l'os humain. On peut noter quelques limitations à ces travaux. Les premières sont liées à la qualité des images utilisées. Par exemple, les images de microscopie confocale à balayage ne permettent d'explorer qu'une profondeur assez réduite et souffrent d'une moins bonne résolution dans cette direction, ce qui peut biaiser les mesures en résultant. Les images de nano-CT standard 3D ont un très mauvais rapport signal sur bruit, ce qui introduit des erreurs de segmentation ayant également un impact sur les paramètres mesurés. D'autre part, cette technique n'a été utilisée que dans deux études et a été limitée à l'analyse des lacunes. D'autres techniques d'imagerie à très haute résolution spatiale telles que la ptychographie ou la FIB/SEM ont pour l'instant un champ de vue trop réduit pour extraire des paramètres représentatifs. Si la micro-CT synchrotron a récemment commencée à être exploitée pour extraire des paramètres sur les lacunes, aucune étude ne rapporte des paramètres sur les canalicules. De plus, il n'y a encore pas eu de méthode rigoureuse proposée pour extraire les propriétés du réseau lacuno-canaliculaire, ni dans la définition des paramètres, ni dans leur validation et les études ont très souvent été limitées à l'analyse d'un petit nombre de lacunes. Notre contribution portera donc sur le développement d'algorithmes efficaces permettant de traiter le plus automatiquement possible

des données de micro/nano CT synchrotron pour évaluer les propriétés du réseau lacuno-canaliculaire.

Partie II : Contributions

Chapitre 5 Acquisition d'images CT Synchrotron à l'échelle micro et nanométrique

Dans ce chapitre, nous décrivons les systèmes de micro/nano CT synchrotron qui ont été utilisés pour acquérir des images d'échantillons osseux à différentes échelles. Pour cela, principalement deux systèmes de CT synchrotron, installés sur deux lignes de lumière ID19 et ID22, ont été utilisés à l'ESRF de Grenoble.

Nous rappelons d'abord le principe d'une source de rayonnement synchrotron, puis nous décrivons les montages expérimentaux des deux systèmes et le principe des méthodes de reconstruction d'image. Enfin, nous présentons les expériences que nous avons effectuées pour acquérir des données à plusieurs échelles.

Rayonnement Synchrotron

L'installation Européenne de Rayonnement Synchrotron (ESRF) est la source de rayonnement synchrotron la plus puissante d'Europe. L'ESRF est composée d'un accélérateur linéaire, d'un accélérateur circulaire et d'un anneau de stockage connecté aux lignes de lumière. Les électrons sont tout d'abord accélérés dans l'accélérateur linéaire, puis dans l'accélérateur circulaire jusqu'à une énergie de 6GeV, puis circulent dans l'anneau de stockage. Ils sont maintenus à des vitesses quasi relativistes par différents éléments électro magnétiques et émettent un rayonnement synchrotron sur les lignes de lumière qui partent tangentiellement à l'anneau. Nous avons principalement utilisé deux lignes de lumière, ID19 et ID22 sur lesquels des systèmes de micro et de nano tomographie ont été installés.

Micro CT sur ID19

Un système de micro CT synchrotron a été développé sur la ligne ID19, qui est une ligne longue, c.a.d. située à 145m de la source. Il s'agit d'un système 3D à faisceau parallèle. Un faisceau monochromatique extrait du rayonnement synchrotron arrivant sur la ligne de lumière est utilisé pour irradier un échantillon. Le principe consiste à acquérir des radiographies 2D de cet échantillon pour différentes positions de rotation. Les images sont acquises sur un détecteur 2D composé d'un scintillateur convertissant les X en lumière visible, d'une optique adaptée en fonction du grandissement voulu et d'une caméra CCD, la caméra FRELON développée à l'ESRF. Les images 3D sont ensuite reconstruites par un algorithme de rétro projection filtré 3D. La ligne permet d'obtenir des images 3D avec des tailles de voxels entre 30 et 0.2 µm.

Nano CT de phase sur ID22

Le système de nano-CT synchrotron de la ligne ID22 a été développé pour travailler dans des gammes de résolutions spatiales inférieures à la centaine de nanomètres. Il utilise un faisceau focalisé par une optique de type Kirkpatrick-Baez permettant un grandissement du faisceau. On peut utiliser soit une énergie de 17 keV, soit de 30 keV. Ce système exploite le phénomène du contraste de phase qui se produit lors de la propagation d'un faisceau de rayons X cohérent. En pratique, il suffit de faire des acquisitions en positionnant le détecteur à une certaine distance de l'échantillon pour observer du contraste de phase. En général, on

acquiert plusieurs scans de l'échantillon pour différentes distances échantillon-détecteur. Dans les expériences que nous avons effectuées, nous avons utilisé 4 scans et les distances ont été choisies de manière à avoir une taille de voxel dans l'image de 60nm.

Reconstruction d'image

En tomographie X standard, le principe physique utilisé est l'atténuation des rayons X par la matière. Ce phénomène est modélisé par la loi de Beer-Lambert. En chaque point de la radiographie, on mesure la somme du coefficient d'atténuation linéaire de l'objet sur la droite joignant la source de rayons X au point du détecteur. D'un point de vue mathématique, le problème revient à reconstruite une image, celle du coefficient d'atténuation, à partir de ses projections. La méthode classique est la méthode par rétro projection filtrée d'abord proposée en 2D, qui se généralise facilement dans le cas d'une géométrie parallèle 3D. Dans ce cas, cette méthode a l'avantage d'être exacte contrairement aux méthodes de reconstruction à partir d'une source conique de rayons X utilisés dans la plupart des micro-CTs commercialisés.

En tomographie de phase, le problème de reconstruction nécessite une étape supplémentaire, appelée inversion de la phase (phase retrieval en anglais) avant la reconstruction par rétro projection filtrée. Les méthodes diffèrent selon que l'acquisition est réalisée à partir d'une ou de plusieurs distances de propagation. Avec une seule distance, la méthode de Paganin est la plus simple car elle se ramène à un filtrage fréquentiel de l'image d'intensité. Elle est utilisable sous l'hypothèse que l'objet est homogène, ce qui permet de supposer une proportionnalité entre le coefficient d'atténuation linéaire et l'indice de phase. Le facteur de proportionnalité, noté δ/β, qui est un paramètre de l'algorithme, dépend de la composition chimique de l'échantillon et de l'énergie utilisée. Avec plusieurs distances de propoagation, la méthode qui a été utilisée pour les acquisitions sur ID22 repose sur la méthode linéarisée dite « approche mixte », exploitant également un a priori d'homogénéité sur l'objet sous la forme d'un terme de régularisation dépendant également d'un facteur δ/β. Cette méthode est ensuite raffinée par des itérations supplémentaires prenant en compte le problème non linéaire.

Acquisitions réalisées dans le cadre de ce travail

Nous avons participé à différentes expériences à l'ESRF pour acquérir des images sur des échantillons osseux à différentes résolutions. Outre la partie acquisition proprement dite, il a été nécessaire d'effectuer tous les prétraitements sur les données acquises, les reconstructions, le recadrage des données sur 8 bits ainsi que la sauvegarde des données.

Nous avons utilisé des échantillons d'os cortical humain, prélevés au niveau du fémur (collaboration avec le LIP, Paris). Des acquisitions ont été réalisées à 1.4 µm dans les conditions suivantes : 3000 projections, énergie 25 keV. Ces images seront utilisées dans le chapitre 6 pour la quantification des lacunes ostéocytaires.

Nous avons également réalisé des acquisitions sur des os humains prélevés au niveau de différents sites (collaboration avec le groupe de S Majumdar, Université de San Francisco). Les échantillons ont tout d'abord été imagés à 3.5 µm sur la ligne BM05 qui dispose d'un système de micro-CT identique à celui de ID19 afin d'avoir une vue globale de l'échantillon. Un protocole de découpe a ensuite été mis en place pour en extraire des échantillons plus petits pouvant être imagés à plus haute résolution. Sur une partie de ces découpes, des acquisitions ont été réalisées à 1.4 µm. Ensuite les échantillons les plus fins ont été imagés à

300nm sur le système de micro-CT ID19 dans le but d'analyser le système lacuno-canaliculaire. Pour cela, nous avons utilisé le protocole décrit dans un travail précédent de l'équipe permettant d'optimiser le rapport signal sur bruit par rapport à la dose. Les conditions d'acquisition sont les suivantes : énergie 19keV, scintillateur LSO d'épaisseur 4.5 µm, caméra CCD E2V, 2400 projections, taille de pixel de 300nm. Les données acquises ont subi différentes corrections : correction de mouvement et correction d'artefacts circulaires. Les reconstructions ont été faites à la fois par rétroprojection filtrée, et en utilisant au préalable la méthode de Paganin compte tenu qu'à très haute résolution, le contraste de phase apparaît même si la distance de propagation est faible (à une dizaine de mm). Ces données seront exploitées dans le chapitre 8, où les deux types d'images seront comparés.

Enfin, des échantillons de cette même série ont également été imagés par nano-CT de phase sur ID22 à une taille de voxel de 60nm. Les images obtenues ont été exploitées dans un autre travail, en collaboration avec Bernhard Hesse (non décrit dans ce manuscrit).

Chapitre 6 : Développement d'une méthode de quantification 3D des lacunes à partir des images de micro-CT synchrotron

Ce chapitre décrit la méthodologie pour mettre en place un algorithme permettant d'extraire des paramètres quantitatifs sur les lacunes ostéocytaires, allant de la segmentation des images à l'analyse statistique des paramètres sur des groupes d'échantillons. Compte tenu du grand nombre de lacunes (de l'ordre de 20000/mm3), et de la grande taille des données, nous avons souhaité développer une méthode la plus automatique possible. Cette méthode sera appliquée à une série de 12 images micro-CT à 1.4 µm d'échantillons d'os cortical humains. Un nombre moyen de 13000 lacunes par volume a pu être analysé. Les paramètres obtenus ont été discutés par rapport aux résultats de la littérature. Une partie de ce chapitre a fait l'objet d'une publication à paraitre dans Bone.

Segmentation

Dans un premier temps, la segmentation des lacunes est réalisée par un seuillage hystérésis appliqué au volume original compte tenu du bon contraste entre l'os et les lacunes. Après une analyse en composantes connexes, un filtrage sur la taille des composantes est réalisé pour éliminer du bruit. Nous utilisant à la fois un seuil bas (élimination du bruit) et un seuil haut (élimination d'autres composantes artefactuelles comme des microfissures par exemple). Ce filtrage sera ensuite raffiné dans la partie suivante. De plus, toutes les lacunes touchant les bords de l'image sont éliminées afin de ne pas biaiser l'analyse morphologique.

Extraction des descripteurs morphologiques

L'objectif était d'extraire des paramètres sur la densité et la morphologie des lacunes. Tous les paramètres introduits ont été dénotés conformément à la nomenclature préconisée en histomorpométrie osseuse, c.a.d en utilisant le préfixe Lc pour lacune.

Pour ce qui est de la densité, nous avons compté le nombre de lacunes, Lc.N à partir de l'analyse en composantes connexes. Les densités Lc.N/BV ou Lc.N sont obtenues après avoir évalué le volume de tissu total et le volume de tissu osseux.

Nous avons ensuite utilisé une approche basée sur la matrice des moments géométriques centrés d'ordre 2 afin d'extraite des caractéristiques morphologiques sur les lacunes. Cette approche est cohérente avec le fait que les lacunes sont décrites dans la littérature comme des ellipsoïdes aplatis. La décomposition de la matrice des moments en valeurs propres et vecteurs propres nous permet d'en déduire les orientations principales de la lacune et ses dimensions. Pour cela, nous donnons la relation liant les demi axes de l'ellipsoide aux valeurs propres. Nous dénotons Lc.L1, Lc.L2, Lc.L3 respectivement les 3 dimensions des lacunes classées par ordre décroissant. Nous en déduisons également des facteurs d'anisotropie par les rapports entre les dimensions.

Dans un deuxième temps, nous avons utilisé les décompositions en volumes intrinsèques pour calculer des paramètres supplémentaires. Les volumes intrinsèques sont des invariants topologiques utiles en analyse de formes. En 3D, ils permettent d'accéder à un certain nombre de mesures : le volume, la surface, le nombre d'Euler et la courbure ou l'indice de structure (SMI). Une méthode de calcul efficace lorsque l'image est échantillonnées sur une grille régulière a été proposée par J Ohser. Cette méthode consiste à dénombrer diverses

configurations locales de voxels dans l'image, et ainsi de construire un histogramme des configurations. Les volumes intrinsèques sont alors obtenus en pondérant les valeurs de l'histogramme avec des poids adéquats pour chaque descripteur. Nous obtenons ainsi Lc.V (volume), Lc.S (surface), Lc.χ(nombre d'Euler) et Lc. SMI (structure Model Index).

Après calcul de tous les descripteurs, la segmentation est raffinée en élimant des lacunes dont les paramètres sont :

$$Lc.V > Lc.V\ within\ the\ top\ 1\%\ and\ Lc.V < 82\ \mu m^3;\ Lc.L1/Lc.L2 > 5;$$
$$Lc.\chi\ < 0\ and\ Lc.\chi\ > 2$$

De plus, nous introduisons une carte locale des descripteurs permettant de visuellement apprécier la distribution des paramètres dans l'échantillon.

Analyse statistique

Cette méthode a été appliquée à environ 10000 lacunes par échantillon. Afin de faciliter l'analyse de ces résultats, nous avons développé des scripts permettant de calculer automatiquement des statistiques sur ces distributions : moyenne, variance et histogrammes.

Par ailleurs, nous avons réalisé une étude pour étudier les corrélations entre certains paramètres et la porosité corticale.

Validation de la méthode

La méthode complète, segmentation plus quantification a été validée en comparant les résultats obtenus à partir d'une segmentation manuelle sur un petit volume incluant environ 328 lacunes. Nous avons comparé d'une part les critères de segmentation habituels et d'autre part, les descripteurs mesurés à partir des deux segmentations. Pour la plupart des paramètres,

La moyenne et l'écart est de 93,1% ± 6,6%.

Résultats

Nous donnons les statistiques calculées sur 12 échantillons d'os cortical humain. Le nombre moyen de lacunes analysées par volume est de 12791. Le volume des lacunes était de 409,5 ± 149,7 336,2 ± µm3 et leur surface moyenne de 94,5 µm2. Les dimensions des lacunes ont été les suivantes : 18,9 ± 4,9 µm pour la longueur, 9,2 ± 2,1 µm pour la largeur et 4,8 ± 1,1 µm pour la profondeur. Nous avons trouvé que la densité de lacune et six descripteurs, les trois dimensions, deux rapports d'anisotropie et le SMI étaient significativement corrélée à la porosité de l'os.

Discussion et Conclusion

Dans ce travail, nous avons proposé une méthode d'analyse 3D automatique efficace pour extraire des descripteurs de forme 3D sur des grandes populations de cellules osseuses. Nous avons de plus proposé des cartographies de ces descripteurs permettant de visualiser simplement les propriétés locales des lacunes dans tout l'échantillon osseux. C'est le premier travail qui décrit une méthodologie cohérente pour l'ensemble des paramètres. Par exemple, dans son travail Carter donne les valeurs propres du tenseur d'ordre 2 mais sans lien avec les dimensions des lacunes. Nous avons également cherché à valider notre méthode par rapport à une segmentation manuelle, ce qui n'a jamais été réalisé quelque que soit la qualité de l'image de départ. De plus, par rapport aux travaux précédents nous avons gagné un, voire deux ordres de grandeur sur la taille des populations de lacunes qu'il a été possible d'analyser. Les descripteurs de forme observés sur les lacunes sont cohérents avec ceux de la littérature. Nous

avons également observé des variations locales des propriétés des lacunes qui sont probablement liées aux contraintes mécaniques auxquelles elles sont soumises.

Chapitre 7 : Développement d'une méthode de quantification 3D des canalicules à partir des images de micro-CT synchrotron à l'échelle sub-micrométrique

Dans ce chapitre, nous abordons le problème de la quantification des canalicules à partir des images SR micro-CT acquises à 300nm. Nous avons vu dans le chapitre 4 qu'un paramètre important par rapport à la fonction des ostéocytes, était le nombre de canalicules issues de chaque lacune. Nous chercherons donc à calculer ce nombre. Toutefois, nous avons pu observer sur images à 300nm et encore plus clairement sur les images à 60nm, que les canalicules étaient ramifiées et se subdivisaient. Nous proposons donc une méthode automatique permettant de quantifier la ramification des canalicules autour de chaque lacune.

Méthode

Nous supposons que l'image d'entrée est l'image binarisée du réseau lacuno-canaliculaire.

Dans un premier temps, il est nécessaire de séparer les lacunes et les canalicules, ce que nous réalisons par le biais d'opérateurs de morphologie mathématique. Les lacunes sont ensuite labellisées par une analyse en composante connexe. Nous chercherons ensuite à compter le nombre de canalicules issues de chaque lacune.

Pour cela, nous utilisons les nombres de Betti fournissant en 3D, le nombre de composantes connexes, le nombre d'Euler et le nombre de composantes connexes. En partant de chaque lacune, nous construisons une surface englobante par dilatation de la lacune avec un élément structurant de taille r. Nous faisons ensuite l'intersection entre cette surface et l'image de la lacune et de ses canalicules. Le paramètre r permet de caractériser à quelle distance est faite l'analyse. En répétant l'analyse à différentes distances r, on obtient donc une signature du nombre de canalicules en fonction de la distance au centre de gravité de la lacune.

Evaluation

La méthode a tout d'abord été évaluée sur un fantôme géométrique très simple, puis sur une lacune réelle isolée, présentant des branchements. Les résultats obtenus ont été conformes à ce qui était attendu sur le fantôme et sur la lacune isolée.

Application à des données réelles

La méthode proposée a ensuite été appliquée à une image de SR micro-CT d'une diaphyse fémorale d'os humain. La segmentation de cette image a été réalisée lors d'un travail précédent en utilisant la méthode de croissance de région développée dans la thèse d'Alexandra Pacureanu. Le sous volume analysé contenait 399 lacunes. Nous avons d'une part effectué l'analyse morphométrique des lacunes suivant la méthode décrite dans le chapitre précédent, d'autre part réalisé l'étude du nombre de canalicules et de la ramification de canalicules. Nous avons également calculé la distance moyenne entre deux canalicules.

Les résultats statistiques sont présentés sur 399 lacunes. Les paramètres des lacunes sont les suivant : volume moyen 216.4 ± 84.7 μm^3, surface moyenne 238.9 ± 66.4 μm^2, longueur moyenne 15.2 ± 3.7 μm, largeur 7.8 ± 1.8 μm et 4.0 ± 1.0 μm pour la profondeur.

Pour ce qui est de l'analyse des canalicules, on observe une grande variation au niveau du nombre de canalicules rayonnée de la lacunes entre 3 et 136, avec une valeur moyenne de 37 et un écart type de 17. Ceci peut s'expliquer par le fait qu'en fonction de leur localisation

certaines lacunes sont plus actives que d'autres. Par ailleurs, si on analyse séparément quelques lacunes on trouve une augmentation significative du nombre de canalicules avec la distance, ce qui démontre bien le phénomène de ramification des canalicules. On observe également que cette évolution est bien modélisée par une loi linéaire. En faisant une régression linéaire de cette évolution, on peut donc quantifier le degré de ramification des canalicules pour chaque lacune. Cette tendance ce retrouve sur la plupart des 399 lacunes analysées. Nous avons trouvé une distance moyenne entre deux lacunes de 23.2 ± 4.9, ce qui est encore cohérent avec la littérature.

Discussion et Conclusion

Nous avons proposé une méthode pour quantifier le nombre de canalicules par lacunes ainsi que leur ramification. C'est la première fois que ce calcul est réalisé sur une image 3D et que le phénomène de ramification est mis en évidence quantitativement. Dans des travaux antérieurs, le nombre de canalicules par lacune avait été extrapolé en 3D à partir de mesures faites en 2D. Une valeur moyenne de 41 avait été rapportée. Contrairement à cette méthode d'extrapolation qui permet d'estimer des valeurs statistiques, notre analyse permet de quantifier cette propriété localement sur chaque lacune de l'échantillon. Elle permet en outre d'estimer le degré de ramification.

Chapitre 8 Segmentation et quantification du réseau lacuno-canaliculaire dans une série d'échantillons humains d'os tibial

L'objectif de la dernière contribution de ce travail, était de quantifier le réseau lacuno canaliculaire sur la série d'échantillons humains présentant une variation avec l'âge et acquis en micro-CT synchrotron à 300nm. Ce travail nécessitait donc de maitriser toute la chaine de traitements, allant de la segmentation à la quantification. Pour ce qui est de la segmentation, il nous a paru intéressant d'utiliser une méthode basée sur les chemins géodésiques développée dans un travail précédent par Maria Zuluaga. Toutefois, cette méthode n'était pas exploitable directement pour traiter des images de grande taille, une grande partie de ce travail a porté sur l'amélioration de cette méthode pour pouvoir l'appliquer à nos données. Nous avons ensuite appliqué les méthodes de quantification développées dans les chapitres 6 et 7. Les résultats sur les 8 échantillons sont résumés dans des tableaux.

Images

Les images utilisées dans ce travail ont été choisies parmi les images acquises en SR micro-CT à 300nm. La procédure d'acquisition étant assez délicate du fait des problèmes de dommages liés à la dose, un certain nombre d'images ne présentaient pas une qualité suffisante pour voir des détails au niveau du voxel comme les canalicules. Notre choix a donc été fait d'une part sur la base de la qualité d'image, d'autre part sur la base du type d'échantillon. Nous nous sommes intéressés à sélectionner des échantillons qui présentaient une variation avec l'âge. Nous avons ainsi pu sélectionner des échantillons d'os cortical tibial, 3 échantillons de femmes d'âge respectifs 46, 84, 87 et 5 échantillons d'homme d'âge respectifs 29, 56, 88, 89.

Par ailleurs une étude comparative entre les images d'absorption reconstruites par l'algorithme de rétro projection filtrée et les images de phase reconstruites après application préalable de la méthode de Paganin, nous ont conduit à choisir de travailler sur ces dernières images. En effet, on observe que les canalicules sont toujours visibles, que le rapport signal sur bruit est meilleur et que de plus on distingue mieux les ostéons du tissu interstitiel, information importante pour sélectionner les régions dans lesquelles seront faites l'analyse. Dans chacune des images de ces échantillons, nous avons finalement sélection une région d'intérêt autour d'un ostéon de taille moyenne 700x700x600.

Segmentation des canalicules : travaux antérieurs

Le problème de la segmentation des canalicules est un problème très difficile compte tenu du fait que les canalicules ont une taille de l'ordre du voxel, des effets de volume partiels et du bruit qui peut être présent dans l'image. De plus ce sont des petits canaux cylindriques mais qui sont organisés en un réseau très dense et très complexe. Du fait de la nouveauté des images que nous utilisons, aucune méthode n'a encore été proposée par d'autres groupes. Dans des travaux antérieurs de la thèse d'Alexandra Pacureanu, nous avions étudié une méthode basée sur la croissance de région et une méthode de type level sets. Toutefois, nous avons observé que l'évolution dans ces deux méthodes, peut être stoppée du fait de perte de contraste dans les canalicules, conduisant à des discontinuités dans le réseau. Pour pallier à

ces inconvénients, nous nous sommes alors intéressés à une approche de type chemins minimaux, qui a été initiée dans le travail de Maria Zuluaga.

Le principe de la méthode est de détecter les chemins minimaux qui relient des points de initiaux à des points finaux, de construire une carte de vote géodésique égale au nombre de chemins passant par un point donné, les valeurs les plus élevées de cette carte correspondant à des chemins plus probables. La plupart des travaux réalisés à partir de cette méthode ont été fait sur des images 2D avec des points de départ et de fin choisis interactivement par l'utilisateur. Notre application, doit être traitée en 3D et du fait de la complexité du réseau canaliculaire, il n'est pas possible de développer une méthode interactive. Nous avons donc développé un schéma d'initialisation automatique permettant de définir les points de départ et de fin. Pour cela, nous avons utilisé une tessellation de Voronoi 3D, réalisée à partir des centres de gravité des lacunes Les points de départ sont choisis comme les centres de gravité des lacunes et les points finaux sont choisis à la surface d'une cellule de Voronoi dilatée. La méthode est implémentée par une technique de Fast Marching suivie d'une étape de backpropagation permettant d'identifier les chemins minimaux. Les premiers tests réalisés à partir de cette méthode ont donné de bons résultats sur les lacunes isolées. Toutefois, les temps de calcul étaient prohibitifs pour traiter nos volumes et certains problèmes de déconnection ou de détection de faux chemins sont apparus.

Segmentation des canalicules : contribution

Notre contribution a donc portée sur l'accélération de cette méthode, son analyse et le développement de post traitements pour améliorer le résultat de la segmentation.

Avec la version séquentielle de l'algorithme, nous avons observé un temps de calcul d'environ 30 secondes pour traiter un chemin. Pour un volume contenant 100 lacunes avec pour chacune 1500 chemins, on peut estimer le temps de calcul à 1286h, soit 53 jours !! Pour accélérer cette méthode, nous avons développé une approche parallélisée sur un cluster de machines. Pour cela, nous avons exploité le fait que le traitement peut être réalisé en parallèle sur les différentes cellules de Voronoi. Cette solution est moins simple que le découpage de l'image en blocs parallélépipédiques mais s'adapte mieux à la géométrie de notre problème. Il a donc été nécessaire de découper le volume en cellules de Voronoi étendue, d'effectuer le traitement sur chaque cellule, puis de regrouper les différents volumes traités en gérant la zone de superposition. Le traitement de chaque lacune est effectué sur une machine du cluster. De plus il existe un deuxième niveau de parallélisation qui consiste à lancer le calcul de chaque chemin sur un core de la machine. En travaillant sur 16 machines de 16 cores, le gain théorique en temps de calcul est de 256.

Au niveau des post traitements, nous avons introduit, un filtrage de rang maximal sur la carte de vote géodésique afin de limiter des discontinuités dans les canalicules que nous avons pu observer sur l'image binarisée finale.

Nous nous sommes ensuite aperçus de l'apparition de faux chemins qui n'étaient pas supportés par une observation visuelle. Pour tenter de pallier à cet inconvénient, nous avons mis en place une procédure de pondération de chaque chemin prenant en compte l'information image originale sous la forme de la carte de vesselness. Pour cela, nous avons labellisé chaque chemin et nous leur avons affecté un niveau de gris égale à la moyenne de la carte de vesselness sur ce chemin. Cette carte de chemins pondérés a ensuite été combinée à

l'image de vote géodésique afin de pondérer le vote. Ce traitement est réalisé lacune par lacune. La carte est ensuite normalisée et un seuillage est appliqué afin d'obtenir l'image binarisée finale.

Après cette segmentation, nous appliquons les méthodes de quantification présentées dans les chapitres 6 et 7. Compte tenu de la tessellation de Voronoi qui a été mise en place, nous avons ajouté le calcul du volume des cellules de Voronoi qui nous donne une information sur la zone d'influence de la lacune et nous avons modifié l'algorithme d'évaluation de la ramification pour ne prendre en compte que la région située dans la cellule de Voronoi.

Choix des paramètres et évaluation de la méthode

Nous avons tout d'abord appliqué la méthode à un volume pour sélectionner les différents paramètres de la méthode.

Le problème de l'évaluation de la méthode de segmentation pose toujours la question d'avoir une vérité terrain, généralement construite en comparant les résultats à une segmentation manuelle. Nous avons donc effectué une segmentation manuelle sur un sous volume de 512x512x512 voxels, bien que soit difficile compte tenu de la complexité et de la densité de la structure à segmenter et de la qualité de l'image. Effectuer une telle segmentation manuelle est une tache extrêmement couteuse en temps car aucune des méthodes interactives disponibles sur les logiciels de traitement d'image n'a donné de bons résultats. La solution retenue a été de tracer manuellement les canalicules coupe par coupe, ce qui pose un certain nombre de problèmes. D'une part, les canalicules se présentant comme des chemins tortueux en 3D, leur section suivant une coupe se présente sous la forme de petits segments (repérables) ou de petits cercles (moins faciles à repérer) et suivre la continuité d'une coupe à l'autre n'est également pas simple. D'autre part, du fait de la qualité des images, il existe des pertes de contraste qui soulèvent des ambiguïtés : l'opérateur peut choisir de tracer le chemin en imaginant mentalement la continuité de la canalicule ou s'arrêter. D'autre part, le nombre de segments à tracer par coupe est extrêmement grand (de l'ordre de 100 segments sur une coupe 512x512). Il est donc important de remarquer que cette segmentation manuelle nous paraît loin de constituer une vérité terrain compte tenu qu'elle n'est pas nécessairement reproductible ou correcte. Toutefois, nous présentons dans le manuscrit la comparaison entre l'image segmentée automatiquement et cette segmentation manuelle. On observe une certaine similarité entre les deux images mais la segmentation manuelle est beaucoup plus dense. Toutes les images étant segmentées avec la même méthode automatique, on peut penser que les structures canaliculaires seront sous estimées de la même façon et l'étude comparative entre les échantillons reste possible.

Résultats

Les résultats statistiques sont présentés sur 8 images incluant entre 100 et 200 lacunes pour chaque volume.

Les paramètres des lacunes sont les suivant : Le volume des lacunes était de 372.9 ± 119.6 μm^3 et leur surface moyenne de 377.7 ± 89.7 μm^2. Les dimensions des lacunes ont été les suivantes : 21.1 ± 5.1 μm pour la longueur, 9.0 ± 2.1 μm pour la largeur et 4.5 ± 1.1 μm pour la profondeur. Nous avons trouvé que la densité de lacune et six descripteurs, les trois dimensions, deux rapports d'anisotropie et le SMI étaient significativement corrélée à la porosité de l'os.

Conclusion

Les développements réalisés dans ce chapitre nous ont permis de passer de la segmentation d'une lacune isolée à celle sur des centaines de lacunes. La segmentation des canalicules est un problème difficile pour lequel une solution a été proposée. Toutefois, si la segmentation est compatible avec ce que l'on sait des réseaux canaliculaires, une évaluation rigoureuse de la méthode est difficile. Nous avons tenté de la comparer la méthode à une segmentation manuelle, mais celle ci ne constitue par nécessairement une vérité terrain. Nous avons également observé quelques limitations à cette méthode. Un travail supplémentaire est donc nécessaire pour encore améliorer la segmentation des canalicules. Néanmoins, il a été possible de mesurer les caractéristiques les lacunes et de donner une première évaluation du nombre de canalicules par lacunes sur un série d'échantillons humains.

Chapitre 9 : Conclusion générale et Perspectives

Les travaux regroupés dans ce manuscrit ont permis de développer des méthodes permettant de quantifier le réseau lacuno-canaliculaire à partir d'images de micro CT synchrotron à différentes résolutions spatiales. Les difficultés résidaient dans le traitement de gros volumes de données et la nécessité de développer des méthodes automatiques et efficaces.

Nous avons été amenés dans ce travail à participer à différentes campagnes d'acquisition de données sur des systèmes expérimentaux de micro et de nano CT synchrotron développées à l'ESRF de Grenoble. Nous avons donc du maitriser l'aspect expérimental et toute la chaine de traitements à mettre en œuvre pour arriver jusqu'à une image finale exploitable pour l'analyse ultérieure. Dans ce cadre, nous avons pu acquérir des images d'échantillons osseux à différentes résolutions : 1.4µm, 300nm et 60nm.

Pour ce qui est de l'analyse des lacunes ostéocytaires, nous avons mis en place une chaine de traitements automatique, permettant d'extraire un grand nombre de descripteurs de forme sur ces lacunes et de réaliser des analyses statistiques sur de grandes populations de cellules. Cette méthode a été appliquée à l'analyse de 12 échantillons d'os cortical humain et a fourni des mesures quantitatives robustes notamment sur le volume, les surfaces et les dimensions des lacunes.

Pour ce qui est de l'analyse des canalicules, nous avons proposé d'extraire automatiquement le nombre de canalicules par lacune, ainsi que d'étudier leur ramification. Ceci a été mis en place grâce au calcul de paramètres topologiques sur des voisinages des lacunes. Cette méthode a été illustrée sur un échantillon d'os cortical humain imagé à 300nm. Elle a permis pour la première fois de quantifier la ramification des canalicules dans tout un ostéon.

Nous avons ensuite cherché à appliquer les méthodes développées sur une série d'échantillons présentant des variations avec l'âge. Dans cette étude, il a fallu mettre en place une méthode de segmentation utilisable sur des sous volumes contenant en moyenne 110 lacunes. Pour cela, nous avons contribué au développement d'une méthode basée sur les chemins géodésiques minimaux. Nous avons parallélisé cette méthode afin de la rendre utilisable sur nos données et nous avons apporté divers raffinements. Nous avons également construit une segmentation manuelle pour évaluer nos résultats. Après segmentation, des paramètres quantitatifs ont été extraits sur les lacunes et les canalicules. Malgré les limitations observées, les données obtenues dans le cadre de ce travail sont totalement originales.

Si l'objectif de cette thèse était tout d'abord orienté vers la quantification des structures à partir des images binarisées, il a été nécessaire de travailler sur le problème de la segmentation pour traiter un jeu de données réelles. De ce coté, l'évaluation des méthodes de segmentation des canalicules à 300 nm reste un point difficile qu'il sera nécessaire de poursuivre dans des travaux ultérieurs. Comme nous l'avons fait remarquer, la segmentation manuelle ne garantit pas d'être une vérité terrain. Idéalement imager la même structure à 300nm et à 60nm pourrait permettre d'avoir une vraie vérité terrain. Toutefois, d'un point de vue pratique, cela nécessite d'irradier deux fois l'échantillon, ce qui peut induire des dommages et dégrader la qualité de l'une des images. Une autre piste serait la réalisation d'un

fantôme numérique permettant de tester les méthodes, ce qui nécessiterait le développement d'outils de simulation réaliste.

Au niveau de la quantification, la méthode proposée sur les lacunes paraît assez aboutie. Pour ce qui est de la structure canaliculaire, de nombreux développements restent possibles pour mieux la caractériser. En particulier, des approches basées sur des squelettisation pourraient permettre d'extraire des paramètres du réseau, tels que le nombre de nœuds, les longueurs moyennes des canalicules entre nœuds, le longueur totale des canalicules issues d'une lacune. Par ailleurs, il serait intéressant de voir quels paramètres sont plus adaptés selon que l'on travaille à 300nm ou à 60nm. A 300nm, un problème bloquant étant la segmentation des canalicules à cette échelle comme on l'a vu, une autre perspective pourrait être de travailler directement sur l'image à niveau de gris, sans segmentation, en utilisant par exemple des approches d'anamyse de texture.

Sur le plan biologique, ce travail ouvre de nombreuses perspectives compte tenu qu'il n'existe encore très peu de données quantitatives sur le réseau lacuno canaliculaire en 3D. D'une part, la méthode développée sur les lacunes est suffisamment mure pour pouvoir être exploitée sur des séries d'échantillons, soit afin de mesurer des variations avec l'âge, la maladie ou le site anatomique. Pour ce qui est des canalicules, des développements supplémentaires pourraient également apporter des informations inédites sur ce réseau mal connu. Enfin notons que les images segmentées du réseau lacuno canaliculaire ont également un grand intérêt comme point d'entrée pour réaliser des simulations biomécaniques sur des données réalistes.

SYMBOL LIST

Bone tissue:

N.Lc – number of osteocyte lacunae
Lc.TV – total lacunae volume (mm^3)
Ca.TV – total canaliculi volume (mm^3)
BV – bone volume (mm^3)
TV – tissue volume (mm^3)
BV/TV – bone volume fraction (%)
HCa.V/TV – canal volume fraction or bone porosity (%)
Lc.TV/BV and Lc.TV/TV– lacunar volume density (mm^{-3})
Ca.TV/BV and Ca.TV/TV– canalicular volume density (mm^{-3})
LCN.TV/BV and LCN.TV/TV– lacuno-canalicular network volume density (mm^{-3})
N.Lc/BV and N.Lc/TV– lacunar number density (mm^{-3})
$HCa.SD_{50}$ – average distance of 50% of bone matrix to the nearest Haversian canal (μm)
$HCa.SD_{95}$ – average distance of 95% of bone matrix to the nearest Haversian canal (μm)

Lacunae:

Lc.V – lacuna volume (μm^3)
Lc.Tess.V – lacunar territory volume (μm^3)
Lc.S – lacuna surface area (μm^2)
Lc.L1, Lc.L2 and Lc.L3 – length, width and depth of lacuna (μm)
Lc.L1/Lc.L2 and Lc.L1/Lc.L3 – anisotropy of lacuna
Lc. SMI – structural model index of lacuna
$Lc.SD_{50}$ – average distance of 50% of bone matrix to the nearest lacuna (μm)
$Lc.SD_{95}$ – average distance of 95% of bone matrix to the nearest lacuna (μm)
Ratio (τ) – volume ratio of lacuna to fitting ellipsoid (%)
Ellip.V – fitting ellipsoid volume (μm^3)
Ellip.S -- fitting ellipsoid volume (μm^2)

Canaliculi:

Lc.NCa(r) – number of canaliculi per each lacuna at r distance (μm) from the surface of lacuna

I. BACKGROUND

Chapter 1

Introduction

Contents

1.1 Background.....3
1.2 Thesis objective.....3
1.3 Layout of the thesis.....3

1.1 Background

Osteoporosis is a bone fragility disease, consequently leading to bone fractures, which greatly affect the basic quality of life around the world. According to survey of the International Osteoporosis Foundation, it is reported that one out of three women and one out of five men over the age of 50 will suffer an osteoporotic fracture. About 200 million women, which are more than the combined populations of France, Germany and United Kingdom, have osteoporosis. The number of hip fractures caused by this disease is expected to increase about three-fold in the following decades. Unfortunately, bone fragility remains only partially understood despite decades of research in this area.

Throughout the lifespan, bone is constantly changing its mass and structure adapting to the environmental loading and other biological stimulus. Recently a lot of attention has been focused on the osteocytes which are the most numerous bone cells. They are hypothesized to act as mechanosensors and mechanotransductors, translating the mechanical signals into biochemical signals and propagating these signals to other bone cells to control the bone modeling and remodeling processes. The osteocyte system forms a complex network deeply embedded in the bone matrix, and the imprints of this network is called the lacuno-canalicular network (LCN). The osteocyte bodies are encysted in cavities called lacunae and the cell processes is enclosed in tunnels called canaliculi. Recent studies highlighted the important role of the LCN porosity in terms of mediating osteocyte mechanosensing. It has been pointed out the LCN porosity can dramatically change the fluid flow shear stress exerted on the membrane of the osteocyte, in turns, affecting the osteocyte functionality. However, the exact mechanisms involved in the osteocytes activity and the influence exerted by the LCN are not precisely elucidated and remain controversial since quantitative tools to analyze the LCN are lacking.

In previous studies of our research group, synchrotron radiation (SR) micro/nano-CT was shown to present many advantages for imaging the LCN in 3D at sub-micrometer and nanometer scale. Although some studies have recently been conducted to assess the morphology of the LCN, up to now, there is no specialized automatic method to extract LCN properties, neither in its description nor on its validation, and the numbers of samples and subjects analyzed so far, were quite limited.

1.2 Thesis objective

The aim of this thesis was to develop new three dimensional image analysis methods to obtain characteristics on bone cellular structures, providing tools dedicated to the automatic and quantitative analysis of the large SR micro/nano CT 3D images.

1.3 Layout of the thesis

The manuscript is organized as follows:

- Introduction part: Chapter 1 introduces briefly the general background, points out the aim of this work and explains the layout of this thesis.

- Background part: This part includes 3 chapters introducing the necessary background, knowledge and the state of the art related to this work.
    - In Chapter 2, we describe the hierarchical structure and basic functionality of the bone tissue. The structure and functionality of the osteocytes and the relationship between the osteocyte system and the LCN are presented.
    - In Chapter 3, we briefly review the existing imaging techniques for the investigation of the osteocytes and LCN. The pros and cons of each technique are discussed.
    - In Chapter 4, we review the state of the art related to the quantification of the osteocytes and LCN. We describe the parameters that have been used to characterize both the lacunae and the canaliculi. An exhaustive study of the literature is synthesized on tables which report tissue and morphological parameters of the LCN from 2D and 3D studies, both in human and animals.
- Contribution part: This part presents my main contributions in imaging the LCN and in the developments of new three dimensional image analysis methods to characterize the bone cellular structures.
    - In Chapter 5: we present our work related to image acquisition at various spatial resolutions by using different SR CT system at ESRF. In this chapter we recall the principle of absorption and phase CT, the image reconstruction techniques and the correction techniques that were applied to raw data.
    - In Chapter 6: we propose an automatic and efficient direct 3D analysis to extract 3D morphological descriptors of lacunae on a large population of bone cells. The method was applied to a series of 13 human bone samples.
    - In Chapter 7: we propose an automatic method to quantify the number of canaliculi around each lacuna in 3D based on a previous segmented LCN image. The ramification process of canaliculi was evidenced and quantified.
    - In Chapter 8: we propose an improved automatic LCN segmentation scheme based on geodesic voting. We illustrate the feasibility of using the proposed method to conduct automated quantification on a series of bone specimens.
- Conclusion and perspective part: Chapter 9 concludes the contributions of this thesis and gives the perspectives to the future works.
- Annexes:
    - In Annex 1: we include the tables of the quantitative parameters of the osteocyte and LCN on animal samples.
    - In Annex 2: we include images of the series of samples that were processed in chapter 8 at various spatial scales showing a global view of the sample and the location of the sub samples that were cut for imaging at 300 nm.
    - In Annex 3: we briefly describe the implementation of our automatic quantification tools for the 3D assessment of the LCN.

Chapter 2

Bone tissue and embedded osteocytes

Contents

2.1 Introduction 6
2.2 Hierarchical structure of bone 6
2.3 Bone dynamics 11
2.4 The osteocytes 13
2.4.1 Structure of the osteocyte network 13
2.4.2 Functions of the osteocyte network 14
2.4.3 Relation between LCN morphology and the osteocytes functions 15
2.5 Conclusion 15

2.1 Introduction

Bone is a connective tissue that performs diverse mechanical, biological and chemical functions, such as biomechanical support and protection, red blood cell production and calcium ion homeostasis. It is a stiff composite material mainly consisting of collagen fibers, which gives the bone elasticity to resist the bone fracture, and mineral calcium phosphate, which gives the stiffness of the bone tissue. Bone also contains other small amount of substances such as water, proteins and inorganic salts. As a living material, the bone tissue is embedded with cells, nerves and vessels. It is a structured material with a hierarchical arrangement from the macroscale to the sub-nanoscale, constantly changing its mass and structure throughout the lifespan. Most of bones are hollow and are filled with bone marrow, which produces red blood cells in a process called hematopoiesis and lymphocytes to support the immune system, or only stores fat. As a system, there are over 270 bones in the human skeletal system, and they are connected by tendons and ligaments attached to the ends of bones.

2.2 Hierarchical structure of bone

Bone tissue is not a simple and evenly solid material, but a rather complex structured material with a hierarchical arrangement from the macroscale to the sub-nanoscale. In specific, there are about five levels in length scales, (see Figure 2.1): (1) at macro level (organ level): cortical and cancellous bone; (2) at micro level (from 10 to 500 μm): Haversian system, osteons and single trabeculae; (3) at sub-micro level: (1–10 μm): lamellae; (4) at nano level (from a few hundred nanometers to 1 μm): fibrillar collagen and embedded mineral; and (5) at sub-nano level (below a few hundred nanometers): molecular structure of constituent elements, such as bone mineral crystal and collagen molecule [Rho *et al.* (1998)]. This hierarchical arrangement is complex but optimized to bone constraints.

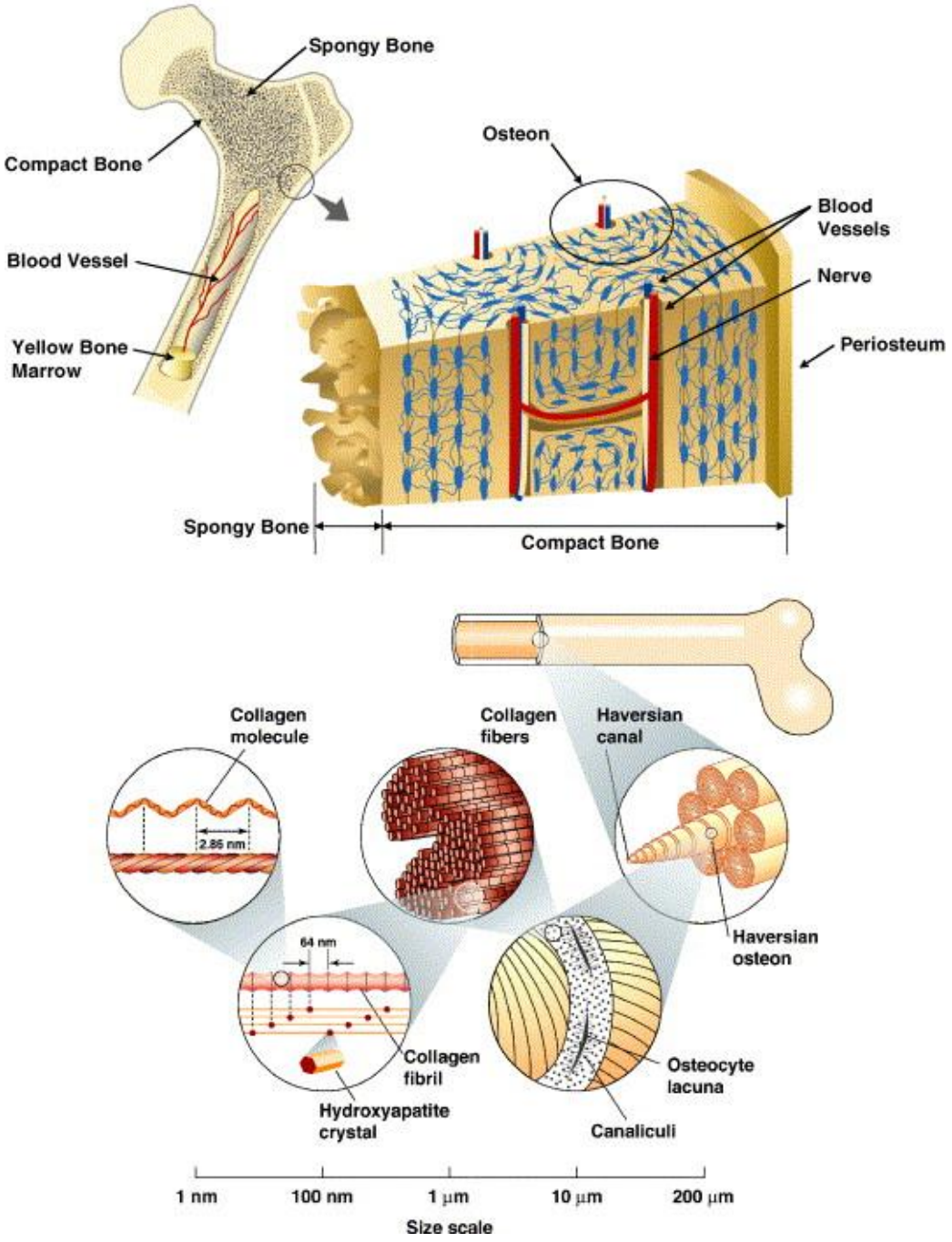

Figure 2.1 Bone hierarchical structure at different length scale. (Image from [Nalla et al. (2006)])

At macroscopic level, human bone is made of two morphological distinctive parts, the cortical bone and cancellous bone.

The cortical bone forms the shell of the bone and ensures a function of mechanical support and protection. It is the densest part of the bone (see Figure 2.2) and contributes to about 80% of the total mass of the skeleton. The cortical bone is quite dense, and its porosity is around 5% to 10% [Martin *et al.* (1998)]. Despite its compactness, the cortical bone contains a small

amount of pores, including the bone cells, blood vessels, nerves and some resorption cavities. The surface of the cortical bone is relatively smaller compared to the cancellous bone, contributing to about 33% of the total bone surface. Since the modifications of the bone tissue occur on the bone surface, the cortical bone undergoes a lower turnover rate than cancellous bone and is comparatively more mineralized.

Figure 2.2 Cortical bone. (Image from http://www.bonebank.com/femur-section.html)

The cancellous bone is enclosed in medullary cavities of the bone tissue, and is composed of trabecular struts, having a thickness of about 150-200 µm [X Wang *et al.* (2010)]. The trabecular struts, which are generally plate or rod like form a spongy-like network. The cancellous bone also known as spongy bone is quite porous with a porosity in the range of 75% to 95%. The porous phase contains blood marrow and vessels. It does not sustain much of the mechanical loading. In contrast to cortical bone, the lamellae in the cancellous bone are in a form of irregular and sinuous shape.

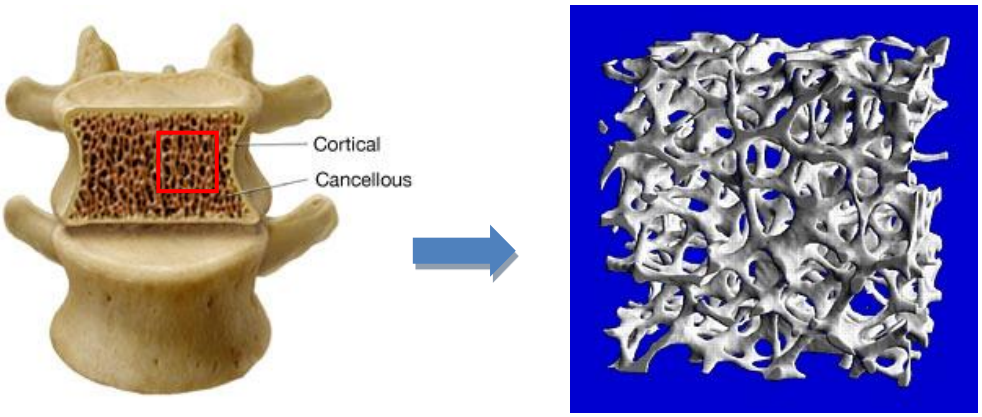

(a) (b)

Figure 2.3 spongy bone and trabecular struts (a) http://stg.centrax.com/ama/osteo/part4/module03/02path/02.htm (b) http://www2.warwick.ac.uk/fac/sci/wmg/project/internships/projectslist_2013/trabecular_bone/

At the microscopic level, there are two types of basic architectures in both cortical and cancellous bone, woven bone and lamellar bone. The woven bone forms quickly in new tissue and is intertwined by random oriented collagens fibers, and it is also known as the primary

bone. After a while (usually one month), the woven bone is began to replace by the lamellar bone, which is characterized by the regular parallel alignment of collagen. After the resorption of the primary bone, the newly formed replacement is called secondary bone. Such bone resorption and formation is known as bone remodeling. Compared to the woven bone, the lamellar bone is laid down slowly, less than 1 µm per day [Currey (2002)] (Figure 2.4(a)). Its observation in polarized light microscopy (Figure 2.4(b)) shows an alternance of bright and dark lines. The thickness of the lamellae can vary from 3 µm to 7 µm [Marotti (1993)], depending on how the mineral crystals are organized. The orientation of the lamellar bone has a large impact on the mechanical property of the bone tissue. Lamellar bone is the basic building blocks of the matured trabecular bone and cortical bone.

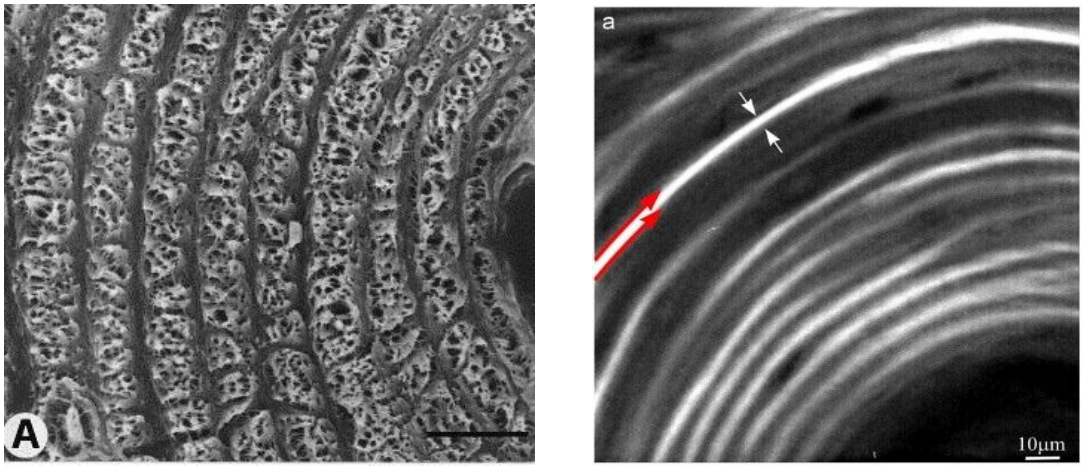

(a) (b)

Figure 2.4 Lamella (a) lamellae under SEM [Ardizzoni (2001)] (b) lamellae under circularly polarized light [Ascenzi *et al.* (2008)]

In cancellous bone, few concentric lamellae build the trabecular bone. In the cortical bone, the lamellae appear in the Haversian or the osteonal system, Figure 2.5. The osteons form a cylindrical structure in the cortical bone, with an average diameter of approximately 200 µm. The Haversian canal is located at the center of osteon, containing blood vessels and nerves. The osteons are basically parallel to each other along the axis of the long bone, but they may also branch and connect to adjacent ones through canals called Volkmann's canals. The osteon has an outer sheath called the cement line, which separate the osteon and the interstitial tissue. The interstitial tissue is formed by interstitial lamellae, which are a mixture of primary bone or the remnants of the primary and secondary osteon, lying between the osteons. The interstitial and the osteonal tissue can be distinguished from the arrangement of the lamellae or from the degree of mineralization of bone. Normally the interstitial tissue has a higher degree of mineralization, because they are older tissue than the osteon.

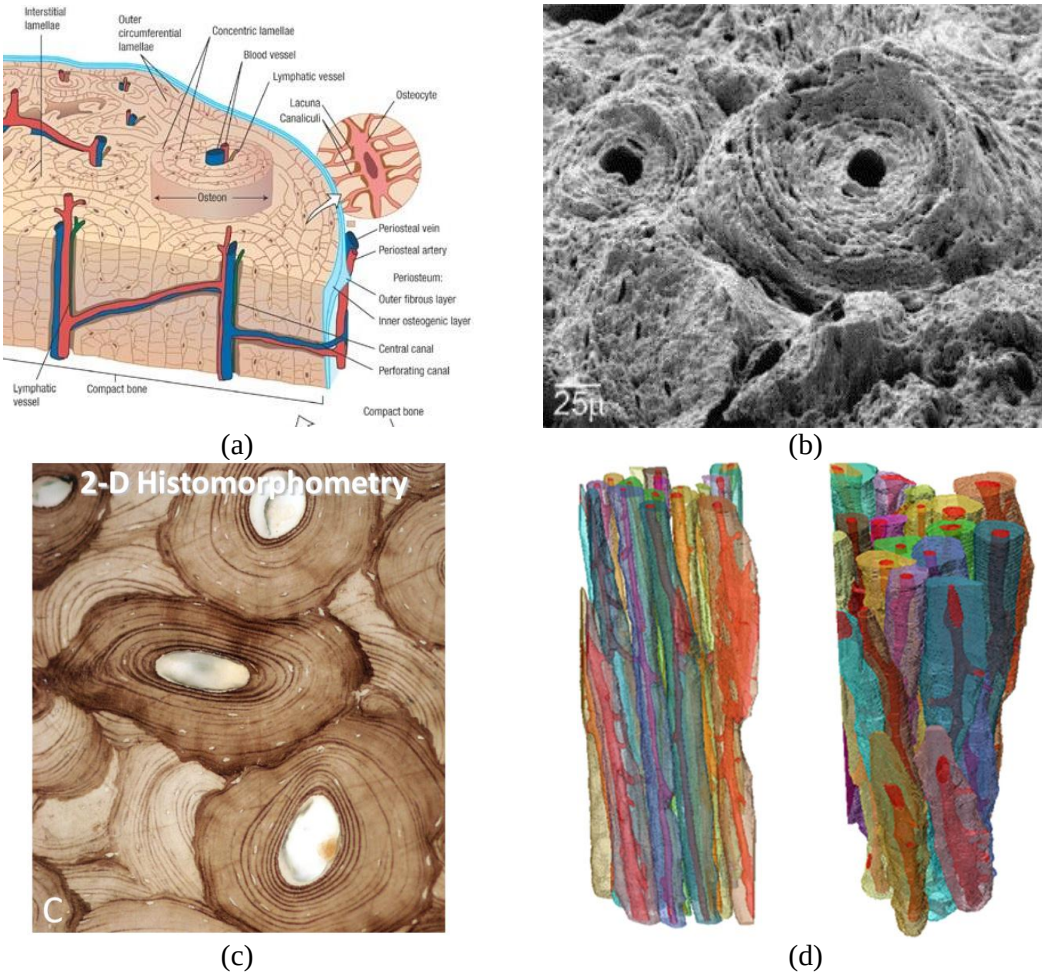

Figure 2.5 Osteon (a) scheme illustration of osteon [Taylor *et al.* (2007)] (b) SEM Image of osteons [Sahar *et al.* (2005)] (c) 2D Histomorphometry of osteon [Busse *et al.* (2010)] (d) 3D rendering of osteons in human femoral bone, segmented from micro-CT image [Arhatari *et al.* (2011)]

At the nanoscale, the bone matrix is composed by water and organic materials, mostly collagen, and infiltrated apatite mineral.

The collagen of bone has the same composition as in skin and tendon, which is known as *type I* collagen. This kind of collagen comprises about 90% of the proteins in bone [Currey (2002)], providing strength and to the bone [Boskey *et al.* (1999); Viguet-Carrin *et al.* (2006)]. The rest of the proteins, which are not contained in collagen, are called noncollagenous proteins (NCPs). These NCPs perform their functions in binding the collagen and mineral together, and in regulation of mineralization [Roach (1994)]. The collagen is made of collagen molecules secreted by osteoblasts [Rho *et al.* (1998)]. These molecules are approximately 300 nm in length and 1.2 nm in diameter [Weiner *et al.* (1999); X Wang *et al.* (2010)]. They are cross-linked into collagen fibrils with a specific structure having a 67 nm periodicity and 40 nm gaps or holes between the ends of the molecules [Rho *et al.* (1998); X Wang *et al.* (2010)], Figure 2.6. These fibrils are aggregated into collagen fibers, the width of which may vary from a few hundreds of nanometers to 1 μm [Rho *et al.* (1998)].

Bone mineral is surrounded and impregnated with the bone collagen. The mineral is in a form of very small crystals, which mainly contains $Ca_{10}(PO_4)_6(OH)_2$ [Rey *et al.* (2009)]. Under electron microscopy and small angle X-ray scattering, these crystals are observed in a shape of plate-like structures, which average dimensions of 50 nm in length, 25 nm in width and 2~3 nm in depth [Rho *et al.* (1998)]. The long axis of the crystal is lining along the collagen fibrils, and they are located periodically in the contiguous gaps along the collagen network, Figure 2.6 [Landis *et al.* (1996)]. The orientation and organization of the bone mineral is important in terms of bone mechanical properties [Sasaki *et al.* (1989)].

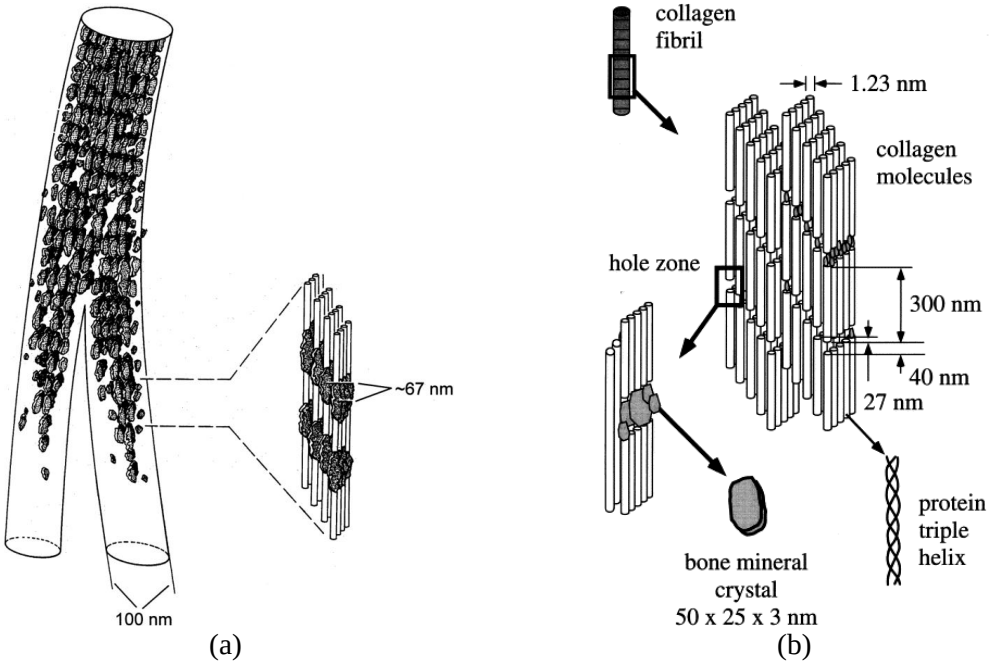

Figure 2.6 Bone collagen and mineral crystal (Image from: [Landis et al. (1996)] and [Rho *et al.* (1998)])

2.3 Bone dynamics

Bone is a dynamic tissue constantly changing its mass and structure though three major biological mechanisms: growth, modeling and remodeling [Deng *et al.* (2005)]. The bone growth expends the size of bone in both the longitudinal and radial directions throughout the childhood and adolescence. Bone modeling changes the bone mass and its skeletal form, and it is quite important during the bone growth. Bone remodeling, coupling sequentially bone resorption and bone formation, allows the adaption of bone to the mechanical and non-mechanical stimuli throughout the life. In aging, the major function of remodeling is to maintain the strength of bone by replacing the old damaged tissues. After the age of 30, it is estimated that the balance between bone formation and resorption begins to decline and on average, about 1% of total bone mass is lost every year [Deng *et al.* (2005)]. After the age of 50, according to the survey from the international osteoporosis foundation, one out of three women (over 200 millions of women) and one out of five men around the world will

experience an osteoporosis fracture due to the insufficient bone mechanical capacity. As a consequence, people endure great pain and make daily activities extremely difficult.

From a biological point of view, the bone remodeling process can be described in five steps, activation, resorption, reversal, formation and quiescence, involving different bone cells (Figure 2.8) to perform specific duties (Figure 2.7).

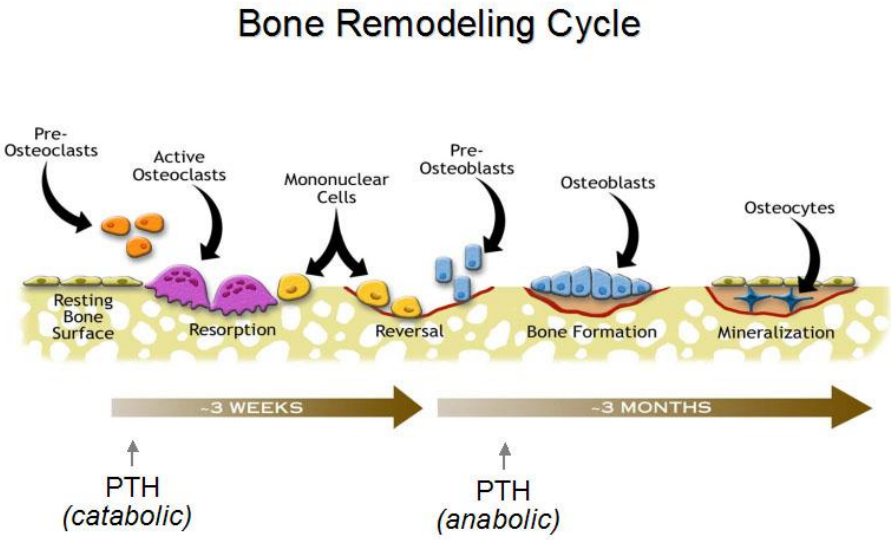

Figure 2.7 Bone remodeling process. (http://www.ns.umich.edu/Releases/2005/Feb05/img/bone.jpg)

During the activation phase, the pre-osteoclasts are differentiated into the osteoclasts under the environmental stimulation. The bone-lining cells migrate to the adjacent marrow. The mature osteoclasts then migrate and attach to the exposed mineral surface [Deng *et al.* (2005)]. During the resorption phase, the osteoclasts digest the bone matrix by creating an acidic environment. These cells are large cells with multiple nuclei, about 40 micrometer in diameter. During the reversal phase, bone resorption stops and bone formation is about to begin through the action of osteoblasts. The collagen matrix is first laid down by these cells and then the bone mineral is deposited later in a long period. During the bone formation, some osteoblasts undergo a series of changes. While most osteoblasts are working on the surface of bone, some of them are left behind and embedded inside the bone matrix. These cells differentiate into osteocytes (see next 2.4). The number of osteoblasts is of importance in terms of bone formation. The decreasing of the number of osteoblasts will cause the unbalance of the bone formation and resorption, potentially leading to osteoporosis. At the end of the bone formation, the osteoblasts are gradually differentiated into bone-lining cells, and the bone turns to a quiescence phase [Deng *et al.* (2005)].

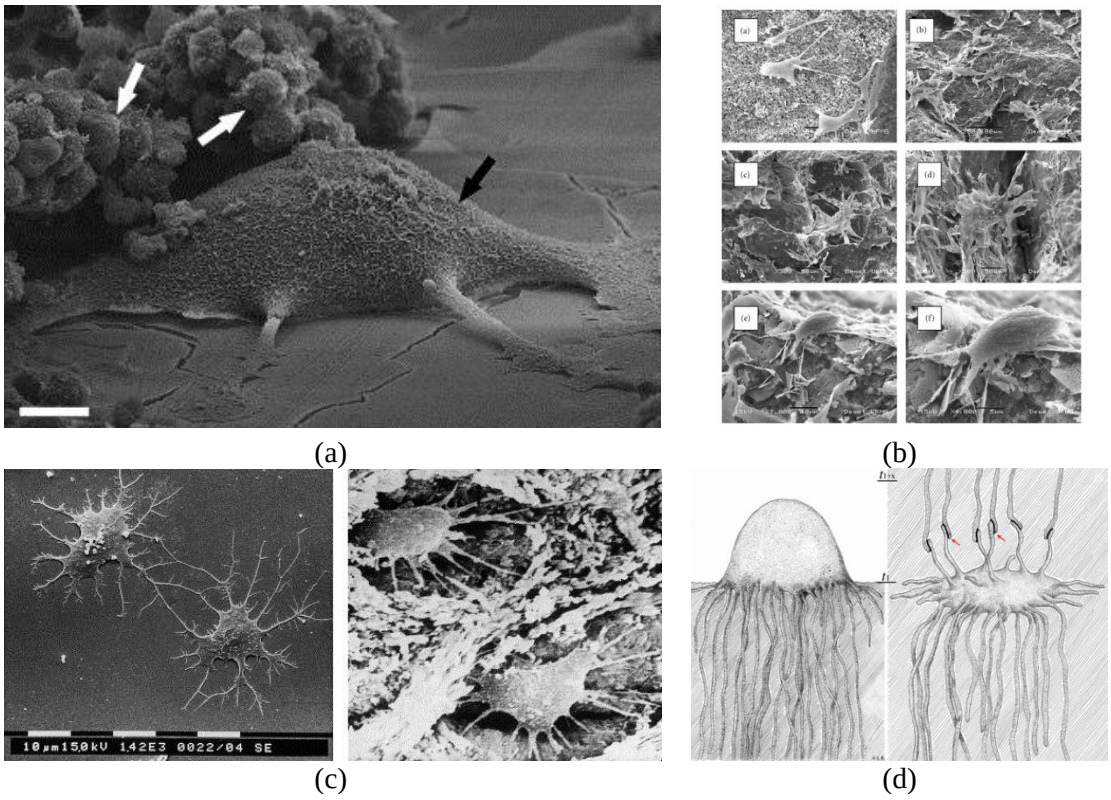

Figure 2.8 Bone Cells (a)SEM image of osteoclast: (Image from: [Gentleman *et al.* (2010)] (b)SEM image of osteoblast (Image from: [Shainberg *et al.* (2012)] (c) SEM image of osteocyte (Image from: [Klein-Nulend *et al.* (2005)] (d) osteoblast and osteocyte (Image from: [Pazzaglia *et al.* (2012)]

2.4 The osteocytes

2.4.1 Structure of the osteocyte network

The osteocytes are derived from embedded osteoblasts during the bone formation process. The body of the osteocyte is encysted in a chamber, called the lacuna. The osteocytes possess dendritic processes enclosed in the slender tunnels, known as canaliculi. These processes connect the osteocytes between them or extend towards the bone cells on the bone surface or the vascular canal. Consequently, the embedded osteocytes form a connected cellular network (CCN) embedded in a complex void network known as the lacuno-canalicular network (LCN), thought out the whole bone tissue, Figure 2.9. The scheme of CCN and LCN is shown in Figure 2.10 (a), and (b) shows the complex structure LCN under the SEM.

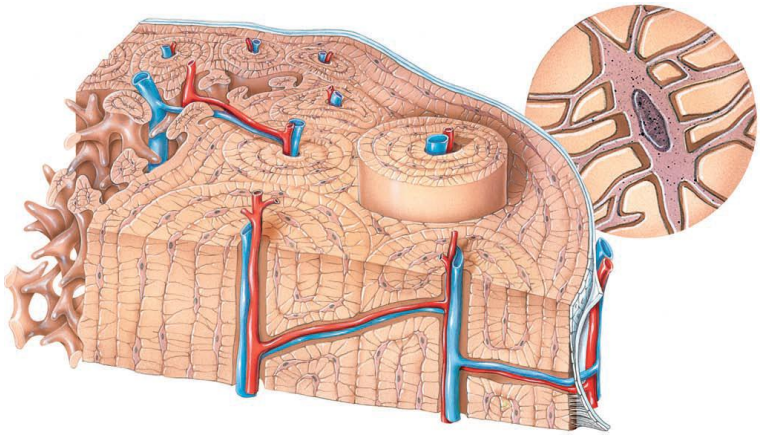

Figure 2.9 Osteocytes and the lacuno-canaliculi network.

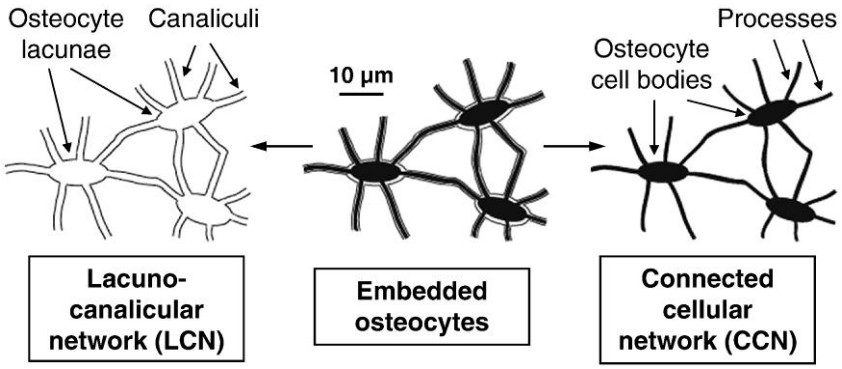

(a)

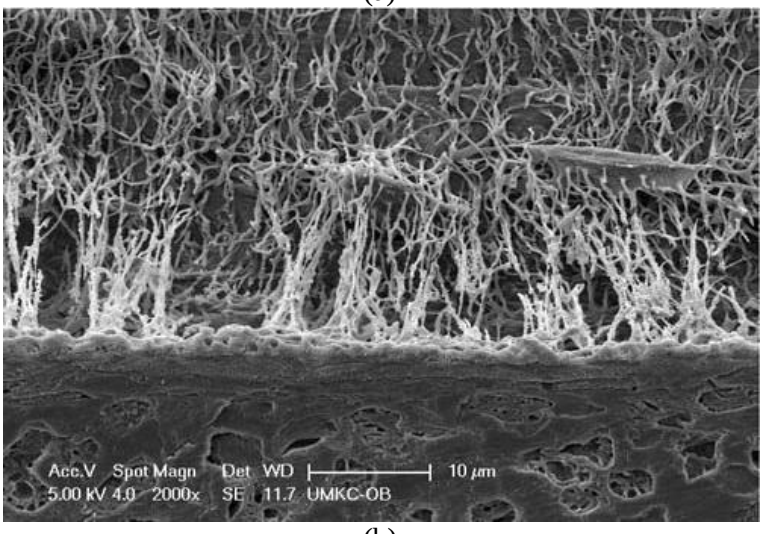

(b)

Figure 2.10 embedded osteocyte and lacuna-canaliculi network (a) scheme of LCN and CCN (Image from: [Schneider *et al.* (2010)]) (b) SEM of LCN (the letter "L" indicate the lacunae) (Image from: [Bonewald (2011)])

2.4.2 Functions of the osteocyte network

While the osteocytes were traditionally thought to be passive static cells buried in the bone matrix, they are now raising increasing interest for their important role in maintaining the proper functionality of the bone tissue.

One of the postulated functions of osteocytes is that they can act as mechanosensors, performing specific functions with respect to the fluid-flow shear stress. On one hand, the osteocytes can sense the mechanical loading through the cell body, the dendritic processes or the cilia of the cell [Bonewald (2006)]. These mechanosensory cells that translate mechanical stimuli into electrical or biochemical signals and orchestrate the osteoclasts and the osteoblasts to perform bone resorption and formation [Burger *et al.* (1999); Bonewald (2006); Bonewald *et al.* (2008)]. On the other hand, the osteocytes might change morphology in response to the environmental stimuli. It was shown that under the fluid-flow shear stress on osteocyte-like MLO-Y4 cell, the number and length of the cell processes increased [Zhang *et al.* (2006)]. Other studies showed that the osteocytes might change their morphology with aging [Okada *et al.* (2002); Holmbeck *et al.* (2005)].

Besides, the osteocytes are also hypothesized to involve the phosphate and biomineralization regulation by secreting molecules [Westbroek *et al.* (2002); Bonewald (2007)]. It was pointed out the osteocyte might perform functions like an endocrine system, which target distant organs, such as kidney, to excrete or absorb phosphate circulated in the body [Bonewald (2011)].

In addition, recent study indicated that the osteocytes could also regulate the perilacunar matrix. They might modify the size of lacuna by removing and replacing their perilacunar matrix and potentially involved in the regulation of mineral homeostasis during a calcium-demanding condition such as lactation [Bonewald (2011)].

2.4.3 Relation between LCN morphology and the osteocytes functions

The lacuno-canalicular network houses the connected osteocyte network. Therefore, it might has an influence on the osteocyte mechanosensation and transduction directly by the contact of the bone matrix or indirectly by the mediated fluid-flow inside the LCN network. In any case, the morphology and the mechanical property of the LCN are important factors to affect and reflect the viability of the osteocytes. Some studies mentioned that different shape of the lacunae can significantly change the magnitude of bone fluid shear stress loaded on the osteocyte [Currey (2003a); Mullins *et al.* (2007); Bacabac *et al.* (2008)]. Besides, the size of the lacunae and canaliculi can be served as an important indicator to reflect the calcium-demanding conditions. It has been observed that the size of osteocyte lacunae and width of the canaliculi are significantly increased in bone, during lactation [Bonewald (2011)].

2.5 Conclusion

In this chapter, a brief review on the hierarchical structure and functions of bone was presented. At the cell level, we highlighted the important role of the LCN in relationship to the proper functions of the osteocytes, which might significantly relate to the quality of bone. This motivated the objectives of this thesis to develop new methods to quantitatively study the morphology of the bone cell network.

Chapter 3

Imaging the lacuno-canalicular network

Contents

3.1 Introduction 17
3.2 2D imaging techniques 18
3.2.1 Optical microscopy 18
3.2.2 Electron Microscopy 19
3.2.2.1 Scanning electron microscopy (SEM) 19
3.2.2.2 Transmitted electron (TEM) 21
3.2.3 Atomic Force Microscopy 23
3.3 3D imaging technique 23
3.3.1 Confocal laser scanning microscopy 23
3.3.2 X-ray computed tomography 24
3.3.2.1 Synchrotron light source CT 25
3.3.2.1.1 SR micro-CT 25
3.3.2.1.2 X-ray magnified phase tomography 26
3.3.2.1.3 Transmission X-ray microscope (TXM) 27
3.3.2.1.4 Ptychographic X-ray CT 28
3.3.2.2 Laboratory source micro/nano CT 29
3.3.3 Focused ion beam - scanning electron microscopy (FIB/SEM) 30
3.4 Conclusion 31

3.1 Introduction

The development of the ideal imaging technique to reveal the ultra-structure of the bone tissue is quite challenging. This challenge arises from two main reasons. A first reason is related to the location of LCN, which is hard to reach since it is deeply embedded in the hard bone tissue. A second reason, is the complexity of the organization of the LCN which form a dense and ramified network: in human cortical bone, the density of lacunae is on an average of 26 to 90 × 10^3 per mm^3, and the width of canaliculi is between 100~500 nm.

Until now, various imaging modalities have been used for the investigation of the LCN. Due to the size of the structures to be examined (lacunae: a few tenths of micrometers, canaliculi: a few hundred nanometers), various imaging techniques at different scale are needed. We review these imaging modalities classified according to their spatial resolution and nature (2D versus 3D), Figure 3.1. The main features of each image technique are summarized in Table 3.1.

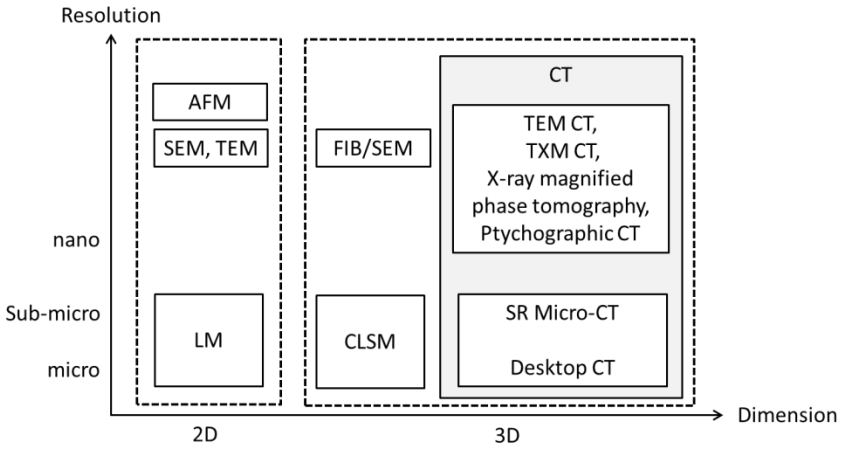

Figure 3.1 Hierarchical imaging techniques for LCN investigation. LM: Light Microscopy, SEM: Scanning Electron Microscopy, TEM: Transmission Electron Microscopy, AFM: Atomic Force Microscopy, CLSM: Confocal Laser Scanning Microscopy, FIB/SEM: Focused Ion Beam coupled with Scanning Electron Microscope, TXM: Transmission X-ray Microscope, SR Micro-CT: Synchrotron Radiation Micro computed tomography

Table 3.1 Imaging modalities for the investigation of LCN and CCN

Technique	2D/3D	Resolution	Main pros	Main cons	References
LM	2D	~ 300 nm	Functional imaging by fluorescent labeling, Soft tissue contrast, No dose damage	Inherently 2D, time-consuming process	[FROST (1960); Shapiro (1988); Marotti *et al.* (1995); Remaggi *et al.* (1998); Ferretti *et al.* (1999); Ardizzoni (2001); Hirose *et al.* (2007); Schneider *et al.* (2010)]
SEM	2D	~ 2 nm	High resolution	Inherently 2D, Ultra-thin sectioning, Limited field of view FOV	[Kubek *et al.* (2010); Pazzaglia *et al.* (2012)]
TEM	2D	~ 1 nm	High resolution	Inherently 2D, Ultra-thin sectioning,	[Wassermann *et al.* (1965); Palumbo *et al.* (1990); Rubin *et al.* (2004), (2005); L You *et al.*

				Limited FOV	(2004); Deligianni *et al.* (2008)]
AFM	2D	~50 nm	High resolution	Destructive, time-consuming processing, small FOV	[Lin *et al.* (2011)]
CLSM	2D/3D	~ 300 nm	Functional imaging by fluorescent labeling, Soft tissue contrast, No dose damage	Limited range of depth (100–150 μm), Requires fluorescent labeling	[Grötz *et al.* (1999); Kamioka *et al.* (2001); Sugawara *et al.* (2005), (2011); Hazenberg *et al.* (2006); Anderson *et al.* (2008); Vatsa *et al.* (2008); van Hove *et al.* (2009a)]
FIB/SEM	3D	~ 10 nm	High resolution	Destructive, time-consuming processing, small FOV	[Stokes *et al.* (2005); Schneider *et al.* (2011)]
Desktop micro-CT	3D	~ 200 nm	Non-destructive, relatively large FOV, Simple sample preparation	Incoherent X-ray, High X-ray radiation dose	[Vatsa *et al.* (2008); van Hove *et al.* (2009)]
SR micro/nano-CT	3D	~ 50 nm	Corehent X-ray, phase contrast, relatively large FOV, sub-μm mineral density quantification		[Peyrin *et al.* (1998); Hannah *et al.* (2010); Britz *et al.* (2012); Carter *et al.* (2012), (2013); Langer *et al.* (2012); Pacureanu *et al.* (2012); Mader *et al.* (2013)]
Ptychographic CT	3D	65nm	Absolute sub-μm mineral density quantification	Limited FOV, time-consuming procressing	[Dierolf *et al.* (2010)]
TXM CT	3D	30 nm	Non-destructive	Limited FOV, High X-ray radiation dose	[Andrews *et al.* (2010)]
TEM CT	3D	~ 50 nm	Non-destructive	Limited penetration depth(3–5 μm), high X-ray radiation dose	[Kamioka *et al.* (2009)]

LM: Light Microscopy, SEM: Scanning Electron Microscopy, TEM: Transmission Electron Microscopy, AFM: Atomic Force Microscopy, CLSM: Confocal Laser Scanning Microscopy, FIB/SEM: focused ion beam coupled with scanning electron microscope, FOV: field of view

3.2 2D imaging techniques

3.2.1 Optical microscopy

Optical microscopy is the earliest and most commonly used technique to investigate the LCN. It has been widely used to visualize LCN in 2D (Figure 3.2), using stained and unstained specimens [FROST (1960); Marotti *et al.* (1995); Remaggi *et al.* (1998); Ferretti *et al.* (1999); Ardizzoni (2001); Hirose *et al.* (2007); Schneider *et al.* (2010)]. The image can be formed by exploiting different physical phenomena (absorption, emission or refraction) in the interaction of light photons with matter. In transmission techniques, the specimens need to be cut in very thin sections (a few micrometers thick), or be prepared using histological staining or fluorochromes through series of steps. The resolution of optical microscopy is limited around 300 nm due to the imperfection of the microscopy lens.

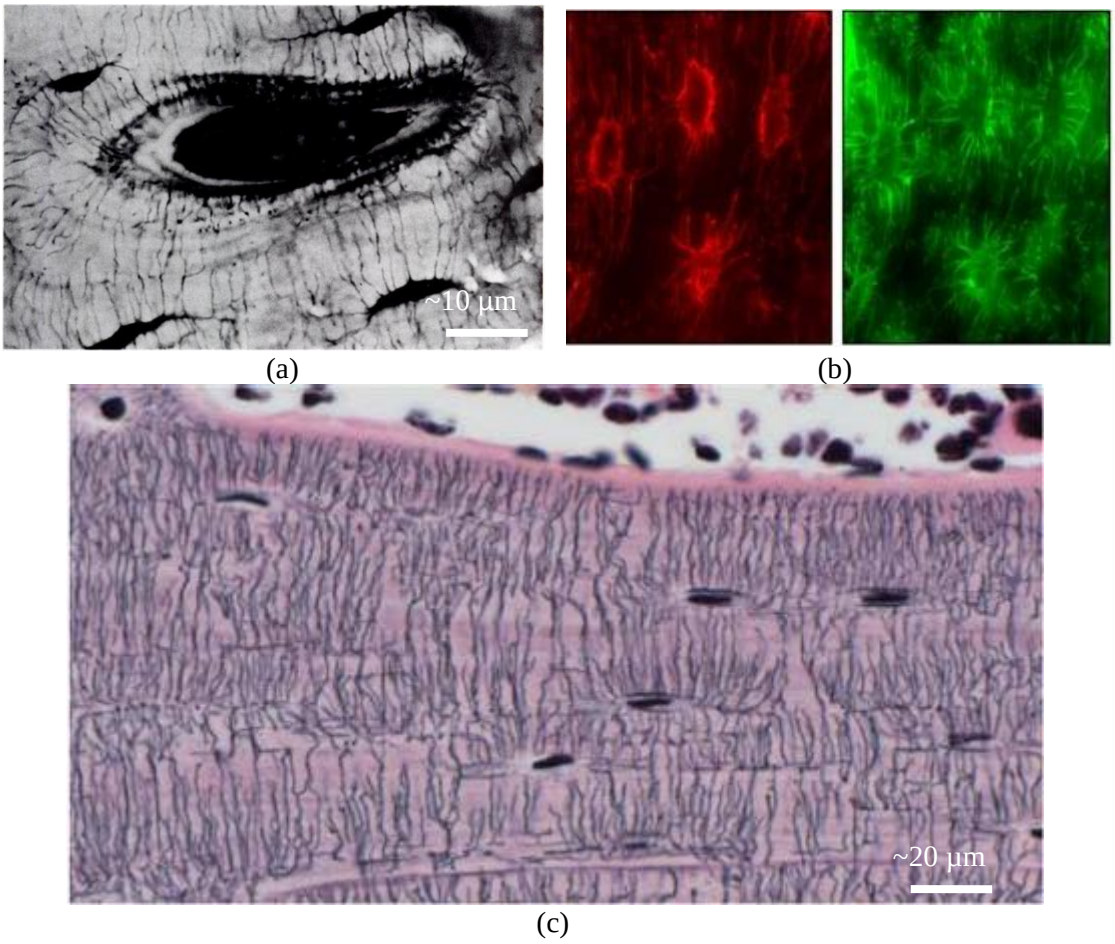

Figure 3.2 LCN under light microscopy (a) Photomicrograph of lacuno-canalicular system (Image from: [Shapiro (1988)]) (b) Early embedded osteocyte visualized by staining (Image from: [Bonewald (2011)]) (c) Schoen's staining of LCN in the endosteal region of cortical bone of 12 week (Image from: [Hirose *et al.* (2007)])

3.2.2 Electron Microscopy

Electron microscopy (EM) can provide images at very high spatial resolution [Erni *et al.* (2009)] and detect structures up to the atomic levels. Several types of EM techniques have been developed so far to detect the structure of the LCN.

3.2.2.1 Scanning electron microscopy (SEM)

Scanning electron microscopy (SEM) images the surface of sample by scanning it with a focused electron beam. Several signals are generated when the electrons beam bombard the atoms of the sample. These signals contain the information about the topology of the surface and the elemental composition of the sample. By capturing these signals with dedicated detectors, the SEM image is generated.

The detection of the secondary electrons (SE) is the most common mode of SEM to reflect the topography of the sample surface. SE are low energy electrons, excited from the inelastic

scattering interaction with atoms of the sample. Due to the low energy, the SE can only be emitted from locations quite near the surface, of the sample and therefore, the SE image reflects mainly the topography of the sample. Also, due to the very narrow electron beams, SE image resolution can reveal details less than 1 nm in size and can show relatively large depth information, presenting three-dimensional appearance which is quite helpful to understanding the surface topology of the specimen. SEM has been used in a number of works to study the accurate morphology of the LCN ([Kubek *et al.* (2010); Pazzaglia *et al.* (2012)], Figure 3.3.

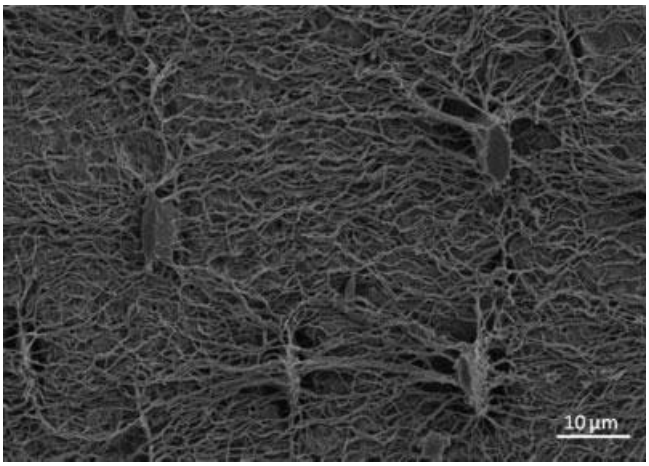

(a)

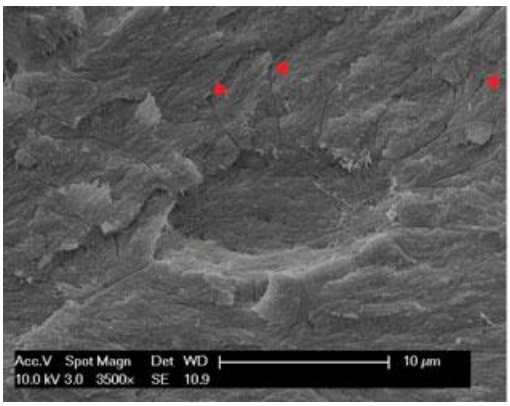

(b)

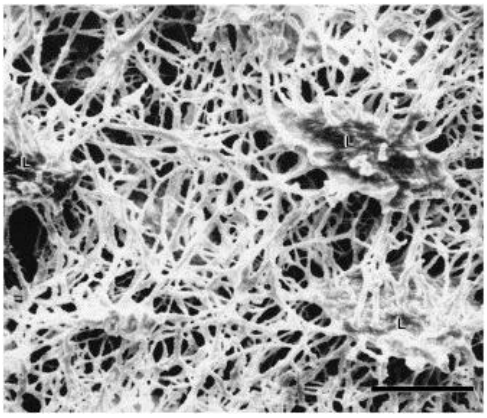

(c)

Figure 3.3 Secondary electrons image from Scanning electron microscopy (a) micrograph of LCN from a mouse femur diaphysis after acid-etching with 9% phosphoric acid for 20 s (Image from: [Kubek *et al.* (2010)]) (b) Osteocyte lacuna (Image from [Pazzaglia *et al.* (2012)]) (c) LCN in rat alveolar bone. Scale bar is 10 µm. Image from ([Schneider *et al.* (2010)])

Another interesting technique in SEM is back-scattered electrons (BSE) imaging. This technique is often used for the investigation of the distribution of bone mineral degree [Kingsmill *et al.* (1998)] (Figure 3.4), since the linear relationship between BSE grey levels and mineral content is well elaborated [Roschger *et al.* (1995); Bloebaum *et al.* (1997)]. BSE are the high energy electrons reflected or back scattered from the incoming electron beam,

due to the elastic interaction with the atom. Since the intensity of the BSE from the different elements depends on the element's atomic number, the BSE image is able to reflect the contrast between different chemical compositions or the local density variation of the sample.

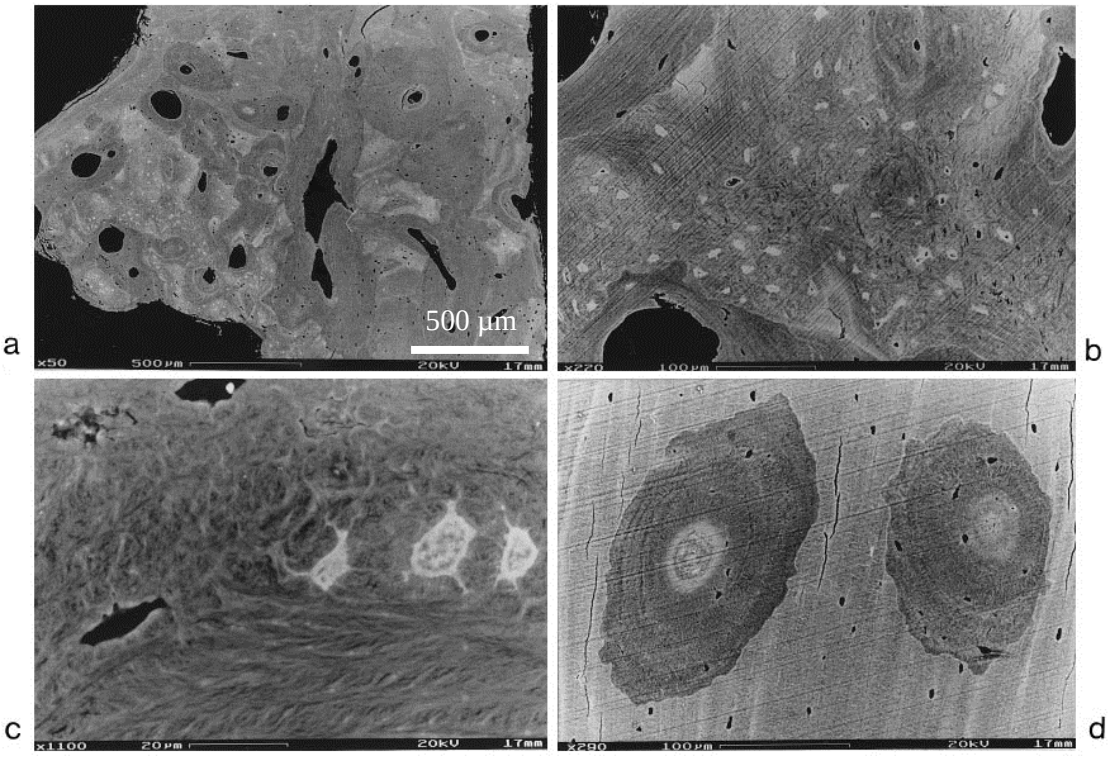

Figure 3.4 BSE of the LCN (Image from:[Kingsmill *et al.* (1998)])

Although SEM is capable of imaging the specimen from low to very high resolution, this technique has also some limitations. First, the SEM image is essentially in two dimensions. Therefore, it cannot provide quantitative 3D data. Second, the preparation of the sample needs to undergo a series of steps, such as sectioning, polishing, staining, acid-etching, dehydration, or conductive coating. Each of these preparation steps may significantly affect the result of the image. Third, when scanning the sample, the ultrastructure of sample may be potentially damaged due to the electron beam bombarding or due to the heating effects.

3.2.2.2 Transmitted electron (TEM)

Conversely to the principle of SEM, which detects the electron signals reflected from the specimen surface, in transmission electron microscopy (TEM) the image is formed from the electrons, which pass through the specimen. TEM is also able to reach a very high spatial resolution, which can resolve objects thousands times smaller than in light microscopy. The contrast of the image depends on the mode of operation, which allows the investigator to discern specific information of interest. The classical mode in TEM is the bright field imaging mode. The contrast is formed directly by the absorption of electrons in the material. The thicker the sample is or the higher is the atomic number of the material, the darker the image will be. Other modes in TEM enable to perform phase contrast imaging. The intensity of the

image is modulated with the complex wave interaction, making the interpretation very complex.

Due to the high definition in TEM, this technique has been widely used to investigate the osteocytes and their processes in the 2D mode [Wassermann *et al.* (1965); Palumbo *et al.* (1990); Rubin *et al.* (2004), (2005); L You *et al.* (2004); Deligianni *et al.* (2008)]. The TEM can also be used for 3D assessment by means of successive sectioning, stereo pair imaging or TEM tomography. By rotating the sample around its central axis, 3D data can be obtained from series of TEM images using the filtered back-projection algorithm [Kamioka *et al.* (2009)]. Nevertheless this procedure is subject to artifacts since the total angle of view is limited.

The high spatial resolution in TEM (~10 nm) requires an extremely specific sample preparation. The sample needs to be sectioned in ultrathin slices, usually within 1 µm. The increase of sample thickness needs a higher voltage setup of TEM. As an example, Figure 3.5 shows a TEM image of bone, setup at 2 MeV to image a section with a thickness of 3 µm [Kamioka *et al.* (2009)]. Besides, since the sample is quite small, the limited number of lacunae and canaliculi may not be representative for the investigation of LCN.

Figure 3.5 TEM micrograph of lacuna and its canaliculi (Image from: [Rubin *et al.* (2005)]

3.2.3 Atomic Force Microscopy

Atomic force microscopy (AFM) is one type of scanning probe microscopy, imaging matters at the nanoscale. The image in AFM is acquired from a mechanical probe (a sharp tip on the order of nanometers), scanning on the surface of the sample. It was recently used to image the LCN at resolution around 20 ~ 50 nm [Cardoso *et al.* (2013)]. However, like SEM, it can only provide 2D images of the sample surface. Due to the high magnification, the field of view is generally limited to about 150 ×150 μm^2, and the acquisition of the depth information is also restricted within 10-20 μm [Lin *et al.* (2011)] (Figure 3.6).

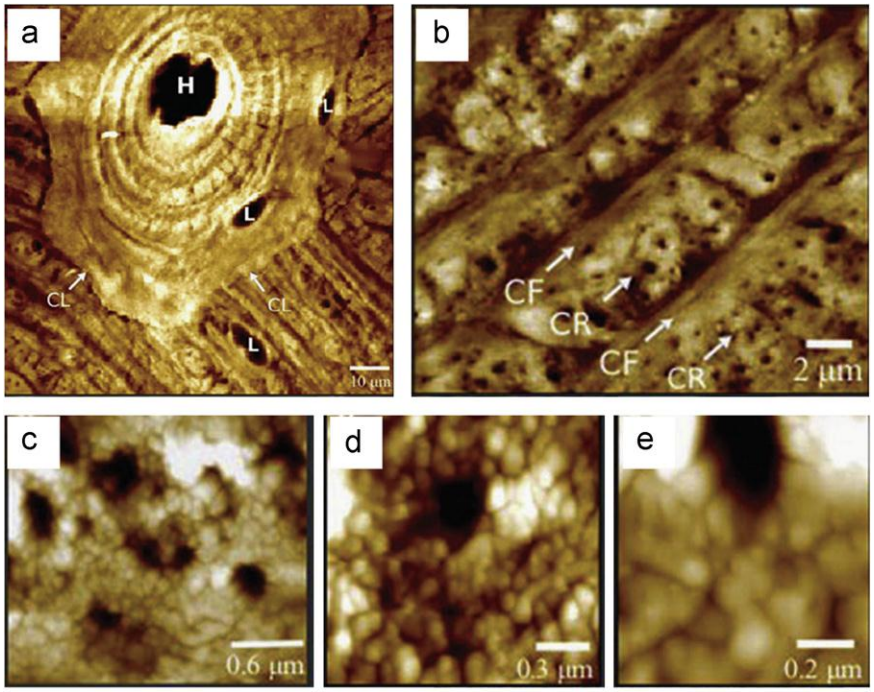

Figure 3.6 Images of LCN using AFM at different magnification (Image from: [Lin et al. (2011)]

3.3 3D imaging technique

3D imaging techniques allow acquiring three dimensional image of a specimen. Some of them are derived from the existing 2D imaging modalities, by taking serial 2D images at consecutive layers by means of manual sectioning, focusing or milling. Later, these 2D images are stacked to produce a 3D image from which a 3D rendering can be generated. Other techniques, such as computed tomography (CT), record series of projection images and reconstruct the 3D image using specific methodology, such as filtered back-projection algorithm. In the next paragraphs, we will review 3D techniques that have been used to image the LCN in 3D.

3.3.1 Confocal laser scanning microscopy

Confocal laser scanning microscopy (CLSM) is capable of acquiring a series of 2D optical images by changing the focal plane inside the sample. Each 2D image is acquired point-by-

point in order to avoid additional light from outside the focal plan. Consequently, the 2D images are sharper and have better contrast than in conventional fluorescence light microscopy. The 3D image is formed by concatenating the 2D image stack. Like the light microscopy, the resolution of CLSM image is also limited by the diffraction limit and can only offer resolutions around 200 nm in the focal plane and approximately 450 nm in the vertical axis.

Nevertheless, CLSM overcomes some limitations of conventional light microscopy. It has the advantages of generating high resolution 3D images from relatively thick samples. Besides, it comparatively does not damage the sample, due to the low energy of visible light. Therefore, it does not require complex sample preparation procedures. Also, coupling with varieties of fluorescence labels, different structures of interest can be easily distinguished from different colors. Therefore, this technique has been widely applied in the study of biological samples, including the bone tissue [Grötz *et al.* (1999); Kamioka *et al.* (2001); Sugawara *et al.* (2005), (2011); Hazenberg *et al.* (2006); Anderson *et al.* (2008); Vatsa *et al.* (2008); van Hove *et al.* (2009a)] (Figure 3.7). However, some limitations remain to analyze bone samples. The maximum depth for bone samples is generally limited to 100-150 µm (Jones et al., 2005). This depth restriction is due to the limited penetration and diffusion of the visible light excited by the laser from the contrasting agent inside the sample. In addition, the spatial resolution in the vertical direction is generally worse making the image more difficult to exploit from a quantitative point of view.

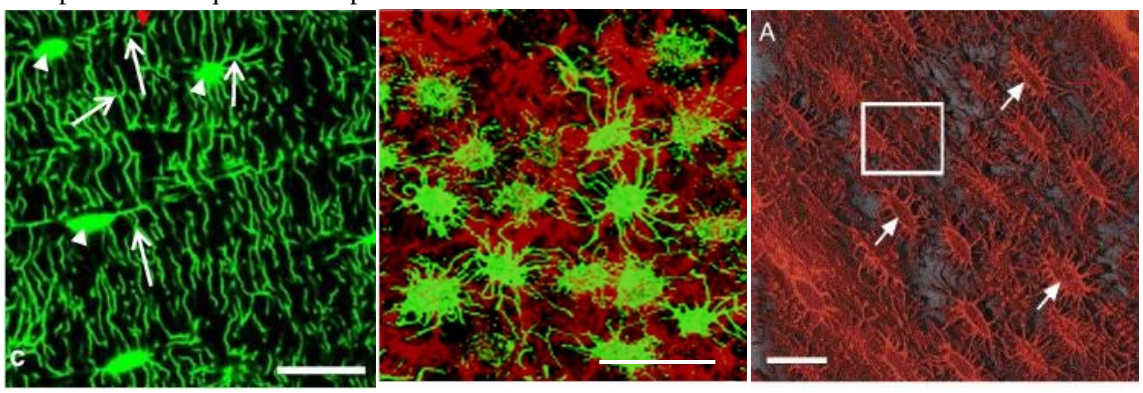

(a) (b) (c)

Figure 3.7 CLSM image of LCN (a) LCN of 50 stacked confocal image from a typical rat tibial diaphysis section (Image from: Sharma et al., 2012) (b) The osteocytes (green) are OB7.3-stained cells, and the osteoblasts (red) are bound with Texas Red-X phalloidin (Image from: Jones et al., 2005) (c) 3D osteocyte network reconstructed from CLSM images (Image from: Sugawara et al., 2005). Bar in (a) is 10 µm, bars in (b) and (c) are 20 µm

3.3.2 X-ray computed tomography

Since X-ray computed tomography (CT) was introduced in the early 1970s, it has become a widely used medical imaging technique. After decades of developments and improvements, CT is capable of providing biomedical images with a wide range of 3D isotropic spatial resolutions between millimeters down to nanometers. With many technical improvements, 3D X-ray micro-CT has become a major analysis tool in bone biology. Basically, there are two

steps to acquire a 3D CT image. First, series of two dimensional projection images are recorded under different angular positions around a single axis of rotation. Then, a tomographic reconstruction algorithm is used to retrieve the internal three-dimensional structure. The fast development of CT has pushed this technique towards revealing fine structures at the Nano level, both using laboratory source and synchrotron light source CT. Recent studies have shown its promising feasibility for the non-destructive and quantitative investigation of the 3D bone morphology and the distribution of mineralization at the cellular level.

3.3.2.1 Synchrotron light source CT

Using the brilliant monochromatic coherent X-rays generated from synchrotron radiation (SR) sources, high resolution tomographic imaging techniques showed as an ideal imaging modality to perform multi-scale imaging, unveiling the micro and ultrastructure of the LCN.

3.3.2.1.1 SR micro-CT

In general, the advantages of synchrotron radiation micro-CT compared to standard X-ray micro-CT reside in three main aspects. First, it offers a high photon flux, up to 100 billion times brighter than a standard hospital X-ray instrument, permitting to acquire datasets with high signal to noise ratio (SNR) in relatively short scanning time. Second, due to the insertion instrument technology, a wide range of monochromatic energy can be selected yielding quantitative studies based on the local density of the specimen. Third, due to the coherent property of the SR sourced X-ray, "phase contrast" imaging can be exploited. This allows to enhance the image contrast of a specimen, which cannot be achieved by only using the X-ray absorption property. With these advantages, the SR micro-CT has shown a suitable imaging modality to reveal the internal microstructure of the bone tissue with voxel size from tens of micrometers to submicron level [Bousson *et al.* (2004).; Larrue *et al.* (2011); Martin-Badosa *et al.*(2003); Nuzzo *et al* (2002b).; Salome *et al.* (1999); Pacureanu *et al.* (2012)].

In context of imaging the LCN, the SR micro-CT allows imaging truly three-dimensional structure of the LCN with the isotropic voxel. At few micrometers, it offers a relatively large field of view, allowing to explore 3D lacunar morphology within a large population [Hannah *et al.* (2010); Britz *et al.* (2012); Carter *et al.* (2012), (2013); Mader *et al.* (2013)] (Figure 3.8 (a) and (b)). At submicrometers, recent research have demonstrated the feasibility to acquire the 3D osteocyte lacuna-canalicular network [Pacureanu *et al.* (2012)] (Figure 3.8 (c)). In particular, , we shall introduce the principle and experimental setup of SR micro-CT for imaging LCN at the beamline ID19 of European synchrotron radiation facility (ESRF) (see chapter 5).

The main limitation of the SR micro-CT technique is that it does not allow the observation of living cells but only that of the empty void of LCN. However, many studies suggest that the analysis of LCN is a good surrogate to the analysis of osteocytes themselves due to the percentage of empty lacunae remains approximately constant.

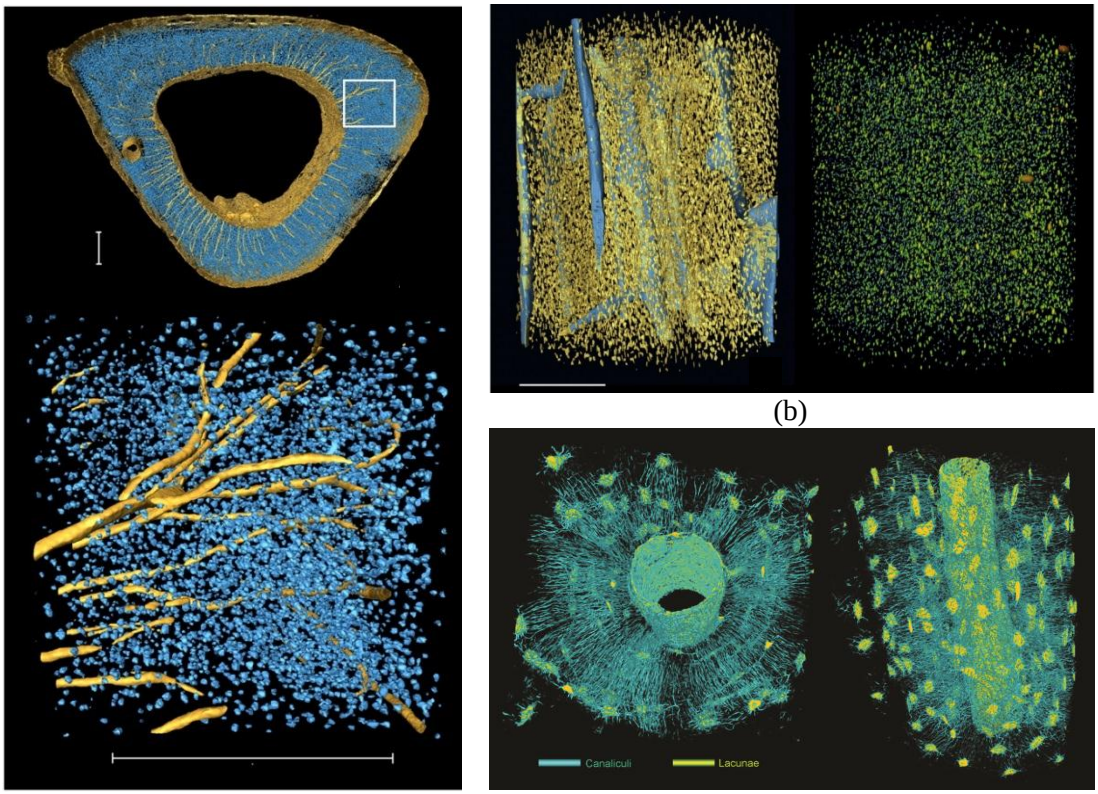

(a) (b) (c)

Figure 3.8 Three dimensional rendering of lacunae from SR micro-CT images (a) and (b) 3D rendering of the lacunae based on the image with voxel size of 1.4 µm (c) 3D rendering of the LCN within one osteon based on the image with voxel size of 280 nm (Images from: (a) [Britz *et al.* (2012)], Scale bar is 300 µm (b) [Carter *et al.* (2012)] Scale bar is 300 µm and (c) [Pacureanu *et al.* (2012)]

3.3.2.1.2 X-ray magnified phase tomography

The ultra-structure of bone tissue has also recently been imaged by X-ray magnified phase tomography at the ERSF, Figure 3.9. This technique offers a high spatial resolution, high sensitivity and relatively large field of view. The spatial resolution, which can achieved to 60 nm, is high enough to resolve the morphology of canaliculi, which width is reported around 100-500 nm. The high sensitivity allows to observe the local density change around the extracellular bone matrix, due to the phase retrieval algorithm. The field of view, which is around 100 µm × 100 µm × 100 µm, may contain around ten lacunae and its canaliculi. The detailed principle will be elaborated in section 5.3.2.

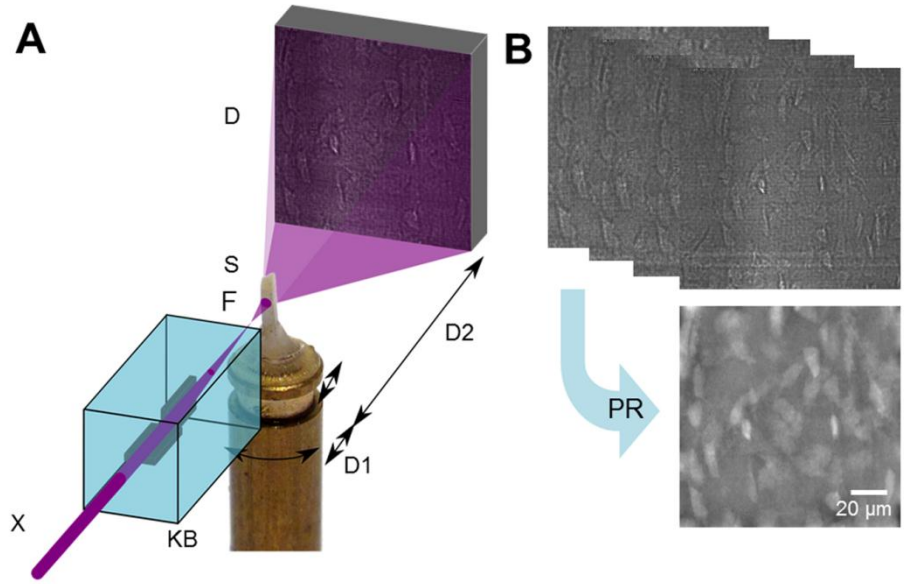

(a)

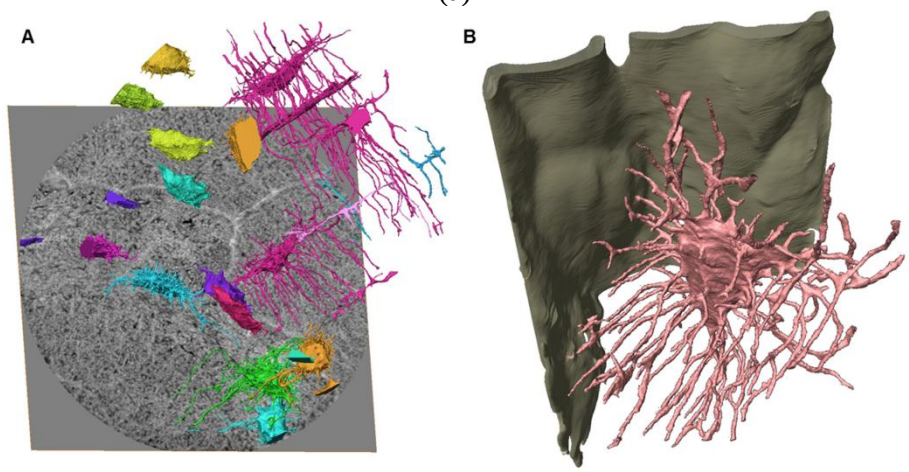

(b)

Figure 3.9 Osteocyte lacunae and its canaliculi imaged by the X-ray magnified phase tomography (Image from: [Langer *et al.* (2012)])

3.3.2.1.3 Transmission X-ray microscope (TXM)

Similar to light microscopy, transmission X-ray microscopy is also an optics-based microscopy. It uses a synchrotron X-ray beam to "illuminate" a specimen, and it produces a magnified image by using the Fresnel Zone Plates (FZPs), Figure 3.10 [Withers (2007); Andrews *et al.* (2010)]. Although the TXM is a essentially a 2D imaging technique, it can be combined to CT techniques to acquire a reconstructed 3D image of an osteocyte lacuna and its canaliculi [Andrews *et al.* (2010)]. In this study, a series of TXM images are taken as projection images, as the bone specimen was rotated by 180 degree with 1 degree angular spacing. The 3D image was reconstructed using a standard filtered back projection algorithm. The advantage of this technique is that it can offer a very high spatial resolution down to 30 nm, which is capable of resolving the fine structure of canaliculi. However, the downsides

of TXM are the limited FOV (15~30 μm) and the radiation damage to the sample [Andrews *et al.* (2010)]. Also, the inefficient usage of X-ray due to the FZPs reduces the SNR of the image.

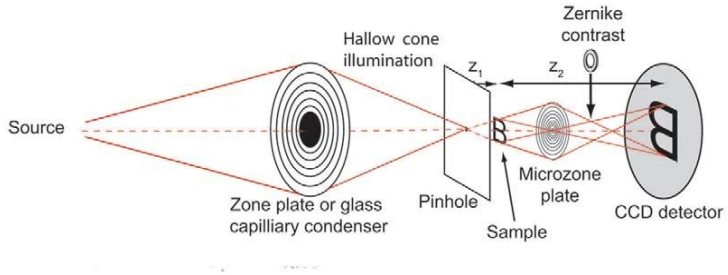

(a)

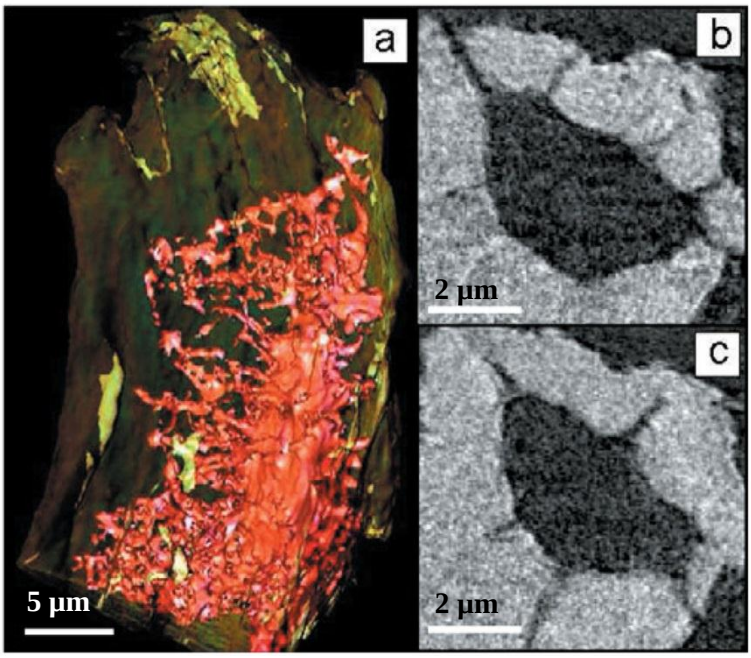

(b)

Figure 3.10 Three dimensional rendering of lacuna from mouse tibia trabeculae reconstructed from TXM images (Image from: [Withers (2007)] and [Andrews *et al.* (2010)])

3.3.2.1.4 Ptychographic X-ray CT

Ptychographic X-ray CT is a recently developed quantitative 3D imaging modality, which exploits the high phase sensitivity of 2D coherent diffractive imaging to generate quantitative 3D density map of specimens on the nanoscale [Dierolf *et al.* (2010)]. It was recently used to image a bone sample with a cubic voxel size of 65 nm, the setup of the instrument is shown in Figure 3.11. The scanning setup employed a pinhole to select a portion of a coherent monochromatic beampencil X-ray beam. Then, the detector recorded 704 diffraction patterns per each projection angle at the scan point shown in Figure 3.11 (b). 181 projections were collected from -90 degree to 90 degree with one degree angular spacing. The total scan time was 36 hours. After that, the projection images were processed by a ptychographic algorithm before performing tomographic reconstruction by a standard filtered back projection

algorithm. The grey level of the final reconstructed 3D image is the phase decrement index, directly representing the electron density.

The feasibility of this technique to image the morphology of the LCN and the density of the surrounding bone tissue was demonstrated but the image was restricted to one lacuna and its canaliculi (Figure 3.11). However, in the current state of the technology, this technique is limited for the delivery of representative biological result due to the limited field of view. Other limitations are the long data acquisition time and low dose efficiency due to the incoming beam loss blocked by the pinhole.

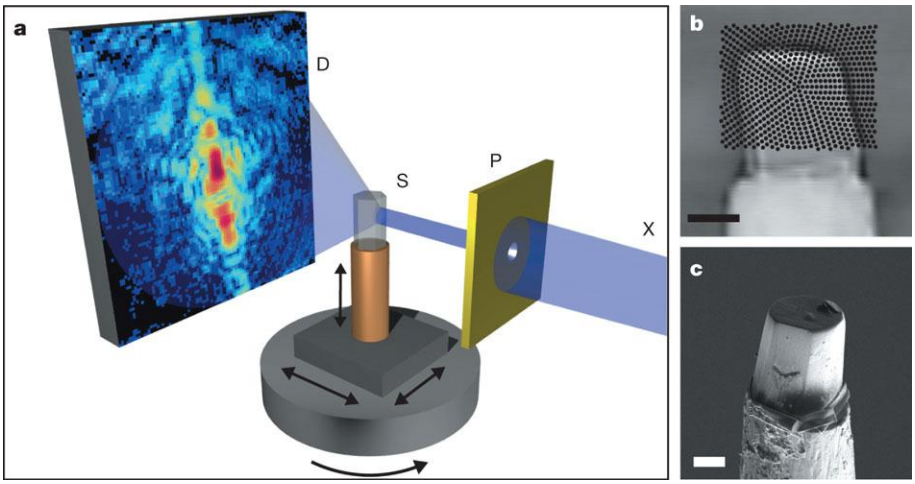

(a)

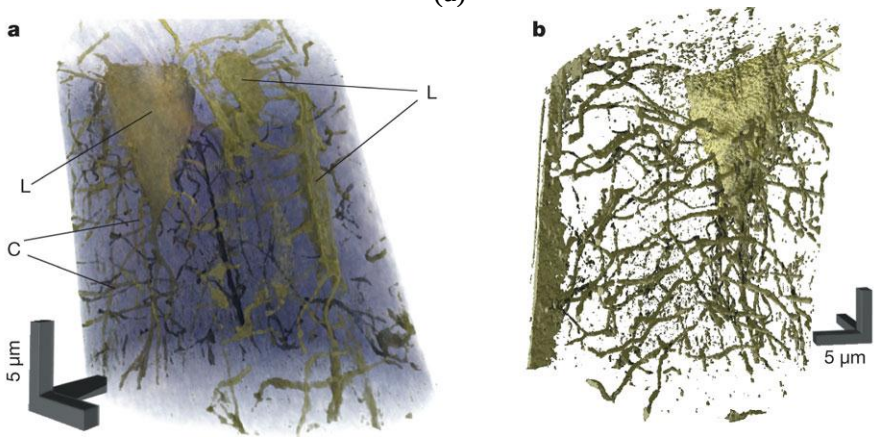

(b)

Figure 3.11 (a) Setup of ptychographic X-ray CT (b) the 3D rendering of osteocyte lacunae and its canaliculi from the tomographic reconstructed image (Image from: [Dierolf *et al.* (2010)])

3.3.2.2 Laboratory source micro/nano CT

In the last decades, progresses in compact laboratory CT have allowed imaging reaching at microscale. Most often, the X-rays are generated in the form of a fine-focus cone beam, the size of the focal spot determining the spatial resolution of the system. Thanks to the magnification that can be fixed by the sample to detector distance (see Figure 3.12(a)), these systems can achieve various spatial resolutions down to the range of hundreds of nanometers. For example, the "Nanotomograph 2011" manufactured by Skycan has been designed to

provide a highest spatial resolution around 200 nm. Despite of the high magnification of the desktop nano-CT, the signal to noise ratio (SNR) can be poor Figure 3.12 (b-c) illustrates the 3D reconstruction of osteocyte lacunae in tibia bone using desktop nano-CT images (voxel size: 580 nm) [Vatsa *et al.* (2008); van Hove *et al.* (2009)]. However going from the raw images to segmented lacunae may be a hard task due to the limited signal to noise ratio (SNR). In addition, the reconstructed value may not be quantitative due to the polychromatic energy of the X-ray spectrum generated from the laboratory source.

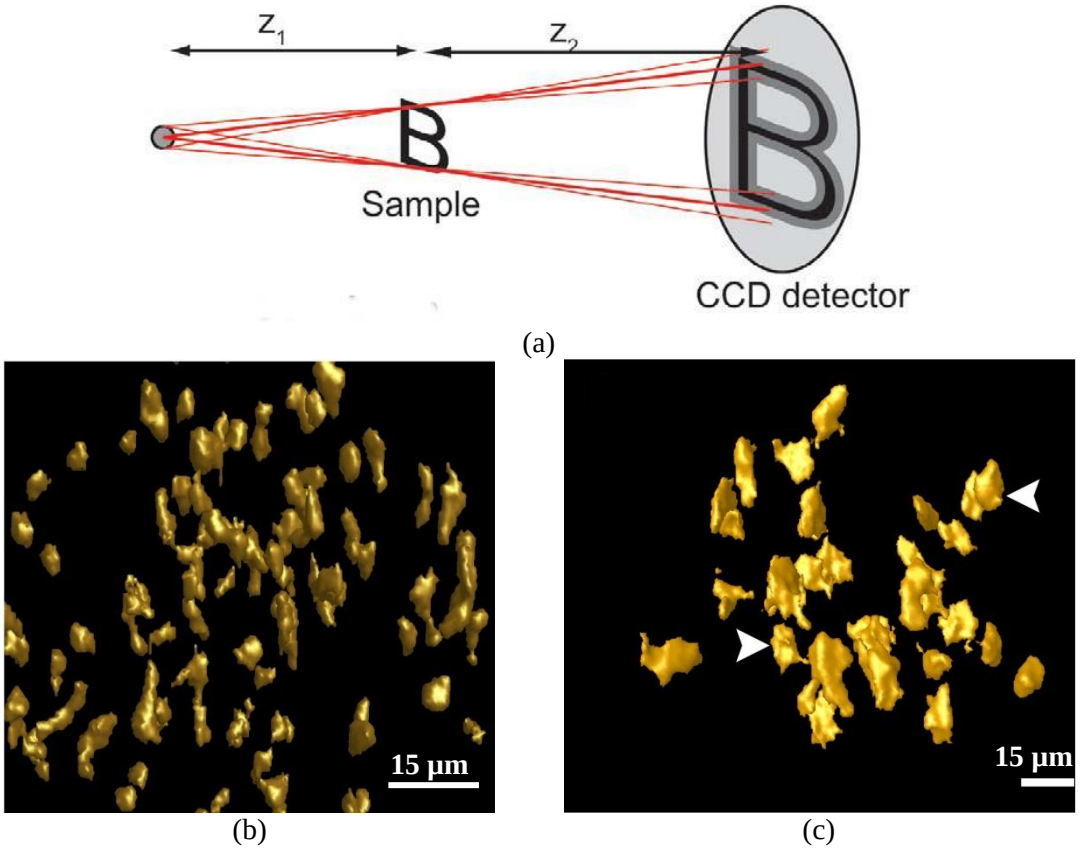

Figure 3.12 The 3D reconstruction of osteocyte lacunae from tibia bone using nano-CT scanning. (a) Cone beam projection system, the size of focal spot is one of the factor to influence the sharpness of the acquired image.(Image from: [Withers (2007)]) (b) Osteocyte lacunae of osteoarthritic bone (Image from: [van Hove *et al.* (2009)]) (c) Osteocyte lacunae of adult mouse calvaria (Image from: [Vatsa *et al.* (2008)])

3.3.3 Focused ion beam - scanning electron microscopy (FIB/SEM)

Focused Ion Beam (FIB) coupled with scanning electron microscope (SEM) permits to generate isotropic 3D images at very high spatial resolution from a stack of SEM images, recorded sequentially as the very thin layers of the tissue are removed by FIB. The FIB/SEM is widely used in the semiconductor industry and material sciences, and was more recently used in the field of life sciences (first application only going back to 2005 [Stokes *et al.* (2005)]). A recent study showed that FIB/SEM can provide a 3D image of the LCN at a

spatial resolution of 30 nm [Schneider *et al.* (2011)], Figure 3.13. The downside of this technique is that it requires a complex sample preparation, in order to avoid problems, such as surface structure distortion or "curtaining" effect induced by the uneven rough surface structure. Besides, the FIB milling and SEM imaging is inherently destructive, which means that the volume of interest (VOI) cannot be imaged for a second time. In addition, the technique has so far only be demonstrated on a small VOI (19.0 μm×14.3 μm×11.5 μm) allowing to imaging only a restricted area of the LCN. Thus, the quantitative result on the morphology of LCN cannot be representative.

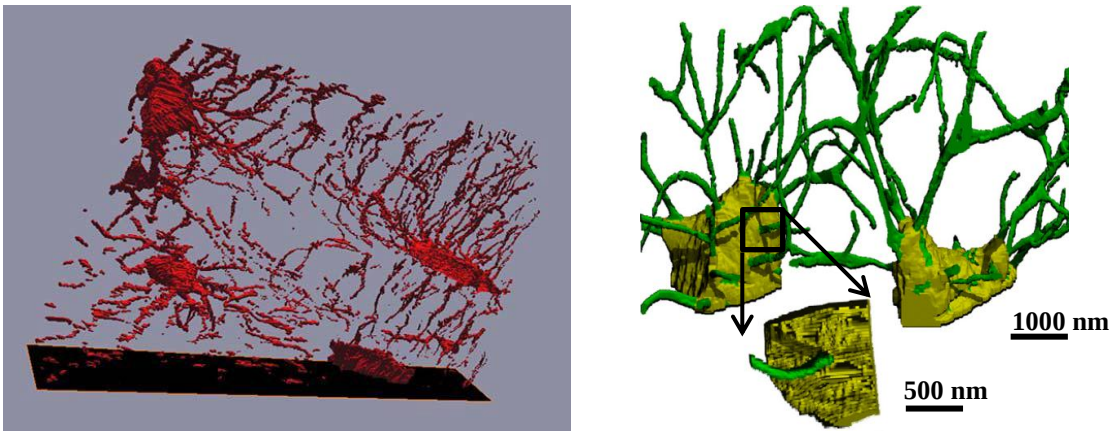

(a) (b)

Figure 3.13 Three dimensional rendering of LCN using FIB/SEM (Image from: (a) [Stokes *et al.* (2005)] Horizontal field width ~ 45 microns, (b) [Schneider *et al.* (2011)])

3.4 Conclusion

In this chapter, we briefly summarized the existing imaging modalities for the investigation of LCN and CCN. These techniques provide hierarchical imaging abilities covering a range in spatial resolution from micrometers to nanometers. The techniques were classified into two-dimensional and three-dimension modalities, and their advantages and disadvantages were briefly explained. New synchrotron-based three-dimensional micro and nano imaging techniques have known a fast development in the recent years. Although some limitations may exist, the advantages in qualitative imaging (for 3D visualization) and quantitative imaging (for morphometry and component analysis) are very important for the structural and functional assessment of LCN and CCN.

Chapter 4

Parameters of the osteocyte network and the lacuno-canalicular network – state of art

Contents

4.1 Introduction 33
4.2 Characterization of osteocyte or lacunae 34
4.2.1 Lacunar properties at tissue level 34
4.2.1.1 Density of lacunae and osteocytes 34
4.2.1.2 Porosity of lacunae 36
4.2.2 Lacunar properties at cellular level 37
4.2.2.1 2D morphological parameters of osteocytes or lacunae 37
4.2.2.2 3D morphological parameters of osteocytes or lacunae 38
4.3 Characterization of osteocyte processes or canaliculi 41
4.3.1 Canalicular properties at tissue level 41
4.3.1.1 Density of canaliculi 41
4.3.1.2 Porosity of canaliculi 42
4.3.2 Morphological parameters of canaliculi and processes 43
4.4 Conclusion 46

4.1 Introduction

As the assessment of the CCN and the LCN is of great interest for the understanding of the osteocyte functionality closely related to the quality of bone, a number of studies have been conducted using a variety of imaging modalities to report 2D and 3D quantitative morphological parameters on the CCN and the LCN, Figure 4.1. In the past, most of the studies were conducted using light microscopy, confocal microscopy, SEM and TEM. The structural properties of the CCN and LCN were investigated mainly by the examination of two-dimensional sections of bone specimens. Several studies used stereology to extrapolate these findings to three-dimensional morphological parameters based on some ideal assumptions [Mullender *et al.* (1996); Skedros *et al.* (2005); Beno *et al.* (2006)]. However, such extrapolations can be biased due to inappropriate model assumptions.

3D imaging allows to overcome such limitations by providing a direct access to 3D parameters which has several advantages compared to previous 2D measurement. First, since direct 3D measurements do not rely on any model assumption. They can provide more accurate results than those derived from 2D images. Second, more features can be extracted from the 3D images, regarding to the morphology and the topology of the CCN and the LCN. Third, 3D morphological quantitative results can serve as the basis to create 3D micro-structural computational models for biomechanical simulations.

Concerning the quantification method, the assessment on the CCN and LCN is largely relied to manual work and to the analysis tools provided by the commercial software. However, up to now, there is no specialized automatic method dedicated for the 3D analysis of the LCN properties.

Due to the absence of review regarding the quantification of the LCN, this chapter aims at providing the current state of the art relative to this topic. The chapter is divided into two parts related to the quantification of the osteocyte/lacunae and of the osteocyte processes/canaliculi. In the lacunar section, we will first review the findings on the tissue level concerning the density and the porosity of the lacunae. Then, on the cellular level, we will provide morphological parameters on the osteocytes and the lacunae. In the canalicular section, first, we introduce the work related with the porosity of the canaliculi at the tissue level. Then, we will provide morphological parameters on the osteocyte processes and the canaliculi. The various findings are synthesized in the tables presented in this chapter.

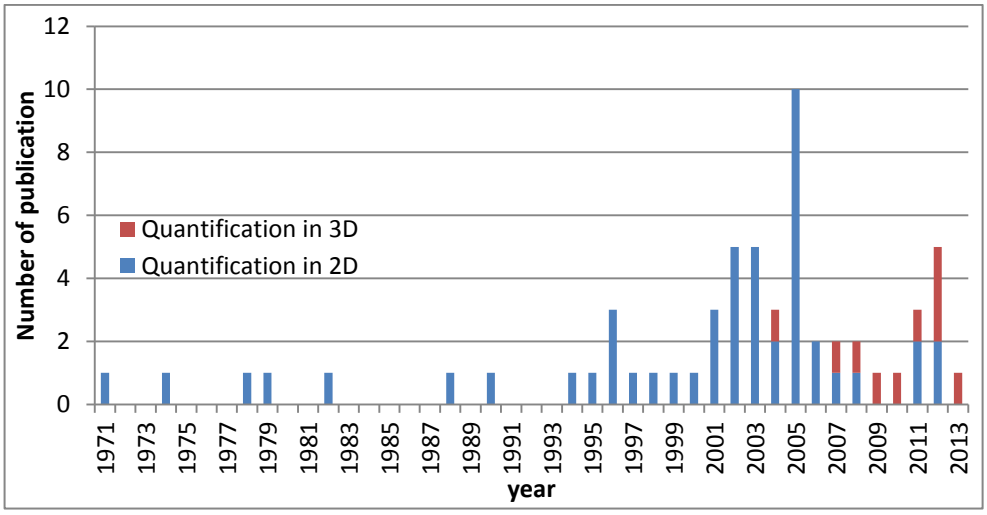

Figure 4.1 number of publications related to the quantification of the CCN and LCN.

4.2 Characterization of osteocyte or lacunae

4.2.1 Lacunar properties at tissue level

4.2.1.1 Density of lacunae and osteocytes

The density of the lacunae and osteocytes has been documented in different species and type of bones. According to the image dimension, different density parameters have been proposed: the number of lacunae (osteocytes) per unit bone matrix area (N.Lc/BA and N.Ot/BA), the number of lacunae (osteocytes) per unit tissue area (N.Lc/TA and N.Ot/TA), the number of lacunae (osteocytes) per unit bone matrix volume (N.Lc/BV and N.Ot/BV) and the number of lacunae (osteocytes) per unit tissue volume (N.Lc/TV and N.Ot/TV). Table 4.1 and Table 4.2 attempt to review the different values found in the literature. A range of lacunae and osteocyte densities between 120 to 850 mm^{-2} has been measured in human bone samples from various 2D imaging methods such as light microscopy (LM), scanning electron microscopy (SEM), transmission electron microscopy (TEM), fluorescence recovery after photobleaching (FRAP) and atomic force microscopy (AFM), Table 4.1. However, in different species, Remaggi [Remaggi *et al.* (1998)] has observed the densities up to 2000 mm^{-2} (in chicken for instance) (See the table in annex.). The density calculation depends on the manual counting on the number of osteocytes/lacunae in the FOV. In some works, the density measured from 2D images was extrapolated to a 3D lacunar density by assuming that the osteocytes have a spherical shape [Mullender *et al.* (1996)] and [Jordan *et al.* (2003)]. The 3D lacunar density either extrapolated or measured from 3D images like desktop micro/nano-CT, SR micro-CT and confocal laser scanning microscopy (CLSM) can vary between 8,000 to 90,000 mm^{-3} depending on species, types of bone, location of bone and diseases of bone as can be observed in Table 4.2.

Table 4.1 human lacunar density reported in 2D

Reference	Imag. Tech.	Location	Groups	# Samples	Lc/ Ot	Value
						N.Lc/BA (#/mm^2)
[Mullender et al. (1996)]	LM	Iliac crest	Control		Lc	165.7 ± 38.3
			Osteoporosis		Lc	212.2 ± 31.4
[Mori et al. (1997)]	LM	Femoral heads trabecular bone	Young, old and fracture	9 young 12 old	Lc	120~510
[Remaggi *et al.* (1998)]	LM	Parallel-fibered in shaft bone			Lc	550
[Ferretti et al. (1999)]	LM	Tibia compact bone		3	Lc	460
[Vashishth et al. (2000)]	LM	Femoral middiaphyseal cortical bone		16 men, 9 women	Lc	448 ~ 888
[Qiu et al. (2002b)]	LM, CLSM	Iliac cancellous bone	Pre-menopausal	38	Lc	232 ± 28.8
			Post-menopausal	56	Lc	206 ± 22.0
	LM, CLSM	Iliac cancellous bone	Pre-menopausal	38	Ot	221 ± 30.6
			Post-menopausal	56	Ot	188 ± 22.4
[Qiu et al. (2002a)]	LM	Iliac cancellous bone	White	92	Ot	130~350
[Jordan et al. (2003)]	LM	Femur	Control		Lc	507.65 ± 9.05
			Osteoporotic femoral neck fracture (FNF)		Lc	610 ± 12.55
			Coxarthrosis (cOA)		Lc	387.48 ± 6.72
			Male		Lc	433.8 ± 37.7
			Female		Lc	447.5 ± 14.8
			Anterior		Lc	498.19 ± 16.9
			Inferior		Lc	458.21 ± 20.61
			Posterior		Lc	510.04 ± 19.3
			Superior		Lc	504.33 ± 16.54
[Qiu et al. (2003a)]	LM	Rib sections		9	Lc	848 ± 129
[Qiu et al. (2003b)]	LM	Iliac bone biopsy	Fracture	44	Lc	134 ± 35.7
			Healthy post-menopausal	56	Lc	206 ± 22.0
		Iliac bone biopsy	Fracture	44	Ot	125 ± 38.8
			Healthy post-menopausal	56	Ot	188 ± 22.4
[Mullender et al. (2005)]	LM	Anterior-superior iliac spine	Control female	13	Ot	271.3 ± 28.2
			Control male	21	Ot	223.2 ± 29.9
			Osteoporotic female	40	Ot	222.6 ± 55.7
			Osteoporotic male	15	Ot	198.9 ± 54.2
[Vashishth et al. (2005)]	LM	Vertebrae T12	Female	29	Lc	644 ± 123

			Male	35	Lc	435 ± 130
[Qiu et al. (2006)]	LM	Iliac cancellous bone	Black	34	Lc	248 ± 44.0
			White	94	Lc	217 ± 28.6
		Iliac cancellous bone	Black	34	Ot	226 ± 43.3
			White	94	Ot	202 ± 30.6
[Power et al. (2012)]	LM	Femoral neck cortex	Controls	11	Ot	577.4~880.0
			Fracture	10	Ot	527.9~830.5

Mean ± standard deviation

Table 4.2 human lacunar density reported in 3D

Reference	Dim	Imag. Tech.	Location	Groups	# Samples	Lc/ Ot	Value
							N.Lc/BV (#/mm^3)
[Mullender et al. (1996)]	2D->3D	LM	Iliac crest	Control		Lc	12900 ± 3200
				Osteoporosis		Lc	17100 ± 2500
[Jordan et al. (2003)]	2D->3D	LM	Femur	Control		Lc	35×10^3
				Coxarthrosis (coa)		Lc	25×10^3
.				Osteoporotic femoral neck fracture (FNF)		Lc	39×10^3
[van Hove *et al.* (2009)]	3D	Nano-CT	Proximal tibial	Osteoarthritis	1	Lc	$21.8 \pm 4.0 \times 10^3$
				Osteopenia	1	Lc	$8.0 \pm 0.5 \times 10^3$
				Osteopetrosis	1	Lc	$15.6 \pm 3.4 \times 10^3$
[Carter et al. (2013)]	3D	SR µCT	Femur shaft anterior mid-cortical		30	Lc	23,942 ± 2529
							N.Lc/TV (#/mm^3)
[Hannah et al. (2010)]	3D	SR µCT	Right femoral shaft		1	Lc	40000~90000
							Density (category unknown)(#/mm^3)
[Carter et al. (2012)]	3D	SR µCT	Femur shaft anterior		3	Lc	27169 ± 1935
			Femur shaft Posterior		3	Lc	26343 ± 1262
			Femur .shaft Medial		3	Lc	37521 ± 6416
			Femur .shaft Lateral		4	Lc	33972 ± 2513

Mean ± standard deviation

4.2.1.2 Porosity of lacunae

Up to now, only few studies reported the porosity of the lacunae (Lc.TV/TV) in 3D, Table 4.3, due to limited imaging resolution compared to the size of the lacunae. One of the first study was that of Schneider et al. who used SR micro-CT to analyze lacunar properties within murine cortical bone from two different strains [Schneider *et al.* (2007)] In this work they found a mean lacunar porosity of 1.3%. This result was consolidated in a recent report of

Tommasini et al., who measured a lacunar porosity in the femoral diaphysis of rats between 1.3% and 1.6% from SR micro-CT images[Tommasini *et al*. (2012)].

Table 4.3 The porosity of the total lacunae

Reference	Dim	Imaging Tech.	Species	Location	Groups	# Samples	Lc/Ca	Value
								Porosity (%)
[Schneider et al. (2007)]	3D	SR µCT	Mice	Femoral mid-diaphysis			Lc	1.3
[Tommasini et al. (2012)]	3D	SR µCT	Rat	Femoral diaphysis	Control	6	Lc	1.50 (0.25)
					OVX	6	Lc	1.62 (0.53)
					ALN	6	Lc	1.33 (0.29)
					PTH	6	Lc	1.58 (0.29)

4.2.2 Lacunar properties at cellular level

4.2.2.1 2D morphological parameters of osteocytes or lacunae

Few parameters regarding the morphology of osteocytes and lacunae have been reported in the literature, since the rapid development of the three-dimensional imaging modalities. Until the recent years, mainly 2D morphological parameters were reported: osteocyte or lacunar area (Ot.Ar or Lc.Ar), distance between the nearest two osteocytes or lacunae (Ot-Ot or Lc-Lc), perimeter of osteocyte or lacunae (Ot.Pm or Lc.Pm), the length, width and depth of the lacuna (Lc.L1, Lc.L2 and Lc.L3).

The area of lacunae was mainly measured from light microscopy (LM) images and found in a range from 20 μm^2 to 140 μm^2. The average lacunar length is about 23 µm, width about 10 µm and depth about 5 µm, measured manually under the LM, Table 4.4.

Table 4.4 2D Human morphological parameters of osteocytes or lacunae

Reference	Imag. Tech.	Location	Groups	# Samples	Lc/ Ot	Value
						Area (μm^2)
[Wright et al. (1978)]	LM	Iliac crest	Control		Lc	65.6 ± 25.6 (smaller than osteoporosis)
			Osteoporosis		Lc	81.0 ± 21.4 (larger than control)
[Mullender *et al.* (1996)]	LM	Iliac crest	Control		Lc	39.1 ± 4.9
			Osteoporosis		Lc	44.1 ± 7.3
[Remaggi *et al.* (1998)]	LM	Parallel-fibered in shaft bone			Lc	26
[Ferretti et al. (1999)]	LM	Tibia compact bone		3	Lc	25
[Jordan et al. (2003)]	LM	Femur	Control		Lc	37 ± 5.4
			Coxarthrosis (coa)		Lc	49 ± 7
			Osteoporotic femoral neck fracture (FNF)		Lc	51 ± 1.1

[Mullender et al. (2005)]	LM	Anterior-superior iliac spine	Control female	13	Lc	44.8 ± 7.7
			Control male	21	Lc	41.3 ± 5.2
			Osteoporotic female	40	Lc	42.1 ± 5.1
			Osteoporotic male	15	Lc	40.7 ± 5.2
						Length (µm)
[Marotti (1979)]	LM	Tibiae mid·diaphyseal cortical bone			Lc	22 ± 0.51
[Remaggi *et al.* (1998)]	LM	Parallel-fibered in shaft bone			Lc	25
						Width (µm)
[Marotti (1979)]	LM	Tibiae mid·diaphyseal cortical bone			Lc	9 ± 0.16
[Remaggi *et al.* (1998)]	LM	Parallel-fibered in shaft bone			Lc	10
						Depth (µm)
[Marotti (1979)]	LM	Tibiae mid·diaphyseal cortical bone			Lc	4 ± 0.06
[Remaggi *et al.* (1998)]	LM	Parallel-fibered in shaft bone			Lc	5

FRAP: Fluorescence recovery after photobleaching

L1, L2, L3: Length, width, depth of lacunae

MIL: The degree of anisotropy measured by using the mean intercept length (MIL)

4.2.2.2 3D morphological parameters of osteocytes or lacunae

Recently, 3D parameters were also introduced. The volume of osteocyte or lacuna (Ot.V or Lc.V) can be calculated straightforwardly. By considering a tensor representation, it is also possible to calculate eigenvalues of the tensor and estimate the anisotropy of osteocyte/lacunae. The surface area of osteocytes or lacunae (Ot.S or Lc.S) is calculated from the 3D rendered lacunae based on the algorithms such as Marching Cubes on the ANT^{TM} software (SkyScan, Kontich Belgium) [van Hove *et al.* (2009)]. Carter et al. have reported the three eigenvalues (EV1, EV2 and EV3) of the lacunar fitting ellipsoid calculated with the commercial software AMIRA microscopy module [Carter *et al.* (2012), (2013)], but not directly the three axis lengths of the osteocyte or lacuna (Ot.L1, Ot.L2, Ot.L3 or Lc.L1, Lc.L2, Lc.L3). They also introduced related parameters named lacunar equancy (Lc.Eq), lacunar elongation (Lc.El), and lacunar flatness (Lc.Fl) defined by three eigenvalues as:

$$\begin{aligned} Lc.Eq &= EV3 : \mathrm{EV1} \\ Lc.El &= 1 - EV2 : EV1 \\ Lc.Fl &= 1 - EV3 : EV2 \end{aligned} \tag{4.1}$$

In addition, they also reported the orientation of the lacunae (Lc.Φ), defined as the value of the angle between the longest lacunar axis and the horizontal axis of the sample. Their reported approximate values are listed in Table 4.5.

The volume of the osteocyte or lacunae varies from 50 µm^3 to 850 µm^3. Hannah et al. reported a bimodal distribution of the osteocyte lacunae volume by analyzing eleven osteons in human bone from SR micro-CT images at a voxel size of 1.4 µm [Hannah *et al.* (2010)].

The surface area of the osteocytes or lacunae varies from 90 μm^2 to 1100 μm^2 in different species. The average distance between the nearest two lacunae in human was found about 20 μm [Hannah *et al.* (2010)], which is about only one third of that measured in horse [Skedros *et al.* (2005)]. The average varies between different species and different types of bones: length of the osteocyte or lacunae varies between 9 μm to 28 μm, the width varies between 5 μm to 9 μm, and the depth varies between 4 μm to 13 μm. The anisotropy of osteocyte or lacunae also varies between different species and different types of bones. By means of commercial X-ray nano-CT, Vatsa et al. found more elongated osteocytes in fibula (ratio lengths: 5.9:1.5:1), compared to more spherical shape in calvaria [Vatsa *et al.* (2008)]. Table 4.5 reviews the different parameters found in the literature in human and in animal.

Table 4.5 3D Human morphological parameters of osteocytes or lacunae

Reference	Dim	Imag. Tech.	Location	Groups	# Samples	Lc/ Ot	Value
							Volume (μm^3)
[Remaggi *et al.* (1998)]	2D->3D	LM	Parallel-fibered in shaft bone			Lc	570
[McCreadie *et al.* (2004)]	3D	CLSM	Femoral head.trabecular bone	Control	10	Lc	455 ± 200
				Fractured	18	Lc	488 ± 235
				All	28 (10 control + 18 fracture)	Lc	476 ± 224
[van Hove *et al.* (2009)]	3D	Nano-CT	Proximal tibial	Osteoarthritis	1	Lc	51.2 ± 2.2
				Osteopenia	1	Lc	179.1 ± 15.6
				Osteopetrosis	1	Lc	97.6 ± 4.5
[Hannah et al. (2010)]	3D	SR-μCT	Right femoral shaft		1	Lc	290 ± 107
[Carter et al. (2012)]	3D	SR-μCT	Femur.shaft multiple regions		13	Lc	~399 ± 48
[Carter et al. (2013)]	3D	SR-μCT	Femur shaft anterior mid-cortical		30	Lc	252 ± 63
							Surface (μm^2)
[van Hove *et al.* (2009)]	3D	Nano-CT	Proximal tibial	Osteoarthritis	1	Lc	94.6 ± 2.8
				Osteopenia	1	Lc	211.9 ± 14.4
				Osteopetrosis	1	Lc	142.0 ± 5.0
							Length (μm)
[van Hove *et al.* (2009)]	2D+	CLSM	Proximal tibial	Osteoarthritis	1	Ot	17.3 ± 0.7
				Osteopenia	1	Ot	15.6 ± 0.4
				Osteopetrosis	1	Ot	11.1 ± 0.5
[Hannah et al. (2010)]	3D	SR μCT	Right femoral shaft		1	Lc	8.96 ± 5.5
							Width (μm)
[van Hove *et al.* (2009)]	2D+	CLSM	Proximal tibial	Osteoarthritis	1	Ot	8.4 ± 0.4

				Osteopenia	1	Ot	8.9 ± 0.4
				Osteopetrosis	1	Ot	5.5 ± 0.3
							Depth (µm)
[van Hove *et al.* (2009)]	2D+	CLSM	Proximal tibial	Osteoarthritis	1	Ot	12.2 ± 0.6
				Osteopenia	1	Ot	13.4 ± 0.6
				Osteopetrosis	1	Ot	10.8 ± 0.4
							Anisotropy
[McCreadie *et al.* (2004)]	3D	CLSM	Femoral head.trabecular bone	Control	10	Lc	0.305 (L3:L1)
				Fractured	18	Lc	0.299 (L3:L1)
				All	28 (10 control + 18 fracture)	Lc	0.301 (L3:L1)
[van Hove *et al.* (2009)]	3D	Nano-CT	Proximal tibial	Osteoarthritis	1	Lc	2.8 ± 0.1 (MIL)
				Osteopenia	1	Lc	3.1 ± 0.8 (MIL)
				Osteopetrosis	1	Lc	1.8 ± 0.3 (MIL)
							Distance (µm)
[Hannah et al. (2010)]	3D	SR µCT	Right femoral shaft		1	Lc	21.9 ± 6.3
							Orientation (degree)
[Carter et al. (2012)]	3D	SR µCT	Femur.shaft.multiple regions		13	Lc	~55.9 ± 3.8
[Carter et al. (2013)]	3D	SR µCT	Femur shaft anterior mid-cortical		30	Lc	59.45 ± 3.44
							EV1
[Carter et al. (2012)]	3D	SR µCT	Femur.shaft.multiple regions		13	Lc	~15.4 ±1.2
[Carter et al. (2013)]	3D	SR µCT	Femur shaft anterior mid-cortical		30	Lc	13.00 ± 2.39
							EV2
[Carter et al. (2012)]	3D	SR µCT	Femur.shaft.multiple regions		13	Lc	~4.2 ± 0.6
[Carter et al. (2013)]	3D	SR µCT	Femur shaft anterior mid-cortical		30	Lc	3.33 ± 0.63
							EV3
[Carter et al. (2012)]	3D	SR µCT	Femur.shaft.multiple regions		13	Lc	~1.7 ± 0.4
[Carter et al. (2013)]	3D	SR µCT	Femur shaft anterior mid-cortical		30	Lc	1.55 ± 0.45
							Elongation
[Carter et al. (2012)]	3D	SR µCT	Femur.shaft.multiple regions		13	Lc	~0.73 ± 0.03
[Carter et al. (2013)]	3D	SR µCT	Femur shaft anterior mid-cortical		30	Lc	0.66 ± 0.04
							Equancy
[Carter et al. (2012)]	3D	SR µCT	Femur.shaft.multiple regions		13	Lc	~0.19 ± 0.03
[Carter et al.	3D	SR	Femur shaft anterior		30	Lc	0.18 ± 0.03

(2013)]		µCT	mid-cortical			
						Flatness
[Carter et al. (2012)]	3D	SR µCT	Femur.shaft.multiple regions	13	Lc	~0.58 ± 0.02
[Carter et al. (2013)]	3D	SR µCT	Femur shaft anterior mid-cortical	30	Lc	0.41 ± 0.9

4.3 Characterization of osteocyte processes or canaliculi

4.3.1 Canalicular properties at tissue level

4.3.1.1 Density of canaliculi

The density of canaliculi is much less reported than that of lacunae, Table 4.6. Using a technical procedure proposed by Marotti, see Figure 4.2, the canalicular density, defined as the number of canaliculi per 10 µm length, varies in the range [2.3, 6.3] (#/10 µm) when measured using light microscopy in different species [Marotti *et al.* (1995); Remaggi *et al.* (1998); Ferretti *et al.* (1999)]. However, the method was not well elaborated and mainly relies on manual counting. The canalicular density in human tibia, expressed as the number of canaliculi opening on 100 μm^2 of Haversian surface, was measured to be 5.50 (#/100 μm^2) using SEM [Marotti *et al.* (1995)]. More recent study reported a canalicular density of 0.85 (#/μm^2) in bovine tibia.

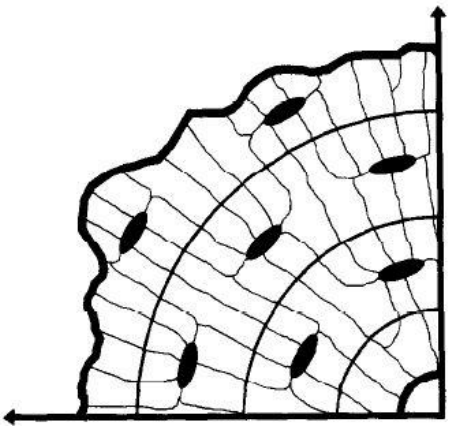

Figure 4.2 Illustration of calculating canalicular density based on the three concentric lines proposed by [Marotti *et al.* (1995)]

The canalicular 3D density, defined as the number of canaliculi per micrometer square of their lacunar surface, was counted 0.18 (#/μm^2) in mice in 3D rendering images.

Table 4.6 Density of canaliculi and osteocyte processes

Reference	Dim	Imaging Tech.	Species	Location	Groups	# Samples	Ca /Pr	Value
								Density
[Marotti *et al.* (1995)]	2D	SEM	human	tibia. Middiaphyseal compact bone	46 yrs	1	Ca	5.50 ± 1.90 (#/100 µm2)
		LM			25 yrs	1	Ca	2.35 ± 0.40 (#/10 µm)
					46 yrs	1	Ca	2.27 ± 0.39 (#/10 µm)
					78 yrs	1	Ca	2.32 ± 0.40 (#/10 µm)
[Remaggi *et al.* (1998)]	2D	LM	frog, chick, rabbit, bovine, horse, dog and human	parallel-fibered in shaft bone		?	Ca	2.9~4.8 (human 2.9) (#/10 µm)
[Ferretti et al. (1999)]	2D	LM	frog, sheep, dog, bovine, horse and human	tibia compact bone		3	Ca	4.5 ~ 6.3 (human 4.5) (#/10 µm)
[Lin et al. (2011)]	2D	AFM	Bovine	tibia cortical	Longitudinal	1	Ca	0.85 ± 0.31 (0.78 ~ 2.05) (#/µm^2)
								3D Density N.Ca/Lc.S
[L Wang *et al.* (2005)]	3D	FRAP	mice	left tibia diaphysis		5	Ca	0.18 ± 0.03 (#/µm^2)

L1, L2, L3: Length, width, depth of lacunae

MIL: The degree of anisotropy measured by using the mean intercept length (MIL)

4.3.1.2 Porosity of canaliculi

In a recent study, FIB/SEM imaging allowed to measure the canaliculi porosity but this evaluation was limited to a very small field of view (19×14×12 µm^3) [Schneider *et al.* (2011)]. In a further study, the authors used confocal microscopy to compare LCN properties in ovariectomized and control rats [Sharma *et al.* (2012)]. If the technique was valuable to assess differences between the groups, it provided values of canalicular porosity overestimated by about one order of magnitude due to the partial volume effects of the confocal microscopy with a spatial resolution of 200nm. Table 4.7 summarizes the values of 3D lacunar or canalicular porosity found in the literature.

Table 4.7 literatures related with the value of canalicular porosity within cortical bone

Reference	Dim	Imaging Tehc.	Species	Location	Groups	# Samples	Lc/Ca	Value
								Porosity (%)
[Schneider *et al.* (2011)]	3D	FIB/SEM	mouse	femur mid-diaphysis		1	Ca	0.70
[Sharma et al. (2012)]	2D+	CLSM	Rat	Cortical bone: metaphysis	SHAM	6	Ca	14%
					OVX			19%

4.3.2 Morphological parameters of canaliculi and processes

Morphological parameters of canaliculi and osteocyte processes, including canalicular/processes diameter, canalicular/processes length, number of canaliculi/processes per lacunae/osteocyte, surface and volume of canaliculi/processes have been reported in several studies. The canalicular/processes diameter is summarized in Table 4.8. The number of canaliculi/processes per lacunae/osteocyte is reviewed in Table 4.9. And the rest of the parameters are presented in Table 4.10 and Table 4.11.

The average diameter of canaliculi/processes spans a range of 100~700 nm, using electron microscopy [L You *et al.* (2004); Schneider *et al.* (2011); Sharma *et al.* (2012)], AFM [Lin *et al.* (2011)], and CLSM [Sugawara *et al.* (2005), (2011); Sharma *et al.* (2012)]. The average length of the canaliculi varies from 1 μm to 26 μm measured using FIB/SEM [L Wang *et al.* (2005)] and FRAP [L Wang *et al.* (2005)]. The average total length process of one osteocyte is reported between 1000 ~ 2700 μm [Sugawara *et al.* (2005), (2011)]. By using, CSLM Sugawara et al., measured the average value of surface and volume of the processes connected to the single osteocyte, however, the reported value can be overestimated due to the partial volume effect [Sugawara *et al.* (2005), (2011)].

The number of canaliculi or processes per lacuna or osteocyte has been documented in several studies. The value measured in 2D lies between 5 to 115 using light microscopy [Beno *et al.* (2006)] and AFM [Lin *et al.* (2011)]. [Beno *et al.* (2006)] extrapolated the value from a previous study of Ferretti et al. [Ferretti *et al.* (1999)] by using an ideal ellipsoid model, and reported an average number of canaliculi in human of 41. More recently, Sharma et al. was able to measure a number of primary and secondary canaliculi per lacunae, which put in evidence the branching morphology of canaliculi [Sharma *et al.* (2012)]. In a recent study Schneider estimated 78 canaliculi radiating from one osteocyte lacunae using FIB/SEM images [Schneider *et al.* (2011)]. He also reported other morphological parameters of canaliculi (see Table 4.11), but the reported values may not be biologically representative since they were calculated from only one third of the lacuna.

Table 4.8 Diameter of the canaliculi and processes

Reference	Dim	Imaging Tech.	Species	Location	Groups	# Samples	Subject	Value
								Diameter (nm)
[L You *et al.* (2004)]	2D	TEM	Mice	Humeri.Diaphysis		3	Pr	104 ± 69 (50 ~ 410)
						3	Ca	259 ± 129 (80~710)
[Lin et al. (2011)]	2D	AFM	Bovine	Tibia cortical	Transverse	1	Ca	426 ± 118 (155 ~ 844)
					Radial	1	Ca	459 ± 144 (120 ~ 214)

					Longitudinal	1	Ca	419 ± 113 (185 ~ 196)
[Sharma et al. (2012)]	2D	SEM	Rat	Tibia cancellous bone: metaphysis	Control	6	Ca	335 ± 32
					OVX	6	Ca	341 ± 32
[Sharma et al. (2012)]	2D	TEM	Rat	Tibia cancellous bone: metaphysis	SHAM	6	Ca	228 ± 11
					OVX	6	Ca	242 ± 22
[Sugawara *et al.* (2005)]	2D+	CLSM	Chick	Calvarial		?	Pr	<500
[Sharma et al. (2012)]	2D+	CLSM	Rat	Tibia cortical bone: metaphysis lamellar region	Control	6	Ca	553 ± 33
					OVX	6	Ca	697 ± 51
				Tibia cancellous bone: metaphysis lamellar region	Control	6	Ca	483 ± 24
					OVX	6	Ca	714 ± 82
[Schneider *et al.* (2011)]	3D	FIB/SEM	Mouse	Femur mid-diaphysis	Local	1	Ca	73 ± 29

Table 4.9 the number of canaliculi/processes per lacunae/osteocyte

Reference	Dim	Imaging Tech.	Species	Location	Groups	# Samples	Subject	Value
								# canaliculi/processes per lacuna/osteocyte
[Shapiro (1988)]	2D	LM	Rabit	Femoral mid·diaphyseal cortical bone		17 male and 12 female rabbit	Ca	17.7 ± 4.0
[Fritton et al. (2005)]	2D	CLSM	Rat	Tibia		6	Ca	63
[Hirose et al. (2007)]	2D	LM	Mice	Femur metaphyseal cortical bone	Wild type Periosteal region	1	Ca	18.38 ± 3.64
					Wild type Endosteal region	1	Ca	20.23 ± 4.13
					OPG−/− Periosteal region	1	Ca	17.85 ± 3.26
					OPG−/− Endosteal region	1	Ca	16.62 ± 4.07
[Lin et al. (2011)]	2D	AFM	Bovine	Tibia cortical		1	Ca	5 ± 2
[Beno et al. (2006)]	2D->3D	CLSM	Chick	Cortical locaions		?	Ca	54
			Rabbit			?	Ca	60
			Bovine			?	Ca	85

			Horse			?	Ca	115
			Dog			?	Ca	81
			Human			?	Ca	41
[L Wang *et al.* (2005)]	3D	CSLM	Mice	Left tibia diaphysis		5	Ca	12 ± 2.6
[Schneider *et al.* (2011)]	3D	FIB/SEM	Mouse	Femur mid-diaphysis		1	Ca	78
[Kamioka et al. (2001)]	2D+	CLSM	Chicken	Calvariae		1	Pr	26.05 ± 5.28
[Sugawara *et al.* (2005)]	2D+	CLSM	Chick	Calvarial		?	Pr	52.7 ± 5.7
			Chick	Parietal bone		6	Pr	52.7 ± 6.4
			Mouse			7	Pr	49.7 ± 9.7
[Sharma et al. (2012)]	2D->3D	CLSM	Rat	Tibia cortical bone: metaphysis	SHAM	6	Ca	83.9 ± 14 *
					OVX	6	Ca	89.7 ± 15 *
					SHAM	6	Ca	387 ± 34 **
					OVX	6	Ca	365 ± 40 **

*: Number of primary canaliculi per lacuna

**: Number of secondary canaliculi per lacuna

Table 4.10 Other morphological parameters of canaliculi and osteocyte processes

Reference	Dim	Imaging Tech.	Species	Location	Groups	# Samples	Subject	Value
								Mean Length (µm)
[L Wang *et al.* (2005)]	3D	CSLM	Mice	Left tibia diaphysis		5	Ca	26 ± 4.1
[Schneider *et al.* (2011)]	3D	FIB/SEM	Mouse	Femur mid-diaphysis	Local	1	Ca	0.958 ± 1.122
								Total Length (µm)
[Sugawara et al. (2011)]	2D+	CLSM	Chick	Parietal bone		10	Pr	1,131 ± 139
			Mouse	Parietal bone		10	Pr	2,668 ± 596
[Sugawara *et al.* (2005)]	2D+	CLSM	Chick	Calvarial		?	Pr	1070 ± 145
								Surface (µm^2)
[Sugawara *et al.* (2005)]	2D+	CLSM	Chick	Calvarial		?	Pr	785
[Sugawara et al. (2011)]	2D+	CLSM	Chick	Parietal bone		10	Pr	461
			Mouse			10	Pr	1,587

								Volume (µm^3)
[Sugawara *et al.* (2005)]	2D+	CLSM	Chick	Calvarial		?	Pr	137
[Sugawara et al. (2011)]	2D+	CLSM	Mouse	Parietal bone		10	Pr	688
			Chick			10	Pr	123

Table 4.11 Other morphological parameters of canaliculi

Reference	Dim	Imaging Tech.	Species	Location	# Samples	Subject	Descriptors	Value
								Others
[Schneider *et al.* (2011)]	3D	FIB/ SEM	mouse	femur mid-diaphysis	1	Ca	structure model index (SMI)	2.31
					1	Ca	percent canalicular bone interface	0.90
					1	Ca	Spacing	1.88
					1	Ca	mean canalicular slenderness	13 ± 15
					1	Ca	mean lacuna surface per canaliculus	3.1
					1	Ca	Thickness	95

4.4 Conclusion

In this chapter, we briefly described which measurements on osteocytes and canaliculi have been reported so far, in 2D and in 3D. We provided an extensive review of the literature which will be useful to specify the characteristics of the imaging system according to the properties of the structures to be imaged, and in comparing our final results to those of the literature. The main conclusion is that the osteocyte density is relatively large ($> 10^6$ mm^{-3}), that of canaliculi is even worse ($> 10^7$ mm^{-3}) with respective characteristic sizes of tenth of micrometers and hundreds of nanometers, thus requiring very high spatial resolution imaging methods and efficient computing tools.

In the last decade, the first 3D characteristics of the LCN have been reported, but still these measurements remain limited. These limitations are due to several reasons. First, there is still no gold standard for acquiring high quality 3D images of the LCN within a relatively large field of view. Second, the quantification of the LCN is restricted by the available commercial image analysis software, which are not dedicated to this problem. Third, getting reliable statistical results will require analyzing thousands of structures, but, up to now, data on the LCN has been reported from limited populations. Therefore, the development of sophisticated methods to automatically quantify the complex LCN morphology is crucial, to help to unveil the osteocyte mechanosensation and mechanotransduction processes.

II. CONTRIBUTION

Chapter 5

Image acquisition from synchrotron radiation CT from micro to nanoscale

Contents

5.1 Introduction 49
5.2 European synchrotron radiation facility 50
5.3 Synchrotron radiation micro and nano CT 51
5.3.1 SR micro-CT setup at beamline ID19 51
5.3.2 X-ray magnified phase tomography setup at ID22 52
5.4 Data reconstruction 53
5.4.1 Absorption CT 53
5.4.2 Phase nano CT 54
5.5 Experiments and image acquisition 56
5.5.1 SR CT at the submicrometer scale (300 nm voxel size) 58
5.5.2 Magnified SR phase CT at the nanometer scale (50 nm voxel size) 62
5.6 Conclusion 64

5.1 Introduction

Using synchrotron radiation (SR) micro-CT instead of standard X-ray micro-CT possesses significant advantages for the investigation of bone samples[Flannery *et al.* (1987)][Salome *et al.* (1999)]. SR micro-CT generally uses monochromatic synchrotron radiation beams with a high photon flux, avoiding beam hardening artifacts and providing high Signal to Noise Ratio (SNR) images. The image can be directly interpreted as a map of the X-ray linear attenuation coefficient within the sample at the given energy. When applied to bone research, these properties enable not only to study bone micro-structure but also its mineralization. The assessment of the distribution of the degree of mineralization from synchrotron micro-CT has been successfully compared to quantitative micro-radiography [Nuzzo *et al.* (2002 b)].

SR micro-CT has been widely used in bone research for the quantitative assessment of trabecular bone microstructure in humans and in animal models [Nuzzo *et al.* (2002 a)][Martin-Badosa *et al.* (2003)]. While cortical bone has been neglected in the past, it is now receiving increasing interest, since recent works suggests that cortical porosity is a crucial determinant of bone fragility [Zebaze *et al.* (2010)]. SR micro-CT is also well suited to study the 3D micro-structure of cortical bone [Bousson *et al.* (2004)]. By virtually taking the negative of bone, it is possible to display the porous network, composed of the Havers' and Volkmann's networks. The choice of acquisition conditions has been shown to have a great impact on the rendering of the porous network and the estimation of porosity[Cooper, D.M. *et al.* (2007)]. In particular, due to the small porosity of cortical bone, it is generally necessary to use a higher incident beam energy compared to trabecular bone, to avoid beam hardening. In this respect, SR micro-CT is perfectly suited to image cortical bone since the energy can be flexibly selected.

In association with appropriate software for the calculation of direct 3D parameters, X-ray micro-CT is now routinely used for the analysis of trabecular bone and increasingly used for that of cortical bone micro-structure. This is typically achieved by using micro-CTs with spatial resolutions in a range of 3 to 10µm.

Less attention has been devoted to imaging bone at higher spatial resolution but the characterization of the bone properties at the cellular scale is also of major interest. However, at the submicrometer or nanometer scale, SR micro-CT is a tool of choice to image bone tissue.

In this chapter, we describe two synchrotron CT systems developed at the ESRF on which we have performed experiments to acquire images of bone samples. Parallel-beam 3D micro-CT has been developed on beamline ID19 and can provide images of samples up to submicrometer spatial resolution. X-ray magnified phase nano CT has been designed to achieve nanometric spatial resolution and implemented on beamline ID22. In the latter, by using phase retrieval prior to tomographic reconstruction, the system provides maps of the 3D refractive index distribution.

We first recall the principle of a synchrotron source, then we describe the experimental setups of the two systems, and the principle of image reconstruction. Finally, we present two types of experiments that we have performed to acquire data at several scales.

5.2 European synchrotron radiation facility

Located in Grenoble, the European synchrotron radiation facility (ESRF) is one of the most powerful (6 GeV) synchrotron radiation sources in the world. Together with the Advanced Photon Source (APS) at Argonne National Laboratory in the United States and the Super Photon Ring–8 GeV (Spring-8) in Hyogo Prefecture in Japan, the ESRF belongs to third generation synchrotron light sources.

The ESRF is composed of a linear accelerator (Linac), a booster synchrotron and a storage ring connected to beamlines, Figure 5.1. In the Linac, the electrons are generated by an electron gun, a device similar to the cathode ray tube. These electrons are accelerated nearly to the speed of light by a pulsed electric field in a hollow vacuum chamber. Before these electrons are sent into the storage ring, they are increasingly accelerated from 200 MeV to the final 6 GeV energy in about 50 milliseconds in the booster synchrotron. In this 300 m racetrack-shaped ring of electromagnets, the accelerating force is supplied by electrical fields in the radio frequency cavities. To maintain the orbit of the electrons inside this booster, the bending and focusing magnets need to increase the magnetic field strength in synchronization with the speed of electrons. This is why the accelerator is called a synchrotron. Inside the storage ring, the electrons circulate nearly at the speed of light for hours in a long evacuated tube (844 meters in circumference). As the electrons pass through bending magnetics and insertion devices (Figure 5.2), synchrotron light is radiated into different beamlines for various scientific researches.

Each beamline is dedicated to a given type of experiment, going from X-ray diffraction to imaging. The beamlines are typically composed of three hutches: an optic hutch, where the beam is put in shape; an experimental hutch, where the sample is exposed to synchrotron light; and a control hutch, from which the experimentalist has a remote control of the different devices in the experimental hutch.

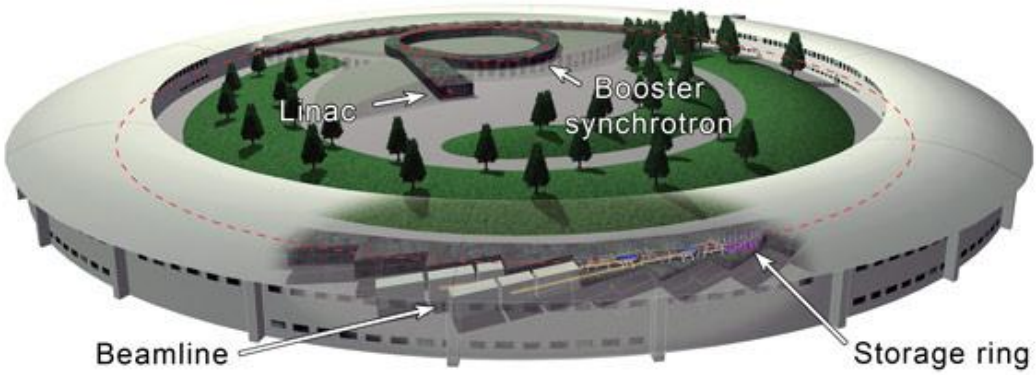

(a)

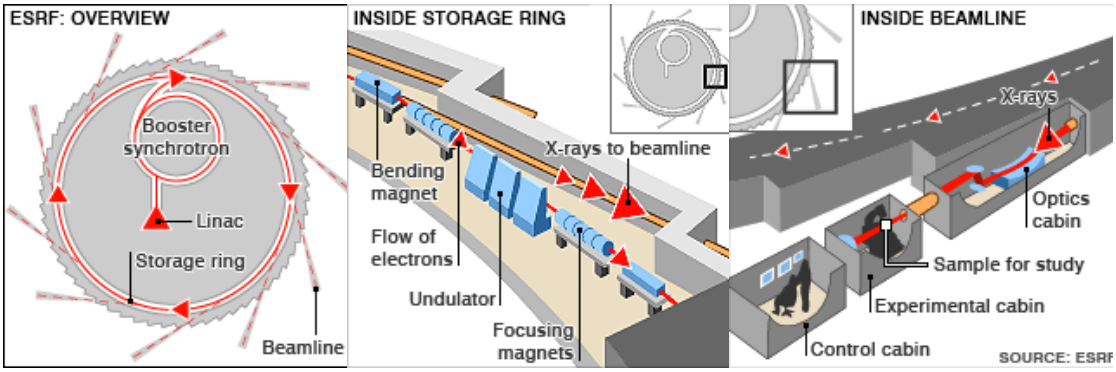

(b) (c) (d)

Figure 5.1 basic compositions of a synchrotron radiation instrument ((a): http://www.esrf.eu/Accelerators/Accelerators (b)-(d) image from: http://news.bbc.co.uk/2/hi/science/nature/7760380.stm)

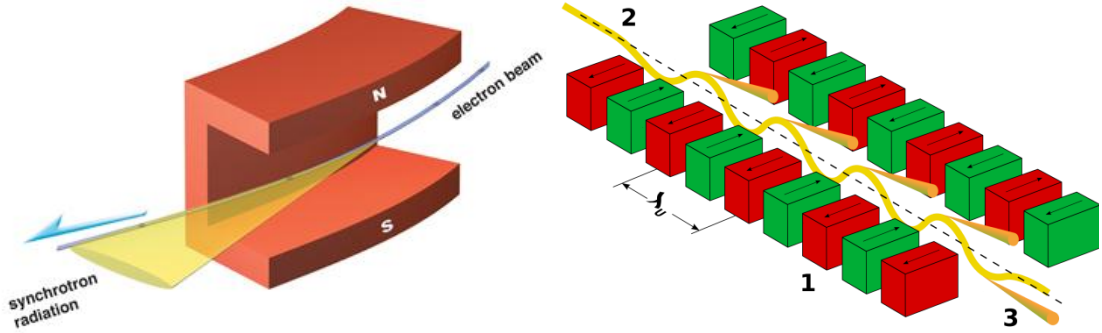

(a) (b)

Figure 5.2 Synchrotron radiation from (a) bending magnets and (b) undulators (Image from: (a): http://www.nsrrc.org.tw/english/lightsource.aspx (b):http://en.wikipedia.org/wiki/Synchrotron_radiation)

5.3 Synchrotron radiation micro and nano CT

5.3.1 SR micro-CT setup at beamline ID19

The beamline ID19 (the X-ray is generated from the insertion device (ID)) of ESRF is a long imaging beamline, designed for full-field parallel-beam imaging techniques. It is a 145-meter long beamline, containing three insertion devices: a wiggler and two undulators. For imaging the bone specimen at high resolution, the undulators and the multilayer monochromator are used to generate high photon flux. While the single-bounce Bragg geometry multilayer monochromator can select a monochromatic beam with monochromaticity $\Delta E/E \approx 10^{-2}$ (Figure 5.3), the undulator U17.6 allows producing a pseudo-monochromatic "pink beam", but with extremely high flux [Pacureanu *et al.* (2012)].

The micro-CT setup developed on ID19 was based on truly 3D parallel beam CT [Salome *et al.* (1999); Weitkamp *et al.* (2011)]. The principle is to acquire 2D parallel radiographs of a sample mounted on a sample stage for different angles of rotations spanning 180° or 360°. In

addition to the rotation stage, two precise translation stages are used to control the position of the specimen in the beam.

The detector is composed of a scintillator, a visible-light lens system and a charge-coupled device (CCD) sensor. The scintillator converts the X-ray beam into the visible light. Different scintillators of different sizes and thicknesses and made of different materials are available. The optical lens is capable of provide a magnification using different combinations of objectives and eyepieces, which offers an effective pixel size from 0.18 to 30 µm. The CCD camera, which is called FReLoN (Fast Readout Low Noise) camera, was developed by the instrument support group of ESRF and provides 2048×2048 pixels with a 16 bits resolution [Labiche *et al.* (2007)].

A typical experiment requires choosing the adapted detector configuration including scintillator, optics and CCD, selecting the appropriate energy and flux, fixing the imaging conditions (number of projections, counting time for each projection). Then each sample has to be mounted on the sample stage and correctly centered in the beam at 0° and 90° before launching a macro to scan the sample. Afterward, the linear attenuation map of the sample can be reconstructed by processing the recorded radiographs (see section 5.4).

Note that, while micro-CT is usually based on absorption contrast, another mode of contrast, called phase contrast can also be used on this setup [Cloetens *et al.* (1997)]. With the coherent X-ray sources, such as available at synchrotron sources, phase contrast is formed when the detector is put further away from the sample. In this case, the X-ray beam transmitted through the sample propagates in free space and interference patterns are recorded on the detector. This simple implementation of phase contrast imaging is called in-line propagation. Phase CT consists in acquitting one of several tomographic scans of the sample at different propagation distances. In this case, after a phase retrieval process, tomographic reconstruction provides the phase decrement index of the sample (see section 5.4.2).

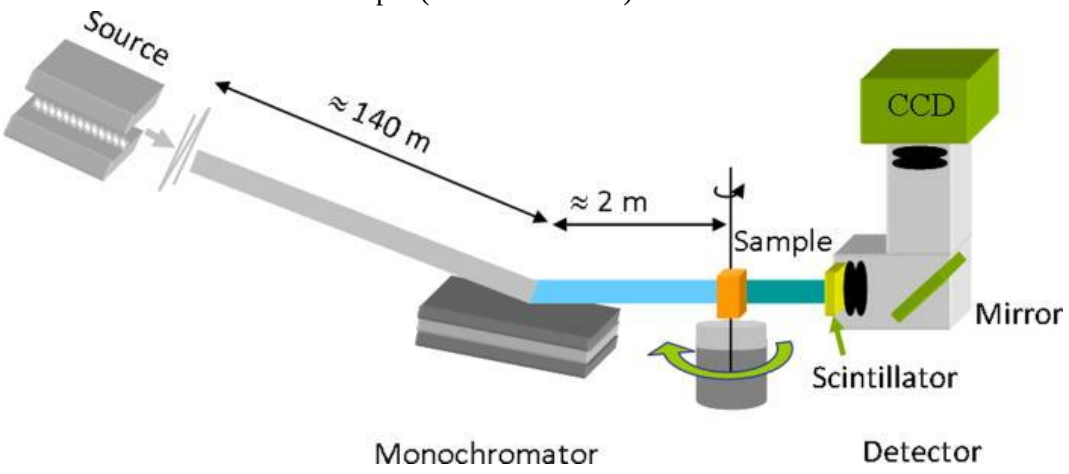

Figure 5.3 SR micro-CT setup at beamline ID19 using single-bounce Bragg geometry multilayer

5.3.2 X-ray magnified phase tomography setup at ID22

The nano-CT setup has been developed at the nano-imaging station ID22NI of the ESRF [Martínez-Criado *et al.* (2012)]. The technique uses as illumination source the X-ray spot

focus produced by dynamically figured multilayer-coated mirrors (Kirkpatrick-Baez crossed mirror geometry). The X-ray energy can be set between 17 keV and 30 keV. For the X-ray energy of 17 keV, used in the present work, the first harmonic of a single-line undulator (19 mm period U19) is used. No other monochromatization than the one provided by the multilayer coatings is used, assuring a high flux and short acquisition times. The undulator-multilayers system provides a medium monochromaticity of $\Delta E/E$=1.6×10^{-2}.

The nano-CT setup exploits phase contrast imaging by recording several scans at different distances. Conversely to the ID19 parallel beam setup, the detector remains at a large distance from the focus while the sample will be moved downstream of the focus. The geometric magnification M of the image is given by $M = (d_1 + d_2)/d_1$, where d_1 is the distance between the focal point and the sample, and d_2 the distance between the sample and the detector (see Figure 5.4). In practice, in the experiments that we performed, radiographs were recorded at four sample-source distances d_1 while keeping the detector position fixed at $d_1 + d_2 = 525$ mm. This geometry results in a final pixel size between 25 and 400 nm.

The detector consisted of a high efficiency LSO:Tb luminescent converter screen [Douissard *et al.* (2010)], lens coupled to a large dynamic range and the FReLoN camera. The X-ray magnification allows overcoming the spatial resolution limit of the X-ray detector. Due to the free-space propagation in this geometry, the radiographs always show significant phase contrast.

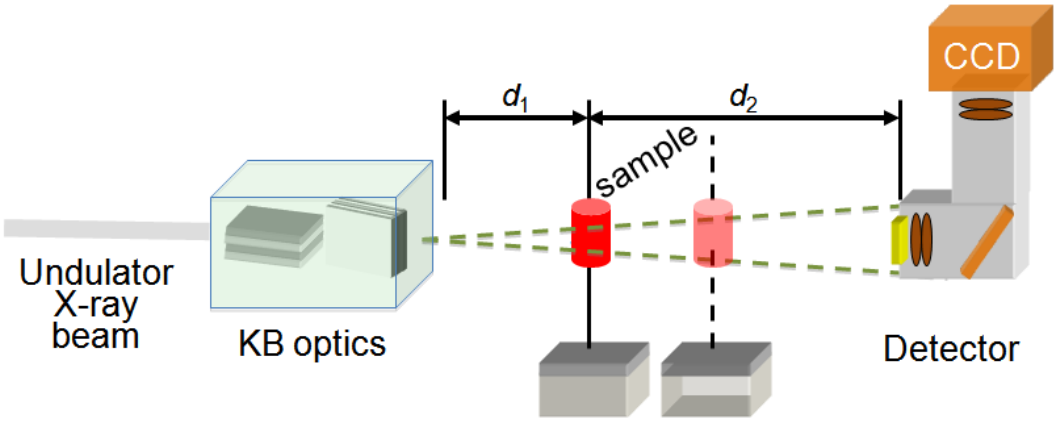

Figure 5.4 Illustration of divergent-beam phase SR nano-CT at the nano-imaging station ID22NI (ESRF).

5.4 Data reconstruction

We present image reconstruction in the case of absorption CT (standard case) and we briefly outline the case of phase CT.

5.4.1 Absorption CT

In absorption CT, the underlying physical phenomenon is the attenuation of the X-ray beam after passing through the sample. This effect is modeled by the Beer-Lambert law. Let $\mu(\boldsymbol{x})$ be the 3D linear attenuation coefficient image for the X-ray beam of wavelength λ where

$\boldsymbol{x}$=*(x,y,z)*. Let $p_\theta(u,v)$ be its 2D projection at a point (u,v) on the detector and for a rotation angle θ around the z-axis. Thanks to the Beer-lambert law $p_\theta(u,v)$ can be expressed as:

$$p_\theta(u,v) = \ln\left(\frac{I_\theta^0(u,v)}{I_\theta(u,v)}\right) = \int_{D_{\theta,u,v}} \mu(x,y,z)ds \tag{5.1}$$

where $D_{\theta,u,v}$ is the line describing the X-ray path, $I_\theta^0(u,v)$ and $I_\theta(u,v)$ are the intensity recorded respectively without and with the sample in the beam.

The linear attenuation coefficient image $\mu(\boldsymbol{x})$ can then be obtained from the set of its 2D projections $p_\theta(u,v)$ by solving an inverse problem. This problem is a straightforward extension of the 2D case, which is well known in tomography. From a theoretical point of view, $\mu(\boldsymbol{x})$ relies on the inversion of the Radon Transform. A conventional and efficient reconstruction method is the Filtered Back Projection (FBP) algorithm. Thus, the 3D parallel beam tomographic reconstruction can be performed by using the standard FBP [Bracewell *et al.* (1967)] algorithm for each slice at height z:

$$\mu(x,y,z) = \int_0^\pi \tilde{p}\theta(xcos\theta + ysin\theta, z)d\theta \tag{5.2}$$

where $\tilde{p}\theta(u,v)$ is the projection filtered with respect to the first variable with the conventional 1D ramp filter.

We may note that the reconstruction is exact, unlike in most standard X-ray micro-CT systems where a cone beam source is rotated along a circular trajectory. This is another advantage of the 3D parallel beam setup, since no distortions or blurring will be introduced by the tomographic reconstruction.

5.4.2 Phase nano CT

The modeling of phase contrast involves the 3D complex refractive index $n(\boldsymbol{x}) = (1 - \delta(\boldsymbol{x})) + i\lambda\mu(\boldsymbol{x})/4\pi$ [Engelke *et al.* (1993)]. Let us introduce the transmittance function $T_\theta(u,v)$ corresponding to the ratio of the wave exiting the object and the incident is defined as:

$$\begin{aligned} T_\theta(u,v) &= \exp\big(-B_\theta(u,v) + i\varphi_\theta(u,v)\big) \text{ with} \\ B_\theta(u,v) &= \tfrac{1}{2}\textstyle\int_{D_{\theta,u,v}} f(\boldsymbol{x})ds \text{ and} \\ \varphi_\theta(u,v) &= \frac{-2\pi}{\lambda}\int_{D_{\theta,u,v}} \delta(\boldsymbol{x})ds \end{aligned} \tag{5.3}$$

By modeling the effect of propagation, the intensity of the recorded phase radiographs for rotation angle θ and distance *d* can be expressed as the modulus of a Fresnel Transform as:

$$\begin{aligned} I_{\theta,d}(u,v) &= |(T_\theta * P_d)(u,v)|^2 \\ P_d(u,v) &= \frac{-i}{\lambda d}\exp\left(\frac{i\pi}{\lambda d}(u^2+v^2)\right) \end{aligned} \tag{5.4}$$

Since only the intensity is available, the phase term $\varphi_\theta(u,v)$ is encoded in this expression but not directly available. Thus, reconstruction of the 3D refractive index decrement $\delta(\boldsymbol{x})$ requires first to solve a "phase retrieval" problem to estimate $\varphi_\theta(u,v)$ from images at different propagation distances, and second, to perform tomographic reconstruction from the phase maps for the different rotation angles.

Phase retrieval is a non-linear ill-posed inverse problem. It is not straightforward to use the non-linear relation in Equation (5.4) directly for phase retrieval. Most reported methods are based on the linearization of Equation (5.4) to provide a linear forward problem, which yields efficient reconstruction algorithms. Two main classes of algorithms can be identified in literature: algorithms based on a linearization with respect to the propagation distance, which yield what is known as the transport of intensity equation (TIE) [Teague (1982)] and algorithms based on linearization with respect to the object, which yield the contrast transfer function (CTF) [Cloetens *et al.* (1999)].

The simplest method when a signal propagation distance is used is the Paganin's method [Paganin *et al.* (2002)]. It is based on the assumption that the object is homogeneous in terms of its chemical composition thereby assuming a proportionality between the linear attenuation coefficient and the phase index. The proportionality factor, denoted δ/β, which is a parameter of the algorithm, depends on the composition of the sample and the energy used. The method relies on the TIE approach, which in this particular case can be expressed as a simple frequency filtering in the Fourier domain of the image intensity. The filter is directly dependent of the δ/β ratio.

When using several distances, the CTF approach can be used but is more suited to low absorbing objects. A so-called mixed approach unifying the the TIE and CTF approaches and valid for strongly absorbing objects, was later proposed [Guigay *et al.* (2007)]. The different approaches have been compared quantitatively from simulated and constructed phantoms, and have showed that the mixed approach performed best in most cases in terms of precision and sensitivity [Engelke *et al.* (1993)]. The mixed approach is derived by linearizations of Equation (5.4) in two steps, yielding the linear contrast model:

$$\tilde{I}_d\,(\boldsymbol{f}) = \tilde{I}_d^{\varphi=0}(\boldsymbol{f}) + 2\sin(\pi\lambda d|\boldsymbol{f}|^2)\mathcal{F}\{I_0\varphi\}(\boldsymbol{f}) + cos(\pi\lambda d|\boldsymbol{f}|^2)\frac{\lambda d}{2\pi}\mathcal{F}\{\nabla\cdot(\varphi\nabla I_0)\}(\boldsymbol{f}). \tag{5.5}$$

where I_0 is the intensity at d=0 (that is supposed to be known), $\mathcal{F}$ and ~ denotes the Fourier Transform operator and **f** is the 2D spatial frequencies vector.

This equation can be used to pose a linear least squares optimization problem:

$$arg\min_{,\tilde{\psi}(\boldsymbol{f})}\sum_d \left\|\tilde{I}_d\,(\boldsymbol{f}) - \tilde{I}_d^{rec}(\boldsymbol{f})\right\|^2 + \alpha\left\|\tilde{\psi}(\boldsymbol{f})\right\|^2 \tag{5.6}$$

where $\psi(\mathbf{x}) = I_0(\mathbf{x})\varphi(\mathbf{x})$. The last term of Equation (5.6) limits the energy of the solution and corresponds to a standard Tikhonov regularization. The optimization problem has the iterative solution

$$\tilde{\psi}^{(n+1)}(\boldsymbol{f}) = \frac{\sum_d C_d(\boldsymbol{f})\left[\tilde{I}_d(\boldsymbol{f}) - \tilde{I}_d^{\varphi=0}(\boldsymbol{f}) - \Pi_d^{(n)}(\boldsymbol{f})\right]}{\sum_d C_d^2(\boldsymbol{f}) + \alpha} \tag{5.7}$$

In the presence of noise, the reconstructions are often corrupted by low frequency artifacts introducing a non-constant background. To solve this problem, a better regularization method based on a homogeneity prior was proposed and has given improved results in various applications [Langer *et al.* (2010)]. In this approach, the solution is searched as:

$$arg\,min_{\psi(\boldsymbol{f})} \sum_d \left\|\tilde{I}_d(\boldsymbol{f}) - \tilde{I}_d^{rec}(\boldsymbol{f})\right\|^2 + \alpha\left\|\tilde{\psi}(\boldsymbol{f}) - \tilde{\psi}_0(\boldsymbol{f})\right\|^2 \tag{5.8}$$

with the homogeneous composition prior:

$$\tilde{\psi}_0(\boldsymbol{f}) = H(\boldsymbol{f})\mathcal{F}\left\{\frac{\delta}{2\beta} I_0 ln(I_0)\right\}(\boldsymbol{f}) \tag{5.9}$$

The prior assumes that the chemical composition of the sample is made of a single material. In this case the real and imaginary part of the complex refractive index are proportional, proportionality expressed by the ratio δ/β. $H(\mathbf{f})$ is a suitable low-pass filter to limit the action of Equation (5.9) to the low frequency range.

5.5 Experiments and image acquisition

The parallel beam micro CT setup of ID19 at the micrometer scale was used to acquire images of osteocyte lacunae. Since, osteocyte lacunae are described as flattened ellipsoids, with axis of a few micrometers, a spatial resolution of the order of the micrometer is necessary. The possibility of observing osteocyte lacunae by using a voxel size in the range of the micrometer was demonstrated earlier [Peyrin *et al.* (2000); Hengsberger *et al.* (2003)]. In a previous work from the team, bone micro-cracks in human trabecular bone were also observed by using SR micro-CT at a voxel size of 1.4µm [Larrue *et al.* (2011)]. The segmentation of the micro-cracks is a challenging problem due to their very thin aperture (generally smaller than the voxel size). A specific technique based on a non linear enhancement method was developed [Larrue *et al.* (2011)]. This technique allowed to display the 3D morphology of micro-cracks and their location within trabeculae as well as quantitative measurements about their dimensions in all three directions. Although osteocyte lacunae were also visible in the images, they had not been studied in detail.

I participated to six experiments in view to quantify osteocyte lacunae in bone tissue. These experiments were performed within the framework of a Long Term Project MD431 entitled "Multi-scale analysis of bone tissue using Synchrotron Radiation micro-CT" including 11 academic partners (5 national and 6 international).

The experiments were performed on human or mice samples. The energy was set according to the sample size (typically between 20 and 25 keV). The number of projections varied between 2000 and 3000. The voxel size was set at 0.7 µm or 1.4 µm. The larger voxel size of 1.4 µm provides a larger field of view, i.e a cubic region of side 2.8 mm instead of 1.4 mm at 0.7 µm. The smaller voxel size is better for sampling the osteocyte lacunae shapes, but it also increases the radiation dose on the sample. Radiation dose may damage the sample by

producing local heat, destruction of the organic material in the sample, or creating micro cracks in the sample. As a consequence of these phenomenons, motion artifacts could appear in the reconstructed images. These artifacts may somehow be corrected under the assumption that a pure translation that can be estimated from the projections, Figure 5.5. In practice this assumption was only fulfilled for limited sample motion.

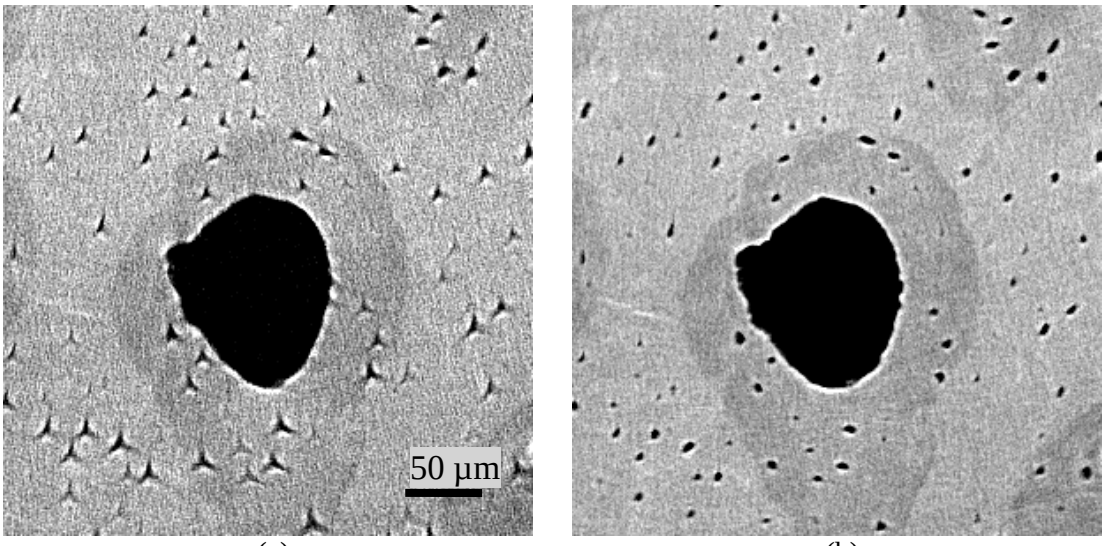

(a) (b)

Figure 5.5 Illustration of the motion artifacts and its correction on a slice of reconstructed image with voxel size of 1.4 µm

Using smaller acquisition times and/or a smaller number of projections may also reduce radiation dose, but this automatically reduces the signal to noise in the image. Thus finding appropriate conditions requires making a compromise between radiation dose and image quality. The setting was also dependent of the mode of preparation of the sample, for instance, dry sample versus sample embedded in resin.

As an illustration, renderings of SR micro-CT images of human cortical bone samples are presented. The samples were cut in parallelepipeds (50×4×2mm) and imaged using a voxel size set to 1.4 µm. An energy of 25keV was selected and the 3D image was reconstructed from 3000 projections taken over a rotation of total angle of 360°. The acquisition time was about 15 minutes. Figure 5.6 a) illustrates a region of interest in a typical CT slice. The large pores correspond to sections of the Haversian canals and the small ellipse-shaped ones to sections of osteocyte lacunae. The good densitometry contrast of SR micro-CT also permits to distinguish osteonal and interstitial tissue. The osteon having a lower degree of mineralization appear darker in the reconstructed linear attenuation map. By carefully examining the slice, it is also possible to see, linear micro-cracks appearing as small line segments. A segmentation method was applied to identify segmentation of Haversian canals, osteocytes and microcracks for the purpose of visualization. The segmentation of Haversian canals is quite straightforward due to the enough contrast to apply on a simple thresholding. The lacunae are extracted by a hysteresis thresholding (see section 6.2.4). The microcracks are segmented from a non-linear enhancement method, which was developed previously [Larrue *et al.*

(2011)]. The 3D renderings were generated by using the commercial software Avizo® 7.1. Figure 5.6 b) illustrates a 3D rendering of a volume of interest, showing the Haversian canals in gray, the osteocyte lacunae in yellow and micro-cracks in blue. In chapter 6, we shall address the problem of extracting quantitative information from these images.

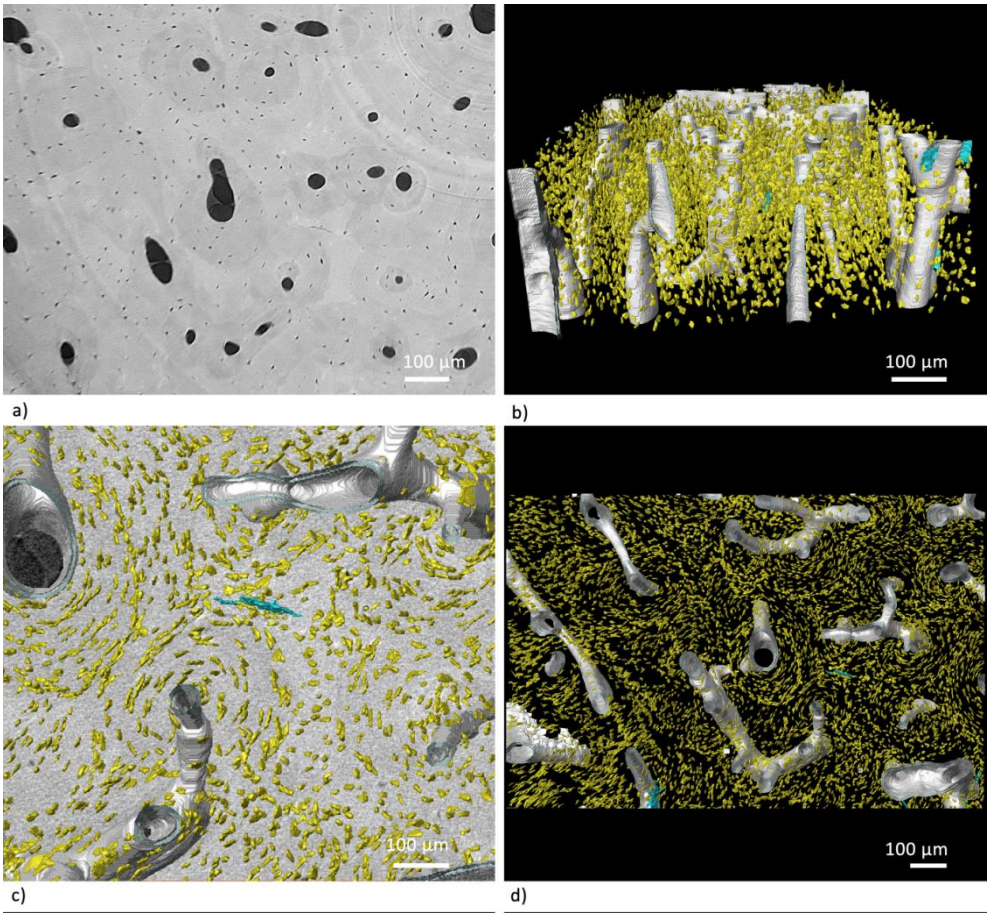

Figure 5.6. SR micro-CT images of a human cortical bone (voxel size of 1.4µm), a) ROI in a typical slice, b) and d) 3D displays (side and top view) of the Haversian canals (gray), osteocyte lacunae (yellow) and micro-crack (blue). c) zoom of the 3D display showing a micro-crack located in the center of slice a)

5.5.1 SR CT at the submicrometer scale (300 nm voxel size)

Other features of interest in the osteocyte system are the connections between the cells. As reviewed in chapter 4, these connections are hosted in the canaliculi which are thin channels with a diameter between 100 and 700 nm. In previous works, the team showed the feasibility of imaging the 3D architecture of the complex LCN system by using parallel beam SR micro-CT [Pacureanu *et al.* (2012)]. Due to the size of canaliculi, we acquired SR micro-CT images using a nominal pixel size on the detector of 300 nm, yielding a field of view in the 3D image of 600×600×600 μm^3. As discussed above, problems related to radiation damage are even more pronounced. Figure 5.7 illustrates the main problems encountered when imaging the

LCN with this technique (left image shows a slice of low SNR image acquired from a low dose; right image shows a much better SNR image. However, due to the higher dose damage, cracks and motion artifacts appears). In order to achieve imaging of the lacuno-canalicular network, it was necessary to optimize the acquisition setup. A key point was the sensitivity of the detector. The best settings were obtained by using a LSO: Tb_4.5 µm scintillation screen, a magnifying optic system and an E2V CCD camera.

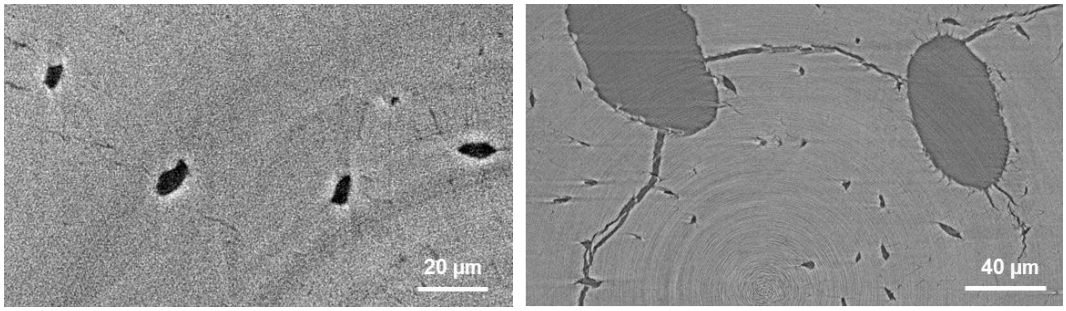

Figure 5.7 Imaging setup and experimental parameters need to be adapted to improve image quality and to avoid sample damage. Signal to noise ratio is increased with the radiation dose, but the sample is damaged by the high level of radiation, inducing motion artifacts.

A series of human tibial cortical bone samples were prepared for the image acquisition at the 300 nm resolution. The specimens were provided by G Kazakia from the group of S Majumdar at the University of California, San Francisco. For image acquisition, we used the SR micro-CT installed on beamline ID19 at the ESRF (European Synchrotron Radiation Facility, Grenoble, France). The experimental setup used the following conditions. An undulator was used as the insertion device, generating a nearly monochromatic X-ray beam at a beam energy of 19 keV. For each sample, 2400 projection images were recorded over a total angle of 180°. The acquisition time was about 65 minutes.

A 3D image volume with an isotropic spatial resolution of 300 nm was reconstructed by a filtered back-projection algorithm implemented in PyHST software (High Speed Tomography in python version 26, ESRF), coupled with a single distance phase retrieval process [Paganin *et al.* (2002); Weitkamp *et al.* (2011)]. For the phase reconstruction, the delta/beta was set to 153.8, calculated by XOP 2.1 software (ESRF).

Two kinds of artifacts often appear in the reconstructed SR micro-CT images. One is motion artifacts, caused by the radiation induced damage [Pacureanu *et al.* (2012)]. The other is ring artifacts, occurred as full or partial circles centered on the rotation axis. Figure 5.8 illustrate the two artifacts, and image after the artifact correction.

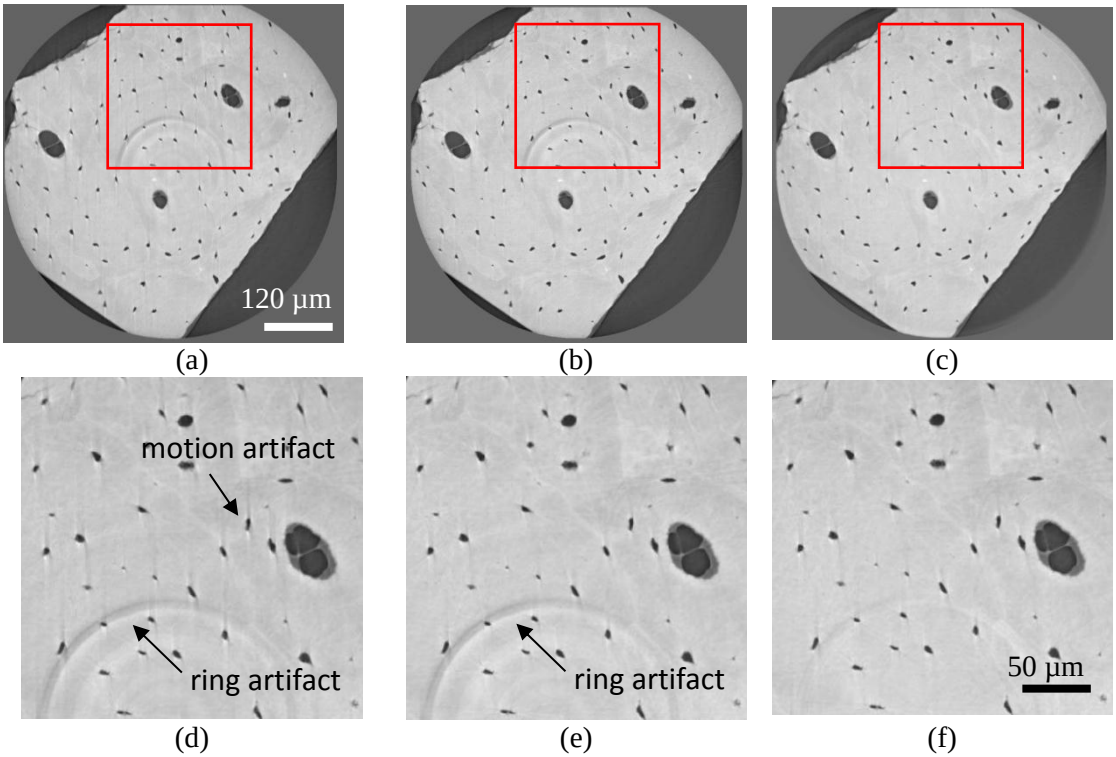

Figure 5.8 Illustration of the artifacts correction. (a) A slice of the reconstructed image shows the motion artifact and the ring artifact. (b) The slice after the motion correction (c) The slice after the ring correction. (d)-(f) are the zoom images corresponding to (a)-(c).

Figure 5.9 presents orthogonal slices in a volume of interest of a reconstructed 3D image, showing sections through two osteons. As can be seen on these slices, black ellipses correspond to osteocyte lacunae, while very small linear features or spots correspond to the intersection of canaliculi with the sectioning plane. Canaliculi appear as slender linear features in the transverse plane or as spots and linear segments in the sections parallel to the vessel canals. The orientation of the canaliculi is preponderantly perpendicular on the Haversian canals. The cylindrical osteons and the older interstitial tissue can be discriminated due to the variations in mineral density. The radial distribution of the ellipsoidal osteocyte lacunae can be observed around the Haversian canals. By using a non-linear line-enhancement method described in [Pacureanu *et al.* (2013)], it was possible to obtain 3D displays of the lacuno-canalicular network. The principle of this filtering is based on Hessian-based 3D line enhancement combined with bilateral filtering, which uses the grey level information from the original image. The kernel of the filter not fixed, changing its size with the response of the local 3D line filter function. This filter allows to smooth the background, without affecting the sharpness of the canaliculi and the lacunae.

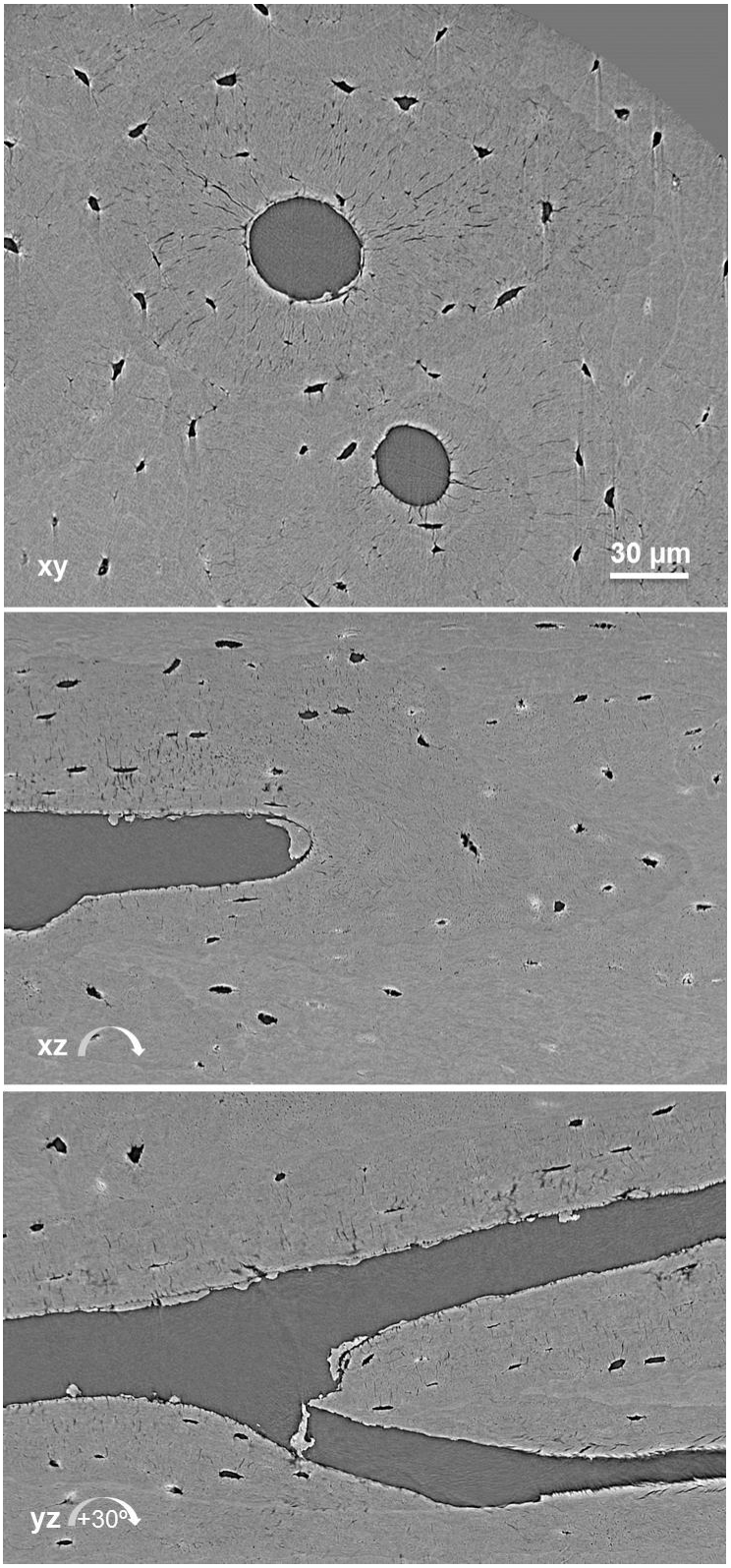

Figure 5.9: Orthogonal slices in a reconstructed sub-volume showing two adjacent osteons and the distribution of lacunae and canaliculi within the osteons and the surrounding older tissue

Figure 5.10 shows 3D lateral and top renderings of the LCN in an osteon, [Pacureanu *et al.* (2012)]. The shape, orientation and distribution of the osteocyte lacunae around the blood vessels Haversian canals can be observed with the canalicular network interconnecting the osteocyte lacunae. Detailed rendering of osteocytes and their canaliculi requires accurate methods to segment canaliculi, which is challenging because of their small size in the image (around 1~2 voxels), noise and artifacts. Among various approaches, a promising one is based on geodesic voting, that will be further described in chapter 8. The 3D rendering demonstrates the high complexity of this cellular structure.

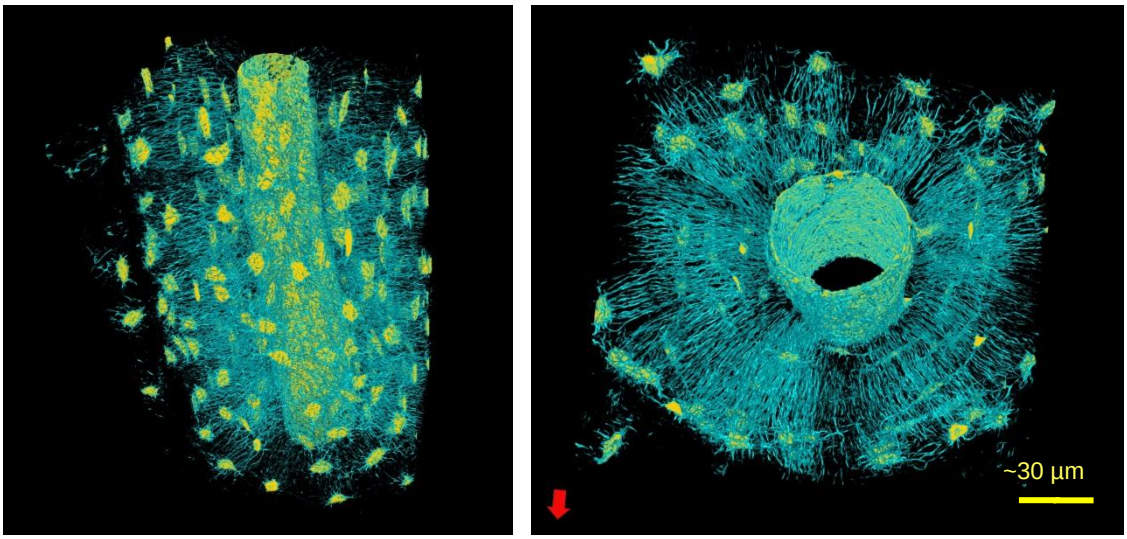

(a) (b)

Figure 5.10 Imaging the LCN by parallel beam SR CT (ESRF, ID19) at 300 nm voxel size: (a): 3D display of osteocytes and their canaliculi around an Haversian canal. (b): top view of (a)

5.5.2 Magnified SR phase CT at the nanometer scale (50 nm voxel size)

During my PhD, I also had the opportunity to perform the experiments on the SR nano-CT. Three tibial bone specimens, imaged with good quality at 300 nm at ID19, were selected to be scanned at ultra-high resolution. These samples measuring 0.4×0.4×5 mm^3 were extracted from the mid-diaphysis of human tibial bones, and were imaged at the nano-imaging station ID22NI of the ESRF. The experimental setup was described in section 5.3.2. Projection images were taken at four sample-source distances (d_1 = {32.6, 33.6, 37.6, 47.6} mm) while keeping the detector position fixed at $d_1 + d_2 = 525$ mm. This geometry results in a final pixel size of 50 nm and a field of view of 100^3 μm^3. For tomography, images were recorded at 2999 angular positions of the sample around a vertical rotation axis over a total angle of 360°. The total acquisition time for one sample, scanned at four distances, was about 2 hours.

In the reconstructed volumes, several structural details can be seen and quantified directly. Osteocyte lacunae and canaliculi are resolved in exceptional detail (Figure 5.11 (a-d)). Shape, volume, surface area and connectivity can clearly be seen Figure 5.11 (c). The cement lines can be seen as brighter sheets in the volumes, Figure 5.11 (d). Since contrast is approximately linear in mass density, this shows that the cement lines have a higher degree of mineralization than the surrounding matrix. In a homogenous tissue region (Figure 5.11 (c)), lacunae are of

approximately similar sizes and are well connected by canaliculi. In tissue region close to the cement line (Figure 5.11 (d)), however, lacunae are of varying sizes. In addition, the connectivity between the lacunae via canaliculi is very low.

The relationship between osteocyte lacunae and the cement line can also be studied. In the imaged volume, Figure 5.11 (d), no canaliculi cross the cement line, but some terminate there, indicating that there is no interconnection between osteonal and interstitial tissue. Figure 5.12 (a) represents a detailed view of a lacuna and its dendritic canaliculi. Further, detail in the bone matrix can for the first time be studied directly in 3D. In particular, these images permit to display collagen orientation in 3D (Figure 5.12 (b)). The collagen seems to be organized in a plywood-like structure. We achieved, to our knowledge, the first non-destructive truly 3D images of bone at the ultrastructural level [Langer *et al.* (2012)].

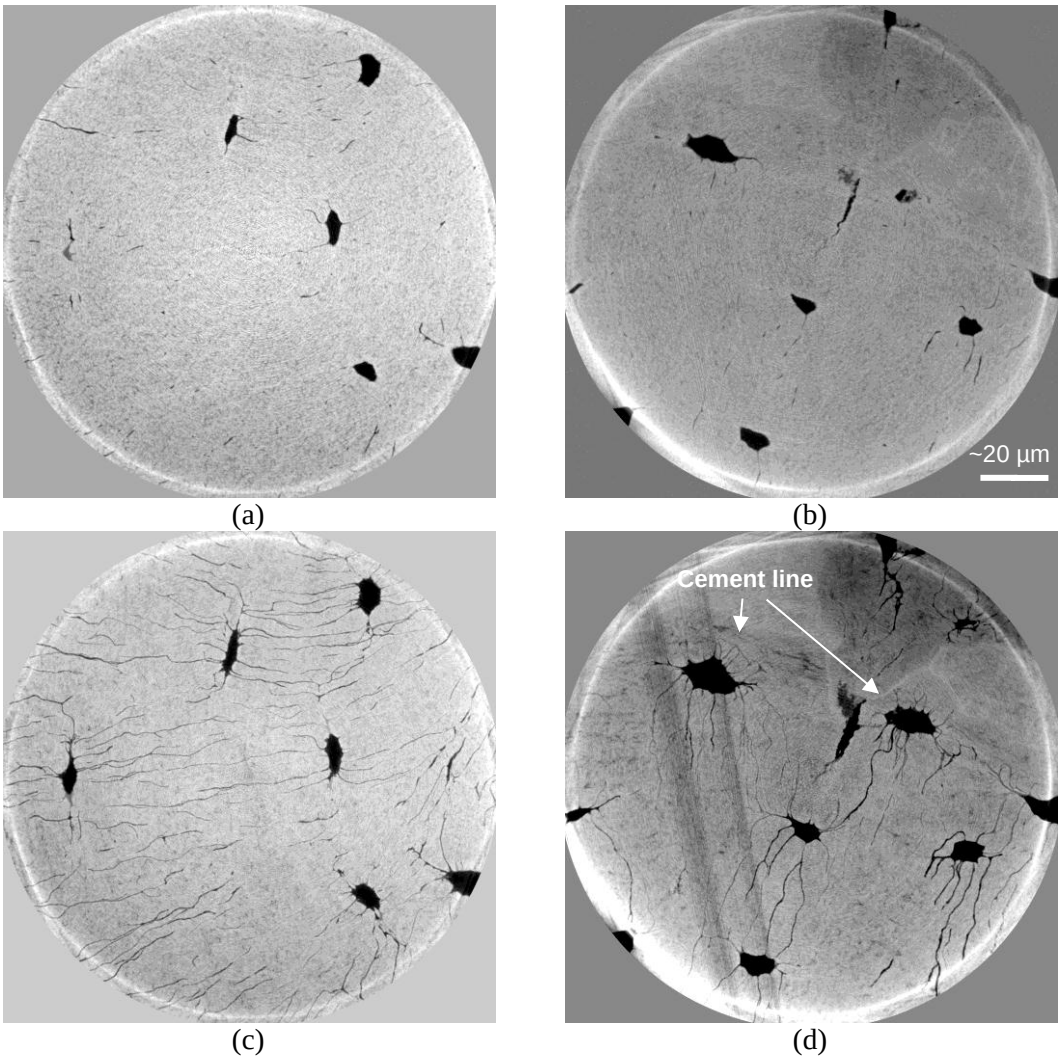

Figure 5.11 Imaging the LCN of human tibial specimens by divergent beam phase SR CT (ESRF, ID22) at 50 nm voxel size: (a) and (b): a slice of reconstructed volume; (c) and (d): minimum intensity projection view of 100 consecutive slices of (a) and (b)

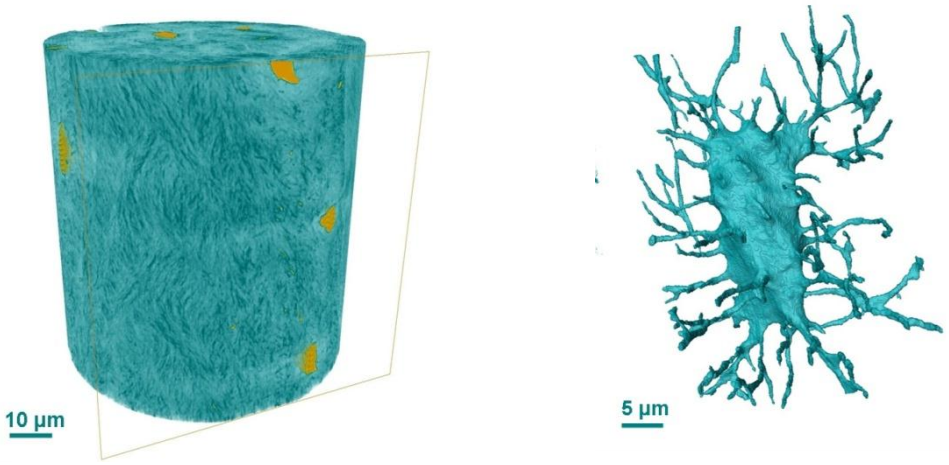

(a) (b)

Figure 5.12 (a) 3D rendering of the reconstructed volume at 60 nm voxel size (bone tissue is in blue, osteocyte lacunae in yellow): Note the oriented texture supposed to reflect that of the collagen fibers. (b): zoom on an isolated lacuna and its canaliculi. Image are original from: [Langer *et al.* (2012)]

5.6 Conclusion

The recent developments in micro/nano-CT allow using the technique as a novel 3D imaging tool at the cellular scale. With spatial resolution up to a few hundreds of nanometers, the feasibility of observing the morphology of osteocyte lacunae and micro-cracks has recently been proven by using either commercial nano-CT or SR micro-CT. The major improvement over conventional techniques is to allow a real three-dimensional quantification of these structures. It results that the measurements of morphometric parameters such as density, areas, and lengths will be more accurate. In addition, micro/nano-CT provides the analysis on larger bone volumes than other regular techniques, thus providing statistically more representative parameters.

The use of synchrotron sources enables to push these developments towards the nanoscale with a good densitometric resolution. This has permitted to display the complex LCN at two scales, allowing either a global appreciation of the network within one or several osteons, or a detailed analysis around a few lacunae. To our knowledge, at the present time, these achievements are only possible with synchrotron techniques. They open new opportunities for studying the 3D spatial distribution of bone cells, their connectivity, and the surrounding micro-cracks.

There are also some limitations to synchrotron micro/nano CT techniques. First, as other X-ray techniques, it does not allow the observation of living cells but only that of the porosity embedding the cells. So the number of osteocyte lacunae can overestimate the number of living osteocytes. However, many studies suggest that the analysis of osteocyte lacunae is a good surrogate to the analysis of osteocytes themselves provided that the percentage of empty lacunae remains approximately constant. Second, the access to synchrotron sources remain limited at a few facilities in the world.

While most of the time, the analysis of these images has remained qualitative, it is important to develop dedicated methods to extract quantitative information from these images. Due to the novelty of such images, there are still few works presenting such methods. This will be the goal of the remaining of this work. Although image segmentation is a crucial step, the primary interest of our work was to define and propose three-dimensional parameters to characterize the structures of interest, i.e the osteocytes and their canaliculi. Reminding that there are more than 20,000 osteocytes per mm^3 and more than 1 million canaliculi per mm^3, this requires efficient methods in terms of computation. In addition each data set represents 32 GB of images which requires sufficient means in terms of computing power to process the data.

Chapter 6

Development of a 3D quantification method of Lacunae from Synchrotron CT images at micrometer scale

Contents

6.1 Introduction 68
6.2 Material and methods 70
6.2.1 Sample Description 70
6.2.2 Synchrotron radiation microtomography (SR-μCT) 70
6.2.3 Image Processing 71
6.2.4 Segmentation of osteocyte lacunae 71
6.2.5 Labeling, number of lacunae (N.Lc) 72
6.2.6 Calculation of 3D individual osteocyte lacunae descriptors 72
6.2.6.1 Volume of lacuna (Lc.V) 72
6.2.6.2 Distance distribution of lacunae, $Lc.Dist_{50}$ $Lc.Dist_{95}$ 72
6.2.6.3 Moment based descriptors, length (Lc.L1), width (Lc.L2), depth (Lc.L3), and anisotropy 73
6.2.6.4 Intrinsic volumes based descriptors: surface area (Lc.S), Euler number (Lc.χ), structure model index (Lc.SMI) 73
6.2.7 Calculation of tissue indices 74
6.2.8 Artifacts elimination 75
6.2.9 Local analysis 76
6.2.9.1 Qualitative analysis 76
6.2.9.2 Quantitative analysis 76
6.2.10 Statistics analysis 77
6.3 Results 77
6.3.1 Evaluation of the segmentation method 77
6.3.2 Histomorphometry parameters of the bone tissue 79
6.3.3 3D shape descriptors of osteocyte lacunae 80
6.3.4 Osteocyte lacunar density distribution 84
6.3.5 Correlations between bone porosity and osteocyte lacunae features 86
6.4 Discussion 88

Abstract

Osteocytes, the most numerous bone cells, are thought to be actively involved in the bone modeling and remodeling processes. The morphology of osteocyte is hypothesized to adapt according to the physiological mechanical loading. Three-dimensional micro-CT has recently been used to study osteocyte lacunae. In this work, we proposed a computationally efficient and validated automated image analysis method to quantify the 3D shape descriptors of osteocyte lacunae and their distribution in human femurs. Thirteen samples were imaged using Synchrotron Radiation (SR) micro-CT at ID19 of the ESRF with 1.4 µm isotropic voxel resolution. With a field of view of about 2.9×2.9×1.4 mm^3, the 3D images include several tens of thousands of osteocyte lacunae. We designed an automated quantification method to segment and extract 3D cell descriptors from osteocyte lacunae. An image moment-based approach was used to calculate the volume, length, width, height and anisotropy of each osteocyte lacuna. We employed a fast algorithm to further efficiently calculate the surface area, the Euler number and the structure model index (SMI) of each lacuna. We also introduced the 3D lacunar density map to directly visualize the lacunar density variation over a large field of view. We reported the lacunar morphometric properties and distributions as well as cortical bone histomorphometric indices on the 13 bone samples.

The mean volume and surface were found to be 409.5±149.7 μm^3 and 336.2±94.5 μm^2. The average dimensions were of 18.9±4.9 µm in length, 9.2±2.1 µm in width and 4.8±1.1 µm in depth. We found lacunar number density and six osteocyte lacunar descriptors, three axis lengths, two anisotropy ratios and SMI, that are significantly correlated to bone porosity at a same local region.

The proposed method allowed an automatic and efficient direct 3D analysis of a large population of bone cells and is expected to provide reliable biological information for better understanding the bone quality and diseases at cellular level.

Keywords— *osteocyte lacunae, synchrotron radiation micro-CT, 3D image analysis, lacunar descriptors, cortical bone*

6.1 Introduction

Intensive studies have been carried out over the last decades to explain the bone fragility in diseases such as osteoporosis. Bone mass measurement has proved to be a valuable parameter in the evaluation of bone fragility. However, bone mass could explain only a fraction of change in bone strength among individuals [Ciarelli *et al.* (1991)]. Other factors known as bone quality factors are believed to have an impact on bone mechanical properties [Seeman *et al.* (2006)]. They include both bone microstructure and the material properties of bone tissue at different scales.

At the cellular scale, the osteocyte system is raising increasing interest since it is hypothesized to have an important role in bone adaptation to stresses [Bonucci (2009); Bonewald (2011)]. The osteocytes, which represent about 90% of the bone cells are the mechanosensory cells that translate mechanical stimuli into electrical or biochemical signals and orchestrate the osteoclasts and the osteoblasts to perform bone resorption and formation [Burger *et al.* (1999); Bonewald (2006); Bonewald *et al.* (2008)]. The osteocytes also regulate bone metabolism, for example bone phosphate metabolism [Westbroek *et al.* (2002)], and were recently shown to remodel their pericanalicular matrix [Qing *et al.* (2012)]. However, the exact mechanisms involved in the osteocyte activity are not precisely elucidated and remain controversial.

Osteocytes have been less studied than osteoblasts and osteoclasts, partly because of their anatomical location [Bonucci (2009)]. While osteoblasts and osteoclasts are performing their duties on the surface of bone, the osteocytes are deeply embedded in the bone matrix. The latter are encysted in cavities called lacunae, and they connect to each other and to bone cells at surface through slender dendritic processes located in tunnels called canaliculi. The geometry of the lacuno-canalicular network (LCN) is believed to affect the magnitude of bone fluid shear stress loaded on the osteocyte [Bacabac *et al.* (2008)] [Mullins *et al.* (2007)] [Currey (2003b)], which in turn affects the process of mechanosensation and mechanotransduction [Burger *et al.* (1999)]. We believe that a better investigation on the morphology of LCN will lead to a better understanding of bone tissue regulation and bone mechanical properties at the cell level.

Direct observation of osteocytes is difficult and there are relatively few quantitative data on their morphology [Schneider *et al.* (2010)]. In the past, osteocytes were mainly examined using microscopic modalities such as light microscopy [Hirose *et al.* (2007)], confocal microscopy [Sugawara *et al.* (2005); van Hove *et al.* (2009a)], scanning electron microscopy (SEM) [Boyde *et al.* (1996); Okada *et al.* (2002)] and transmission electron microscopy (TEM) [LD You *et al.* (2004); Rubin *et al.* (2004)]. These techniques provide only 2D observations or are limited to at most several hundreds of micrometers in depth. To overcome this limitation, several 3D imaging techniques have recently been proposed. Novel 3D imaging techniques, such as focused ion beam/scanning electron microscopy (FIB/SEM) [Schneider *et al.* (2011)] and ptychography [Dierolf *et al.* (2010)] look promising for very high resolution imaging of the LCN, but remain limited to the analysis of one or a few osteocyte lacunae. Recently, the feasibility of commercialized nano-CT was also demonstrated to visualize the 3D morphology of osteocyte lacunae [Vatsa *et al.* (2008); van

Hove *et al.* (2009)]. Coupling micro-CT to synchrotron sources (SR) permits the use of parallel monochromatic high flux X-ray beams. Thus, SR micro-CT possesses several advantages over conventional desktop micro-CT in terms of signal to noise ratio, spatial and density resolution [Salomé *et al.* (1999)]. Moreover, due to the high brilliance source, the acquisition time is considerably reduced. Early 3D observations of osteocyte lacunae in trabecular bone were reported with SR micro-CT at a spatial resolution around the micrometer [Peyrin *et al.* (1998); Hengsberger *et al.* (2003); Schneider *et al.* (2010)]. More recently, quantitative properties of osteocyte lacunae in the midshaft of human femoral cortical bone were measured from SR micro-CT images [Hannah *et al.* (2010); Carter *et al.* (2012)].

Quantitative morphometric data on osteocytes or osteocyte lacunae were mostly obtained from 2D images, most of the time by manual measurements. Osteocyte lacunae are typically described as flattened ellipsoids [Marotti (1979)] with a size of a few micrometers. They were reported to have a long and a short axis respectively about 20 and 9 micrometers from 2D microscopic images [Mullender *et al.* (1996)]. However, when observed from 2D sections, there may be incertitude in their actual 3D dimensions due to the slicing direction. Although geometric models for the osteocytes have been established to extrapolate the 2D measurements to 3D quantitative values [Mullender *et al.* (1996); Skedros *et al.* (2005); Beno *et al.* (2006)], this method can lead to unpredictable errors if these ideal model assumptions are not verified. Since some results could turn out to be contradictory [McCreadie *et al.* (2004)], direct 3D measurements are required to get unbiased results.

Such 3D morphometric data on osteocyte lacunae were first obtained with confocal microscopy. McCreadie [McCreadie *et al.* (2004)] provided a method to evaluate osteocyte lacunae shape and size in 3D among 600 lacunae. However, this imaging modality presents some inherent artifacts impacting quantification. First, the lower spatial resolution in depth may yield inaccuracies. Second, the limited field of view (FOV) in depth also restricts the region of interest. Besides, since the osteocyte lacunae are deeply embedded in the bone matrix, some osteocyte lacunae may be lost during the staining process, thus yielding an underestimation of lacunae density. Micro and nano-CT imaging overcome these drawbacks and provide 3D images with isotropic voxels without requiring staining. Van Hove [van Hove *et al.* (2009)] and Vatsa [Vatsa *et al.* (2008)] measured lacuna volume, surface area, degree of anisotropy from the SkyScan nano-CT device. Recently, Hannah [Hannah *et al.* (2010)] reported morphometric parameters, such as volume, long axis length and orientation angle, and mean nearest neighbor distance in 11 non-branched osteons from SR micro-CT images. He observed a bimodal distribution of osteocyte lacunae size in human femoral cortex [Hannah *et al.* (2010)]. Carter [Carter *et al.* (2012)] reported volume, orientation, equancy, elongation, and flatness of osteocyte lacunae at different locations in one healthy male femur. He reported that lacunae were more flattened in the anterior and posterior regions than in the medial and lateral regions. Nevertheless, in the previous works, there has not been a lot of focus on the method to extract lacunae descriptors, neither in its description nor on its validation, and the numbers of samples and subjects analyzed so far, were quite limited.

The aim of this work is to describe a clear and reproducible methodology to quantify large population of osteocyte lacunae and report new data on human cortical bone samples to

improve our knowledge about the 3D properties of osteocyte lacuna in human bone. Our approach was (1) to use SR micro-CT at 1.4 µm, a good candidate for imaging such a network since it provides images with isotropic voxel size over large FOV ($2.9\times2.9\times1.4$ mm^3) allowing to enclose between 10^5 and 10^6 cells [Carter *et al.* (2012)], (2) to develop a fast and efficient image analysis method for the automatic quantification of the 3D cell morphometry, (3) to extract reliable statistical morphological descriptors from 13 samples in human midshaft cortical bone and look for correlations between those descriptors and bone porosity.

6.2 Material and methods

6.2.1 Sample Description

Thirteen human cortical bone specimens were prepared from the femoral mid-diaphysis of two female donors (seven specimens from donor A with death age of 78 years and six specimens from donor B with death age of 80 years). Ethical approval for the collection of samples was granted by the Human Ethics Committee of the Centre du don des Corps at the University Paris Descartes (Paris, France). Informed written consent was signed by the donors or their legal guardians to provide the tissue for investigation in accordance with legal clauses stated in the French Code of Public Health. The specimens were wet machined (Isomet 4000, Buehler GmbH, Düsseldorf, Germany) as rectangular parallelepipeds ($50\times4\times2$ mm^3), defatted [Granke *et al.* (2011)] and stored at -20°C until experiments.

6.2.2 Synchrotron radiation microtomography (SR-µCT)

SR micro-CT was performed on beamline ID19 at the ESRF (European Synchrotron Radiation Facility, Grenoble, France). For each sample, 3000 projection images were recorded over a total angle of 360° at a fixed energy of 25keV. A 3D image volume with an isotropic spatial resolution of 1.4µm was reconstructed by a filtered back-projection algorithm. To decrease the computational burden and to avoid geometrical distortion at the periphery of the image, a volume of interest (VOI) was selected with size of 1000×1000×251 voxels, which corresponds to a physical size of 1.4mm×1.4mm×0.35mm (see Figure 6.1(a)). Figure 6.1(b) illustrates a reconstructed slice from the VOI, the light gray part of the images corresponds to mineralized cortical bone. The large black pores are cross sections of Haversian canals and Volkmann's canals. Figure 6.1(c) shows a zoom around on an osteon, where the small black cavities scattered around the Haversian canal on the gray background are osteocyte lacunae.

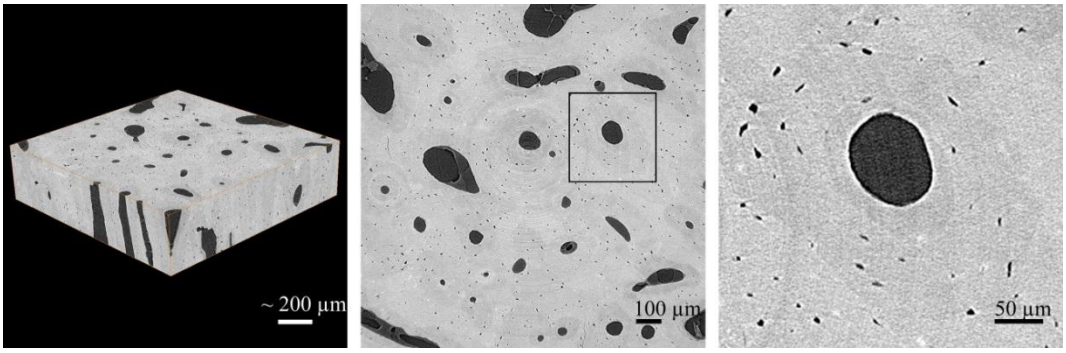

(a) (b) (c)

Figure 6.1 (a) A 3D rendering of the reconstructed image (1000×1000×251 pixels). (b) A slice of reconstructed image from SR-CT with voxel resolution of 1.4µm (image size: 1000×1000 pixels). (c) zoom around an Haversian canal.

6.2.3 Image Processing

The method was developed to extract parameters at two levels, the cell level and the tissue level. At the cell level, we calculated the three-dimensional descriptors on individual cells: length (*Lc.L1*), width (*Lc.L2*), depth (*Lc.L3*), anisotropy, surface area (*Lc.S*), Euler number (*Lc.χ*), structure model index (*Lc.SMI*). At the tissue level, we quantified the following parameters: bone volume fraction (*BV/TV*), canal volume fraction (H*Ca.V/TV*), and the number and volume of osteocyte lacunae (*N.Lc* and *Lc.TV*) and its 3D density. Furthermore, properties characterizing the distance of the mineralized matrix to canals and lacunae were computed. To obtain these parameters, the following steps were performed:

6.2.4 Segmentation of osteocyte lacunae

First, by using a Gaussian low pass filter and a simple thresholding, it was straightforward to acquire a mask volume including the bone cortex and excluding the canals, Figure 6.2(a). This mask volume was further used to calculate the bone volume (*BV*). Then, to segment the osteocyte lacunae within the region of the mask volume, a hysteresis thresholding with two thresholds was employed [Canny (1986)]. The first lower threshold was used to select the voxels belonging to osteocyte lacunae with a high confidence. Then a second higher threshold was used to refine the segmentation by selecting the voxels with higher intensity values but only if they were connected to the previously detected voxels. After rescaling the reconstructed images between 0 and 255, the segmentation of lacunae was achieved by setting the two hysteresis thresholds respectively to 40 and 70. As a result, a binary volume of osteocyte lacunae was acquired Figure 6.2(b).

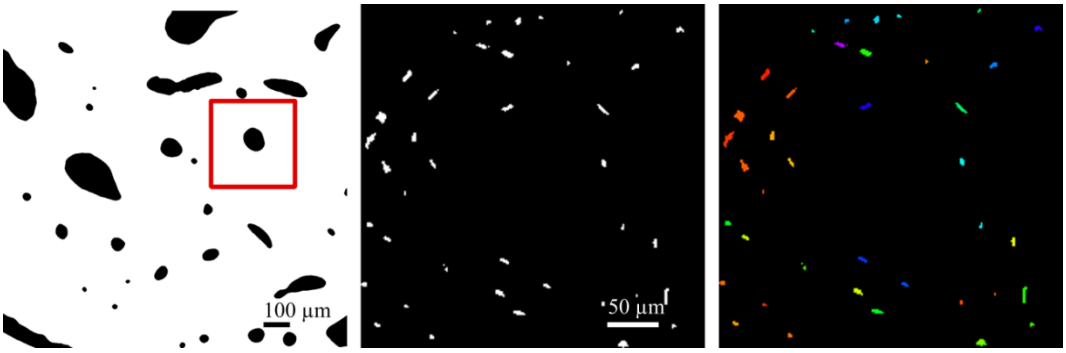

(a) (b) (c)

Figure 6.2 (a) A slice of bone matrix mask. (b) Binary segmented osteocyte lacunae around an osteon (c) Labeled osteocyte lacunae around an osteon.

6.2.5 Labeling, number of lacunae (N.Lc)

To quantify each individual cell, a connected component process was first performed to assign a label to each of them. Considering the large dimensions of the 3D images to be processed, an efficient labeling method was chosen. Hoshen and Kopelmanm proposed a fast labeling algorithm for 2D images requiring scanning the image only twice [Hoshen *et al.* (1976)]. We extended and implemented this algorithm for labeling 3D images. In this work, the labeling was performed with a connectivity of 26 (meaning that each voxel was connected to its 26 3D neighbors). Figure 6.2(c) illustrates some labeled osteocyte lacunae around an osteon. After labeling, all lacunae connected to the image borders were deliberately erased from the labeled volume to avoid the biased results that could be related to truncated lacunae. The total number of labels corresponds to the number of lacunae and is denoted *N.Lc*.

6.2.6 Calculation of 3D individual osteocyte lacunae descriptors

At the cell level, a number of descriptors were calculated for each labeled lacuna. Let $L(\bar{u})$ be the labeled image where $\bar{u} = (\mathrm{x}, \mathrm{y}, \mathrm{z})$ are the spatial coordinates belonging to a finite domain of $\mathbb{N}^3$. An osteocyte lacuna X_n is defined as the set of voxels labeled with n:

$$X_n = \{\bar{u} = (\mathrm{x}, \mathrm{y}, \mathrm{z}) \in \mathrm{I} \,/ L(\bar{u}) = n\} \qquad (6.1)$$

6.2.6.1 Volume of lacuna (Lc.V)

The volume of lacuna X_n is denoted $Lc.V(X_n)$ and can be simply obtained by counting the number of voxels labeled as n.

6.2.6.2 Distance distribution of lacunae, Lc.Dist$_{50}$ Lc.Dist$_{95}$

The distance transform, also known distance map, labels each pixel of the image with the distance to the nearest object. Numbers of the algorithms have been developed to calculate the Euclidean distance [Rosenfeld *et al.* (1966); Paglieroni (1992); Saito *et al.* (1994); Maurer, C.R. *et al.* (2003)]. Recently, the distribution of the distance map of the lacunae was used to explore their spatial arrangement [Kerschnitzki *et al.* (2013)]. It depicts what is the distance of

the bone matrix from the nearest osteocyte lacuna, denoted as *Lc.Dist*. First, we calculated the distance map of binary lacunae image, giving at each bone voxel its shortest distance to the surface of the nearest osteocyte lacuna. Second, the normalized cumulative histogram of the distance map is calculated. Finally, the values corresponding to 50% and 95% of the distribution, denoted as $Lc.Dist_{50}$ *and* $Lc.Dist_{95}$, are determined. The two calculated parameters show that 50% and 95% of the bone matrix are located within a distance of $Lc.Dist_{50}$ *and* $Lc.Dist_{95}$ from the nearest lacunae.

6.2.6.3 Moment based descriptors, length (Lc.L1), width (Lc.L2), depth (Lc.L3), and anisotropy

Since the shape of osteocyte lacunae is generally assumed to be ellipsoidal, second order moments can efficiently be used to find the main orientations and the lengths of the main axes of the best fitting ellipsoid. First, we defined the second-order central moments μ_{pqr} of X_n, with $p+q+r=2$ for $(p,q,r) \in [0,2]$ given by:

$$\mu_{pqr} = \sum_{(x,y,z)\in X_n} (x-\bar{x}_n)^p \cdot (y-\bar{y}_n)^q \cdot (z-\bar{z}_n)^r \tag{6.2}$$

where the $(\bar{x}_n, \bar{y}_n, \bar{z}_n)$ is the center of mass of X_n.

The second order moment matrix can be expressed as :

$$M(X_n) = \begin{pmatrix} \mu_{200} & \mu_{110} & \mu_{101} \\ \mu_{110} & \mu_{020} & \mu_{011} \\ \mu_{101} & \mu_{011} & \mu_{002} \end{pmatrix} \tag{6.3}$$

Let $\lambda_1 \geq \lambda_2 \geq \lambda_3$ be the eigenvalues of $M(X_n)$. It can be shown that the half axes of the best fitting ellipsoid are:

$$a_k = \sqrt{5\lambda_k / Lc.V(X_n)}, \qquad k = 1,2,3 \tag{6.4}$$

The sizes of the osteocyte lacunae sorted in descending order, that will be referred as length, width, and depth, can thus be given by :

$$Lc.L_1(X_n) = 2a_1, \qquad Lc.L_2(X_n) = 2a_2, \qquad Lc.L_3(X_n) = 2a_3 \tag{6.5}$$

The ratio between the volume of the actual osteocyte lacunae and the fitting ellipsoid is given by:

$$\tau = 3Lc.V(X_n)^{5/2} / 20\pi\sqrt{5\lambda_1\lambda_2\lambda_3} \tag{6.6}$$

The major orientation of the lacuna is given by that of the eigenvector associated to λ_1. The anisotropy of the lacunae can also be quantified by the ratios of axis lengths $Lc.L_1/Lc.L_2$ and $Lc.L_1/Lc.L_3$.

6.2.6.4 Intrinsic volume based descriptors: surface area (Lc.S), Euler number (Lc.χ), structure model index (Lc.SMI)

To further quantify each object X_n we propose to use the intrinsic volumes. The intrinsic volumes are invariant geometric functions serving as a basis of object features. In 3D, there are four intrinsic volumes $V_j(X_n)$, $j \in [0,3]$, respectively representing the Euler number, integral of mean curvature, surface area and volume of the object. To compute these characteristics efficiently, we use a discretization formula derived by Ohser [Ohser *et al.* (2009a)]. The principle is to exploit a Crofton formula which reduces the computation of the

intrinsic volumes of a compact and polyconvex set X_n to Euler numbers χ in lower dimensional intersections:

$$\frac{1}{2}V_{3-k}(X_n) = \int_{\mathcal{L}^k} \int_{\perp_L} \chi\big(X_n \cap (\mathrm{L} + \mathrm{y})\big) V_{\perp_L}(dy)\, \mu(dL), k = 1,2 \qquad (6.7)$$

where $\mathcal{L}^k$ is the set of all k-dimensinal linear subspaces of $\mathbb{R}^3$; ${}^{\perp}L$ is the orthogonal complement of $L \in \mathcal{L}^k$; $V_{\perp_L}$ is the $3-k$ dimensional Lebesgue measure on ${}^{\perp}L$, and μ denote the rotation invariant measure on $\mathcal{L}^k$ with $\mu(\mathcal{L}^k)=1$. By discretizing this formula in the case of a cubic lattice of spacing Δ, the approximation $\hat{V}_{3-k}$ of V_{3-k} can be expressed as:

$$\hat{V}_{3-k}(X_n) = 2\Delta^{3-k} \sum_{\ell=0}^{\nu} v_\ell^{(k)} h_\ell(X_n) \qquad (6.8)$$

where ℓ is an index spanning local configurations of voxels, $h_\ell(X_n)$ is the number of configuration ℓ in the set X_n and $v_l^{(k)}$ is the weight coefficient of the local configuration. The surface area $Lc.S(X_n)$, the integral of the mean curvature $Lc.M(X_n)$, and the Euler number $Lc.\chi(X_n)$ of the lacuna X_n can be estimated as:

$$\begin{aligned} Lc.S(L_n) &= 2\hat{V}_2(L_n) = 4\Delta^2 v_\ell^{(1)} h \\ Lc.M(L_n) &= \pi\hat{V}_1(L_n) = 2\pi\Delta v_\ell^{(2)} h \\ Lc.\chi(L_n) &= \hat{V}_0(L_n) \end{aligned} \qquad (6.9)$$

The surface area weight $4v_\ell^{(1)}$, integral of the mean curvature weight $2\pi v_\ell^{(2)}$, and the weights $v_\ell^{(3)}$ for the Euler number for each configuration are given in [Ohser *et al.* (2009b)].

In addition, we also calculated the structure model index of each lacuna ($Lc.SMI(L_n)$) from the intrinsic volumes [Ohser *et al.* (2009a)], expressed as:

$$Lc.SMI(L_n) = 12 Lc.V(L_n) Lc.M(L_n) / Lc.S(L_n)^2 \qquad (6.10)$$

It characterizes the lacunar shape with values of 0, for a pure plate, 3 for a rod and 4 for a sphere[Hildebrand *et al.* (1997)].

Due to the symmetry of the 3D cubic lattice, only $\nu = 22$ congruence classes of configurations can be considered. This method allows a fast calculation of the different characteristics by computing only once the number of configurations $h_\ell(X_n)$. The latter can be efficiently calculated as the histogram of the convolution of the binary image with a suitably chosen 2×2×2 mask [Ohser *et al.* (2000)].

6.2.7 Calculation of tissue indices

At tissue level, bone histomorphometric indices were calculated. The bone volume (*BV*) was evaluated from the 3D mask image already used in the stage of lacunae segmentation. The tissue volume (*TV*) was obtained by taking the convex hull algorithm of the mask volume. The Haversian and Volkmann canals volume (H*Ca.V*) was evaluated as TV minus BV. This allows evaluating the bone volume fraction *BV/TV*, the canal volume fraction H*Ca.V/TV* or

bone porosity. The total lacunar volume *Lc.TV* can be obtained either directly from the binary image of lacunae or by summing the individual volume of each lacunae. The lacunae number density, denoted as *N.Lc/BV* and *N.Lc/TV*, and the lacunae volume density, denoted as *Lc.TV/BV* and *Lc.TV/TV* was also calculated.

In addition, we also calculated the distance distribution function of the Haversian canal. It depicts the average distance of the bone matrix from the nearest Haversian canal. First, we calculated the distance map of the binary Haversian canal image, giving at each bone voxel its shortest distance to the surface of the nearest Haversian canal. Second, the normalized cumulative histogram of the distance map is calculated. Finally, the values corresponding to 50% and 95% of the distribution, denoted as $HCa.Dist_{50}$ and $HCa.Dist_{95}$, are determined. The two calculated parameters represent that 50% and 95% of bone matrix are located within a distance of $HCa.Dist_{50}$ and $HCa.Dist_{95}$ from the nearest Haversian canal.

6.2.8 Artifact elimination

The hysteresis thresholding provided a binary image but, as in every automatic segmentation method, there may be artifacts, for instance due to ring artifacts, micro-cracks or noise. These artifactual structures have different shapes than that expected for lacunae. Thus we took advantage of the descriptors calculated on each object to eliminate them. The objects with volume smaller than 82 μm^3 (30 voxels) were removed considered as noise. The objects, which volumes were within the top 1% of the distribution, were assumed to be artifactual lacunae, such as micro-cracks and canals, and were removed. Besides, the objects with an anisotropy ratio $Lc.L1/Lc.L2$ larger than 5, which often appeared to be ring artifacts, were also eliminated. Furthermore, the 3D Euler number $Lc.\chi$ was exploited to examine the topology of the structure. Finally, the rule applied to filter out artifactual components was the following

$$Lc.V > Lc.V \text{ within the top } 1\% \text{ or } Lc.V < 82\ \mu m^3;\ Lc.L1/Lc.L2 > 5;$$
$$Lc.\chi < 0 \text{ or } Lc.\chi > 2 \tag{6.11}$$

The method was evaluated by comparison to a semi-manual segmentation on a volume of interest made of 200^3 voxels in representative micro-CT image. To this aim, we used a semi-interactive process based on region growing. For each lacuna, we selected interactively a seed close to the center of gravity of the lacuna. Then a region growing starting from this seed was performed using MeVisLab (Version 2.1). The resulting binary image was overlapped with the original image using ImageJ (version 1.45s). A manual refinement was performed on individual lacuna to achieve the ideal segmentation result by a manual modification on the binarized lacuna compared with the same lacuna in original image.

To compare the automatic segmentation with respect to the manually segmented image, we used the Dice coefficient, conventionally used in medical imaging and defined as twice the number of voxels common to both images by the sum of the voxels in each image [Dice (1945)]. The calculation was given by the formula:

$$DICE = 2(R \cap S)/(R \cup S) \tag{6.12}$$

where R, S are set of voxels respectively belong truth volume and segmented volume. An ideal segmentation corresponds to a Dice value of one. Besides, the sensitivity and specificity were calculated as well. The sensitivity gives the fraction of the true positives segmented from the truth volume and the specificity measures the fraction of negatives that are correctly detected. They are defined by the formula:

$$Sensitivity = \mathrm{TP}/(\mathrm{TP} + \mathrm{FN}) \tag{6.13}$$

$$Specificity = TN/(TN + FP) \tag{6.14}$$

where the TP is the true positive, FN is the false negative, FP is the false positive and TN is the true negative. In addition, we also compared the descriptors extracted from the automatic and manually segmented images.

6.2.9 Local analysis

6.2.9.1 Qualitative analysis

In order to study the lacunar density variation with respect to the bone porosity, we introduced a 3D lacunar density map. First, we calculated a local lacunar density *N.Lc(r)/BV(r)* at the gravity center of each lacuna. This parameter was calculated in a local region which was defined by a bounding box with length of 2*r*+1 voxels. The number of lacunae *N.Lc(r)* and the bone volume *BV(r)* were calculated within the local region. After that, each lacuna was labeled with the value of the local density. The 3D local lacunar density map gives a 3D image, the intensity of which represented the local lacunar density. It was used to visually identify the local regions with high or low lacunar density.

This analysis was performed on two of the thirteen samples. Since the density analysis is not sensitive to the shape of lacunae, a larger VOI (1000×1500×261 voxels) was cropped from the reconstructed 3D image. Minimum intensity projections of these two samples are shown in Figure 6.6(a) and (b). It can be clearly seen that in one sample there are large variations of bone porosity, while the second one is quite homogenous. To calculate the 3D lacunar density map, we used a region of 22.28×10^{-3} mm^3 (r=140 µm) around each lacunar gravity center, which is appropriate to reflect the density variation across the whole region of interest.

6.2.9.2 Quantitative analysis

To quantitatively evaluate the relationships between local bone porosity and lacunar density and descriptors, the sample, containing variations of local bone porosity, was divided into seven sub-volumes with size of 300×1500×261 voxels. Each of them owns different bone volume fraction (*BV/TV*) ranging from 67% to 97% (Figure 6.7). The lacunae were segmented, and the artifacts were eliminated according to Equation 7. Besides bone volume fraction (*BV/TV*), lacunar density (*N.Lc/BV*), axes length (*Lc.L1, Lc.L2, Lc.L3*), anisotropy (*Lc.L1/Lc.L2, Lc.L1/Lc.L3*), structural model index (*Lc.SMI*), volume (*Lc.V*) and surface (*Lc.S*) of osteocyte lacunae were calculated from each sub-volume.

6.2.10 Statistics analysis

Descriptive statistics were used to describe the features on the quantification result of the thirteen samples. For the local quantitative analysis, we used StatView® 5.0 to perform the linear regression analysis between bone porosity and lacunae descriptors extracted from the seven sub-volumes. F-test was used to check the significance of the overall fit, followed by t-test on the significance of slope and intercept. The significance level was measured using a p-value $p<0.05$.

6.3 Results

6.3.1 Evaluation of the segmentation method

From a visual point of view, the hysteresis method seemed to perform well. However, a more detailed observation revealed the presence of artifacts. Figure 6.3(a) and (d) respectively illustrate a 3D rendering and an overlay of a reconstructed slice and the result of hysteresis thresholding. Ring artifacts are visible on both displays. Figure 6.3(b) and (e) shows the same images after artifact elimination, showing that the ring artifacts have successfully been eliminated. Figure 6.3(c) and (f) present the semi-manually segmented images, which look close to the final segmentation result.

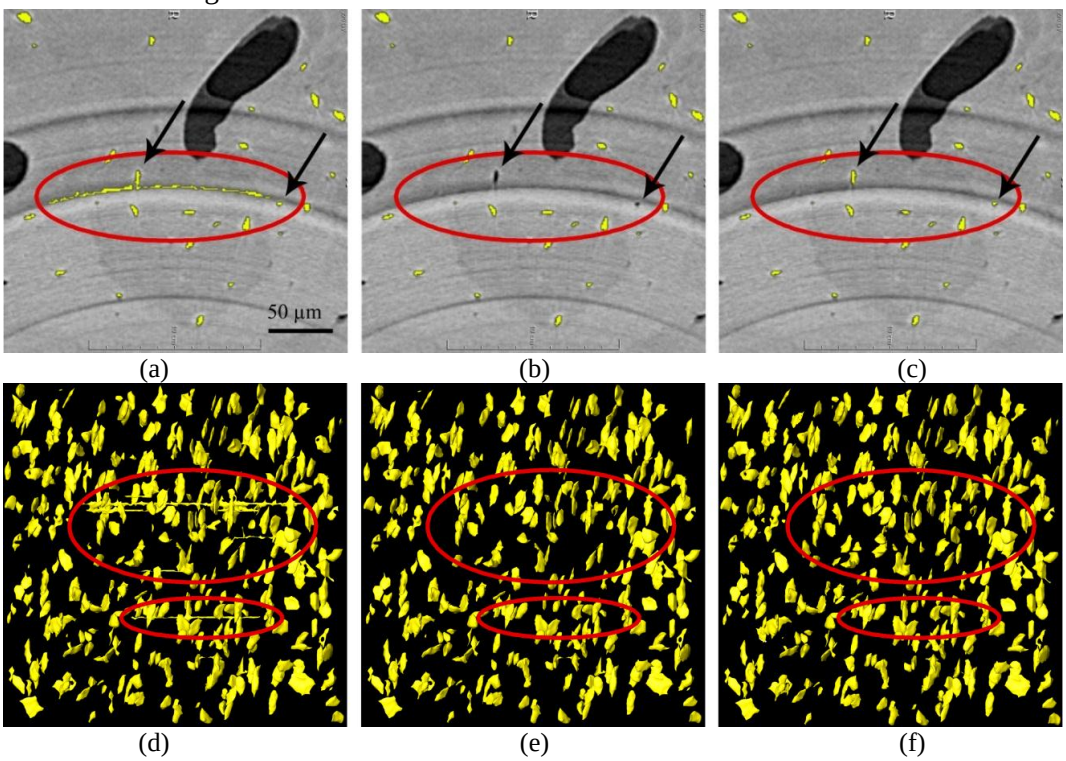

Figure 6.3 Comparison of before and after artifact elimination with the reference image. (a) Before artifact elimination (b) After artifact elimination (c) Reference image. (d)-(e) the corresponding results of (a)-(c) in 3D.

The quantitative evaluation of the method is reported in Table 6.1. The Dice coefficient reflected a satisfactory segmentation compared with the reference image. The ratios of the main descriptors were above 98%, which indicate highly reliable statistical results. There were about 8% of cells missing after segmentation. This was mainly due to the loss of the cells which were connected to the artifacts.

Table 6.1 Segmentation validation

Descriptor	Segmentation	Reference Image	Ratio	DICE	Sensitivity	Specificity
N.Lc	328	357	91.9%	94.57%	92.10%	99.98%
Lc.V(μm^3)	357.36	350.66	98.1%			
Lc.S(μm^2)	314.66	308.16	97.9%			
Lc.L1 (μm)	18.46	18.04	97.7%			
Lc.L2 (μm)	9.08	9.02	99.3%			
Lc.L3 (μm)	4.70	4.64	98.7%			
Lc.L1/Lc.L2	2.16	2.12	98.1%			
Lc.L1/Lc.L3	4.17	4.13	98.8%			

N.Lc – number of lacunae
Lc.V – lacuna volume (μm^3)
Lc.S – lacuna surface area (μm^2)
Lc.L1, Lc.L2 and Lc.L3 – length, width and depth of lacuna (μm)
Lc.L1/Lc.L2 and Lc.L1/Lc.L3 – anisotropy of lacuna

Figure 6.4(a) and (b) show a top and a side 3D view of one of the sub-volumes, with the Haversian and Volkmann canals and the segmented lacunae. From Figure 6.4(a), the osteocyte lacunae can be clearly recognized as they were distributed in concentric circles around the Haversian canals. Figure 6.4(c) shows a zoom around one osteon. By using the tensor field visualization rendered by Avizo® (version 6.1), it was possible to visualize the best fitting ellipsoid of each osteocyte lacunae calculated from the second order matrix (Figure 6.4(d)). This display shows that the fitting was in agreement with the original data.

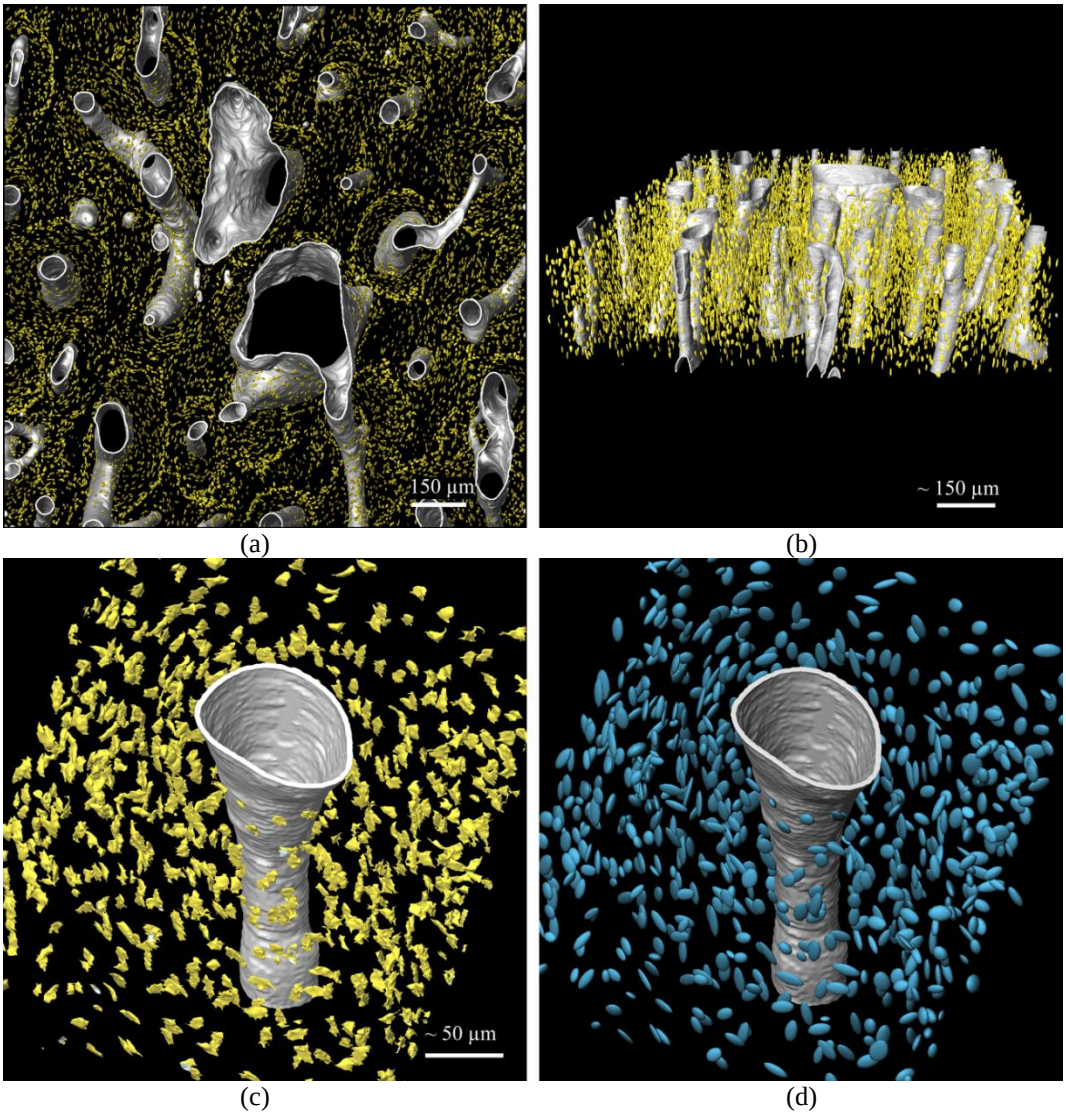

(a) (b)

(c) (d)

Figure 6.4 3D rendering of segmented image (1000×1000×251) (rendered by Avizo v6.1) (a) (b) Top view and side view of the volume. The Harversian canal (white) is surrounded by osteocyte lacunae (yellow) (c) A 3D rendering of an osteon (d) A corresponding 3D rendering of (c) with equivalent ellipsoids of osteocyte lacunae.

6.3.2 Histomorphometry parameters of the bone tissue

Table 6.2 reports the descriptive statistic features of the bone tissue. Of the thirteen samples, the average number of lacunae was 12791, with the total lacunae volume of 0.013 mm^3. The bone volume fraction (*BV/TV*) and canal volume fraction (H*Ca.V/TV*) are of 89.6%±9.3% and 10.4%±9.3%. The average and standard deviation of lacunae number densities were 20573±2850/mm^3 (*N.Lc/BV*) and 18572±3675/mm^3 (*N.Lc/TV*). The lacunae volume densities were 0.84%±0.17% (*Lc.TV/BV*) and 0.76%±0.19% (*Lc.TV/TV*). The 50% and 95% of bone voxels are located within a distance of 64.6±7.9 µm and 134.2±12.5 µm from the nearest Haversian canal.

Table 6.2 Histomorphometry parameters of the bone tissue from 13 specimens

Sample ID	N.Lc	Lc.TV (mm^3)	BV (mm^3)	TV (mm^3)	BV/TV (%)	HCa.V/TV (%)	Lc.TV/BV (%)	Lc.TV/TV (%)	N.Lc/BV (mm^3)	N.Lc/TV (mm^3)	$HCa.Dist_{50}$ (μm)	$HCa.Dist_{95}$ (μm)
A1	12177	0.0054	0.59	0.69	86.4%	13.6%	0.91%	0.79%	20471	17680	58.8	123.2
A2	13673	0.0055	0.65	0.69	94.6%	5.4%	0.85%	0.80%	20981	19852	60.2	120.4
A3	10851	0.0046	0.57	0.69	82.4%	17.6%	0.82%	0.67%	19122	15755	56.0	114.8
A4	12578	0.0046	0.63	0.69	92.1%	7.9%	0.72%	0.67%	19836	18262	61.6	138.6
A5	16808	0.0069	0.62	0.69	89.9%	10.1%	1.11%	1.00%	27155	24404	60.2	128.8
A6	13613	0.0048	0.63	0.69	91.5%	8.5%	0.76%	0.70%	21607	19765	64.4	128.8
A7	16449	0.0083	0.67	0.69	97.8%	2.2%	1.23%	1.20%	24429	23883	79.8	155.4
B1	6499	0.0025	0.43	0.69	62.6%	37.4%	0.58%	0.36%	15084	9436	50.4	123.2
B2	13505	0.0052	0.67	0.69	96.8%	3.2%	0.77%	0.75%	20259	19608	68.6	134.4
B3	12477	0.0054	0.67	0.69	96.9%	3.1%	0.80%	0.78%	18693	18116	72.8	144.2
B4	11913	0.0049	0.60	0.69	87.2%	12.8%	0.81%	0.71%	19839	17297	68.6	149.8
B5	13477	0.0051	0.66	0.69	95.7%	4.3%	0.77%	0.74%	20445	19568	67.2	134.4
B6	12266	0.0049	0.63	0.69	91.2%	8.8%	0.79%	0.72%	19528	17809	71.4	148.4
Mean A	13736	0.0057	0.62	0.69	90.7%	9.3%	0.92%	0.83%	21943	19943	63.0	130.0
Std.A	2195	0.0014	0.04	0.00	5.1%	5.1%	0.19%	0.20%	2856	3187	7.8	13.5
Mean B	11690	0.0047	0.61	0.69	88.4%	11.6%	0.76%	0.68%	18975	16972	66.5	139.1
Std.B	2624	0.0011	0.09	0.00	13.2%	13.2%	0.09%	0.15%	2004	3810	8.2	10.2
Mean.All	12791	0.0052	0.62	0.69	89.6%	10.4%	0.84%	0.76%	20573	18572	64.6	134.2
Std.All	2531	0.0013	0.06	0.00	9.3%	9.3%	0.17%	0.19%	2850	3675	7.9	12.5

N.Lc – number of osteocyte lacunae
Lc.TV – total lacunae volume (mm^3)
BV – bone volume (mm^3)
TV – tissue volume (mm^3)
BV/TV – bone volume fraction (%)
HCa.V/TV – canal volume fraction or bone porosity (%)
Lc.TV/BV and Lc.TV/TV– lacunar volume density (mm^{-3})
N.Lc/BV and N.Lc/TV– lacunar number density (mm^{-3})
$HCa.Dist_{50}$ – average distance of 50% of bone matrix to the nearest Haversian canal (μm)
$HCa.Dist_{95}$ – average distance of 95% of bone matrix to the nearest Haversian canal (μm)

6.3.3 3D shape descriptors of osteocyte lacunae

Table 6.3 reports the descriptive statistic features of the osteocyte lacunae descriptors. The average lacuna volume was 409.5±149.7 μm^3. The lacuna surface was 336.2±94.5 μm^2. With the length of 18.9±4.9 μm and the width of 9.2±2.1 μm and the depth of 4.8±1.1 μm, the average anisotropy (length: width: depth) of the osteocyte lacuna was approximately 4:2:1. The average and standard deviation of ratio (τ) between the volume of the actual osteocyte lacunae and the fitting ellipsoid was around 93.1%±6.6%. The lacunae structural model index was 3.3±0.3. The 50% and 95% of bone voxels are located within a distance of 13.8±1.0 μm and 27.5±2.5 μm from the nearest lacuna. Besides, we also calculated the orientation of each lacuna. The results showed that the main direction of each cell was mainly in the direction of

the Haversian channels. Figure 6.5 illustrates the distributions of lacunae descriptors over 13 samples.

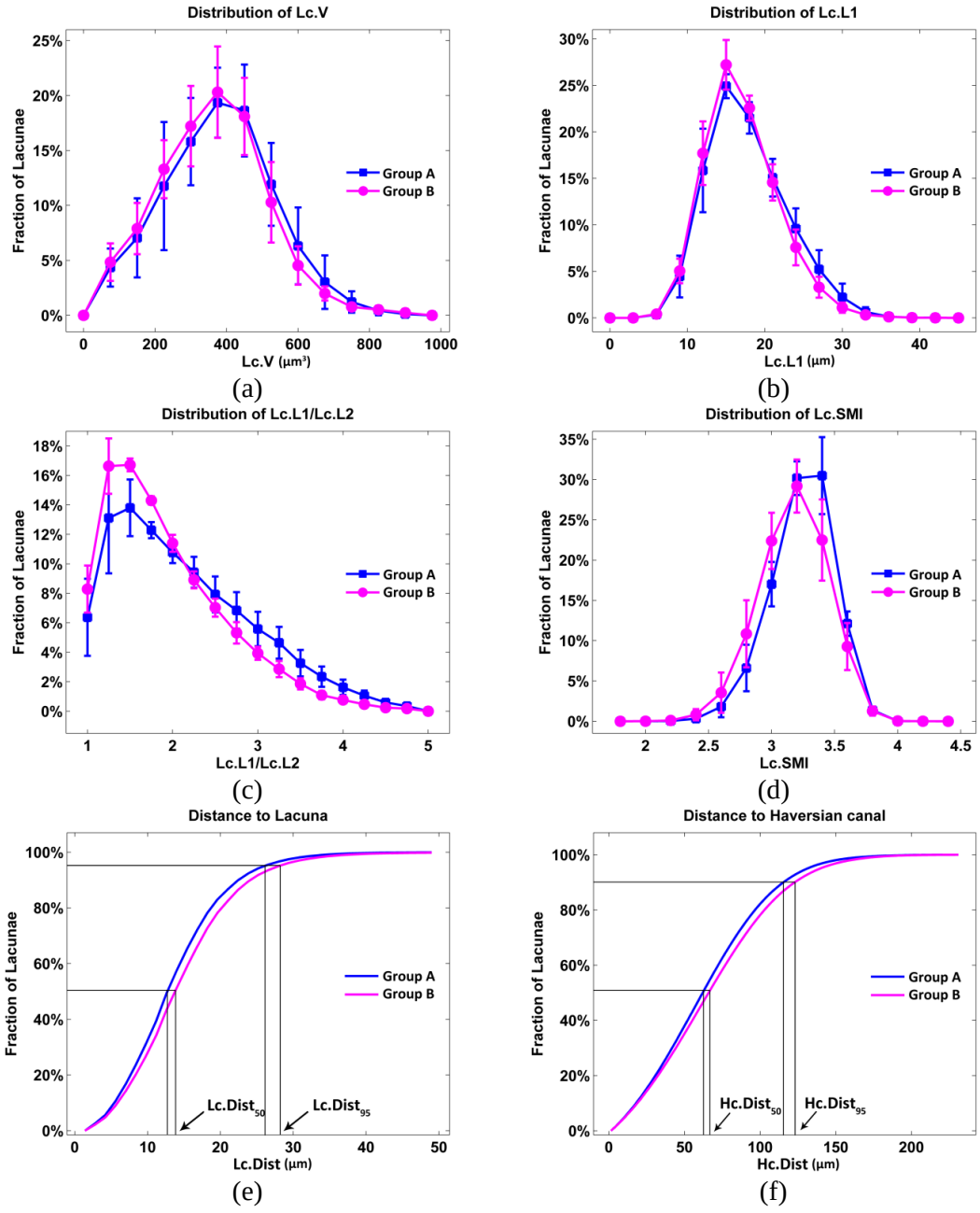

Figure 6.5 Lacunar descriptor distributions of group A (blue curve) and group B (pink curve). (a)-(d): Average distribution (line) and standard deviation (bars) of lacunae volume (a), main axis length (b), anisotropy (c) and structure model index (d). (e)-(f): Average distance distribution from bone matrix to osteocyte lacunae (e) and from bone matrix to Haversian canals (f).

Table 6.3 Osteocyte lacunae descriptors from 13 specimens

"*" parameters reported with standard deviation and range [minimum, maximum]

SampleID	Lc.V (μm^3)*	Lc.S (μm^2)*	Lc.L1 (μm)*	Lc.L2 (μm)*	Lc.L3 (μm)*
A1	446.2±153.5	354.9±94.4	20.1±4.9	9.0±2.1	5.0±1.0
	[82.3,965.9]	[93.2,761.7]	[6.9,43.8]	[3.7,21.1]	[1.9,10.1]
A2	405.4±147.7	330.5±92.4	19.1±4.8	8.7±2.0	4.9±1.0
	[82.3,902.8]	[97.9,734.0]	[7.5,40.5]	[3.8,18.2]	[1.0,9.9]
A3	427.0±140.3	340.7±86.5	19.8±4.8	8.6±1.9	5.1±1.0
	[82.3,839.7]	[95.0,661.2]	[8.0,41.3]	[3.6,18.6]	[1.5,9.7]
A4	364.3±147.1	311.5±95.9	17.6±4.7	9.1±2.0	4.9±1.2
	[82.3,954.9]	[93.1,724.7]	[6.4,40.9]	[3.3,19.0]	[1.4,10.8]
A5	410.0±130.3	342.9±85.7	18.9±4.9	9.7±2.0	4.9±1.2
	[82.3,834.2]	[94.8,735.0	[6.4,45.2]	[3.6,19.1]	[1.5,10.4]
A6	353.3±142.5	300.5±90.3	18.4±4.9	8.3±1.9	4.6±0.9
	[82.3,798.5]	[90.1,622.5]	[7.3,39.5]	[3.7,18.7]	[1.9,9.3]
A7	502.3±151.2	386.5±96.7	20.7±5.6	9.5±1.9	5.2±1.0
	[82.3,902.8]	[96.8,738.7]	[8.0,40.3]	[3.7,18.0]	[0.7,11.1]
B1	386.2±175.6	323.1±112.1	18.4±4.9	9.3±2.3	4.4±1.0
	[82.3,974.1]	[95.3,770.8]	[7.2,41.6]	[3.6,20.4]	[1.0,10.0]
B2	381.9±138.1	312.7±82.6	17.6±4.0	9.1±2.0	4.8±1.0
	[82.3,902.8]	[96.4,688.5]	[7.4,37.2]	[3.5,20.4]	[1.6,10.3]
B3	430.5±149.9	348.5±92.4	19.1±4.6	9.5±2.0	4.8±1.0
	[82.3,935.7]	[96.9,711.5]	[6.9,39.0]	[3.3,18.3]	[1.4,10.5]
B4	409.7±137.4	349.0±93.4	19.2±4.9	10.0±2.1	4.6±1.1
	[82.3,974.1]	[93.8,800.8]	[7.0,42.7]	[3.9,20.5]	[1.5,10.7]
B5	377.4±129.7	320.1±86.1	17.8±4.4	9.6±2.0	4.8±1.1
	[82.3,880.8]	[93.2,742.0]	[6.7,46.5]	[3.9,19.2]	[1.0,11.1]
B6	402.6±146.5	334.1±91.2	18.8±4.5	9.5±2.1	4.5±0.9
	[82.3,809.5]	[95.9,680.3]	[7.6,36.6]	[4.0,18.4]	[0.9,10.1]
A	417.6±152.4	339.7±95.8	19.3±5.1	9.0±2.0	5.0±1.1
	[82.3,965.9]	[90.1,761.7]	[6.4,45.2]	[3.3,21.1]	[0.7,11.1]
B	398.4±145.2	331.4±92.5	18.5±4.6	9.5±2.1	4.7±1.0
	[82.3,974.1]	[93.2,800.8]	[6.7,46.5]	[3.3,20.5]	[0.9,11.1]
All	409.5±149.7	336.2±94.5	18.9±4.9	9.2±2.1	4.8±1.1
	[82.3,974.1]	[90.1,800.8]	[6.4,46.5]	[3.3,21.1]	[0.7,11.1]

SampleID	Lc.L1/Lc.L2*	Lc.L1/Lc.L3*	Lc.SMI*	$Lc.Dist_{50}$ (μm)	$Lc.Dist_{95}$ (μm)	Ratio (τ)
A1	2.4±0.8	4.2±1.2	3.3±0.2	14.0	28.0	94.8%±5.0%
	[2.8,7.2]	[1.3,11.3]	[2.4,4.0]			
A2	2.3±0.8	4.1±1.3	3.4±0.2	14.0	26.6	94.5%±5.2%
	[2.8,7.1]	[1.3,14.9]	[2.3,4.3]			
A3	2.4±0.8	4.1±1.2	3.4±0.2	14.0	28.0	95.3%±4.8%
	[1.0,5.0]	[1.3,12.3]	[2.2,4.1]			
A4	2.0±0.7	3.8±1.5	3.3±0.3	14.0	29.4	88.1%±8.6%
	[2.8,6.8]	[1.2,27.5]	[2.3,4.4]			
A5	2.1±0.8	4.1±1.6	3.3±0.3	12.6	23.8	89.1%±7.6%
	[2.8,6.9]	[1.1,12.6]	[1.9,4.3]			
A6	2.3±0.8	4.1±1.3	3.4±0.2	14.0	26.6	94.6%±4.8%
	[2.8,7.1]	[1.4,14.3]	[2.3,4.4]			
A7	2.3±0.8	4.1±1.4	3.3±0.2	12.6	23.8	94.8%±4.9%
	[2.8,7.5]	[1.2,34.9]	[2.3,4.4]			
B1	2.1±0.7	4.3±1.3	3.3±0.3	16.8	33.6	95.0%±5.4%
	[2.8,6.5]	[1.3,16.7]	[2.2,4.0]			
B2	2.1±0.7	3.8±1.2	3.4±0.2	14.0	28.0	94.5%±5.3%
	[2.8,7.1]	[1.3,12.8]	[2.4,4.1]			
B3	2.1±0.7	4.2±1.3	3.3±0.2	14.0	28.0	94.5%±5.5%
	[2.8,7.2]	[1.4,15.5]	[2.4,4.1]			
B4	2.0±0.7	4.5±1.6	3.2±0.3	14.0	26.6	90.1%±7.4%
	[2.8,6.8]	[1.2,15.5]	[2.0,4.2]			
B5	1.9±0.7	4.0±1.5	3.3±0.3	14.0	26.6	90.5%±7.4%
	[2.8,6.9]	[1.2,18.8]	[2.1,4.3]			
B6	2.1±0.7	4.3±1.3	3.2±0.2	14.0	28.0	95.6%±4.3%
	[2.8,7.1]	[1.2,21.1]	[2.2,4.1]			
A	2.3±0.8	4.1±1.4	3.3±0.2	13.5±0.7	26.3±2.1	92.9%±6.7%
	[1.0,7.5]	[1.1,34.9]	[1.9,4.4]			
B	2.0±0.7	4.2±1.4	3.3±0.3	14.3±1.1	28.0±2.6	93.2%±6.5%
	[2.8,7.2]	[1.2,21.1]	[2.0,4.3]			
All	2.2±0.8	4.1±1.4	3.3±0.3	13.8±1.0	27.0±2.5	93.1%±6.6%
	[1.0,7.5]	[1.1,34.9]	[1.9,4.4]			

Lc.V – lacuna volume (μm3)
Lc.S – lacuna surface area (μm2)
Lc.L1, Lc.L2 and Lc.L3 – length, width and depth of lacuna (μm)
Lc.L1/Lc.L2 and Lc.L1/Lc.L3 – anisotropy of lacuna
Lc. SMI – structural model index of lacuna
Lc.Dist50 – average distance of 50% of bone matrix to the nearest lacuna (μm)
Lc.Dist95 – average distance of 95% of bone matrix to the nearest lacuna (μm)
Ratio (τ) – volume ratio of lacuna to fitting ellipsoid (%)

6.3.4 Osteocyte lacunar density distribution

To visualize the lacunar density variation, Figure 6.6(c) and (d) show the 3D local lacunar density maps of the two samples. It appeared that osteocyte lacunar density was higher in the bone matrix where the bone porosity was lower, Figure 6.6(c). As a comparison, the lacunar density remains more homogenous in the sample, which is more uniform in term of porosity, Figure 6.6(d).

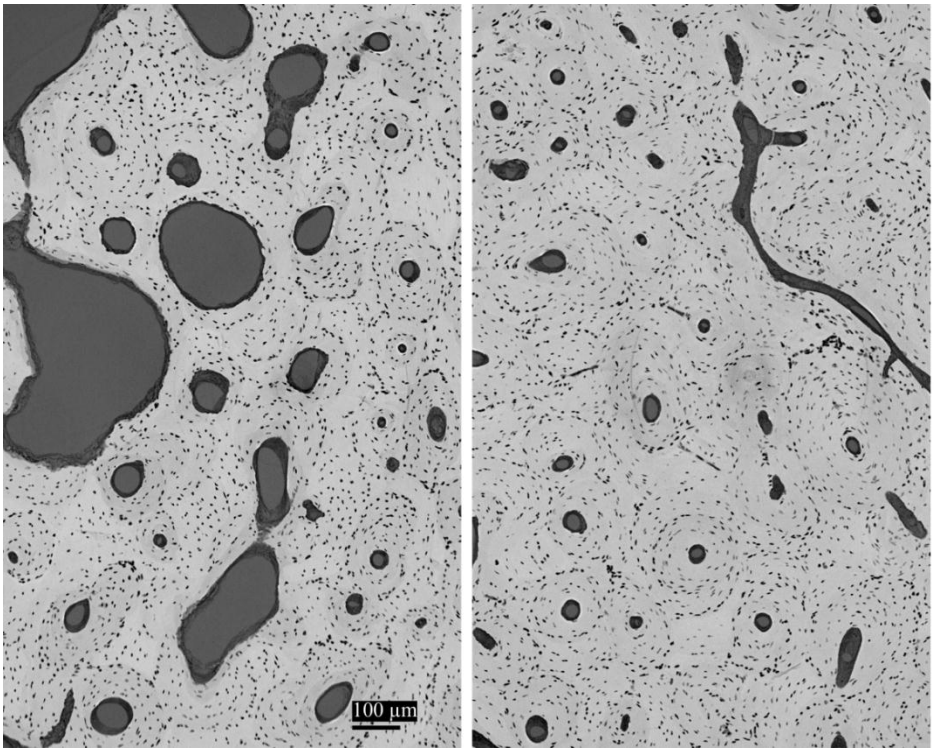

(a) (b)

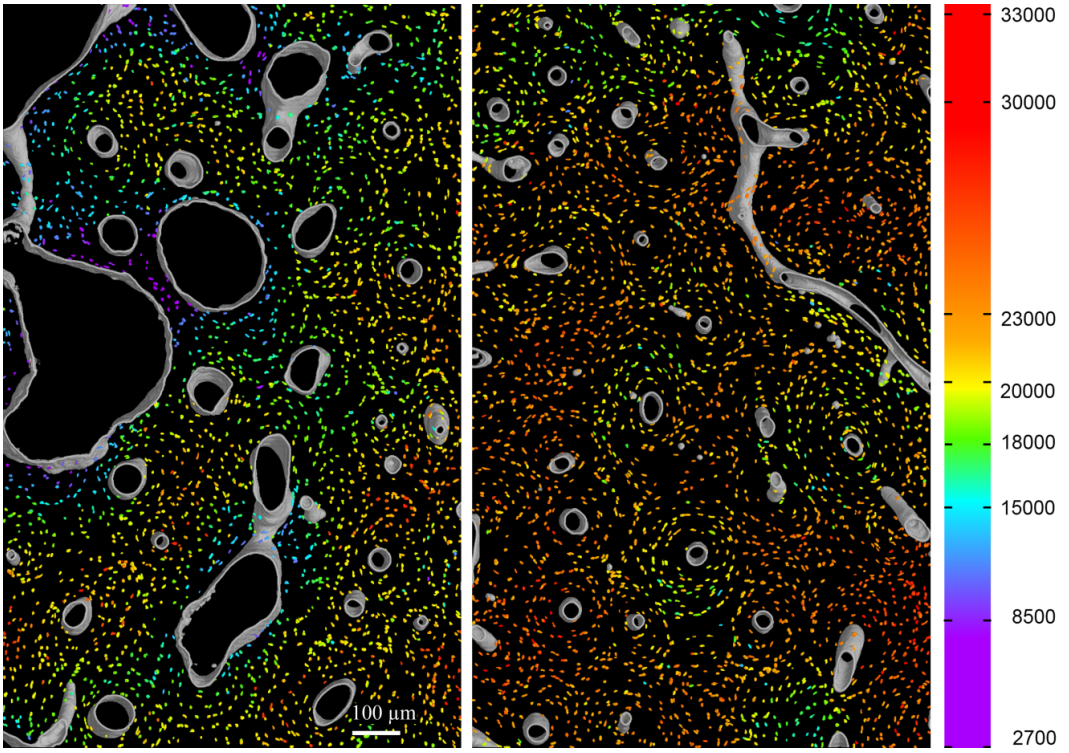

(c) (d)

Figure 6.6 (a) and (b) minimum of projection of 61 slices of the reconstructed images. The bone porosity of (a) (sample A3) varies a lot, while in comparison, the bone porosity of (b) (sample B2) remains quite homogeneous. (c) and (d) are the corresponding 3D lacunar density maps (*N.Lc(r)/BV(r)*) (*r*=140µm) of (a) and (b). The unit of the colored legend bar is #/mm^3. The cold color (blue) represents a low lacunar density, and warm color (red) represents a high lacunar density.

6.3.5 Correlations between bone porosity and osteocyte lacunae features

A quantitative evaluation of the relationships between osteocyte density and bone porosity was conducted on the sample displayed in Figure 6.6(c). Lacunar density and lacunar descriptors were extracted from the seven sub-volumes displayed on Figure 6.7. The linear regression analysis shows that several descriptors were strongly correlated with the *BV/TV* (Figure 6.8 and Table 6.4). Among the correlations, lacunae number density, the three axes length of lacunae (*Lc.L1, Lc.L2, and Lc.L3*) and the anisotropy of the lacunae (*Lc.L1/Lc.L2* and *Lc.L1/Lc.L3*)were significantly correlated with the bone volume fraction (*BV/TV*). The volume and surface of the lacunae were not correlated to bone porosity.

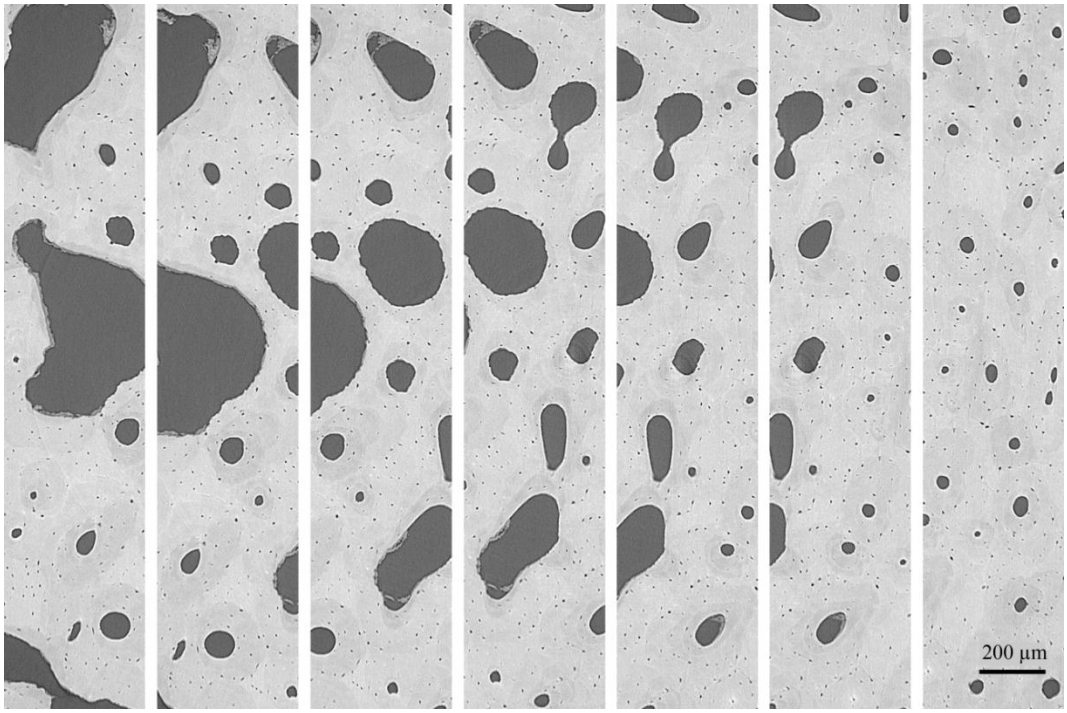

Figure 6.7 A series of regions with different tissue porosities from a single sample.((a)-(g): *BV/TV* ranging from 67% to 97%).

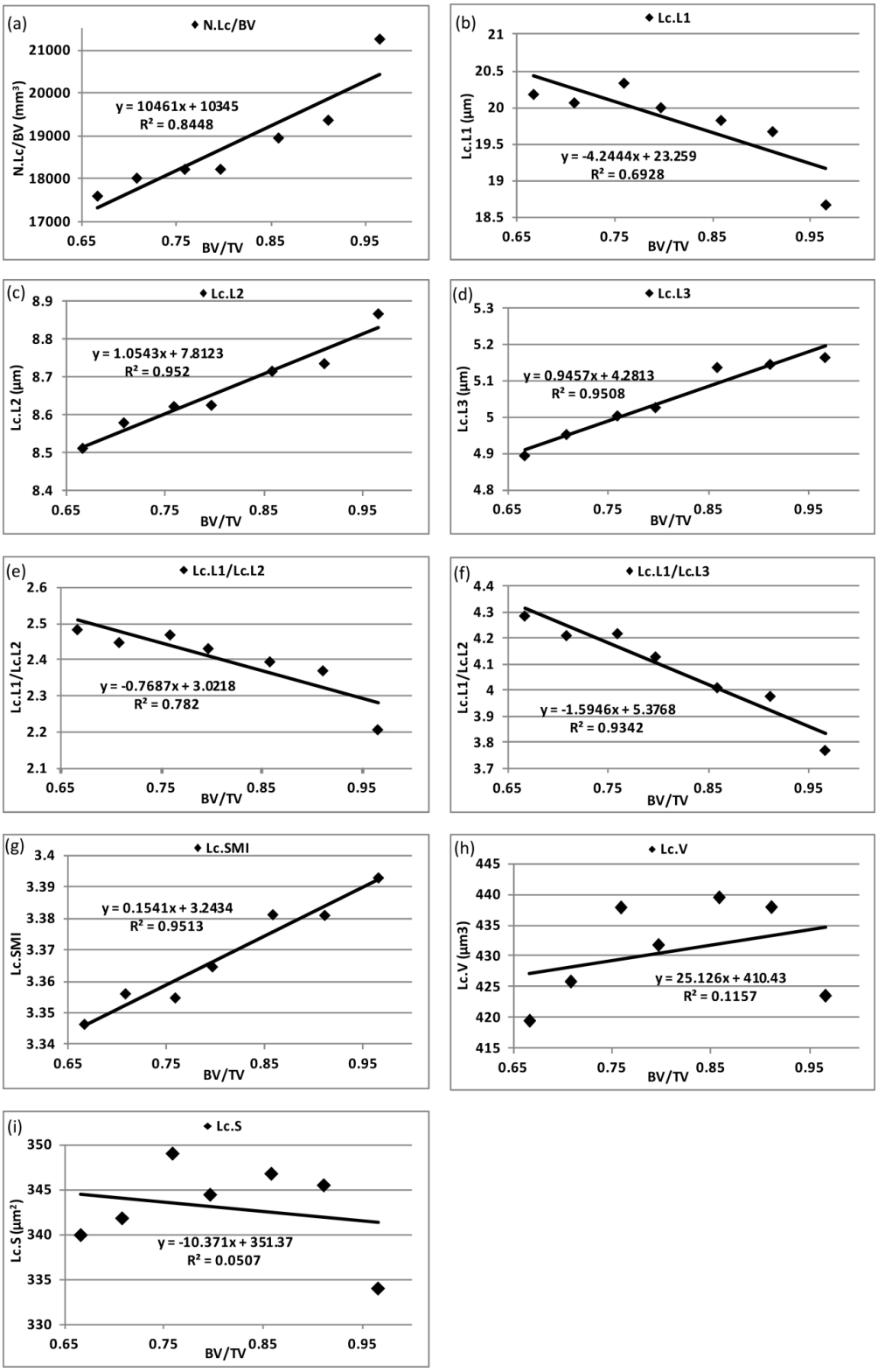

Figure 6.8 Correlation of bone porosity with osteocyte lacunae density (a), axes lengths (b)-(d), anisotropy (e)-(f), SMI (g), volume(h) and surface area(i).

Table 6.4 Regression statistics on the parameters calculated on the seven subvolumes displayed in Figure 6.7

"*" indicate parameters reported with $p<0.05$

Regression Statistics	BV/TV	R^2	Slope	Intercept
N.Lc/BV	Positive	0.85*	10461*	10345*
Lc.L1	Negative	0.69*	-4.24*	23.26*
Lc.L2	Positive	0.95*	1.05*	7.81*
Lc.L3	Positive	0.95*	0.95*	4.28*
Lc.L1/Lc.L2	Negative	0.78*	-0.77*	3.02*
Lc.L1/Lc.L3	Negative	0.93*	-1.59*	5.38*
Lc.SMI	Positive	0.95*	0.15*	3.24*
Lc.V	Positive	0.12	25.13	410.43*
Lc.S	Negative	0.05	-10.37	351.38*

N.Lc/BV – lacunar number density (mm^{-3})
Lc.L1, Lc.L2 and Lc.L3 – length, width and depth of lacuna (μm)
Lc.L1/Lc.L2 and Lc.L1/Lc.L3 – anisotropy of lacuna
Lc. SMI – structural model index of lacuna
Lc.V – lacuna volume (μm^3)
Lc.S – lacuna surface area (μm^2)

6.4 Discussion

In this paper, after describing the imaging conditions with SR micro-CT and the segmentation of osteocyte lacunae, we proposed an automated method for extracting 3D shape descriptors on each osteocyte lacuna. We also introduced the 3D local lacunar density map to visualize the lacunar density variation within the bone sample. We reported the distribution and statistics on various morphological descriptors. Several strong correlations between osteocyte lacunae descriptors and bone porosities were also reported for the first time in 3D quantification.

The osteocytes are deeply enclosed in the compact bone matrix, making their quantification challenging with conventional imaging techniques. The proposed method has three main features: first it is based on a gold standard 3D imaging technique, second, it describes a robust segmentation of lacunae, and third, it rigorously defines and extracts 3D descriptors of lacunae. We want to emphasize that a well-controlled methodology, at each step of the process, is required to be able to draw reliable biological conclusions.

CT coupled to synchrotron radiation is considered as a gold standard for imaging the micro- and ultra-structure of the bone tissue [Müller (2009)]. It has recently been used to quantify the morphometry of osteocyte lacunae [Hannah *et al.* (2010); Carter *et al.* (2012)]. Using SR-micro CT to image the osteocyte lacuna has many advantages compared to other imaging techniques. First, it provides a 3D image with isotropic spatial resolution, allowing accurate and direct 3D measurements without any destruction of the sample. Most of the conventional studies on osteocyte lacunae were based on 2D imaging of thin section. However, the mechanical sectioning of the sample does not guarantee keeping the integrity of the structure. Nevertheless, with the rapid development of imaging techniques, the acquisition of three

dimensional images of the osteocyte network has become possible The FIB/SEM technique has been demonstrated to deliver a very high resolution in depth and looks promising to quantify the osteocyte LCN at the order of tens of nanometers [Schneider *et al.* (2010), (2011)], but it still requires the physical destruction of the sample and the imaging process is quite time consuming. Second, SR-micro CT allows to image relatively large fields of view containing more than ten thousands of osteocyte lacuna. Therefore one can expect that the estimate of the average of the mean properties of lacunae to be improved compared to smaller populations. This can be assessed by the standard error of the mean (SEm) defined as the standard deviation divided by the square root of the number of analyzed lacunae. For example to give an order of the magnitude, in our study according to table 4, the SEm of the lacunar volume in A1is 1.4, while it can be estimated to be 15.5 in the work of Sugawara. Comparatively, 3D confocal laser scanning microscopy (CLSM) has been successfully applied in several studies [McCreadie *et al.* (2004); Sugawara *et al.* (2005); Vatsa *et al.* (2008); van Hove *et al.* (2009a)]. It has the advantages of high resolution and no ionizing radiation damage on the sample, but due to the limited penetration of light, up to now, the field of view within bone tissue has been confined to a maximum depth of 100-150 µm [Jones *et al.* (2005)]. Third, the high X-ray flux available on synchrotron sources, which is several orders of magnitude higher than conventional X-ray, permits to acquire images with high signal to noise ratio (SNR) in relatively short scanning time. Although new generations of high resolution desktop CTs have also been demonstrated to analyze lacunae [Vatsa *et al.* (2008); van Hove *et al.* (2009)], they suffer from a lower SNR, making the segmentation of small objects such as lacunae more difficult. Apart from the advantage mentioned above, SR micro-CT techniques can also reach nanometric resolution [Dierolf *et al.* (2010); Langer *et al.* (2012); Pacureanu *et al.* (2012)] to image lacunae and canaliculi but this was out of the scope of this chapter.

In this work, we detailed a robust automatic method based on hysteresis thresholding followed by a step of artifact elimination to segment the osteocyte lacunae from the SR micro-CT images. The need for an automatic method is clear when considering that the 3D images enclose thousands of lacunae. With a voxel size of 1.4µm, the osteocyte lacunae appear as quite small structures. By applying the hysteresis thresholding on the reconstructed image, the osteocyte lacunae with various grey values could be well preserved. By taking into account the morphology of the osteocyte lacunae, artifacts, such as noise, ring artifacts, and irregular shaped objects were well eliminated, thus the method is robust to noise. This automatic method was compared to a semi-manually segmented image. The quantitative results indicate reliable results since the Dice index was 94.6% and the relative errors between the descriptors calculated on the segmented and on the reference image differed by less than 2%. It would be desirable to validate the method on more reference images but the manual segmentation is not a trivial task since it requires a lot of user interaction. The reference image segmented here contained 357 lacunae, which is already a large number compared to most manual studies (for instance in [Mullender *et al.* (1996)], there were only 75 lacunae per sections). Thus, the manual segmentation of more images would be a very time-consuming task and subject to bias from human fatigue and subjectivity. Our method also excluded those fragmented lacunae on the border of the 3D image, which might not be done in previous

studies [Hannah *et al.* (2010); Carter *et al.* (2012)]. The removal of these fragmented lacunae is important, since they can influence the lacunae descriptors distribution on the whole population. Actually, the segmentation is a crucial step when quantitative parameters are expected since an incorrect segmentation may bias the results. To the best of our knowledge, no other segmentation method of osteocyte lacunae has so far been evaluated. In previous works based on 2D imaging, the segmentation of the osteocyte lacunae was mostly performed interactively by using 2D commercial image processing software [McCreadie *et al.* (2004); Jones *et al.* (2005); Sugawara *et al.* (2005); Vatsa *et al.* (2008); van Hove *et al.* (2009a)]. In other works based on 3D imaging, simple thresholding was generally used. For instance, in Carter [Carter *et al.* (2012)], lacunae were extracted from global thresholding, followed by the elimination of noise based only on the volume of each object, but the authors did not report validation results.

At the tissue level, on average, 12791±2531 lacunae were successfully segmented from a tissue region of 1.4mm×1.4mm×0.35mm, corresponding to a density of 20573±2850 lacuna per mm^3. This finding is in range of previous 3D reports on the number of lacunae per bone volume both at high (580 nm) [van Hove *et al.* (2009)] and lower (1.4 µm) [Carter *et al.* (2012)] spatial resolution. We also reported the distances reflecting the distribution of Haversian canals. To the best of our knowledge, it is the first time that these values are reported in human. The results are similar to that found by Shahar in dogs and horses by using 2D microscopic images [Shahar *et al.* (2011)]. These parameters, for which estimation is more reliable in 3D, may be important indicators of how efficiently blood can support the nutrient for the bone tissue.

We calculated a number of direct 3D lacunar descriptors. In general, many studies highlighted the important role of the osteocyte in mechanotransduction and in controlling bone remodeling. However, relatively few descriptive parameters on the size, shape, density and spatial organization of the osteocyte lacunae are available in 3D. It is known that these morphological characteristics impact the biomechanical parameters. For instance, it was shown that the mechanical environment of the stress-sensitive osteocyte varies with the geometry of the osteocyte lacuna [McCreadie *et al.* (2004)]. More recently the shape of the osteocyte was found to have a direct impact on elasticity and mechanosensing [Bacabac *et al.* (2008)]. In addition, most theoretical biomechanical models require assumptions about the density, shape and size of lacunae. In a simulation study, Mullins et al. showed the impact of varying lacunae porosity on the macroscopic properties of cortical bone [Mullins *et al.* (2007)]. Thus the descriptive parameters we provide can further be used as realistic input to biomechanical models.

In addition, this study provides an analysis of the spatial organization of lacunae within bone matrix that could have some interpretation in terms of the bone mineral homeostasis process. While the role of osteocytes in this process is still a subject of debate [Teti *et al.* (2009)], a recent work suggests that osteocytes contribute directly to the calcium homeostasis by removing their surrounding mineral matrix [Qing *et al.* (2012)]. We found that although the total lacunar volume is smaller than that of the Haversian canals, their spatial distribution put them closer to the mineral matrix than the Haversian canal. This spatial organization might be important for the interplay of the cell network and the bone matrix.

Three dimensional measurements are more accurate than those derived from 2D images, generally based on ideal geometric assumption. For example, Mullender estimated the 3D lacunar density from 2D lacunar density based on the a spherical shape assumption [Mullender *et al.* (1996)]. By simulating a 2D image from our 3D binary lacunar image by stacking 4 consecutive slices (equivalent slice thickness 5.6µm), we used the same method to extrapolate 2D density measurements in 3D. We obtained a 2D density of about 380 mm^{-2}, and an extrapolated 3D density of 30600 mm^{-3}, while the actual 3D lacunar density (N.Lc/BV) was 20471 mm^{-3}. This illustrates the bias than can be introduced by an incorrect model assumption. In addition, the lower lacunar 3D density values obtained in Mullender's work can be related to the fact that when counting manually in 2D, only the large lacunae may be kept, thus underestimating the density.

In this study, the average and standard deviation of the lacunar volume was 409.5±149.7 μm^3, and its surface was 336.2±94.5 μm^2. Compared to the previous results, differences existed in donor age and sex, anatomic location of the measurements and the imaging modality between the current and previous studies, but the values of lacuna volume measured in the current study are consistent with previously reported values. For instance, Carter [Carter *et al.* (2012)] measured lacunae volumes between 378 to 409 μm^3 at different anatomic locations within a healthy young male femoral shaft from SR micro-CT images. McCreadie also found a similar average value (476 μm^3) on 609 lacunae from 28 women femoral head using 3D CLSM image [McCreadie *et al.* (2004)]. The measurement of the lacunae surface in 3D was less often reported. Van Hove [van Hove *et al.* (2009)], found lacuna surfaces between 94.6±2.8 μm^2 to 211.9±14.4 μm^2 from desktop nano-CT images in three human proximal tibial bone samples, from osteopenic, osteoarthritic and osteopetrotic patients. In our work, we found a larger lacunae surface and larger lacunae volume. The different result may be due to the differences in methodology but also to the differences in site location and age of donors. Also, the higher noise to signal ratio in nano-CT could also influence the result.

We found that the axis lengths were on average 18.9±4.9 µm, 9.2±2.1 µm and 4.8±1.1 µm. The ratio of the three axis lengths is quite close to 4:2:1. These values are quite in agreement with the result reported by Van Hove [van Hove *et al.* (2009)]. Defining the anisotropy as the ratio of minimum to maximum dimensions, McCreadie [McCreadie *et al.* (2004)] found the similar degrees of anisotropy (0.271 and 0.279) of osteocyte in female femoral fracture and controlled samples, which is quite similar to the value we reported (0.254). Our findings also support the result of Vatsa [Vatsa *et al.* (2008)] who found a stretched structure of osteocytes in fibular bone, where osteocytes were aligned along the direction of loading, whereas osteocytes in calvarial bone, which do not bear a mechanical loading, had a more spherical shape with ratio of 2.1:1.3:1, and were not aligned to a particular direction. Carter [Carter *et al.* (2012)] did not directly report the axis lengths but three eigenvalues (EV) supposed to be the square of half-length of each main axis. However, the corresponding half-length values derived by using this relationship seem to give underestimated axis lengths compared to the literature. Besides, Carter also reported a degree of equancy (1- EV3/EV1), a degree of elongation (1 – EV2/EV1) and a degree of flatness (1 – EV3/EV2) to describe the shape of

lacunae. By using the same definition, we found a similar average degree of elongation (0.760) but flatter lacunae (0.725).

Besides the usual parameters, such as volume, surface, axis lengths and anisotropy, we also calculated other descriptors: the 3D Euler number depicts the lacunae topology, the SMI characterizes the plate-rod like nature of the lacuna, and the distance map describes the distance of bone matrix to the nearest osteocyte lacunae. In theory the Euler number of an ideal lacuna is 1. However, in practice, due to noise and artifacts in image acquisition, we observed different values (for instance for irregularly-shaped artifact which are not lacunae). Thus the 3D Euler number was mainly used to eliminate this kind of noise. The Lc.SMI was on average 3.3±0.3 showing a structure between a cylinder and a sphere [Hildebrand *et al.* (1997)]. The average distance of bone matrix to the nearest osteocyte lacunae is larger than the value found by Kerschnitzki [Kerschnitzki *et al.* (2013)]. He reported that 80% of the bone matrix is within a distance of 10μm to the adjacent osteocyte in sheep. The difference could be explained by the different species used in the experiment. The reported $Lc.Dist_{50}$ and $Lc.Dist_{95}$ might be a well-suited descriptor which summarizes not just the amount of pores, but also their spatial distribution which is of importance in term of calcium homeostasis and its microenvironment remodeling [Qing *et al.* (2012)]. These descriptors are generally not reported since they are not available in standard commercial software.

Furthermore, our method provides the statistical distribution of each descriptor (see Figure 6.5). The distribution of the lacunar volume did not reveal a bimodal distribution contrary to what was found by Hannah [Hannah *et al.* (2010)]. The reason that we do not find the bimodal lacunar volume distribution could be due to the differences in the analyzed region of interest and different aged samples. While our study included lacunae from both osteon and interstitial tissue, Hannah restricted within osteons.

Proper 3D display is a powerful method for exploratory research. By introducing 3D renderings of the local density of osteocyte lacunae (*N.Lc(r)/BV(r)*) (Figure 6.6), it was easy and intuitive to find the possible relationship between osteocyte lacunar density and bone porosity even before doing any statistical studies. Figure 6.6(c) reveals that lacunar density can be quite low (2700/mm^3) close to very porous region and can rise up to 30000/mm^3 around dense bone matrix regions. However, such large density variations were not observed in more homogenous bone regions (Figure 6.6(d)).

The quantitative study on different bone porosity regions showed that lacunar density (*N.Lc/BV*) was strongly correlated (R^2=0.845, p=0.0034) with the change of bone porosity. The linear regression showed that with every 1% increase of bone porosity, the lacunar density decreases of 104.61/mm^3. Such negative correlation between bone porosity and lacunar density is in agreement with the work of Power [Power *et al.* (2001)] conducted in 2D using light microscopy. His work was based on several regions across different sites of bone including superior, inferior, anterior and posterior regions on female femoral neck across biopsy (fractured) and post-mortem (controlled) samples. A strong correlation between lacunar density and BV/TV bone porosity, was reported by Vashishth et al [Vashishth *et al.* (2000), (2002)], who conducted the study with a series of different aged subjects using light microscopy. Our results, although limited, support the hypothesis that the lacunar density determines the bone volume fraction. More interestingly, we also found that several other

lacunae descriptors correlated with *BV/TV*. The lacunae anisotropies (*Lc.L1/Lc.L2* and *Lc.L1/Lc.L3*) were significantly larger in a more porous bone region. The increase of anisotropy was mainly due to the increase in the length of lacunae in the more porous bone region, as the width and depth were slightly decreased in contrast. The correlation between BV/TV and Lc.SMI also confirm that the lacunae were on average more rod-like structures than sphere-like in regions of higher bone porosity. Information on lacunar shape might be important since they might reflect the mechanical properties of the cortical bone [Currey *et al.* (2013)].

There are some limitations of this study. First, although thirteen samples were analyzed, we acknowledge that they arise from only two donors thus limiting the generality of the results. Also, the correlation study between the bone porosity and lacunar density was based on a single sample but with diverse porosities. However, our results are quite consistent with previous work conducted in 2D [Vashishth *et al.* (2000), (2002); Power *et al.* (2001)]. Since our results were 3D descriptors calculated from SR CT images on a large number of cells, they can be more reliable. The lacunae characteristics as well as their correlations to porosity need to be further studied on more samples of different individuals and at different anatomical locations. Second, the voxel size of 1.4 µm could be limited to image very small lacunae, but it was our choice to provide a large field of view that allows the analysis of a large population of cells. Third, the imaging technique used in this study can only detect the hard tissue. Therefore, it was impossible to image and quantify the osteocytes inside the lacunae. We believe that reporting descriptive data on the osteocyte lacunae contribute to the field since there are relatively few 3D data available in the literature. But it is difficult to give an extensive interpretation of the results since we have relatively few information on the donors. In further study, we plan to compare osteocyte lacunae in samples from healthy donors and diseased patients.

To summarize, in this study, we presented an automatic and well controlled methodology for quantitative analysis on a large population (more than 150000) of osteocyte lacunae. The 3D images were acquired through a SR micro-CT system, which is currently considered a gold standard for the observation of the osteocyte lacunae. We delivered an automated method to perform the segmentation, parameters extraction and statistics. Considerations, such as artifact elimination and partial lacunae removal, were carefully handled in the process. Since the calculation on each parameter was performed directly in 3D, unbiased results can be delivered compared to the previous results derived from ideal model assumptions. The results were compared with a reference image, and were proved to be reliable. We developed our own software, including novel parameters regarding the shape of lacunae. By introducing the 3D local lacunar density map, it was possible to visualize the lacunar density variation over large field of view. Further, by using these tools, we found several significant relationships between the osteocyte lacunae descriptors and bone porosity at the same local region in 3D. We believe that using such method will boost the efficiency on the investigation of osteocyte lacunae shape analysis over a large number of specimens. Therefore, it will help the researchers to investigate the bone related problems associated with the reliable statistical data at cell level more directly, effectively and quantitatively.

Chapter 7

Development of a 3D Quantification method of Canaliculi from Synchrotron CT images at sub-micrometer scale

Contents

7.1 Introduction 95
7.2 Material and method 96
7.2.1 Sample preparation 96
7.2.2 Synchrotron radiation micro-CT imaging 97
7.2.3 Segmentation 97
7.2.4 Quantification Method 98
7.2.4.1 Labeling 98
7.2.4.2 Quantification of lacunae 99
7.2.4.3 Quantification of ramification of canaliculi 99
7.3 Results 100
7.3.1 Validation of the canaliculi counting method 100
7.3.2 Application to SR micro-CT image 102
7.4 Discussion 105

Abstract

In the context of bone diseases research, recent works have highlighted the crucial role of the osteocyte system. This system, hosted in the lacuno-canalicular network (LCN), plays a key role in the bone remodeling process. However, few data are available on the LCN due to the limitations of current microscopy techniques, and have mainly only been obtained from 2D histology sections. Here we present, for the first time, an automatic method to quantify the LCN in 3D from synchrotron radiation microtomography images. After segmentation of the LCN, two binary images are generated, one of lacunae (hosting the cell body) and one of canaliculi (small channels linking the lacunae). The binary image of lacunae is labeled, and for each object, lacunar descriptors are extracted after calculating the second order moments and the intrinsic volumes. Furthermore, we propose a specific method to quantify the ramification of canaliculi around each lacuna. To this aim, a signature of the numbers of canaliculi at different distances from the lacunar surface is estimated through the calculation of topological parameters. The proposed method was applied to the 3D SR micro-CT image of a human femoral mid-diaphysis bone sample. Statistical results are reported on 399 lacunae and their surrounding canaliculi.

Keywords: 3D image analysis, morphology of lacuno-canalicular network, synchrotron micro-CT, cortical bone, ramification of canaliculi

7.1 Introduction

Bone diseases severely affect the quality of life around the world. According to a survey of International Osteoporosis Foundation, 1 of 3 women and 1 of 5 men with age over 50 suffer from osteoporosis, which is associated to bone fractures. Bone fragility remains only partially understood despite decades of research in this area. Recently, the crucial role of the osteocyte system at the cellular scale was highlighted [Bonewald (2011)]. The osteocyte system, which is composed of osteocytes communicating through dendrites, is essential in bone mechanosensation and bone mechanotransduction and is supposed to play an important role in orchestrating bone adaptation [Burger *et al.* (1999)][Han *et al.* (2004)](Gu et al. 2007).

The osteocyte system is hosted in the lacuno-canalicular network (LCN). Although the LCN is raising increasing interest, it is a structure difficult to assess since it is deeply embedded in calcified bone matrix and it is composed of a huge number of nanometric structures. Lacunae are flat ellipsoidal voids housing the osteocyte bodies and with a density between 26000 to 90000/mm3 [Cardoso *et al.* (2013)]. Canaliculi are narrow tunnels, enclosing the cell processes of the osteocytes with a reported diameter around 100-700nm [L You *et al.* (2004)]. The canaliculi connect lacunae and allow the circulation of interstitial fluid. Osteocytes are hypothesized to be stimulated by load-induced interstitial fluid displacement circulating in the LCN. Computational transport models have been proposed to estimate shear stresses [Weinbaum *et al.* (1994)][Anderson *et al.* (2005)][Anderson *et al.* (2008)], but they are generally based on idealized lacuno-canalicular geometries. Therefore, the assessment of the LCN geometry is important to help understanding the strain-sensing mechanisms of the osteocyte network.

However, the 3D assessment of the LCN is still limited. Conventionally two-dimensional imaging techniques, such as light microscopy, atomic force microscopy (AFM), scanning

electron microscopy (SEM) or transmission electron microscopy (TEM), have been proposed to visualize and quantify the LCN [Marotti *et al.* (1995)][Lin *et al.* (2011)] [Sharma *et al.* (2012)][Kamioka *et al.* (2009)]. Confocal microscopy can provide three-dimensional images, however, the limited penetration of light restricts the thickness of the visualized specimen and the spatial resolution is anisotropic [Sugawara *et al.* (2005)]. Recently, new 3D imaging techniques such as ptychography and serial FIB/SEM have been reported to image the LCN respectively at spatial resolutions of 65nm [Dierolf *et al.* (2010)] and 30nm [Schneider *et al.* (2011)]. Due to the very high spatial resolution of these techniques, the field of view remains limited to a few cells, which restricts the possibility to obtain statistically significant results on the osteocyte network.

3D synchrotron radiation microtomography (SR micro-CT) has been postulated to be an ideal technique for visualizing the LCN [Müller (2009)]. In previous works, we have demonstrated the feasibility of SR micro-CT to image the LCN at beamlines of the European Synchrotron Radiation Facility (ESRF) [Langer *et al.* (2012); Pacureanu *et al.* (2012)]. SR CT presents a number of advantages over conventional cone-beam CT. In particular, since the photons flux is several orders of magnitude higher than the one of conventional X-ray tubes, sub-micrometric spatial resolution can be reached while keeping good signal to noise ratio in relatively short time. With a 3D isotropic voxel size of 280 nm, this technique can provide a relatively large field of view (FOV) of about 600^3 μm^3. Compared to the other 3D approaches, a few thousands of cells may be imaged in a single scan.

However, due to the novelty of these images and the complexity of the LCN, the current quantification tools cannot provide an automatic analysis of the LCN. Previous efforts have been made for the segmentation of LCN from the reconstructed images [Pacureanu *et al.* (2009)][Pacureanu *et al.* (2010)][Pacureanu *et al.* (2011)][Zuluaga *et al.* (2011)]. In order to quantify this network, techniques for extraction of dedicated parameters need to be designed.

Our aim is to propose new automated methods to quantify the LCN from such 3D SR micro-CT images. The next section briefly describes image acquisition and segmentation and presents the methods used to quantify the lacunae and canaliculi. In particular we present a new scheme to assess the distribution of canaliculi around each lacuna. The last section reports the validation of the method on a simple geometrical phantom, an isolated lacuna and finally results on a large volume encompassing 399 lacunae.

7.2 Material and method

7.2.1 Sample preparation

The specimen was extracted from a human (woman, 78 years old) femoral mid-diaphysis, obtained from a multi-organ collection. The sample was prepared following a series of treatments (Biobank, Presles en Brie, France), which underwent delipidation, elimination of medullary protein and sterilization. Then, the sample was stored at a room temperature until the imaging acquisition. The collection of sample followed the procedure of the Human Ethics Committee of the “Centre du don des Corps” at the University Rene Descartes (Paris, France) and is in accordance with legal clauses stated in the French Code of Public Health.

7.2.2 Synchrotron radiation micro-CT imaging

Image acquisition, at spatial resolution of 300 nm, was performed on the 3D parallel beam SR micro-CT setup developed at beamline ID19 at ESRF. The experimental setup, image reconstruction and the artifacts elimination were described in section 5.5.1.

7.2.3 Segmentation

The segmentation of the LCN from the micro-CT images is challenging due to the small size of canaliculi compared to the voxel size in the reconstructed image. Here, we followed a method introduced in a previous work to perform the segmentation [Pacureanu *et al.* (2010)]. First, a mask including the relevant parts of the bone tissue and excluding Haversian canals is computed. This was generated by using a large median filter (radius=25) followed by a simple thresholding (see Figure 7.1(b)). The segmentation of the LCN was performed through a variational region-growing method based on an energy functional combining grey level information from the original image and shape information extracted via a 3D tube enhancement filter. Subsequently, the lacunae and canaliculi are separated by a 3D opening operation. After this step, two binarized images, of the lacunae and the canaliculi are available. Figure 7.1(c) illustrates a composite image of the segmented LCN.

We can formalize the segmented LCN as the union of each lacuna L_n with its set of canaliculi C_n:

$$LCN = \bigcup_{n=1}^{M} (L_n \bigcup C_n) \tag{7.1}$$

where M is the total number of lacunae in the image.

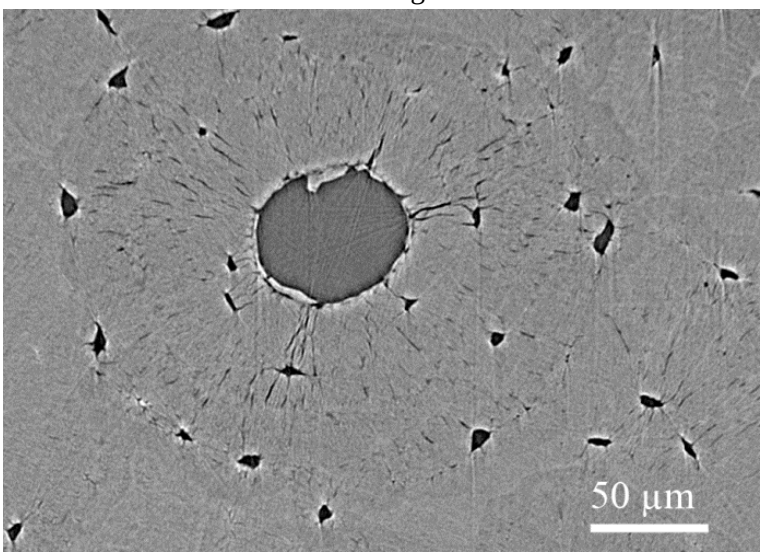

(a)

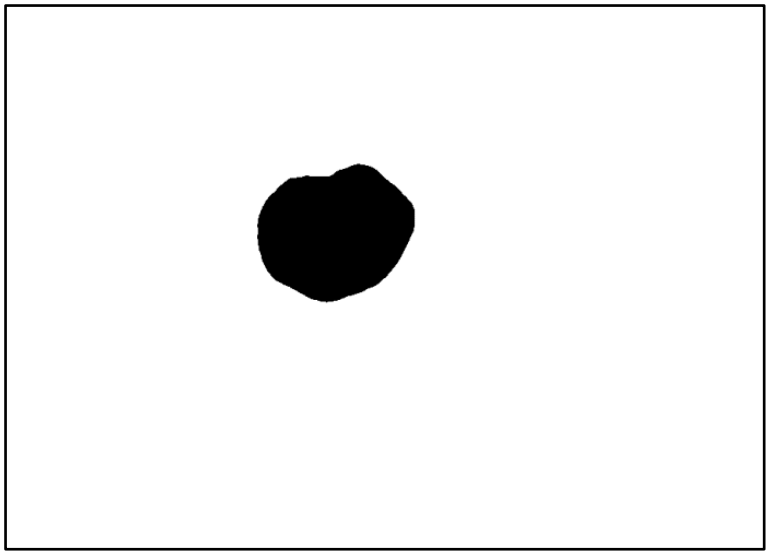

(b)

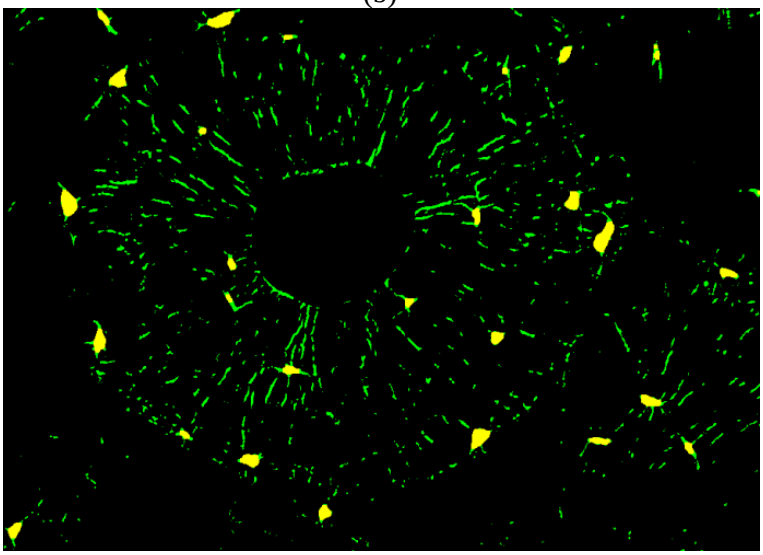

(c)

Figure 7.1 (a) A slice of reconstructed image of SR micro-CT (voxel size 280 nm, FOV: 904 × 649 pixels), including a Haversian canal, lacunae and canaliculi. (b) A slice of mask image which excludes the region of Haversian canal. (bone tissue in white and porosity in black) (c) The corresponding segmented lacunae (in yellow) and canaliculi (in green)

7.2.4 Quantification Method

7.2.4.1 Labeling

In order to quantify each lacuna L_n with its set of canaliculi C_n, the segmented lacunae are labeled by using a connected component analysis. Here, a fast labeling method proposed by Hoshen and Kopelmanm [J.Hoshen *et al.* (1976)] was implemented in 3D. This method allows labeling of all objects by only scanning the image twice in a raster pattern, i.e. from top to bottom and bottom to top.

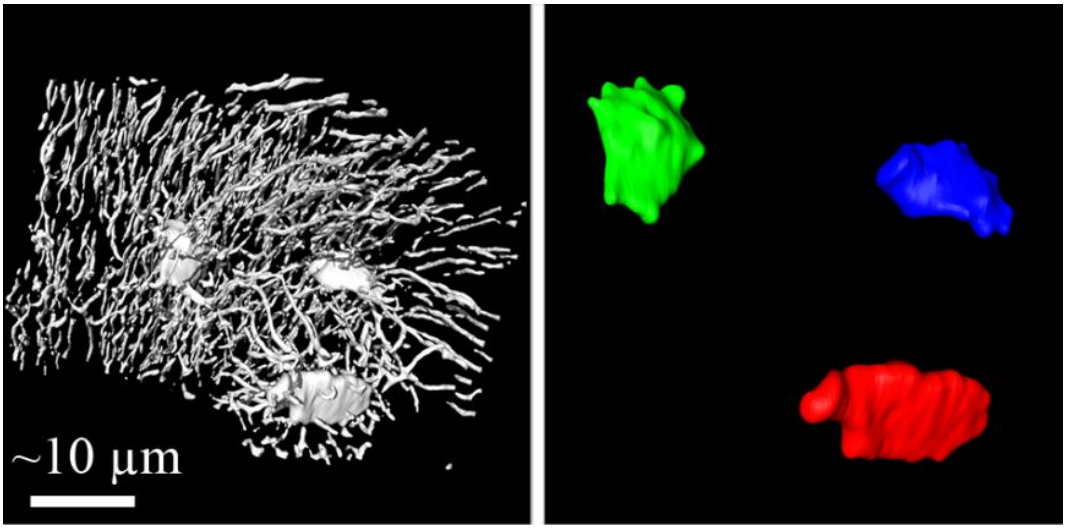

(a) (b)

Figure 7.2 (a) Segmented image with 3 flat elliptic-like lacunae and many tube-like canaliculi. (b) Labeled lacunae after the connected component analysis. Different colors show the different labels. The 3D renderings were generated with the software Avizo®.

7.2.4.2 Quantification of lacunae

After labeling, the total number of the lacunae (N.Lc) and the lacunar density with respect to the bone volume (N.Lc/BV) and the tissue volume (N.Lc/TV) can be easily calculated. The bone volume (BV), the tissue volume (TV) and the canal volume fraction (HCa.V/TV) were quantified from the mask image. Then, a number of descriptors were extracted from each labeled lacuna L_n as described in Chapter 6.

7.2.4.3 Quantification of ramification of canaliculi

We propose a new method to characterize the 3D ramification structure of canaliculi issued from a lacuna. Considering that the canaliculi are branching after radiating from the surface of lacunae, our goal is to give a signature of the number of canaliculi per lacuna at different distances from the lacuna boundary.

This method is based on the use of the 3D Euler number. Let us recall that the Euler number of an object in a three-dimensional space can be expressed as a function of the Betti numbers β_0, β_1, and β_2 as:

$$\chi = \beta_0 - \beta_1 + \beta_2 \tag{7.2}$$

where β_0, β_1, β_2 represent respectively the number of connected components, the number of tunnels and the number of cavities in the object [Odgaard (1997)].

In practice, when the object is represented as a discrete set of voxels, the 3D Euler number can be calculated as [Serra (1982); Toriwaki *et al.* (2002)]:

$$\chi = n_0 - n_1 + n_2 - n_3 \tag{7.3}$$

where n_0, n_1, n_2, and n_3 are respectively the number of vertices, edges, faces, and voxels.

To calculate the number of canaliculi per lacuna at different distances from the lacunar surface, first we extract the bounding surface of the lacuna using morphologic derivative operations. The bounding surface $\partial_r L_n$ can be formulated as the subtraction between the r+1 and r times dilated lacuna:

$$\partial_r L_n = \oplus_{(r+1)} L_n \setminus \oplus_r L_n \tag{7.4}$$

where $\oplus$ denotes dilation. This bounding surface will be used to count the number of canaliculi at the distance r, from the surface of the lacuna. Each bounding surface $\partial_r L_n$ has a single connected component with one cavity inside.

Second, a special bounding surface with holes is generated as:

$$\mathcal{H}_r L_n = \partial_r L_n \setminus (\partial_r L_n \cap C_n) \tag{7.5}$$

After that, the Euler number of the bounding surface with holes ($\mathcal{H}_r L_n$) is considered as:

$$\chi(\mathcal{H}_r L_n) = \beta_0(\mathcal{H}_r L_n) - \beta_1(\mathcal{H}_r L_n) + \beta_2(\mathcal{H}_r L_n) \tag{7.6}$$

where $\beta_0(\mathcal{H}_r L_n)$ = 1 (one connected component), $\beta_1(\mathcal{H}_r L_n)$ = the number of holes on the bounding surface, $\beta_2(\mathcal{H}_r L_n)$ = 1 (one cavity inside).

Finally, the number of canaliculi per lacuna $\mathrm{Lc.NCa}(L_n)(r)$ at a given distance r can be calculated as:

$$Lc.NCa(L_n)(r) = \beta_1(\mathcal{H}_r L_n) = 2 - \chi(\mathcal{H}_r L_n) \tag{7.7}$$

The dilation parameter reflects the distance at which the count is performed. Thus for each lacuna, the set $\{Lc.NCa(L_n)(r) | r = r_0, r_{max}\}$ gives a signature of the distribution of canaliculi around the lacuna. The r_{max} was chosen smaller than the mean inter lacunar distance Lc-Lc. The evolution of the number of canaliculi with r reflects the ramification of the canaliculi.

To further characterize the branching of canaliculi, we also calculated the ratio between the maximum and minimum number of canaliculi per lacuna at different distances from the surface of lacunae. Besides, we estimated an average length of the primary canaliculi for a given lacuna $r_p(L_n)$. The calculation was done under the assumption that the probability of any canaliculi to bifurcate is uniform in a certain range of distance. When considering only the first bifurcation, the number of canaliculi with respect to the distance (r) to the surface of lacunae increases linearly. Therefore, the relation between the number of canaliculi versus the distance was fit by a straight line $Lc.NCa(L_n)(r) \sim a(L_n)r + b(L_n)$. Then, $r_p(L_n)$ is estimated as the length for which 1.5 times the initial number of canaliculi $Lc.NCa(L_n)(r_0)$ and by correcting the distance step $\Delta r/2$:

$$r_p(L_n) = \frac{1.5 \times Lc.NCa(L_n)(r_0) - b(L_n)}{a(L_n)} + \frac{\Delta r}{2} \tag{7.8}$$

Finally, the descriptive statistic of each parameters were calculated on a whole population of lacunae in a given bone sample.

7.3 Results

7.3.1 Validation of the canaliculi counting method

The quantification of numbers of canaliculi was validated on two test volumes. The first one is a simple geometrical phantom constituted of three ellipses each with six cylinders, simulating three lacunae interconnected by canaliculi (cf. Figure 7.3(a)). This phantom is a binary 3D image, created by a simple program. The volume size is 64^3 voxels. The second is the segmentation of one isolated lacuna with all canaliculi interconnected, shown in Figure 7.3(b). The volume size is 149×149×85 voxels. This phantom was obtained by the manual segmentation on an experimental SR nano-CT image.

The application of the method to the first simple phantom provided 6 canaliculi for each ellipse as expected by construction. Concerning the second experimental image of an isolated lacuna, the validation was carried out by manual check and by a test program. The test program consisted in applying a connected component analysis after removing the lacuna. The method was applied with two choices of the dilation parameter r. For r equals 1 (respectively 15), the number of canaliculi found was 22 (respectively 32). The comparison with the test program in these two cases (Figure 7.3(c), (d)) shows that the correct number of canaliculi was obtained. The difference between the two results reveals that canaliculi are branched as can be observed in the 3D renderings. Thus, the dilation parameter is useful to put in evidence the ramification of canaliculi.

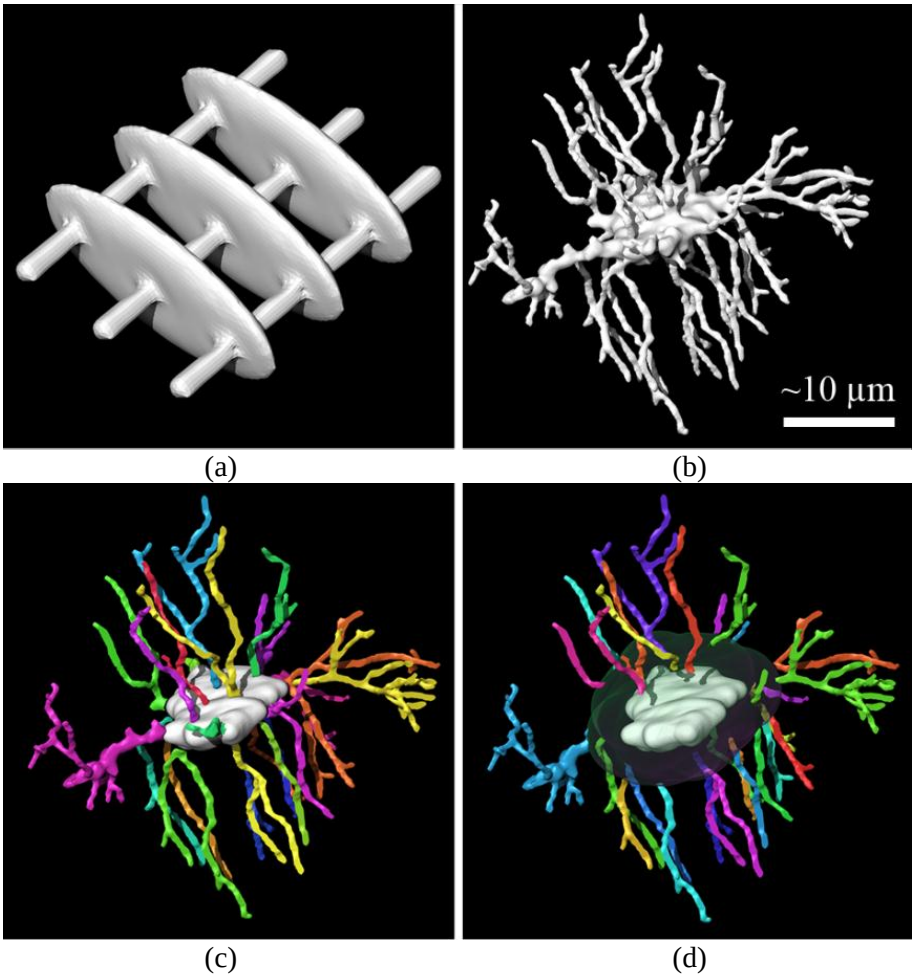

Figure 7.3 3D rendering of test volumes used for the validation. (a) A phantom made of three ellipses each with six rod-like branches, volume size: 643 voxels. (b) An isolated lacuna with fully interconnected canaliculi, volume size: 149×149×85 voxels. (c)-(d) Canaliculi counted by test program and manual check, showed in different colors. (c) 22 canaliculi for dilation parameter r=1 (d) 32 canaliculi for dilation parameter r=15 (4.2 µm away from the lacuna surface).

7.3.2 Application to SR micro-CT image

The proposed method was applied to a large SR-micro-CT image acquired at the ESRF at a spatial resolution of 280 nm. A Volume of Interest (VOI) made of 904×649x998 voxels was extracted from a $(2048)^3$ reconstructed volume. The VOI includes an osteon with hundreds of lacunae Figure 7.1(a). In the segmented osteocyte lacunae image, unacceptable objects such as micro-cracks, ring artifacts, and some irregularly shaped fragments can be extracted as well. From the literature, it is known that the size and shape of lacunae resides in a certain range [McCreadie *et al.* (2004); Dong *et al.* (2014)]. Thus, the segmented lacunae were filtered by thresholding some descriptors as follows: $50\ \mu m^3 < Lc.V < 1000\ \mu m^3$, $Lc.L1/Lc.L2 < 5$, and $0 \leq Lc.\chi \leq 2$. In addition, we also removed the outliers, by excluding the lacunae for which the canalicular regression slope was smaller than 0.5 or higher than 50.

The segmented image included 240 lacunae and their associated canaliculi. Figure 7.4 illustrates the labeled lacunae in different colors. We report the bone tissue histomorphometry parameters in Table 7.1. Besides, the statistical results on the lacunar descriptors with the mean, standard deviation, min and max are reported in Table 7.2. The average distance between nearest lacunae was calculated and was found to be 23.3 µm.

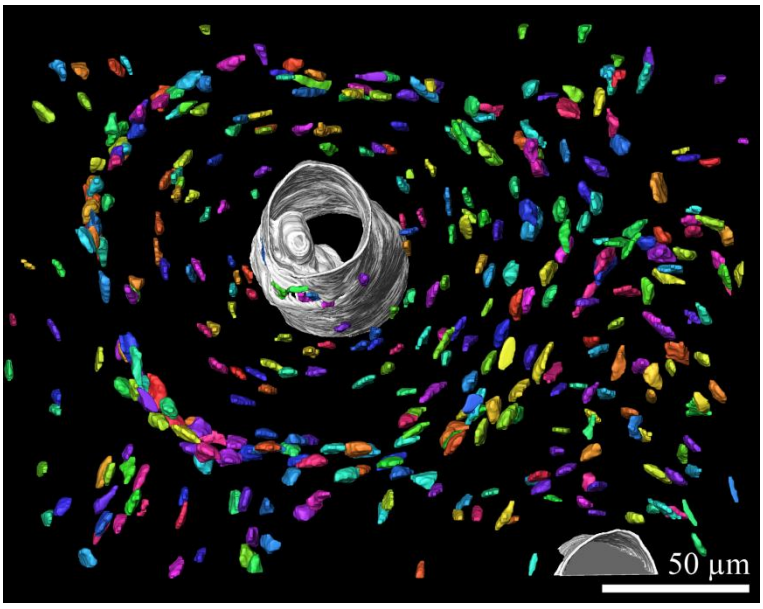

(a)

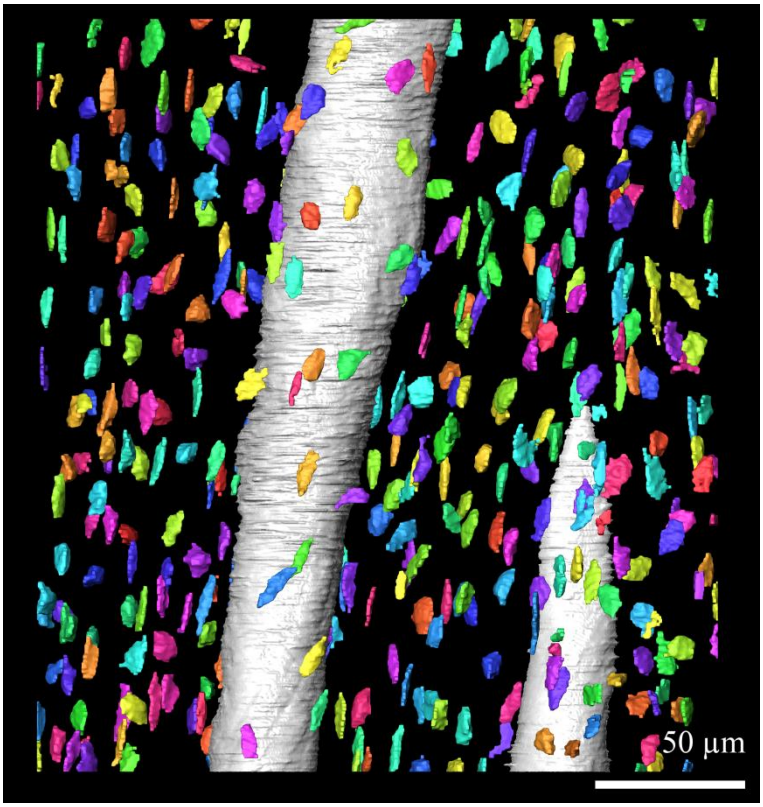

(b)

Figure 7.4 3D rendering of the labeled lacunae (displayed in different colors) concentric distributed around the osteon. (a) top view (b) side view

From the results, the mean and standard deviation of lacunar volume and surface was 229.1 ± 81.1 µm^3 and 248.5 ± 66.5 µm^3. The average lengths of the three axes of lacuna are 15.5, 8.0 and 4.1, and length ratio between the three axes is about 4:2:1. The mean of lacunar SMI is 3.2.

To quantify the numbers of canaliculi, we used 8 different dilation parameters (r), from 5 to 40 with step of 5 corresponding to distances from 1.4 µm to 11.2 µm with step of 1.4 µm. The statistical results are reported in Table 7.3.

The average number of canaliculi per lacuna was found to increase between 41.5 and 139.1 with the distance r. The linear regression explains 98.0% of the variability of the number of canaliculi around their mean (see Figure 7.5). The average length of the primary canaliculi is about 5.6 µm. The median of ratio between the maximum and minimum number of canaliculi per lacuna is 3.4. Figure 7.6 illustrates 3 different lacunae with different number of canaliculi. Figure 7.6(a) shows a lacuna with large number of 98 canaliculi, Figure 7.6(b), the one with most frequent number of 65 canaliculi, and Figure 7.6(c), a lacuna with a small number of 49 canaliculi. The three ramification patterns calculated for each of these lacunae are also shown in Figure 7.6(d).

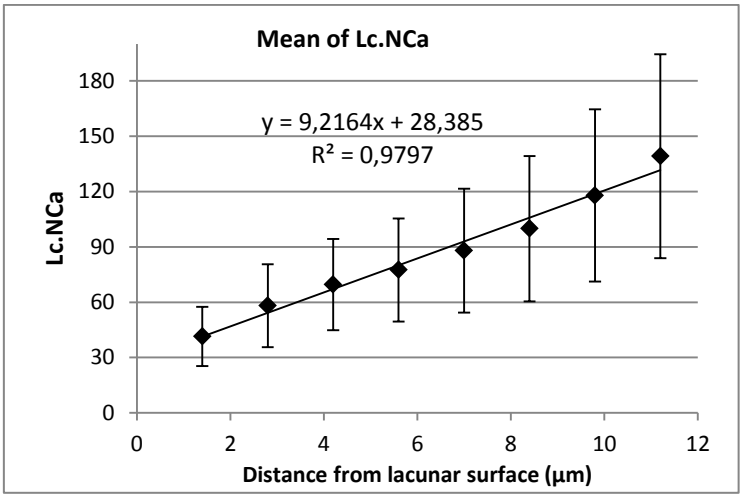

Figure 7.5 The mean and standard deviation of the number of canaliculi counted at the eight different distances from the surface of lacunae (n=240)

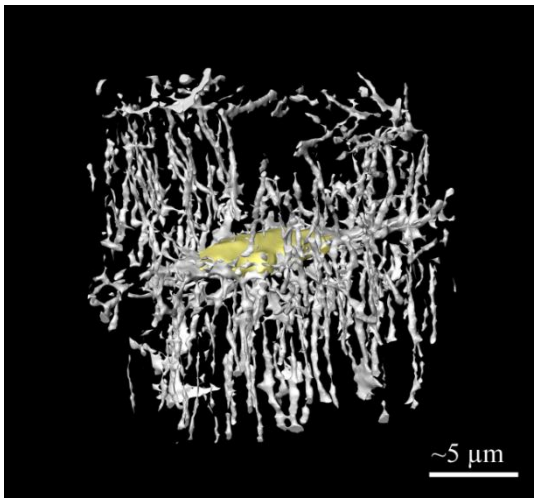

(a)

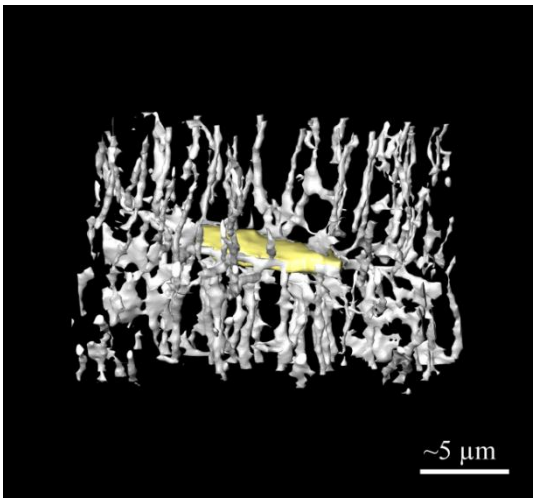

(b)

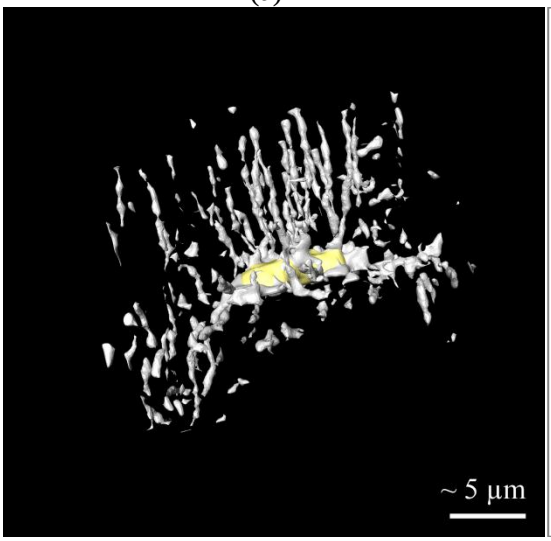

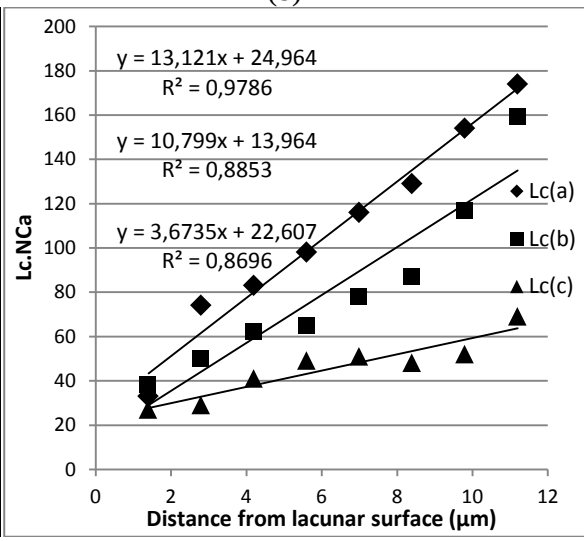

(c) (d)

Figure 7.6 3D renderings of three isolated lacunae cropped from the segmented image. (a) A lacuna with 98 canaliculi counted at 5.6 µm to surface of lacuna. (b) A lacuna with 49 canaliculi counted at 5.6 µm to surface of lacuna. (c) A lacuna on the boundary of the osteon with only 49 canaliculi counted at 5.6 µm to surface of lacuna. (d) Plots of the number of canaliculi calculated at eight different distances from the surface of the three selected lacunae.

Table 7.1 Histomorphometry parameters of the bone tissue from the human femoral sample

N.Lc	Lc.TV ($\times 10^{-5}$ mm^3)	BV ($\times 10^{-3}$ mm^3)	TV ($\times 10^{-3}$ mm^3)	BV/TV (%)	HCa.V/TV (%)	Lc.TV/BV (%)	Lc.TV/TV (%)	N.Lc/BV (mm^3)	N.Lc/TV (mm^3)
399	8.63	12.39	12.85	96.4%	3.6%	0.70%	0.67%	32200	31042

N.Lc – number of osteocyte lacunae
Lc.TV – total lacunae volume (mm^3)
BV – bone volume (mm^3)
TV – tissue volume (mm^3)
BV/TV – bone volume fraction (%)
HCa.V/TV – canal volume fraction or bone porosity (%)
Lc.TV/BV and Lc.TV/TV– lacunar volume density (mm^{-3})
N.Lc/BV and N.Lc/TV– lacunar number density (mm^{-3})

Table 7.2 Osteocyte lacunar descriptors from the human femoral sample

	Lc-Lc (µm)	Lc.V (µm^3)	Lc.S (µm^2)	Lc.L1 (µm)	Lc.L2 (µm)	Lc.L3 (µm)	Lc.L1/Lc.L2	Lc.L1/Lc.L3	Lc.SMI
mean±std	23.3 ± 5.2	229.1 ± 81.1	248.5 ± 66.5	15.5 ± 3.8	8.0 ± 1.8	4.1 ± 1.0	2.1 ± 0.7	4.1 ± 1.6	3.2 ± 0.2
[min, max]	[10.4, 39.8]	[52.8, 611.9]	[87.2, 883.3]	[7.4, 49.7]	[3.8, 14.5]	[2.3, 7.0]	[1.1, 4.5]	[1.4, 11.0]	[2.5, 3.7]

Lc-Lc : nearest distance between two lacunae (µm)
Lc.V – lacuna volume (µm3)
Lc.S – lacuna surface area (µm2)
Lc.L1, Lc.L2 and Lc.L3 – length, width and depth of lacuna (µm)
Lc.L1/Lc.L2 and Lc.L1/Lc.L3 – anisotropy of lacuna
Lc. SMI – structural model index of lacuna

Table 7.3 Number of canaliculi per lacunae at different distance from the surface of lacunae

	Lc.NCa r=1.4 µm	Lc.NCa r=2.8 µm	Lc.NCa r=4.2 µm	Lc.NCa r=5.6 µm	Lc.NCa r=7.0 µm	Lc.NCa r=8.4 µm	Lc.NCa r=9.8 µm	Lc.NCa r=11.2 µm
mean±std	41.5 ± 16.0	58.2 ± 22.5	69.5 ± 24.7	77.5 ± 27.9	88.0 ± 33.6	99.9 ± 39.4	117.9 ± 46.6	139.1 ± 55.3
min, max	[5, 136]	[3, 177]	[1, 192]	[3, 209]	[3, 221]	[11, 262]	[19, 328]	[34, 292]

Lc.NCa – number of canaliculi per lacunae (#)

7.4 Discussion

In this paper, we proposed a technique to automatically calculate LCN descriptors from a segmented 3D SR micro-CT image. An original method to assess the ramification pattern of the canaliculi was proposed based on mathematical morphology operators and the Euler

number. It consists in counting the numbers of canaliculi per lacunae at different distances. Conversely to a method that would try to identify each node of the canaliculi network, this method has the advantage to be more flexible to imperfections in segmentation which are unavoidable with the limited spatial resolution compared to the canaliculi size.

The estimation of the numbers of canaliculi per lacunae was checked on a simple phantom and a complete lacuna with fully interconnected canaliculi. Then, this method was applied to a larger experimental image of human bone tissue.

This is the first time that the numbers of canaliculi at different distances are measured in 3D. We have extracted these measurements on several hundreds of cells in human femoral bone. Traditional investigations are based on 2D histological sections analyzed manually. Compared to the extrapolation of 2D measurements to 3D, the present method does not require any assumption on idealized lacuno-canalicular models. Thus this method is expected to yield unbiased parameters. Since the method is fully automated, it can be applied to bone samples within large field of view including several osteons.

The statistical results have been given on a total number of 240 lacunae, after excluding boundary lacunae. Keeping all lacunae would provide biased results due to truncation and we experimentally found that it had more impact on the descriptive values of the canaliculi. The average number of canaliculi near the surface of lacunae is in agreement with the results published by Beno[Beno *et al.* (2006)] who reported an estimated 3D number of canaliculi of 41 in human bone. The low and high estimates are also consistent with Beno's work. In a more recent work, the number of canaliculi per lacuna was calculated from confocal microscopy images on a limited depth of 25 µm [Sharma *et al.* (2012)]. The authors reported about 85 primary and 387 secondary canaliculi per lacuna on rats' tibial metaphysis. These higher numbers can be explained by differences in method, species and bone site. In our method, the various dilation parameters permitted to put in evidence the increased branching of canaliculi with the radial distance to the lacuna. Our results clearly indicate an increase of the number of canaliculi with the distance to the lacunae. In addition, for most lacunae, this increase could be explained by a linear regression between the number of canaliculi and the distance suggesting the bifurcation of the canaliculi.

The results strongly rely on image segmentation which itself is dependent of the quality of the acquired images. Further advances in optimizing the imaging technique may improve image quality, while progress in the segmentation methods would reduce noise and improve the connectivity of the lacuno-canalicular network. Although the numbers of canaliculi that we found are realistic, it is difficult to evaluate the method due to the lack of comparison data and due to the complexity of the network. These preliminary observations need to be confirmed by further works.

The presented method has the advantages of producing 3D measurements in an automated and model independent manner. We believe that this can contribute to improving our knowledge on the LCN. Furthermore, future work will also be pursued to extract additional characteristics of the LCN, such as the canaliculi length and the canaliculi density per each lacuna.

Chapter 8

Segmentation and quantification of the LCN in a series of human tibial samples

Contents

8.1 Introduction 109

8.2 Samples and image acquisition 110

8.2.1 Sample description and preparation 110
8.2.2 Synchrotron radiation microtomography (SR-µCT) at 3.5 µm 111
8.2.3 Synchrotron radiation microtomography (SR-µCT) at 300 nm 113

8.3 Segmentation and quantification method 113

8.3.1 Background on minimal path extraction through geodesic voting 113
8.3.2 Workflow of the segmentation method 114
8.3.3 Input volume 115
8.3.4 Bone volume and lacunae segmentation 115
8.3.5 Lacunae tessellation 116
8.3.6 Candidate paths extraction via minimal path extraction and geodesic voting 116
8.3.6.1 Start- and end-points 116
8.3.6.2 Potential function 117
8.3.6.3 Geodesic voting 117
8.3.7 Acceleration of the algorithm 117
8.3.8 Post processing: maximum rank filter 119
8.3.9 Enhancement of canaliculi pathways 119
8.3.10 Normalization and thresholding 120
8.3.11 Quantification 120

8.4 Selection of the parameters in the segmentation method 121

8.4.1 Comparison between the reconstructed SR micro-CT images 121
8.4.2 Manual Segmentation 123
8.4.3 Automatic segmentation 125

8.5 Application to human tibial SR micro-CT images 130

8.5.1 Selection of regions of interest 130
8.5.2 Parameters of the lacunae segmentation method 130

8.5.3 Histomorphometry parameters of the tibial tissues 131
8.5.4 Morphological descriptors of the osteocyte lacunae 133
8.5.5 Ramification of the canaliculi..... 136
8.6 Discussion and conclusion.....139

8.1 Introduction

SR micro-CT has been demonstrated as a truly 3D imaging technique suited for imaging the complex LCN at different scale in chapter 5. Using the parallel beam SR micro-CT at the ID19 experimental station of the ESRF, with the setup of 300 nm spatial resolution, the reconstructed images allow to visualize both lacunae and canaliculi, while containing a relatively large field of view, about $(600\ \mu m)^3$. The imaged volume may include up to several hundred of cells. In the chapter 6, we have reported an automated method to characterize the density and morphology of lacunae based on the micro-CT images. In chapter 7, new parameters have been proposed to quantify the canaliculi network but the method has been applied to a single image. In this chapter, the goal was to quantify the LCN on a series of human samples of different ages acquired at 300 nm.

Although the previously proposed method opens the possibility to a true 3D assessment of the number of canaliculi per each lacuna, the statistical result is largely dependent on the accuracy of the binarized canaliculi structure. The segmentation of the LCN is a challenging problem when working with images at 300nm since the width of canaliculi is close to the image spatial resolution. The canaliculi appear as thin structures (1-3 voxel width) that are severely affected by partial volume effects and by a limited signal to noise ratio, making their segmentation difficult. In addition, the complexity of the structure to be segmented and the huge amount of data that needs to be processed, restrain user interaction.

In previous works, Pacureanu used a "vesselness" filter [Frangi *et al.* (1998)] to enhance tubular structures, followed by a variational region-growing (VRG) process [Pacureanu *et al.* (2010)]. In a subsequent work [Pacureanu *et al.* (2011)], a similar "vesselness" filter [Sato *et al.* (1998)] was combined to a level-set based segmentation algorithm to extract the LCN network. Both methods are strongly affected by partial volume effects which generate problematic issues, since both the region growth and the surface evolution tend to stop wherever the canaliculi intensity strongly drops due to partial volume. However, so far, no other methods have been proposed in the literature to solve these issues.

Nevertheless, we may consider the works done in the context of vascular segmentation, although the scale, the image characteristics and the prior on the structure are different. In this domain, geodesic voting methods [Rouchdy *et al.* (2008), (2009), (2011), (2013)] and several related studies [Li *et al.* (2007); Benmansour *et al.* (2011)] possess attractive properties to track vascular structures but have still mainly be applied to 2D images. In a recent work, a 3D approach based on minimum cost paths and geodesic voting has been proposed to segment the LCN and improve its connectivity [Zuluaga *et al.* (2011), (2014)]. However, at this stage, this method suffers from a number of limitations that does not make in applicable to a whole image.

First, the proposed method consumes a huge computational cost. Second, using the minimum-cost paths, the canaliculi pathways can be always traced despite of the real existence of the canaliculi. Therefore, some artificial canaliculi pathways can be also segmented. Third, although the minimum cost path guarantees the connectivity of the traced pathways, the simple thresholding applied to the geodesic voting map may generate discontinuities in the canalicular segmentation, due to the variation of the back propagated

pathways. Fourth, this method was only validated on very small regions of interest, containing very few lacunae (1 to 4). Nevertheless, a clear improvement in the segmentation results was observed compared to the previous ones, since a larger number of segmented canaliculi were obtained with a better preservation of their connectivity, highlighting its potential for segmenting the LCN.

Although it was not the original focus of our work, it was thus necessary to improve this method in order to apply it to a series of images. It was thus necessary to speed up the computation, to analyze the results of the algorithm and to propose solutions to improve the results trying to avoid artificial canalicular pathway and to improve the connectivity of the binary canaliculi image. Concerning quantification, we also introduce here a variant of the method presented in chapter 7 to analyze the number of canaliculi only within each lacunar territory defined through Voronoi Tesselation. Then, we present the application of the entire workflow, including segmentation and quantification, on a series of 8 human tibial samples to demonstrate the feasibility of the proposed method. We may note that there are no equivalent results on this topic so far in the literature.

The remainder of this chapter is organized as follows. Section 2 provides a description of the samples and imaging procedure. Section 3 describes the entire workflow to segment and quantify the LCN. Section 4 presents and evaluates the experimental conditions that were selected to apply the method, whereas Section 5 presents the obtained results on selection regions of interest in 8 human samples. Finally, section 6 is devoted to the discussion of the results and the conclusions of this work.

8.2 Samples and image acquisition

8.2.1 Sample description and preparation

Human cortical bone specimens were prepared from the tibial mid-diaphysis, 3 specimens from 3 female donors (with age of 46 years, 84 years and 87 years) and 5 specimens from 4 male donors (with age of 29 years, 56 years, 88 years and 89 years). The specimens were provided by G Kazakia from the group of S Majumdar at the University of California, San Francisco. For each sample, a three centimeters length of bone was first extracted (by hand saw) from mid-diaphysis of tibia. Then, specimens were wet machined (a rotary diamond blade precision cutting tool) as four to six cylinders (4.2 mm in diameter and 4 mm in height), with long axis of cylinder along the axis of the bone. The best cylinder that does not break through periosteal surface was kept, others discarded. In all cases, specimens spanned the entire width of the cortex (from periosteal to endosteal). Then, the specimens were kept frozen at -20°C until the low resolution imaging experiment.

To image the specimen at higher resolution (300 nm), we had to machine smaller samples. The goal was to obtain nearly rectangular parallelepiped with a cubic section of about 600µm, which requires a delicate handling of the sample. To do so, the cylindrical specimens were wet cut using a wire saw at the SIMAP lab (INP Grenoble). The protocol required several cuts which are summarized in Figure 8.1. The smaller samples, denoted from A to F, were about $2\times0.6\times0.6$ mm^3 and were suited for imaging at 300nm. It also provided different subsamples

adapted to different imaging scales. Before cutting, the entire samples were imaged at 3.5 µm. The "Top, 2nd half" samples were used for imaging at 1.4 µm. All samples were kept frozen at -20°C until the imaging experiments.

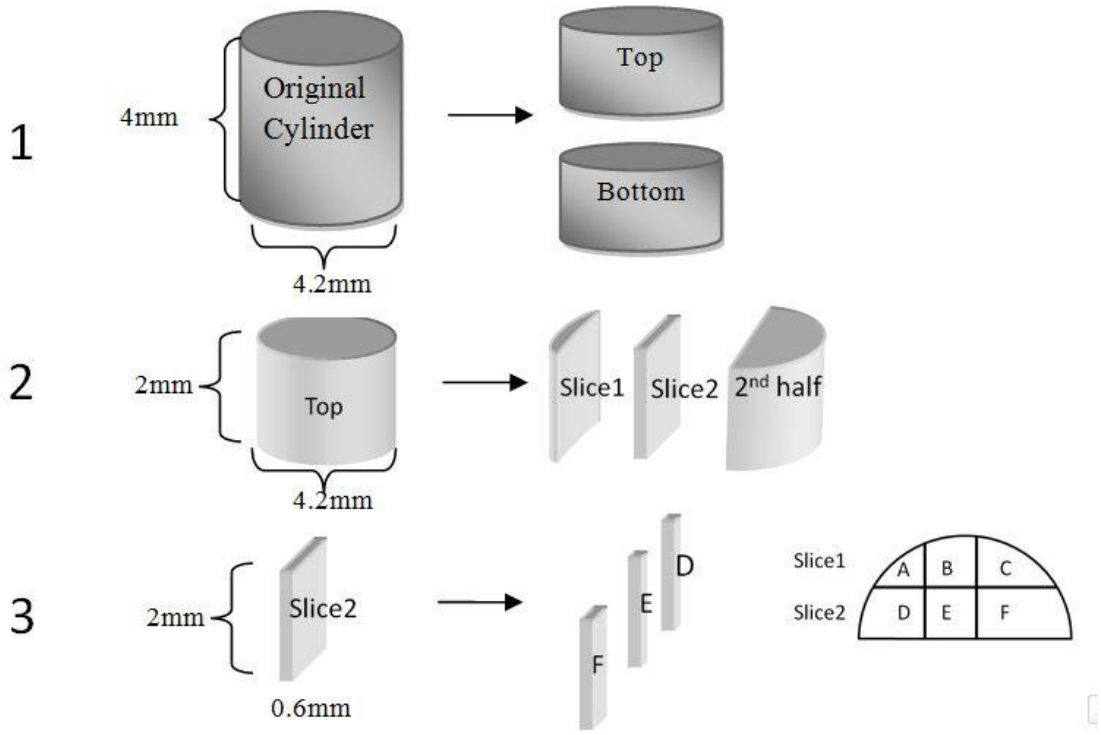

Figure 8.1 Sample preparation scheme for high resolution imaging. The detailed label name of smaller cut specimen, please refer to the annex 1.

8.2.2 Synchrotron radiation microtomography (SR-µCT) at 3.5 µm

The specimens were first scanned at a lower resolution (3.5 µm) providing a field of view of 7×7×4 mm^3 in the aim of acquiring an overview of the inner structure. Therefore, a proper region of interest for the high resolution (300 nm and 50 nm) imaging can be subsequently selected. With this aim, we chose to use phase contrast imaging at high energy to minimize the radiation dose to the specimens since the same samples will be further imaged at higher spatial resolution.

The low resolution SR micro-CT scans were performed on beamline BM05 at the ESRF (European Synchrotron Radiation Facility, Grenoble, France). A pink beam with a mean energy of 70 keV was used. For each sample, 2500 projection images were recorded over a total angle of 360° at a single sample to detector distance of 5 cm. The 3D image was reconstructed by a filtered back-projection algorithm after applying Paganin's phase retrieval method. For the delta/beta ratio in Paganin's algorithm was set to 153.8, calculated by taking into account bone XOP 2.1 software (ESRF).

The reconstructed volume is 1500×1500×1500 voxels, which corresponds to a physical size of 5.3 mm×5.3 mm×5.3 mm (voxel size 3.5µm). In addition to low dose scanning, another

advantage of using phase images is that the contrast between osteons and interstitial tissue is improved. Figure 8.2 illustrates three reconstructed slices from the three different aged specimens. The light gray part of the images corresponds to mineralized cortical bone. The black pores are cross sections of Haversian canals and Volkmann's canals. Figure 8.2 (d) shows a zoom around several osteons, where the very small black cavities (with few voxels) scattered around the Haversian canal on the gray background are osteocyte lacunae.

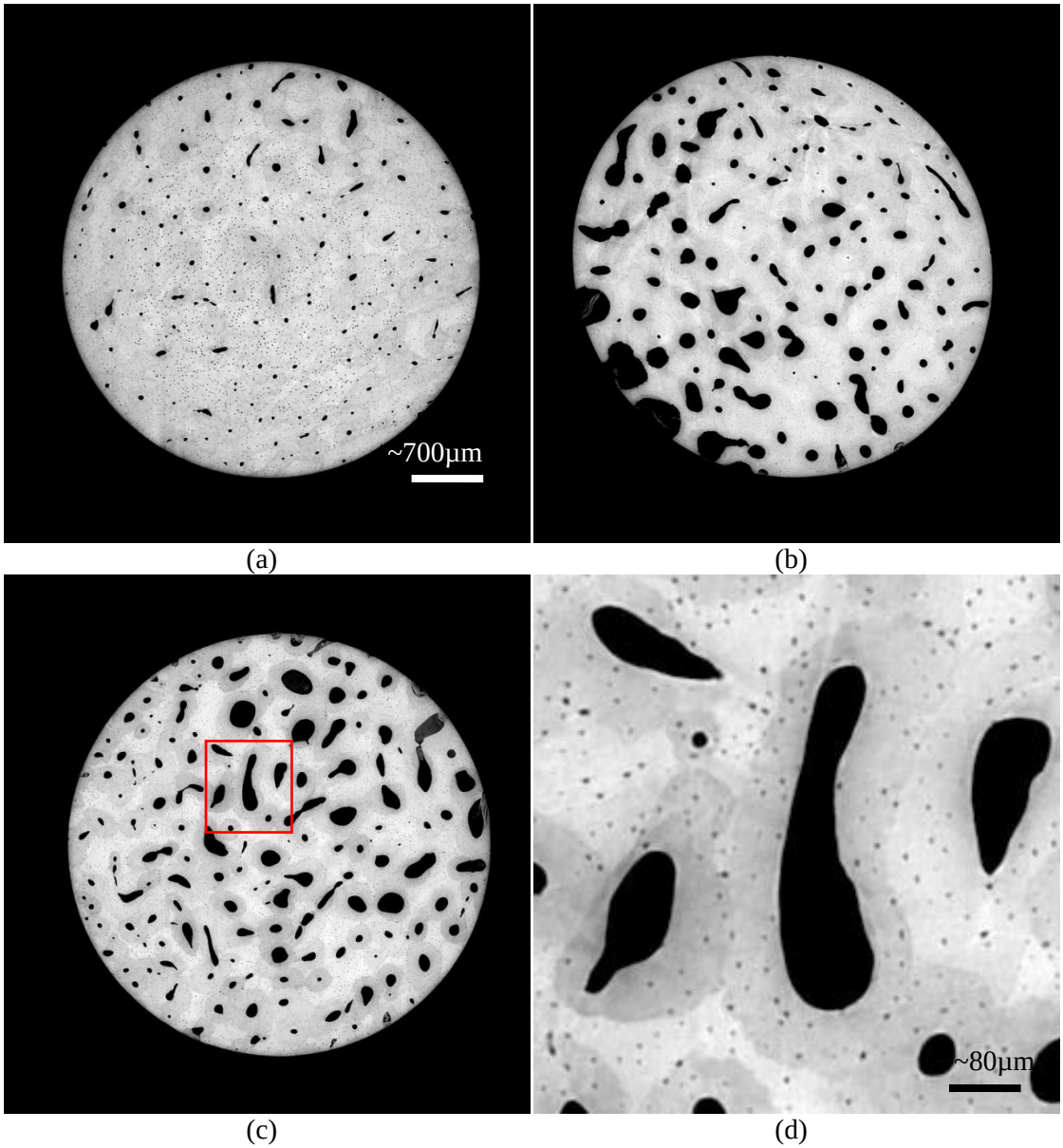

Figure 8.2 Slices of reconstructed image from SR-CT with voxel resolution of 3.5 µm (image size: ~1500×1500 pixels). (a) From a male specimen with age of 29. (b) From a male specimen with age of 56 (c) From a male specimen with age of 88 (d) Zoom of (c) around several osteons

8.2.3 Synchrotron radiation microtomography (SR-µCT) at 300 nm

SR micro-CT at high spatial resolution (300 nm) was performed on beamline ID19 at the ESRF (European Synchrotron Radiation Facility, Grenoble, France). The experimental setup, image reconstruction and the artifacts elimination were elaborated in section 5.5.1.

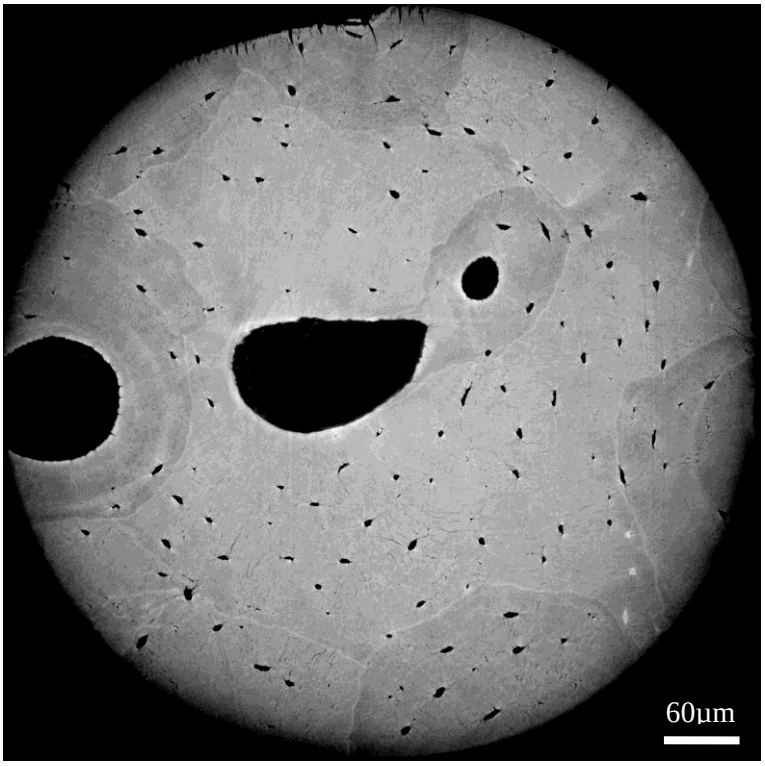

Figure 8.3 a slice of the reconstructed image based on single distance Paganin phase retrieval process

8.3 Segmentation and quantification method

8.3.1 Background on minimal path extraction through geodesic voting

The goal of this work is to enable the biologists to quantitatively assess the 3D organization of the LCN using SR nano-CT images. We focus on detecting canaliculi with the aim to avoid disruptions in the LCN rather than on accurately extracting the boundaries of the canaliculi and lacunae. As canaliculi are thin thread-like structures, the thickness of which is hardly larger than the voxel size, a pathway extraction approach seems to be a good candidate to segment them. To take advantage of the intrinsic benefits of minimum cost path techniques, such as discontinuity avoidance we use the approach based on minimum cost paths and geodesic voting [Rouchdy *et al.* (2008), (2009), (2011), (2013)]. We recall the basic principle of this approach.

The minimal path approach as formulated by Cohen and Kimmel [Cohen et al. (1997)] seeks the curves of minimal length in the Riemannian space, given an isotropic metric. The weighted length L of the path C between points **a** and **b** is defined as follows:

$$L(C) = \int_a^b (w + P(C(s)))ds \tag{8.1}$$

where *s* is the arc length, *w* is a regularization term and *P* is the potential function defining a metric. Given a start-point **a** and an end-point **b**, the minimal path approach determines a global minimum of an energy function. The minimal action map U, which corresponds to the minimal cost integrated between the start-point **a** and any point in the image, satisfies the Eikonal equation $|\nabla U| = w + P$. To solve this equation, a front is propagated in the image domain, from the start-point **a**, using the Fast-Marching algorithm [Sethian (1996)]. Afterwards, back-propagation [Cohen *et al.* (2001)] is used to extract minimal paths C_k that connect the end-points $\mathbf{b_k}$ back to the start-point **a**. In the seminal work on geodesic voting, [Rouchdy *et al.* (2008)] designed a geodesic voting score $g(\boldsymbol{x})$ of a voxel **x** in the image domain, as follows:

$$g(\boldsymbol{x}) = \sum_{\mathrm{k}=1}^{\mathrm{K}} \delta_{\mathrm{p}}(\mathrm{C_k}) \tag{8.2}$$

where K is the number of extracted paths, $\mathrm{C_k}$ the extracted path and $\delta_{\mathrm{p}}(\mathrm{C}) = 1$, if the path *C* crosses the voxel **x,** and $\delta_{\mathrm{p}}(\mathrm{C}) = 0$, otherwise. Voxels with a high geodesic voting score $g(\boldsymbol{x})$, are kept while the others are rejected. In the original formulation, a fixed threshold $T_\mu = \hat{g}/100$ was used [Rouchdy *et al.* (2011)], where $\hat{g}$ is the maximum geodesic voting score encountered in the image.

8.3.2 Workflow of the segmentation method

Selecting the start and end points has been done via user interaction in previous works where the goal was just to segment a given path. Since there are on the order of 10^5 canaliculi per mm^3, there is no way to base our procedure on user interaction. Thus it is required to develop a fully automatic scheme starting from the original image. To this aim, we propose to use our prior information on the LCN. As we know that canaliculi are radiating from lacunae, we propose to use as starting points **a,** the centroids of lacunae. Points located at the boundary of a bounding box around each lacuna could be used as end points. However, this process has to be adaptive in some sense and take into account the information about the neighboring lacunae. For this purpose, we introduce a partition of the image such that each region contains one and only one lacuna. A Voronoi-tessellation performed on the lacunae centroids is a good candidate to perform this partition. For each lacuna, points distributed near the boundaries of each Voronoi cell are used as end points. Such a spatial distribution of the end-points was devised to favor the convergence of the paths towards the canaliculi that are expected to interconnect the lacunae and so to cross the Voronoi-region boundaries. The whole initialization scheme was designed to cope with complex biological structures involving cells interconnected by multiple thread-like, branching processes.

The whole segmentation work flow is presented in Figure 8.4. The mask generation step allows extracting bone versus background. In the two next steps, lacunae are segmented and labeled. Then lacunae tessellation refers to the 3D Voronoi tessellation obtained starting from the lacunae centroid seeds. The next step is the candidate paths extraction by minimal path extraction and geodesic voting. Compared to the initial work, several improvements (yellow parts in Figure 8.4) have been made: 1) choice of the input image; 2) acceleration of the computation of the 3D geodesic voting; 3) post-processing of the geodesic voting volume by

maximum rank filter and 4) enhancement of canaliculi pathways.

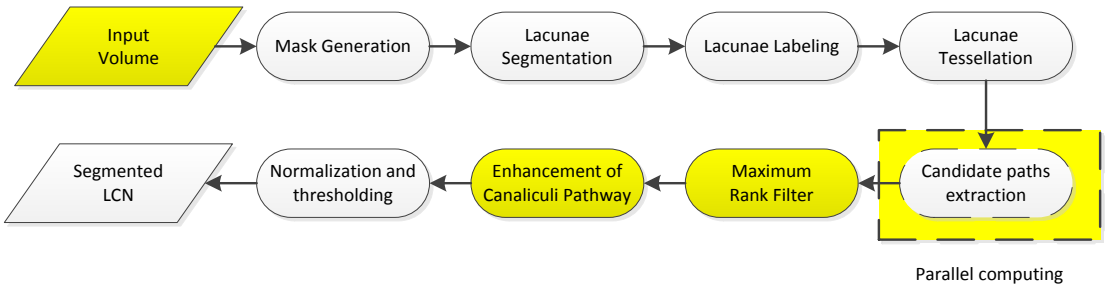

Figure 8.4 work flow of LCN segmentation

8.3.3 Input volume

The input volume of the segmentation work flow (Figure 8.4) is the reconstructed 3D image. At ESRF, using the PyHST reconstruction software, the volume can be reconstructed either by a standard filtered back-projection (FBP) algorithm, or by including a single distance phase retrieval process prior to FBP. The latter method can be used since at very high resolution (300 nm), phase contrast appear in the image at sample to detector distances as small as a few mm. Using the most appropriate reconstructed volume can be important with respect to the final segmentation result. In general, in bone studies aiming at the quantification of the degree of the mineralization of bone, the standard reconstruction volume is used. It is because, in monochromatic X-ray beam CT, the gray level of each voxel in the reconstructed image, reflecting the linear attenuation coefficient, is directly related to the degree of mineralization of the specimen. When phase CT is used, the reconstructed image is related to the phase index decrement which is 2 orders of magnitude higher that the linear attenuation coefficient. It is why the reconstructed volume based on phase retrieval algorithms can greatly enhance the contrast between the osteon and interstitial tissue. In addition it is known that phase contrast method can enhance the visibility of subvoxel structures. Besides, the parameter delta/beta acts as a low pass filter in the reconstruction process, therefore the signal to noise ratio (SNR) in the phase retrieval volume is expected to be higher than the normal reconstructed volume. This characteristic can be a great advantage for the “vesselness” filter to enhance the canalicular structure. Thus, in this work, the 3D single-distance phase CT image was used as input volume to the segmentation process.

8.3.4 Bone volume and lacunae segmentation

The segmentation of the bone volume and the lacunae from the 3D single-distance phase CT image are straightforward. Considering the size of the 3D SR micro-CT image (2048×2048×2048 voxels), the segmented bone volume is used as a image mask to avoid unnecessary computation in the areas that are not of interest. Since the features in the LCN are much smaller than that in the Haversian canal, a median filter with a radius comparable to the size of lacunae was applied to fill the LCN cavities, while preserving the Haversian canals. Then, the bone mask was obtained by applying Ostu thresholding. Similarly, by filling the

canaliculi cavities, using a median filter with a radius comparable to the size of canaliculi on the original reconstructed volume, the lacunae can be easily segmented within the region of bone volume, due to the high contrast between the lacunae and bone matrix. After this step, each lacuna is labeled using a connected component analysis.

8.3.5 Lacunae tessellation

In order to use the geodesic voting method to segment the tree-like structures (canaliculi), we propose to subdivide the image volume into small volume of interest (VOI), each of them containing one lacuna with its stellated canaliculi.

After connected component analysis, a set of lacunar centroids was computed. This set can be written as $\boldsymbol{A} = \{\boldsymbol{a}_i \mid i = 1, 2, \ldots, N_A\}$, where N_A is the total number of segmented lacunae and $\mathbf{a}_i$ is the centroid of the i^{th} labeled lacuna. The points in $\boldsymbol{A}$ are then used as seeds for a Voronoi tessellation. Let $\Gamma = \{\gamma_i | i = 1,2, \ldots, N_A|\}$ be the Voronoi diagram of the point set $\boldsymbol{A}$, where cell γ_i is a region containing only one lacuna with a centroid $\mathbf{a}_i$. A voxel $\mathbf{x}$ is said to belong to a cell $\gamma_i \in \Gamma$, if and only if $\|\mathbf{x} - \mathbf{a}_i\| \leq \|\mathbf{x} - \mathbf{a}_j\|$, for all $\gamma_i \in \Gamma, j \neq i$. Voxels that build up a particular cell are those whose distance to the contained lacuna is minimal. Figure 8.5, left illustrates a slice in the 3D Voronoi tessellation of the SR micro-CT image of a bone sample, and right is a zoom on a few Voronoi cells.

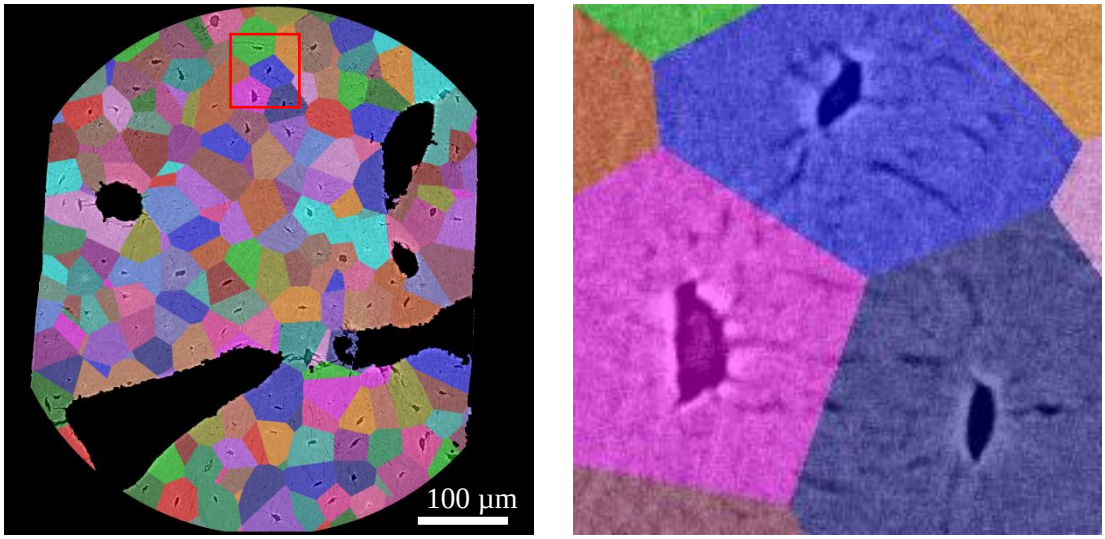

(a) (b)

Figure 8.5 A slice of 3D Tessellated image. The zones in black are those suppressed by the bone volume mask. (a) A slice of the tessellated image of the entire sample. (b) Slice of the tessellated subvolume zoom in from the red square on the left image.

8.3.6 Candidate paths extraction via minimal path extraction and geodesic voting

8.3.6.1 Start- and end-points

To segment the stellated canaliculi using geodesic voting method, the start- and end-points need to be placed automatically. As explained above, we used as start points, the lacunar centroids, *i.e* the set $\boldsymbol{A}$ defined in the previous step. Considering the location of the end points,

a first thought was to use the points on the border of each Voronoi cell γ_i. However, to obtain a high voting score on the path of canaliculi, and to avoid the problems at the frontier between two Voronoi cells, we used an extented VOI denoted $D_r(\gamma_i)$. It was built by dilating the corresponding Voronoi cell γ_i using a ball-shaped structuring element. The radius r of the structuring element was selected to allow achieving large geodesic voting score, Equation (8.3). The set $\boldsymbol{B_i}$ of end-points associated to each lacunae centroid $\mathbf{a}_i$ was then defined by evenly subsampling the surface of the extended VOI $D_r(\gamma_i)$.

$$D_r(\gamma_i) = \oplus_r \gamma_i \tag{8.3}$$

8.3.6.2 Potential function

For the minimum-cost path extraction, a potential image P is required by the fast-marching algorithm. Here, we propose to use the "vesselness" image, serving as the potential image P. The "vesselness" image is calculated from a nonlinear filtering of the original image to enhance tubular structures in the image. The filter is designed by eigenvalue analysis of the local hessian matrix and several formulations proposed by Frangi and Sato [Frangi *et al.* (1998); Sato *et al.* (1998)], and respectively used in the previous segmentation work [Pacureanu *et al.* (2010), (2011)].

8.3.6.3 Geodesic voting

The 3D geodesic voting is applied separately on each VOI $D_r(\gamma_i)$, using the voxels $b \in \boldsymbol{B_i}$ as the end-points to extract minimal paths to the corresponding lacunar centroid $\mathbf{a}_i$. The principle was introduced in section 8.3.1.

8.3.7 Acceleration of the algorithm

Dealing with very large 3D images, the segmentation work flow consumes a tremendous computational cost and considerably a long time to calculate. The most time consuming part of the work flow lies in 3D geodesic voting. For example, using "jupiteros2" (work station equipped with Intel® Xeon® CPU E5530 2.40GHz), it took about 30 s to trace from one end point to the start point. Considering that there are about 1000 end points per VOI, the workload to perform the geodesic voting on one lacuna, it will take about 8 h30 min to finish the process. Therefore, on a single reconstructed volume (600 µm)^3, which contains up to 4000 lacunae (about 20,000 lacunae/mm^3 in human bone), it would take 34,000 hours; *i.e.* 4 years to finish the task! Obviously, to make the algorithm usable for the automatic segmentation on series of large 3D images, a faster implementation is requested.

To reduce the computation time, one of the solutions is to use parallel computing. The parallel computing has become the dominant paradigm in computer architecture, mainly in the form of multicore processors. The parallel computing allows the computation to be carried out simultaneously, based on the principle that large computation workload can be broken into parts, which can be solved concurrently.

The OpenMP is a nonprofit application program interface (API), which supports multi-platform (Linux, Mac OS and Windows) in C, C++ and Fortran. The OpenMP is implemented based on principle of multithreading. It is a parallelizing method whereby a master thread

forks a specified number of slave threads and a task is divided among them. The threads then run concurrently, allocating threads to different processors.

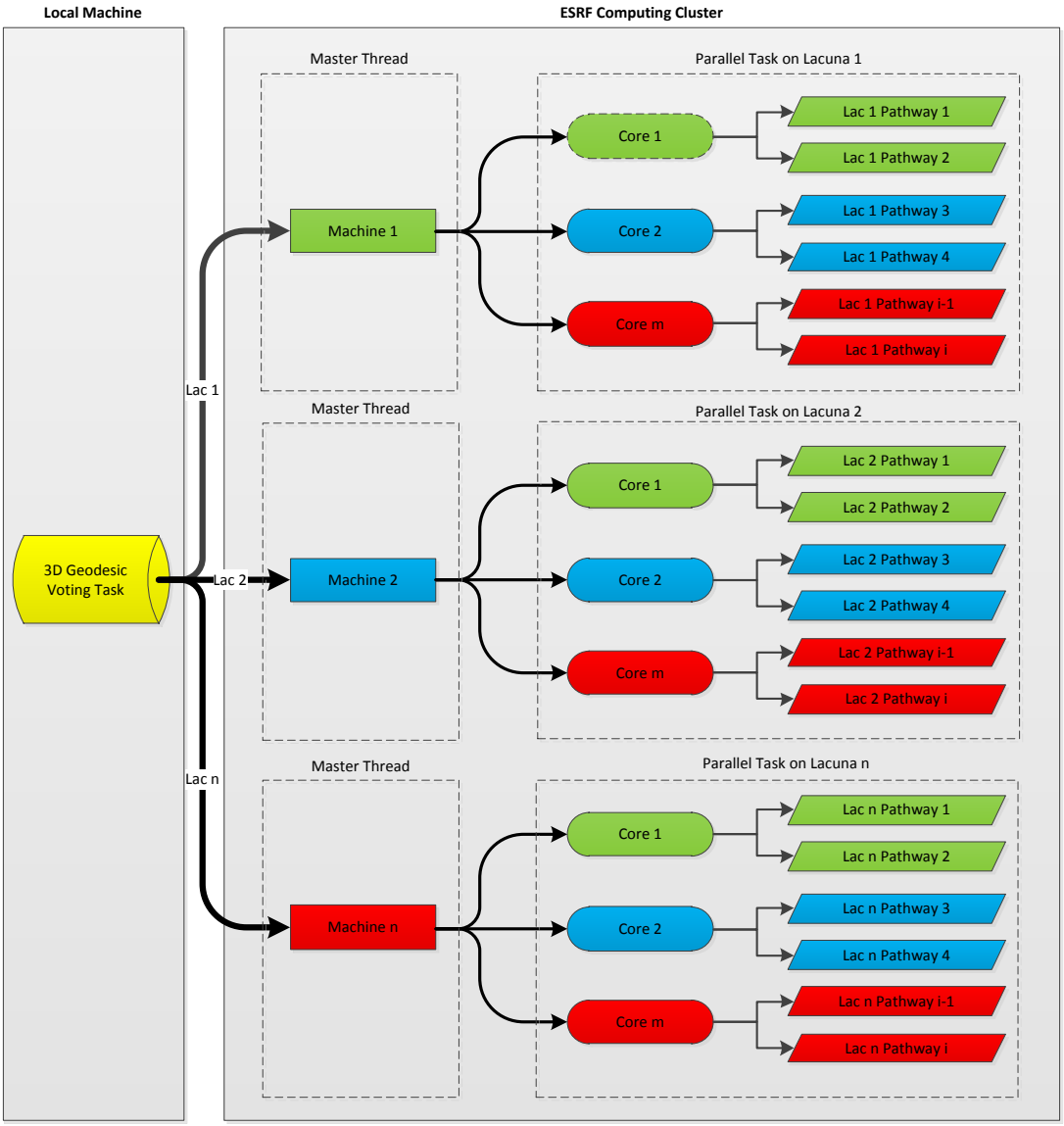

Figure 8.6 Illustration of the parallel computation scheme on 3D geodesic voting process

To compute the 3D geodesic voting on the large 3D image, two parallel schemes were used in our implementation, illustrated by Figure 8.6. First, by dividing the whole 3D image into numbers of the lacunar territory subvolumes, we distributed each calculation task on each subvolume to a single machine on a computing cluster. After processing, these subvolumes will be merged together to re-form the entire volume. Second, we employed the OpenMP in our implementation to master the distribution of each pathway tracing on the cores of the processor. Since each core of the processor can handle multiple threads by means of time-division multiplexing controlled by OpenMP API, the total number of the parallel jobs (N_j) is

determined by the number of machines used in the cluster (N_m) and the number of cores of each machine (N_c):

$$N_j = N_m \times N_c \tag{8.4}$$

8.3.8 Post processing: maximum rank filter

Ideally, after the geodesic voting, the paths converging to lacunae should follow the same route until reaching to the centroid of the lacuna. However, as we observed, that was not always the case in practice. The geodesic paths, after converging together, can chose different but similar routes to back-propagate to the lacunar gravity center. These different routes are weaved tighter in the canaliculi tunnel, as it can be observed in Figure 8.7, showing a disordered color pattern inside the canaliculi. Therefore, the direct thresholding of the geodesic voting image could introduce discontinuities in the binary canalicular path.

To improve the result of the geodesic voting, we propose to use a maximum rank filter applied to the geodesic voting image. For each non-zero voxel in the geodesic voting image, a local gray-level histogram is calculated on its m×m×m neighborhood. Then the current voting score of the voxel is replaced by the maximum value of the histogram. The size of the neighborhood n was selected to improve the geodesic voting path.

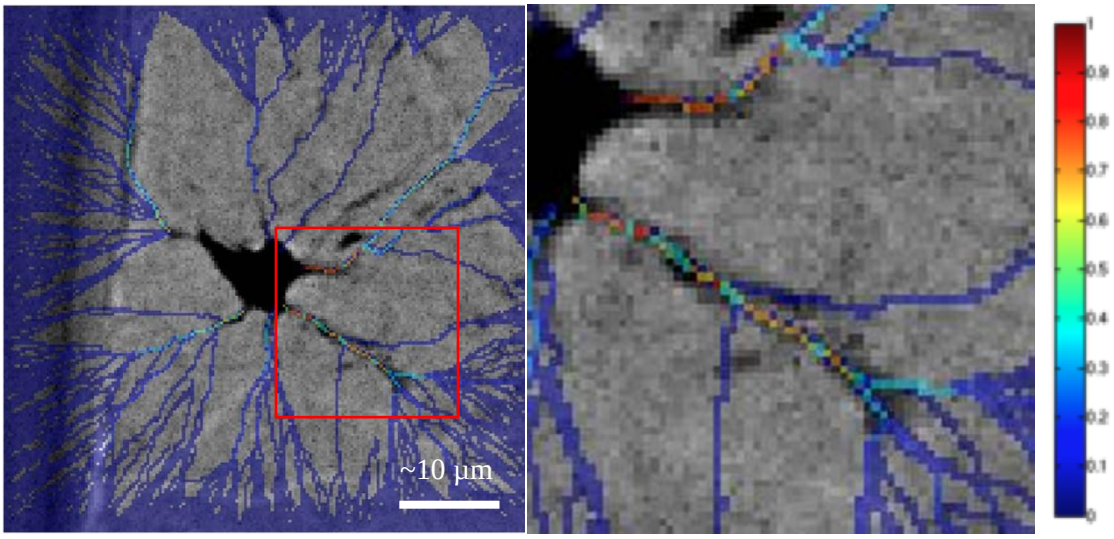

(a) (b)

Figure 8.7 illustration of the variation of the extracted path using geodesic voting (image from [Zuluaga *et al.* (2011)]). (a) MIP view of the extracted geodesic paths superposed onto a minimal intensity projection of the image. (b) a zoom on the extracted path

8.3.9 Enhancement of canaliculi pathways

Another drawback that we observed in running the original version was that the method can create "surplus pathways", by which we mean pathways extracted in regions where visual evidence to support the presence of canaliculi is missing. Our solution that we propose for this problem is to weaken the voting value on the "surplus pathway", while increasing the voting

value on the "real pathway". To this aim, we re-introduce the "vesselness" image as our prior knowledge. The process is summarized in Figure 8.8.

The idea is to improve initial path candidates which are obtained as follows. The geodesic voting image obtained after the maximum rank filter image described above is thresholded with a low threshold to select a maximum of pathways. Remember that the values of the geodesic voting map represent the number of paths crossing a given voxel. To keep as many paths as possible, we thus used a threshold of 2 (T_g=2). The next step is to label these paths. However since they are all connected to the lacunae, we first eliminate the lacunae by using as a mask the negative of the lacunae image which was calculated as step 2 in the geodesic voting method. Then, a connected component analysis is applied to this image, resulting in the labeled paths image, used as input of the workflow described in Figure 8.8.

The second step consists in combining this image with the vesselness map in order to re introduce the tubularity information and have a better control if a path is likely to be a canaliculi. For this purpose, a weight is assigned to each labeled path component. This weight is equal to the average value of the vesselness map on this component. This provides the weighted paths image.

Finally, the weighted paths image is multiplied with the geodesic voting image after the maximum rank filtering to obtain the modified geodesic voting image ($g_i(\boldsymbol{x})$).

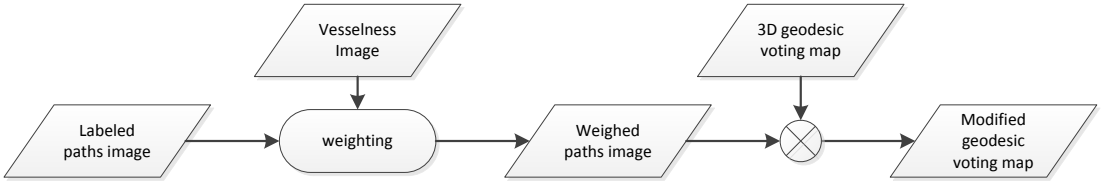

Figure 8.8 Illustration of the "enhancement of canaliculi pathways" step

8.3.10 Normalization and thresholding

The last step of the segmentation is a thresholding procedure based on normalization of the modified geodesic voting image.

Here, we normalize the geodesic voting score by the maximum value $\widehat{g_i}$ encountered in the image portion corresponding to a starting point $\mathbf{a}_i$. If **x** in a voxel corresponding in the extended Voronoi cell $D_r(\gamma_i)$. the normalized geodesic voting image will be :

$$G_i(\boldsymbol{x}) = g_i(\boldsymbol{x})/\widehat{g_i} \tag{8.5}$$

Then, the actual segmentation of the canaliculi is obtained by thresholding the voting scores. The threshold parameter $T_{G_i} \in (0,1)$ can be tuned simultaneously for all the VOIs and the voxels with $G_i(\boldsymbol{p}) > T_{G_i}$ are kept. Once each lacuna and its surrounding canaliculi are segmented independently, the segmented pieces are merged into one single image.

8.3.11 Quantification

After the segmentation process, both the images of lacunae and canaliculi can be quantified separately. Thus the methods presented in chapters 6 and 7 were applied to extract the

quantitative parameters on both lacunae and canaliculi. Apart from the previously defined parameters, more parameters related to canaliculi and lacunar tessellations are calculated.

From the segmented canaliculi, it is straightforward to calculate the tissue parameters related to the canaliculi. The total canalicular volume *Ca.TV* can be obtained directly from the binary image of canaliculi. The canalicular volume density, denoted as *Ca.TV/BV* and *Ca.TV/TV* was also calculated.

Since in this chapter, we have introduced Voronoi tessellation, we also upgraded the quantification method to take into account the Voronoi partition. Thus we also computed the volume of the Voronoi cell which defines the territory of each lacuna. We also restricted the counting process of the number of canaliculi within each Voronoi cell. The implementation of the method is straightforward. The calculation of the number of canaliculi uses the associated Voronoi cell as a mask to restrict the counting process.

8.4 Selection of the parameters in the segmentation method

8.4.1 Comparison between the reconstructed SR micro-CT images

The series of tibial specimens scanned at the ID19 with the 300 nm resolution were reconstructed in PyHST software with the standard filtered back-projection algorithm and with the single distance phase retrieval process.

Both of the reconstructed volumes were evaluated in terms of visual assessment and SNR. From the visual aspect, both of the methods reveal internal structure of the bone tissue, including the Haversian canals (big darker voids inside the bone matrix in both Figure 8.9 (a) and (b)) and the LCN (the smaller darker region distributed around the Haversian canal) shown in zoomed regions in Figure 8.9 (c) and (d). However, as expected, the contrast between the osteon and the interstitial tissue is better in the single distance phase retrieval image. Figure 8.9 (e) and (f) illustrate the profiles along the lines, located in the same region in Figure 8.9 (a) and (b), to show the level of contrast attained. The lines crossed the borders of an osteon and the interstitial tissue. To compare the SNR of the two images, homogenous regions not revealing visually the presence of canaliculi were selected at the same location in the two reconstructed slices (red square in Figure 8.9 (a) and (b), and zoom views in Figure 8.9 (g) and (h)). From the Table 8.1, SNR based on the phase retrieval algorithm is about one magnitude higher than the other. Finally, since the aim of this work is a structural oriented study, the reconstructed volume based on phase retrieval algorithm was selected for the input of the segmentation workflow.

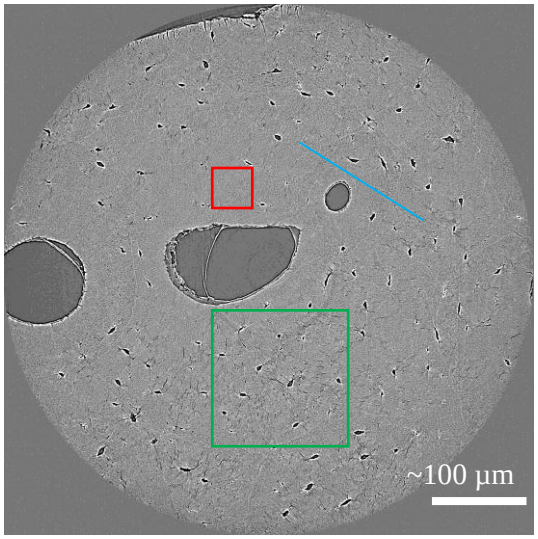

(a)

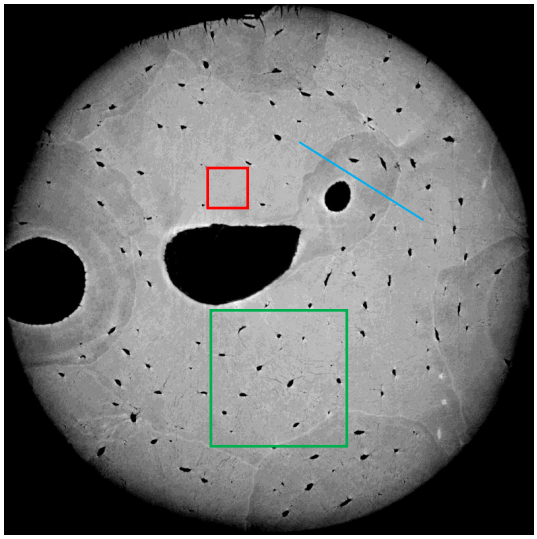

(b)

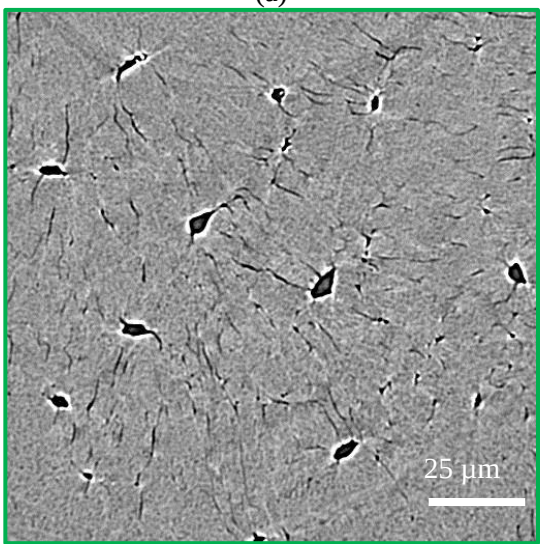

(c)

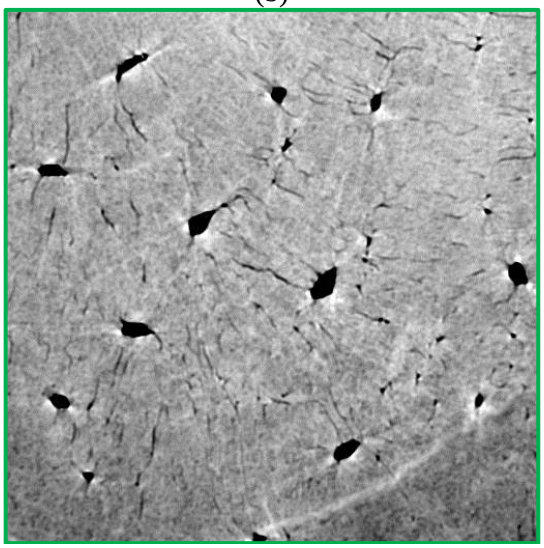

(d)

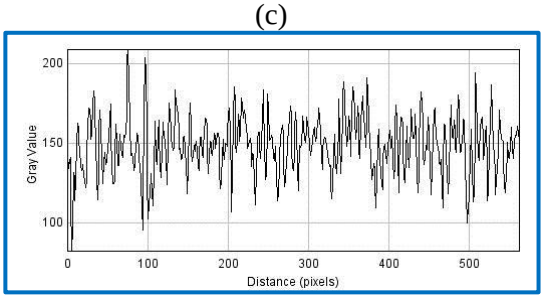

(e)

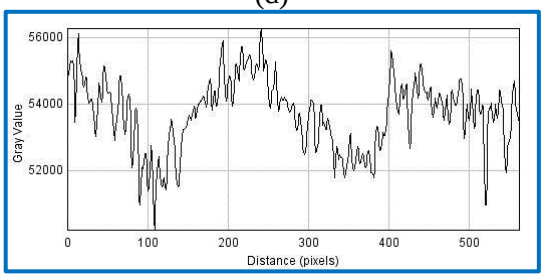

(f)

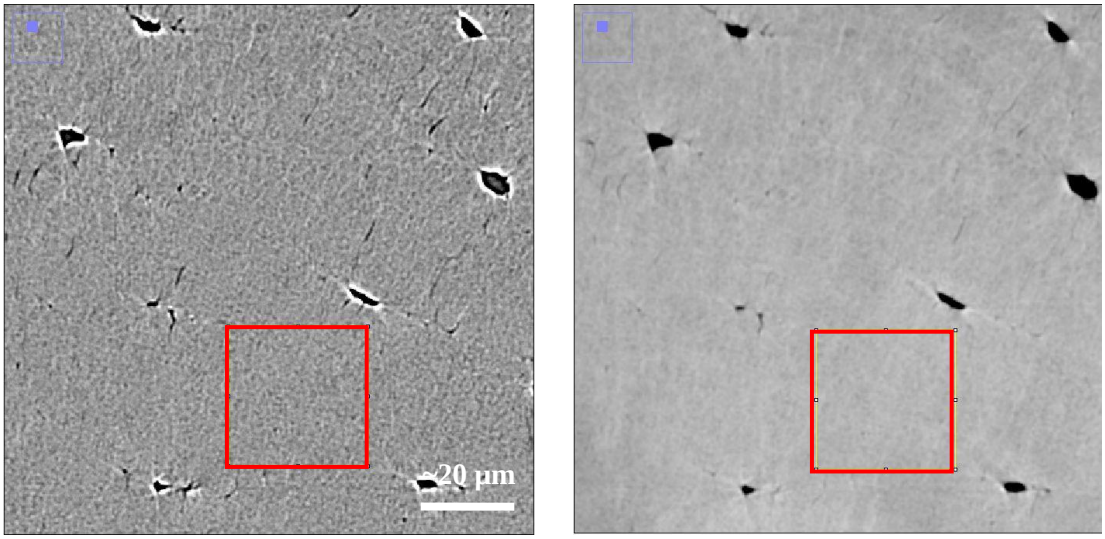

(g) (h)

Figure 8.9 Comparison between the reconstructed images based on the standard filtered backprojection algorithm and the single distance Paganin phase retrieval

Table 8.1 SNR comparison at the homogenous region (red square in Figure 8.9 (g) and (h)) between the two reconstructed volume.

	Area (voxels)	Mean	StdDev	Min	Max	SNR
Normal (8-bits)	14400	151	15.7	59	208	9.6
Phase retrieval (16 bits)	14400	55128	469.3	52737	56685	117.5

8.4.2 Manual Segmentation

We attempted to generate a ground truth segmented image of the LCN by performing a manual segmentation. However, the manual segmentation of the LCN on a large field of view proved to be extremely difficult. The difficulties come from the complex nature of the LCN network, the huge amount of manual work due to the very high density of the LCN, the ambiguities raised from the partial volume effect and the low SNR in the image, and the 3D nature of the canaliculi paths. The discrimination between the canaliculi and the background noise can be sometimes extremely difficult to judge. To better illustrate, here, we showed a partial completed manual segmentation on one slice, Figure 8.10. Besides, the manual segmentation can only be done slice by slice, while it is not easy to follow a given path through several slices. In addition, there are a very large number of paths to segment.

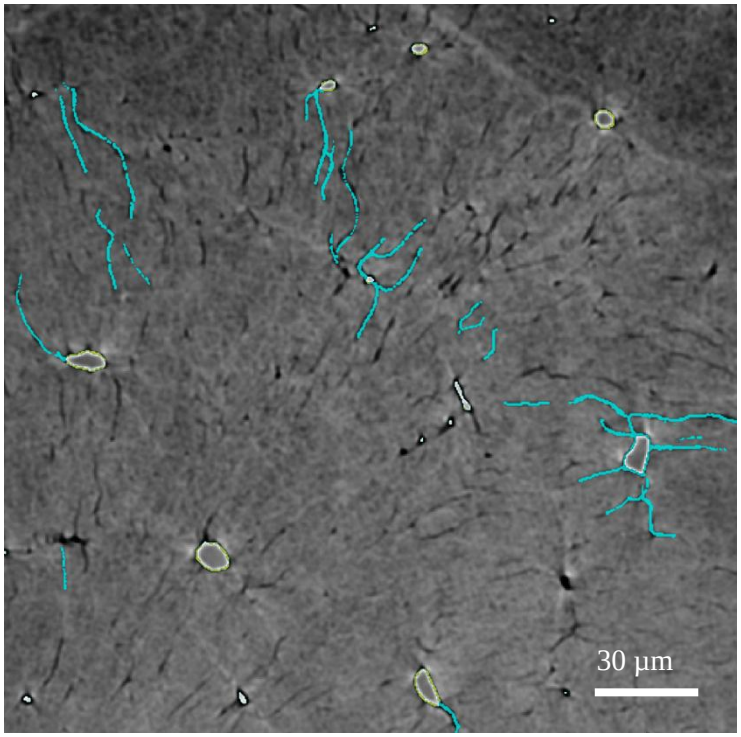

Figure 8.10 illustration of a partial completed manual segmentation on the LCN on one of the slice in the 3D image (512×512 voxels)

Nevertheless, the attempt of the manual segmentation of the LCN was conducted on a relatively large cubic VOI (512×512×512 voxels), containing nearly a hundred lacunae. The segmentation work was performed on a commercial software, VGStudioMax 2.2. Due to the low SNR on the canaliculi structure, the popular interactive 3D segmentation methods, such as 3D region growing, does not work properly to extract the structures. A manual drawing was directly performed on the canaliculi voids, and the segmentation was performed slice by slice throughout the whole volume of interest, illustrated in Figure 8.10 (around 100 canaliculi segments included in one slice of the 3D image (512×512 voxels)). A 3D display of the final manual segmentation of LCN is shown in Figure 8.11.

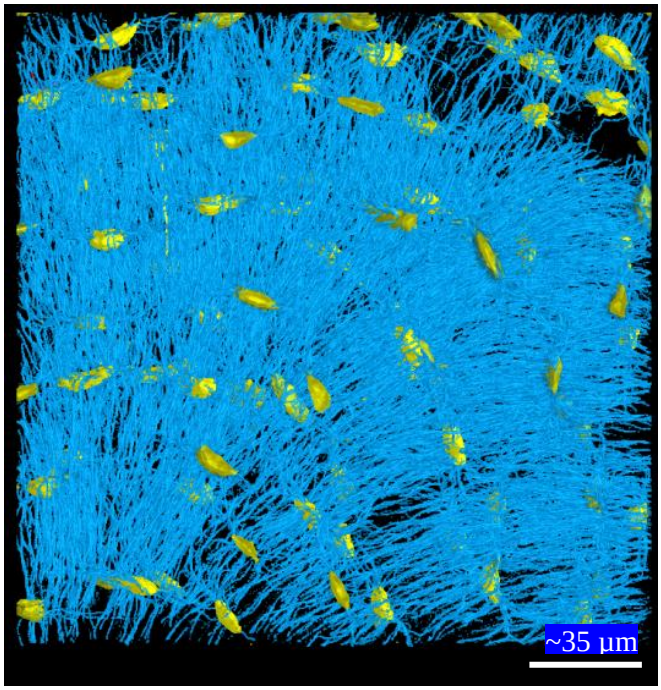

Figure 8.11 3D rendering of the manual segmented LCN (the yellow lacunae and the blue canaliculi) on a large VOI (512×512×512 voxels). (rendered by VGStudioMax®)

8.4.3 Automatic segmentation

Thanks to the parallelization of the method, the segmentation work flow could be successfully applied to selected subvolumes of the SR micro-CT images. However, the application of the method requires selecting a number of parameters, including the cardinality of the $\boldsymbol{B_i}$ set, the radius r of the structuring elements, the voting threshold T_{G_i}, the size of the neighborhood m of the maximum rank filter, and the number of machines N_m and cores N_c used in the parallel computing scheme.

Among these parameters, the choice of the parameters, including cardinality of the $\boldsymbol{B_i}$ set and the radius r of the structuring elements have been discussed in a recent work [Zuluaga *et al.* (submitted)]. Considering the segmentation quality and the computation time on the series of large 3D images, we propose to subsample the B_i set by a factor n = 5, which means that one out of five voxels from the VOI border was included. Thus, the end points in B_i^5 built up a uniformly spaced grid surrounding the lacunae centroid. With a similar consideration, the structuring element radius r was empirically set to 10, allowing sufficient number of paths likely to converge towards the canaliculi section.

To improve the geodesic voting result, the maximum rank filter with a neighborhood 3×3×3 was used. This method solves the weaving back propagation after the geodesic paths converged into the canaliculi sections. Figure 8.12 shows, in the entire VOI and in a zoomed region, the maximum projection (MIP) view of the geodesic voting and the corresponding result after the application of the maximum rank filter. We may notice an improvement in Figure 8.12(d) compared to Figure 8.12(c) since a much more ordered color pattern, from

purple to red, is presented, as the geodesic voting paths converging from the tessellation border to the center gravity of the lacuna.

As explained in section 8.3.9, we noticed that the geodesic voting method could extract pathways which are not supported by visual evidence. Figure 8.13 illustrates such false canaliculi extracted within the red boxes. To enhance the geodesic voting value on the "real" canaliculi path, and to reduce the value on the "false" one, the "vesselness" image was used as the prior knowledge, Figure 8.14 (b). Figure 8.14 (c) illustrates the maximum possible binary paths overlaid on the "vesselness" image. This binary image is obtained with a threshold of 2 on the corrected geodesic voting image, followed by an elimination of the lacuna. Figure 8.14 (d) is the weighed paths image, the color representing the average values of the vesselness map on each component. Figure 8.14 (e) shows the final modified geodesic voting image.

After enhancement, the modified geodesic voting map was normalized and thresholded. A voting threshold $T_{G_i} > 0.05$ was set to acquire the segmentation result. Figure 8.14 (f) shows the segmented result on a lacuna and its connected canaliculi. Figure 8.15 shows the binary LCN on a large VOI (512×512×512 voxels), which has been segmented manually illustrated in Figure 8.11. The thresholding applied here is different than the recent work of Zuluaga [Zuluaga *et al.* (submitted)], since the image has a different meaning. This thresholding is selected according to the visual grading on several voting thresholds based on the volume we used for manual segmentation.

The parallel computing, the calculation of the geodesic voting implementation was applied on the ESRF cluster. Typically we used 16 machines on the ESRF computation cluster, 2 threads per core were performing the task concurrently on 16 cores, thus N_m =16 and N_c =16. Therefore, the theoretical speed up factor is 256. This now makes our method usable for large VOI segmentation. In practice, the actual time was tested on one subvolume including 163 lacunae. The time for the entire procedure observed in one simulation was shown in Table 8.2. The total time of the segmentation is 14.05h.

Table 8.2 Observation of time and the percentage cost on each step of the segmentation work flow (Figure 8.4)

Process	**Time cost (seconds)**	**Percentage (%)**
Mask Generation	21	0.04
Lacunae segmentation	21	0.04
Lacunae Labeling	63	0.12
Lacunae Tessellation	3709	7.33
3D Geodesic Voting	43750	86.49
Maximum Rank Filter	1032	2.04
Pathway Enhancement	1183	2.34
Normalization thresholding	805	1.59

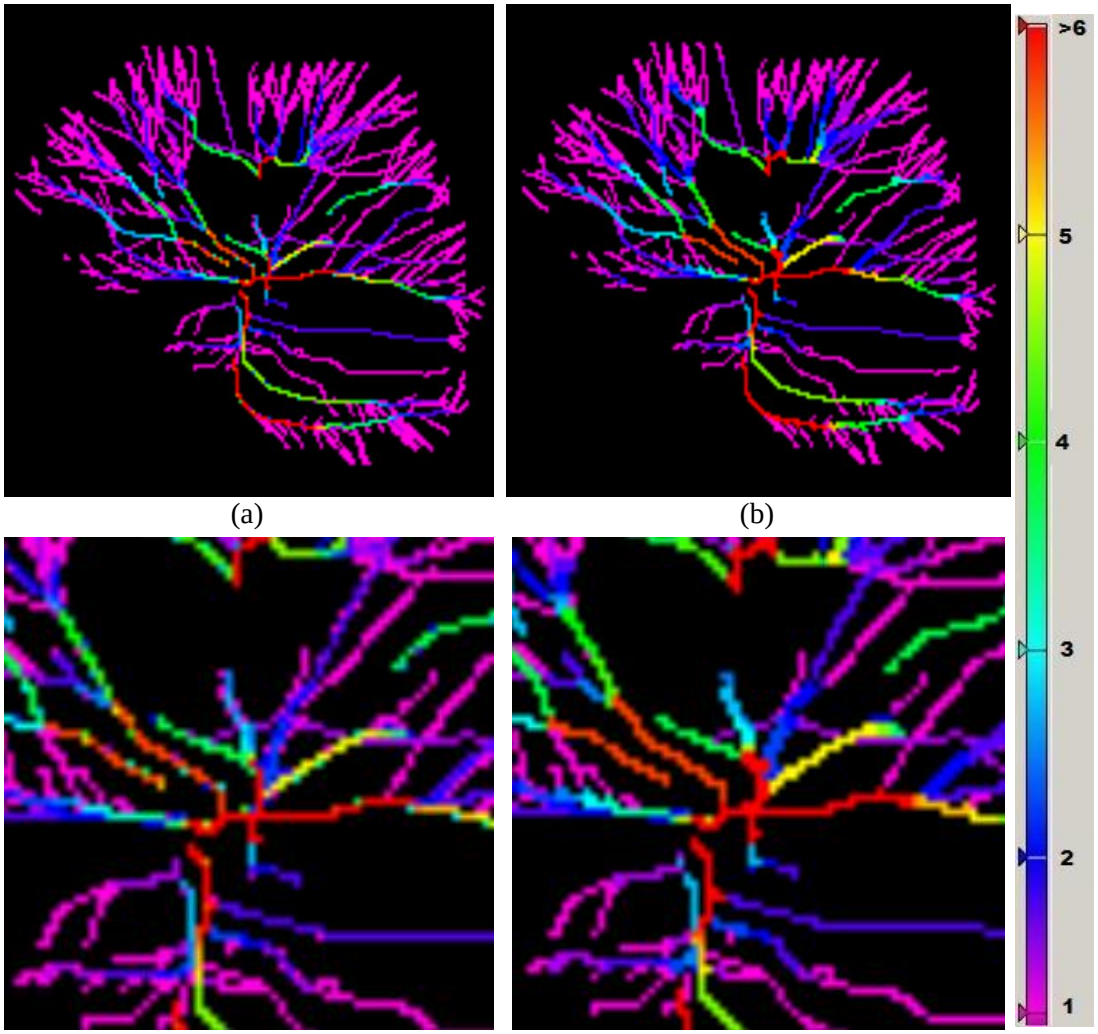

(a) (b)

(c) (d)

Figure 8.12 MIP view of the 42 slices of the extracted geodesic paths (the voting value μ=[1,max] shown in color). ((a) and (c)) and the improved results using the maximum rank filter ((b) and (d)).

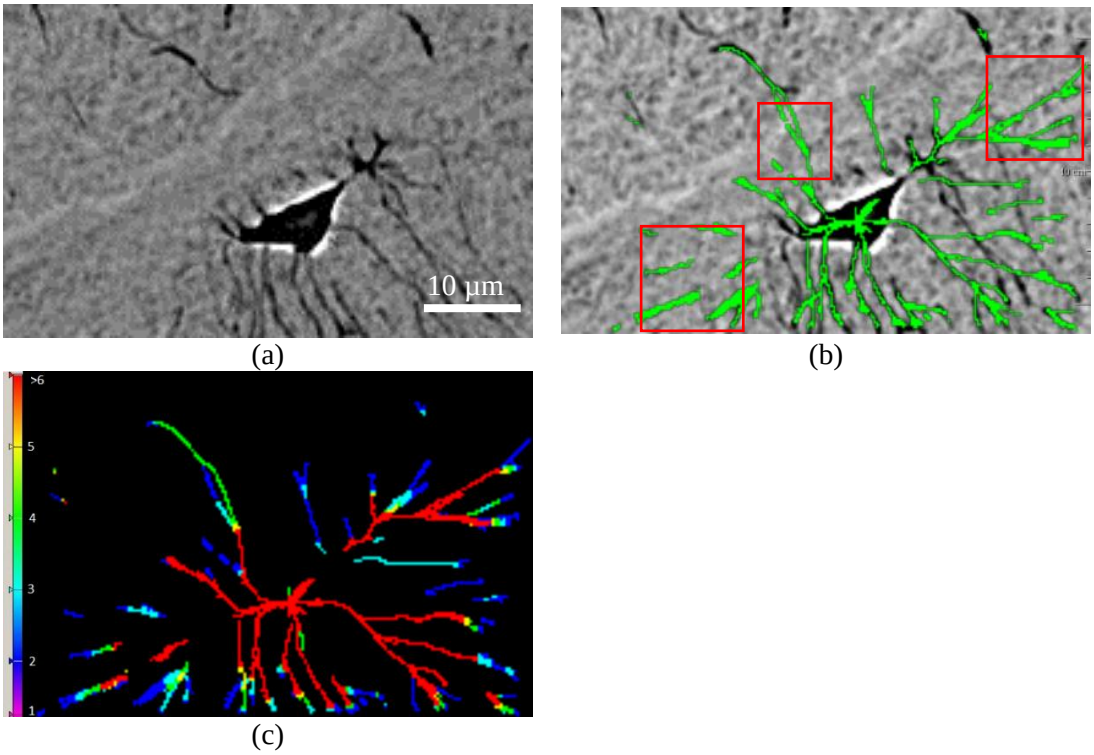

Figure 8.13 geodesic voting on one of the lacunae in the whole 3D volume: (a) minimum intensity projection of 12 consecutive slices. (b) maximum intensity projection of the respective extracted canaliculi pathway superposed onto a minimal intensity projection of the image (a). The red squares in (b) point out the surplus pathways, where no presence of canaliculi are existed in (a). (c): the extracted geodesic paths (the voting value µ=[2,max] shown in color).

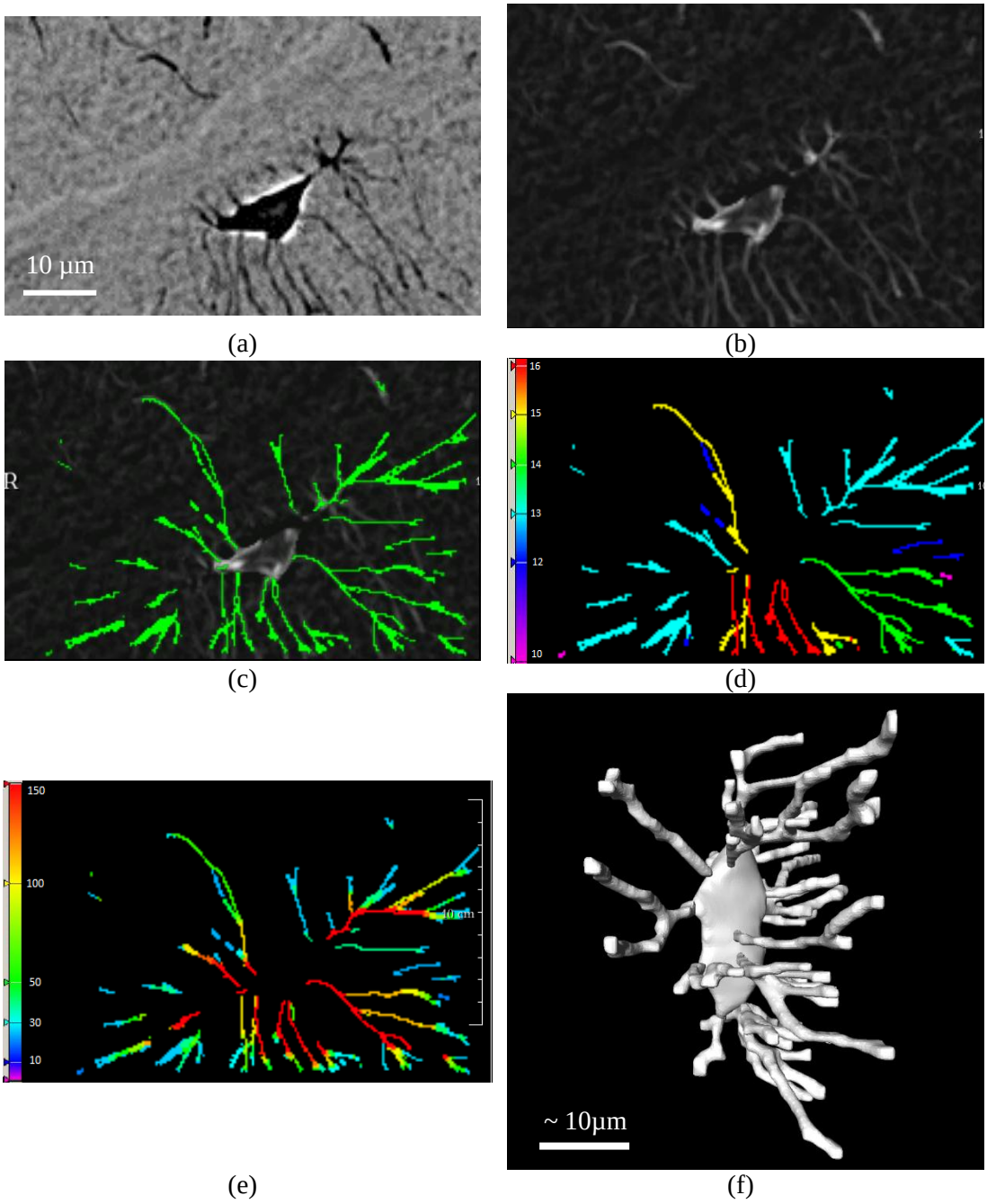

Figure 8.14 The enhancement of canaliculi pathway (a) minimum intensity projection (MinIP) of 12 consecutive slices. (b) maximum intensity projection (MaxIP) of the respective vesselness image of (a). (c) the enhanced pathways superposed image onto the image (a). (d) MaxIP of the weighed value w of the each extracted path of canaliculi (e) MaxIP of the enhanced geodesic paths (the enhanced voting values are shown in color) (f) the segmented LCN using the voting threshold $T_g > 0.05$ (rendered by Avizo®).

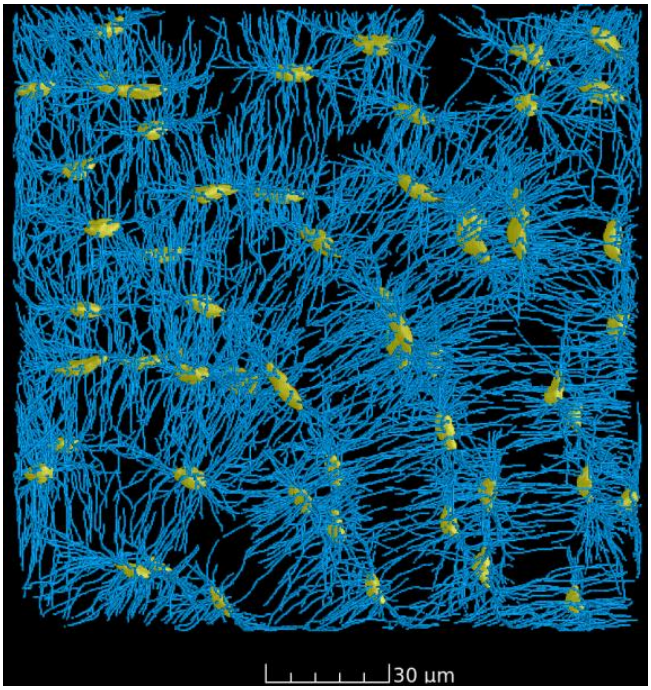

Figure 8.15 : 3D rendering of the automatic segmented LCN on a large VOI (512×512×512 voxles). (rendered by VGStudioMax®).

8.5 Application to human tibial SR micro-CT images

8.5.1 Selection of regions of interest

Eight human tibial samples were first scanned using SR micro-CT at the ESRF beamline BM05 at spatial resolution of 3.5 µm. Then, from the reconstructed images, regions of interest (ROIs) close to the periosteal side of the samples were chosen for the higher resolution imaging using SR nano-CT at the ESRF beamline ID19 at spatial resolution of 300 nm. For the detailed information about the ROIs, which we scanned on the higher resolution, please refer to the Annex 2.

The higher resolution images (300 nm) were reconstructed by the single distance Paganin phase retrieval process. The reconstructed images are also illustrated in Annex 2. For each of the whole volume (2048^3 voxels), a volume of interest, on average about 700×700×600 voxels, was cropped from a osteon region using ImageJ.

8.5.2 Parameters of the lacunae segmentation method

As described in 8.3.4, due to the good contrast in the 3D single-distance phase CT images, the lacunae were segmented by applying Ostu thresholding in the bone mask region. All lacunae connected to the image boarders were deliberately excluded from the segmentation volume, avoiding biasing results due to the partial lacunae. The artificial lacunae, such as micro-cracks, ring artifacts, and some irregularly shaped fragments were filtered by thresholding the morphological descriptors: $50\ \mu m^3 < Lc.V < 1000\ \mu m^3$, $Lc.L1/Lc.L2 <$

5, and $0 \leq Lc.\chi \leq 2$. The parameters were chosen according to the existing literature about shape of lacunae [Dong *et al.*(2014); McCreadie *et al.* (2004)]. Figure 8.15 shows a top 3D view of the segmented lacunae and its canaliculi, where all the lacunae were distributed in a concentric way, since the VOI were cropped on an osteon region.

8.5.3 Histomorphometry parameters of the tibial tissues

The descriptive statistical characteristics calculated on the eight human tibial samples are reported in Table 8.3 and Figure 8.16. On these samples, the number of lacunae calculated is in a range from 54 to 188, depending on the bone matrix volume (BV), ranging from 3.6 mm^3 to 10.3 mm^3. The bone volume fraction (BV/TV) also varies a lot, from 40% to 100%, depending on the size the Haversian canal involved in the VOI. The lacunar number density (N.Lc/BV) is on average of 15575 ± 2389/mm^3. The LCN volume density (LCN.TV/BV) is on average of 0.71% ± 0.16%. The lacunar volume density (Lc.TV/BV) is on average of 0.57% ±0.14%, and the canalicular volume density (Ca.TV/BV) is on average of 0.14% ± 0.03%.

Table 8.3 Histomorphometry parameters of the bone tissue from the human tibial samples

SampleID	Age	N.Lc	Lc.TV ($\times 10^{-5}$ mm^3)	Ca.TV ($\times 10^{-5}$ mm^3)	BV ($\times 10^{-3}$ mm^3)	TV ($\times 10^{-3}$ mm^3)	BV/TV (%)	HCa.V/TV (%)
F1	46	188	7.69	1.96	10.14	10.37	97.8%	2.2%
F2	84	153	4.95	1.16	9.35	10.37	90.2%	9.8%
F3	87	65	1.77	0.55	5.66	5.83	97.1%	2.9%
M1	29	155	6.95	1.35	10.33	10.37	99.6%	0.4%
M2	56	54	2.10	0.55	3.62	3.62	100.0%	0.0%
M3	56	135	4.85	1.34	10.05	25.18	39.9%	60.1%
M4	88	97	3.35	0.77	5.85	6.20	94.3%	5.7%
M5	89	103	3.76	0.86	5.63	5.83	96.6%	3.4%
Mean F	72.3	135.3	4.80	1.22	8.38	8.86	95.0%	5.0%
Std. F	22.9	63.4	2.96	0.71	2.39	2.62	4.2%	4.2%
Mean M	63.6	108.8	4.20	0.98	7.10	10.24	86.1%	13.9%
Std. M	25.3	38.7	1.83	0.36	2.96	8.70	25.9%	25.9%
Mean All	66.9	118.8	4.43	1.07	7.58	9.72	89.4%	10.6%
Std. All	23.1	46.8	2.12	0.48	2.66	6.76	20.2%	20.2%

SampleID	N.Lc/BV (mm^3)	N.Lc/TV (mm^3)	Lc.TV/BV (%)	Lc.TV/TV (%)	Ca.TV/BV (%)	Ca.TV/TV (%)	LCN.TV/BV (%)	LCN.TV/TV (%)
F1	18542	18133	0.76%	0.74%	0.19%	0.19%	0.95%	0.93%
F2	16366	14757	0.53%	0.48%	0.12%	0.11%	0.65%	0.59%
F3	11482	11145	0.31%	0.30%	0.10%	0.09%	0.41%	0.40%
M1	15009	14950	0.67%	0.67%	0.13%	0.13%	0.80%	0.80%
M2	14901	14901	0.58%	0.58%	0.15%	0.15%	0.73%	0.73%
M3	13427	5362	0.48%	0.19%	0.13%	0.05%	0.62%	0.25%

M4	16586	15649	0.57%	0.54%	0.13%	0.13%	0.71%	0.67%
M5	18288	17661	0.67%	0.64%	0.15%	0.15%	0.82%	0.79%
Mean F	15463.6	14678.4	0.53%	0.51%	0.14%	0.13%	0.67%	0.64%
Std. F	3615.5	3494.3	0.22%	0.22%	0.05%	0.05%	0.27%	0.27%
Mean M	15642.2	13704.6	0.60%	0.53%	0.14%	0.12%	0.74%	0.65%
Std. M	1853.9	4796.3	0.08%	0.19%	0.01%	0.04%	0.09%	0.23%
Mean All	15575.2	14069.7	0.57%	0.52%	0.14%	0.13%	0.71%	0.64%
Std. All	2389.0	4109.5	0.14%	0.19%	0.03%	0.04%	0.16%	0.23%

N.Lc – number of osteocyte lacunae

Lc.TV – total lacunae volume (mm^3)

Ca.TV – total canaliculi volume (mm^3)

BV – bone volume (mm^3)

TV – tissue volume (mm^3)

BV/TV – bone volume fraction (%)

HCa.V/TV – canal volume fraction or bone porosity (%)

N.Lc/BV and N.Lc/TV– lacunar number density (mm^{-3})

Lc.TV/BV and Lc.TV/TV– lacunar volume density (mm^{-3})

Ca.TV/BV and Ca.TV/TV– canalicular volume density (mm^{-3})

LCN.TV/BV and LCN.TV/TV– lacuno-canalicular network volume density (mm^{-3})

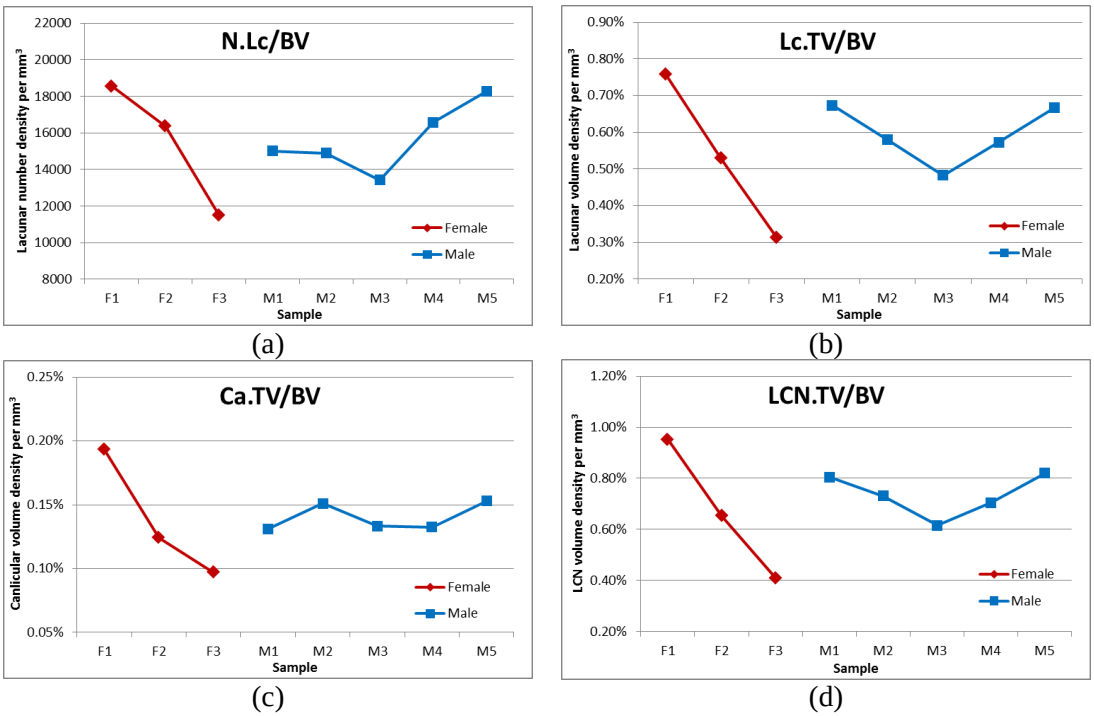

Figure 8.16 Average values of lacuno-canalicular densities between samples associated with age and sex (red: female group, blue: male group). (a) Lacunar number density (b) Lacunar volume density (c) canalicular volume density (d) lacuno-canalicular network volume density

8.5.4 Morphological descriptors of the osteocyte lacunae

Table 3 and Figure 8.17 report the descriptive statistics features of the osteocyte lacunar descriptors. The average lacunar volume was 372.9 ± 119.6 μm^3. The average lacunar territory volume was 64037.5 ± 33150.7 μm^3. The average lacunar surface was 377.7 ± 89.7 μm^2. The fitting ellipsoid of the osteocyte lacuna has an average volume 424.6 ± 134.6 $\mu m^3$of and an average surface of 367 ± 86.2 μm^2. The lacunae show an anisotropic shape with average length (Lc.L1) of 21.1 ± 5.1 μm, width (Lc.L2) of 9.0± 2.1 μm, and depth (Lc.L3) of 4.5 ± 1.1 μm. The anisotropy (length : width : depth) of the tibial osteocyte lacunar is about 5:2:1. The lacunar structural model index was 3.1 ± 0.4.

Table 8.4 Osteocyte lacunar descriptors from the eight human tibial samples
descriptive values of mean ± standard deviation, and range [minimum, maximum] are reported

SampleID	Lc.V (μm^3)	Lc.Tess.V (μm^3)	Lc.S (μm^2)	Ellip.V(μm^3)	Ellip.S(μm^2)
F1	409.1 ± 104.9	52731.5 ± 19646.3	392.8 ± 72.9	465.8 ± 117.7	377.1 ± 66.2
	[125.3, 936.7]	[17119.4, 124600.4]	[193.4, 756.3]	[170.1, 1150.6]	[173.3, 596.7]
F2	323.2 ± 119.2	62844.4 ± 35309.7	326.4 ± 85.1	370.6 ± 138.3	317.8 ± 85.2
	[66.4, 745]	[13562.1, 248990.9]	[120.8, 582.3]	[82.6, 806.3]	[118.7, 578.8]
F3	272.5 ± 99.9	85436.6 ± 34985.1	300.3 ± 83.3	312.7 ± 130.2	294.8 ± 79.3
	[85.2, 713.9]	[31037.5, 185012]	[127.5, 581.5]	[98.9, 1055.5]	[124.5, 591.9]
M1	448.7 ± 134.7	63278.6 ± 23786.2	418.3 ± 85.2	499.5 ± 144.7	405.2 ± 83
	[180.8, 970.9]	[21495.5, 144423.9]	[199.1, 761.4]	[199.7, 1051.9]	[186.2, 738.1]
M2	388.9 ± 95.2	52435.8 ± 13673.6	398.2 ± 71.4	430.8 ± 103	398.4 ± 73.1
	[210.6, 592.1]	[25962.6, 100111.9]	[264.9, 553.7]	[233.7, 644.9]	[260.4, 553.1]
M3	359.5 ± 115.7	84081.1 ± 52551.2	394 ± 100	430.7 ± 140.6	381.7 ± 92.4
	[52.8, 666.1]	[19460.3, 277311.5]	[88.4, 686.2]	[68.6, 961.2]	[88.5, 634.8]
M4	345.3 ± 71.4	67009.4 ± 27612.5	370.1 ± 65.7	388.3 ± 78.7	361.8 ± 65.5
	[215.5, 714.6]	[26742.1, 160774.8]	[251.6, 699.7]	[235.9, 782.4]	[251.1, 685]
M5	364.6 ± 92.5	51096.4 ± 16830.2	389 ± 87.5	410.8 ± 98.4	378.9 ± 86.9
	[155.6, 906.3]	[18093.9, 114399]	[161.5, 848.6]	[164.3, 965.6]	[155.9, 819.8]
F	354.9 ± 121.8	61778.6 ± 31109.6	352.9 ± 87.9	405.4 ± 140.7	341.6 ± 83
	[66.4, 936.7]	[13562.1, 248990.9]	[120.8, 756.3]	[82.6, 1150.6]	[118.7, 596.7]
M	386.3 ± 116.3	65723.4 ± 34527.5	396.1 ± 86.6	439 ± 128.2	386 ± 83.7
	[52.8, 970.9]	[18093.9, 277311.5]	[88.4, 848.6]	[68.6, 1051.9]	[88.5, 819.8]
All	372.9 ± 119.6	64037.5 ± 33150.7	377.7 ± 89.7	424.6 ± 134.6	367 ± 86.2
	[52.8, 970.9]	[13562.1, 277311.5]	[88.4, 848.6]	[68.6, 1150.6]	[88.5, 819.8]

SampleID	Lc.L1 (μm)	Lc.L2 (μm)	Lc.L3 (μm)	Lc.L1/Lc.L2	Lc.L1/Lc.L3	Lc.SMI
F1	20.8 ± 5.3	9.2 ± 2	4.9 ± 1.2	2.4 ± 1	4.6 ± 1.8	3.2 ± 0.3
	[10.1, 32.1]	[5, 15.3]	[2.6, 9]	[1, 4.9]	[1.3, 9.6]	[2.1, 4.1]
F2	19.7 ± 5.1	7.8 ± 1.8	4.6 ± 1.1	2.7 ± 1	4.5 ± 1.7	3.2 ± 0.3
	[10, 35.4]	[4.5, 14]	[2.3, 8.2]	[1.1, 4.8]	[1.6, 12.2]	[1.9, 4.2]

F3	19.7 ± 4.4	7.4 ± 1.5	4.1 ± 0.9	2.8 ± 0.8	5 ± 1.4	3.2 ± 0.3
	[10.8, 30.3]	[4.1, 11.7]	[2.3, 7.6]	[1, 4.7]	[1.9, 8.5]	[2.3, 4.1]
M1	21.3 ± 5.7	9.9 ± 2	4.8 ± 1.3	2.3 ± 0.9	4.9 ± 2.1	3.2 ± 0.4
	[9.8, 34.1]	[6.5, 15.1]	[2.8, 9.3]	[1.1, 4.7]	[1.5, 10.2]	[2.3, 4.3]
M2	24.4 ± 3.9	8.6 ± 1.6	4 ± 0.5	2.9 ± 0.7	6.3 ± 1.6	3 ± 0.3
	[16.9, 33.2]	[5.7, 13.5]	[2.4, 5]	[1.5, 4.4]	[3.5, 11]	[2.4, 3.5]
M3	21.3 ± 4.8	9.4 ± 2.4	4.2 ± 1	2.4 ± 0.9	5.5 ± 2	3.1 ± 0.4
	[7.8, 33.1]	[4.9, 17.1]	[1.7, 7]	[1.1, 4.6]	[1.8, 14.2]	[2, 4.3]
M4	21.8 ± 4.6	8.8 ± 1.7	4.1 ± 0.9	2.6 ± 0.8	5.7 ± 1.8	3.1 ± 0.3
	[11.4, 36.3]	[5.7, 14.9]	[2.8, 6.9]	[1.1, 4.4]	[1.7, 9.9]	[2.3, 4]
M5	21.1 ± 5.2	9.5 ± 1.9	4.1 ± 1	2.3 ± 0.8	5.6 ± 2.1	2.9 ± 0.4
	[9.9, 36.7]	[6.3, 15.9]	[2.3, 7.2]	[1, 4.8]	[1.7, 11]	[2, 3.9]
F	20.2 ± 5.1	8.4 ± 2	4.7 ± 1.1	2.6 ± 1	4.6 ± 1.7	3.2 ± 0.3
	[10, 35.4]	[4.1, 15.3]	[2.3, 9]	[1, 4.9]	[1.3, 12.2]	[1.9, 4.2]
M	21.7 ± 5.1	9.4 ± 2	4.3 ± 1.1	2.4 ± 0.9	5.5 ± 2	3.1 ± 0.4
	[7.8, 36.7]	[4.9, 17.1]	[1.7, 9.3]	[1, 4.8]	[1.5, 14.2]	[2, 4.3]
All	21.1 ± 5.1	9 ± 2.1	4.5 ± 1.1	2.5 ± 0.9	5.1 ± 1.9	3.1 ± 0.4
	[7.8, 36.7]	[4.1, 17.1]	[1.7, 9.3]	[1, 4.9]	[1.3, 14.2]	[1.9, 4.3]

Lc.V – lacunar volume (μm^3)

Lc.Tess.V – lacunar territory volume (μm^3)

Lc.S – lacunar surface area (μm^2)

Ellip.V – fitting ellipsoid volume (μm^3)

Ellip.S -- fitting ellipsoid volume (μm^2)

Lc.L1, Lc.L2 and Lc.L3 – length, width and depth of lacuna (μm)

Lc.L1/Lc.L2 and Lc.L1/Lc.L3 – anisotropy of lacuna

Lc.SMI – structural model index of lacuna

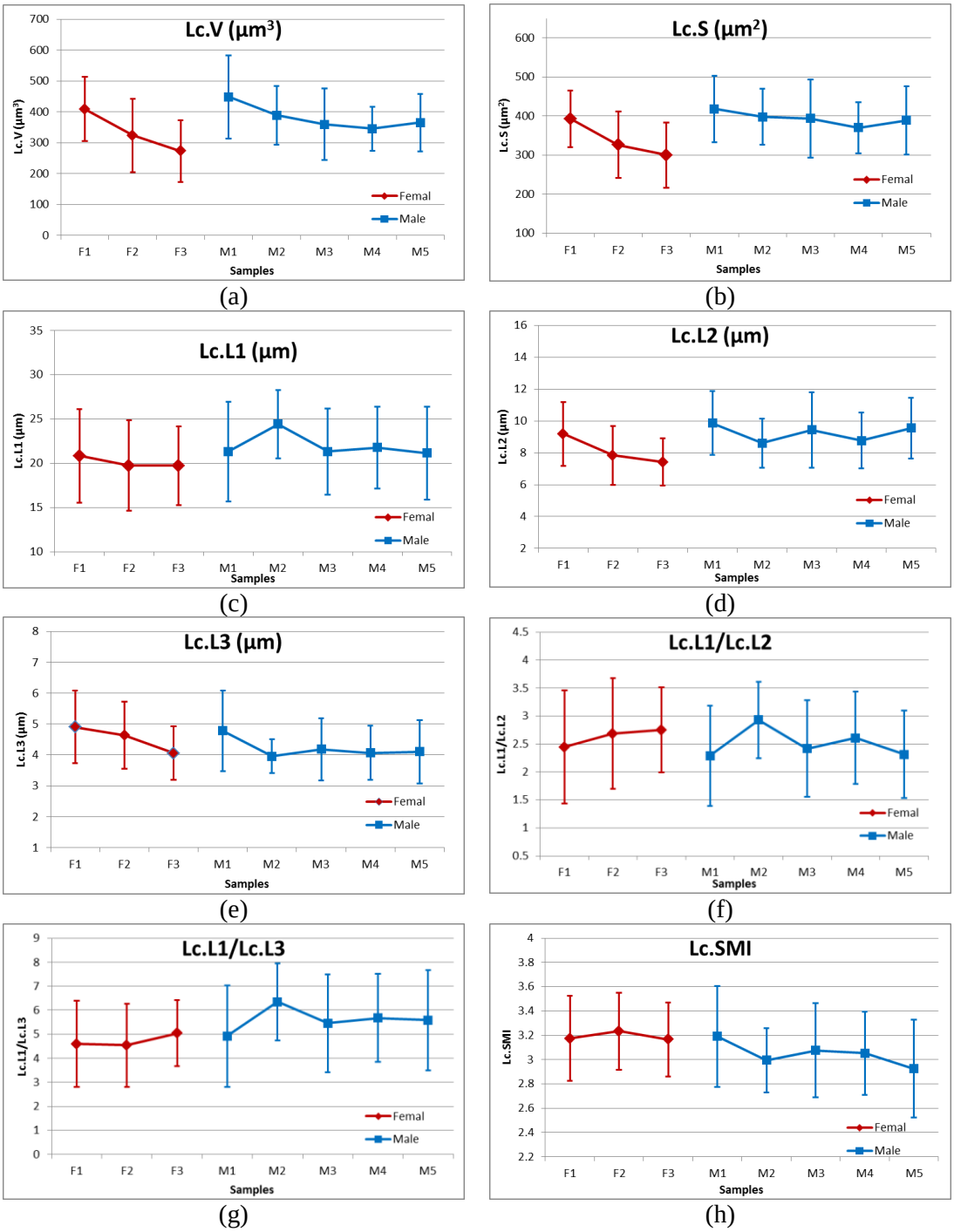

Figure 8.17 Lacunar morphological descriptors between groups (Marker and Bar: Mean and stardard deviation of the descriptor)

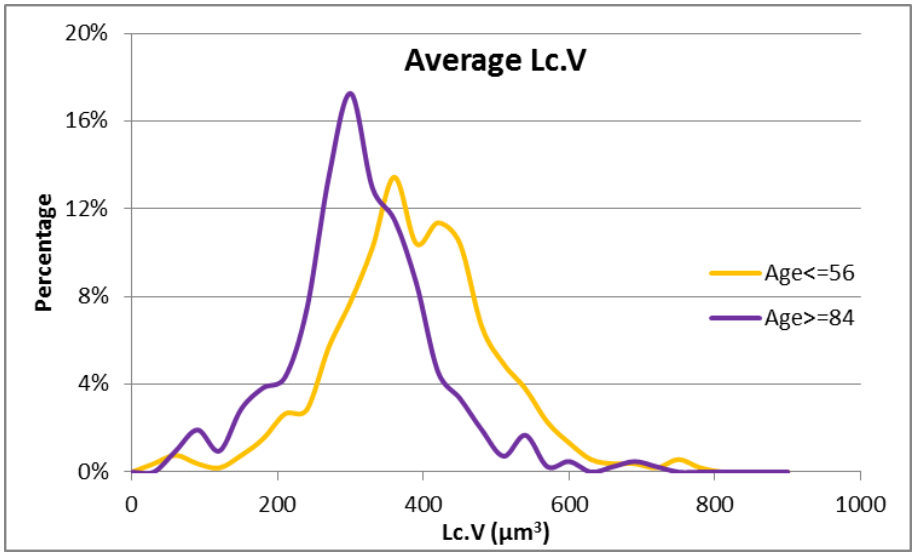

Figure 8.18 Lacunar volume distribution associated with age

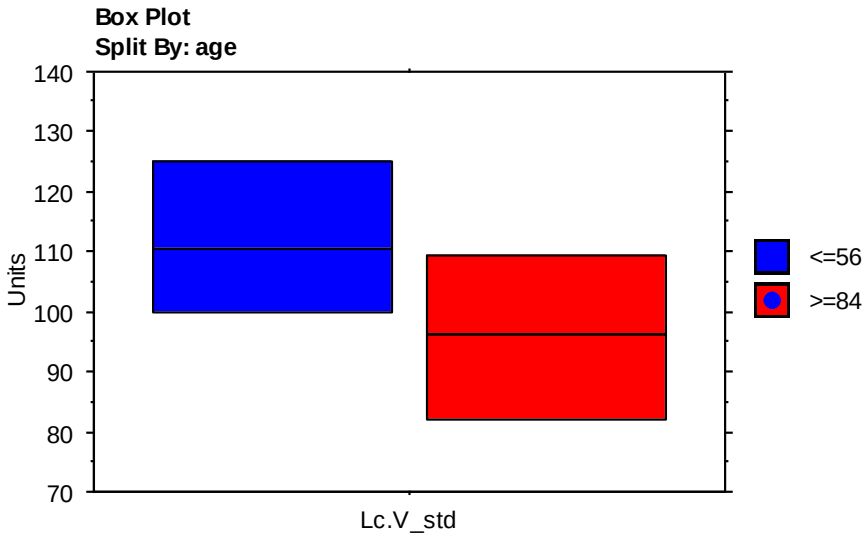

Figure 8.19 lacunar volume standard deviation associated with age

8.5.5 Ramification of the canaliculi

To quantify the ramification of canaliculi, we used 8 different dilation parameters (r), from 5 to 40 with step of 5 corresponding to distances from 1.5 µm to 12.0 µm with step of 1.5 µm. We used the lacunar tessellation image as a mask image to retrict the counting process within each Voronoi cell. Besides, the canalicular ramification was performed within the tessellation partition. Table 8.5 and Figure 8.20 report the ramification of canaliculi at different distances from the lacunar surface between automatic segmented LCN and the manual segmented LCN. Table 8.6 reports the descriptive statistical results of ramification of canaliculi on the series of samples. For the number of canaliculi calculated at the 1.5 µm, Figure 8.21 shows the result

with respect to Table 8.6, and Figure 8.22 shows the distribution between the younger group (age≤56 (n=4)) and elder group (age≥84 (n=4)).

Table 8.5 the result of canalicular ramification between the automatic segmentation and manual segmentation at different distance from the surface of lacunae

desciptive values of mean ± standard deviation, and range [minimum, maximum] are reported

SampleID	Lc.NCa r=1.5 µm	Lc.NCa r=3.0 µm	Lc.NCa r=4.5 µm	Lc.NCa r=6.0 µm	Lc.NCa r=7.5 µm	Lc.NCa r=9.0 µm	Lc.NCa r=10.5 µm	Lc.NCa r=12.0 µm
M2	30.5 ± 9.8	34 ± 11.9	37.1 ± 14.1	37.4 ± 16.2	34.9 ± 15.4	31 ± 14.2	26.4 ± 12.9	20.6 ± 10.1
	[8, 49]	[5, 58]	[6, 63]	[6, 77]	[5, 71]	[6, 64]	[3, 59]	[1, 46]
M2GT	69.5 ± 22.1	86.6 ± 27.2	98.9 ± 33.6	106.8 ± 37.8	108.1 ± 41.3	106.5 ± 43.9	99.5 ± 42.6	88.9 ± 40
	[18, 117]	[26, 143]	[26, 161]	[21, 179]	[7, 197]	[7, 204]	[9, 176]	[4, 158]

Lc.NCa– Number of the canaliculi calculated at distance r(µm)

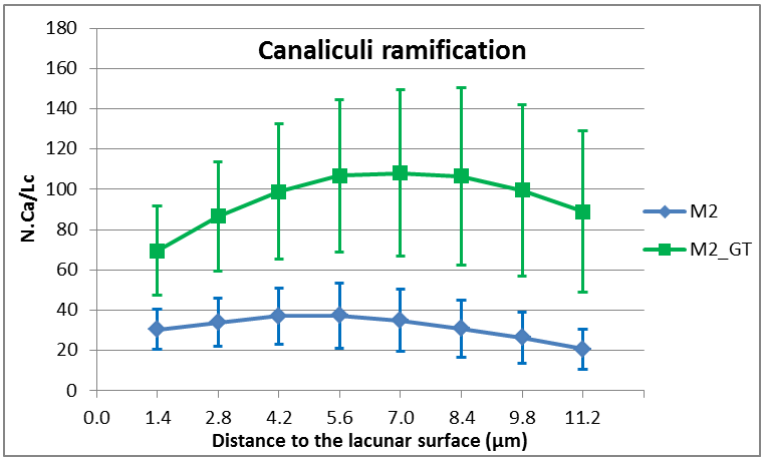

Figure 8.20 Canalicular ramification comparison between the result from the manual segmentation (M2_GT) and the result from automatic segmentation (M2). (Marker and Bar: Mean and standard deviation of the number of canaliculi per lacunae)

Table 8.6 Number of canaliculi per lacunae at different distance from the surface of lacunae desciptive values of mean ± standard deviation, and range [minimum, maximum] are reported

SampleID	Lc.NCa r=1.5 µm	Lc.NCa r=3.0 µm	Lc.NCa r=4.5 µm	Lc.NCa r=6.0 µm	Lc.NCa r=7.5 µm	Lc.NCa r=9.0 µm	Lc.NCa r=10.5 µm	Lc.NCa r=12.0 µm
F1	34.4 ± 11	37.7 ± 14.4	37.9 ± 15.7	35.4 ± 15.7	31.1 ± 13.9	26.3 ± 12.7	20.7 ± 10.5	16.5 ± 9.1
	[5, 72]	[7, 95]	[3, 91]	[2, 94]	[2, 83]	[1, 75]	[1, 56]	[1, 51]
F2	26.5 ± 10.8	27.3 ± 12.5	25.8 ± 13.5	22.1 ± 12.2	18.1 ± 10.8	15 ± 10.1	11.3 ± 8.4	9.2 ± 7.5
	[0, 54]	[0, 60]	[0, 59]	[0, 54]	[0, 50]	[0, 50]	[0, 40]	[0, 36]
F3	22.8 ± 7.8	24.7 ± 9	24.9 ± 11.1	23.6 ± 11	21.2 ± 11.5	18.8 ± 9.8	16.3 ± 8.8	14.3 ± 8.7
	[4, 42]	[4, 48]	[5, 57]	[2, 52]	[1, 55]	[1, 43]	[1, 38]	[1, 40]
M1	32.2 ± 13.1	34.2 ± 15.9	31.1 ± 15.8	26.8 ± 14.2	21.7 ± 12.6	17.2 ± 10.8	13.4 ± 9.2	10.9 ± 8.4
	[4, 86]	[3, 97]	[0, 80]	[0, 67]	[0, 60]	[0, 46]	[0, 42]	[0, 41]
M2	30.5 ± 9.8	34 ± 11.9	37.1 ± 14.1	37.4 ± 16.2	34.9 ± 15.4	31 ± 14.2	26.4 ± 12.9	20.6 ± 10.1
	[8, 49]	[5, 58]	[6, 63]	[6, 77]	[5, 71]	[6, 64]	[3, 59]	[1, 46]
M3	27.4 ± 11.5	29.6 ± 14.2	30.3 ± 15.8	28 ± 16.1	25 ± 14.9	21.7 ± 13.5	17.9 ± 12.1	14.6 ± 10.3
	[0, 51]	[0, 63]	[0, 73]	[0, 76]	[0, 70]	[0, 64]	[0, 57]	[0, 50]
M4	27.4 ± 11.2	29 ± 13.3	27 ± 14	24.5 ± 12.7	19.8 ± 11.1	15.3 ± 8.6	12.2 ± 7.6	10.3 ± 7.3
	[6, 55]	[4, 60]	[2, 59]	[1, 59]	[1, 58]	[0, 39]	[0, 36]	[0, 28]
M5	31.3 ± 11.1	31.5 ± 13.8	28.6 ± 14.2	24.4 ± 12.9	19.2 ± 11.1	14.5 ± 9.3	11.3 ± 7.6	8.6 ± 6.3
	[8, 58]	[4, 69]	[2, 73]	[1, 71]	[0, 62]	[0, 51]	[0, 41]	[0, 33]
F	29.5 ± 11.4	31.7 ± 14.1	31.3 ± 15.5	28.5 ± 15.2	24.6 ± 13.8	20.8 ± 12.5	16.5 ± 10.4	13.4 ± 9.1
	[0, 72]	[0, 95]	[0, 91]	[0, 94]	[0, 83]	[0, 75]	[0, 56]	[0, 51]
M	29.8 ± 11.9	31.6 ± 14.4	30.3 ± 15.2	27.3 ± 14.8	23 ± 13.7	18.9 ± 12.3	15.2 ± 10.8	12.2 ± 9.2
	[0, 86]	[0, 97]	[0, 80]	[0, 77]	[0, 71]	[0, 64]	[0, 59]	[0, 50]
All	29.7 ± 11.7	31.7 ± 14.2	30.7 ± 15.3	27.8 ± 15	23.7 ± 13.8	19.7 ± 12.4	15.7 ± 10.6	12.7 ± 9.2
	[0, 86]	[0, 97]	[0, 91]	[0, 94]	[0, 83]	[0, 75]	[0, 59]	[0, 51]

Lc.NCa– Number of the canaliculi calculated at distance r(µm)

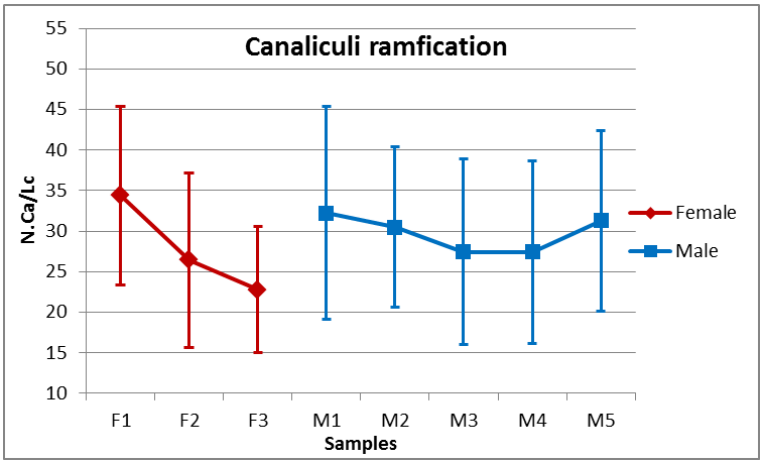

Figure 8.21 Canalicular ramifications between samples (Marker and Bar: Mean and standard deviation of the number of canaliculi per lacunae)

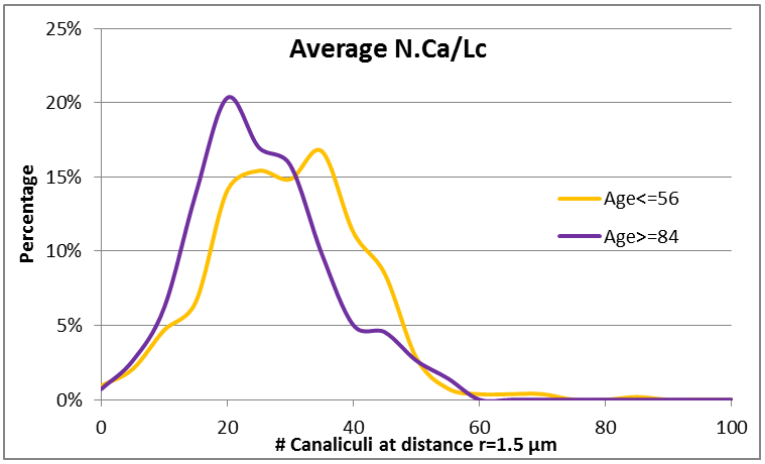

Figure 8.22 Distribution of number of canaliculi radiated from lacunae associated with age, calculated at 1.5 µm away from the lacunar surface

8.6 Discussion and conclusion

In this chapter, we described an automatic approach to perform the segmentation of the LCN in a series of large 3D SR micro-CT images. This method was an improvement of a method previously described in the group, and we could report results on 3D lacuna-canalicular morphological characteristics on the segmented images. It is the first time that 3D canalicular ramifications are reported in a large field of view, including about a hundred lacunae in each VOI.

For the reconstructed image, we compared the reconstructed images based on the standard filtered back-projection algorithm and based on the single phase retrieval algorithm. The reconstructed volume based on the latter algorithm serves as a better image for the structure orientated study, since it has a better image contrast between the osteon and the interstitial tissue and a higher SNR than the image reconstructed from the former algorithm.

Our novel segmentation approach shows its feasibility in application to the large 3D micro-CT images. Compared to the previous approach [Pacureanu *et al.* (2010), (2011)], which suffers from the discontinuities in the segmented canaliculi image, our proposed methods enforce the continuity of the extracted canaliculi by using the 3D geodesic voting and the maximum rank filter. To avoid the strong assumption that all canaliculi in the lacunar tessellation partition will converge to the central lacuna, a canaliculi enhancement was performed based on the "vesselness" image. The fully automatic initialization scheme based on the tessellation of the image domain and the parallel computation implementation make our methods feasible for the heavy segmentation task on large 3D SR micro-CT images. Our implementation allows to handle very large 3D images and to compute quite efficiently by decomposing the large image into several VOIs which can be processed in parallel on many machines within a computing cluster.

For the quantification methods, both lacunar and canalicular morphological parameters were extracted in the series of samples. Considering the lacunar descriptors, apart from the extracted 3D morphological parameters, which were introduced in the chapter 6, we also calculated the lacunar territory volume (Lc.Tess.V), computed from the each lacunar

tessellation cell divided by the Voronoi-region boundaries. The calculation of the lacunar tessellation cells is dependent on the segmented lacunar centroid. Therefore, this method is model independent. Considering the quantification of the canalicular ramification, we applied the method proposed in chapter 7. In addition, as no boundaries or other biological features can be found in the image to define the boundaries between each two lacunae and their canaliculi, the lacunar tessellation can be used as ideal artificial lacunar neighborhood boundaries, where the canalicular ramification can be calculated within this region.

In this study we reported the lacuno-canalicular density, including the lacunar number density (*N.Lc/BV*), lacunar volume density (*Lc.TV/BV*), canalicular volume density (*Ca.TV/BV*) and lacuna-canalicular network volume density (*LCN.TV/BV*). The value of lacunar number density is in agreement of the values in the previous reports [Mullender *et al.* (1996); van Hove *et al.* (2009)]. The value of the lacunar volume density is lower than our previous reported value in human femoral bone, section 6.3.2. To the best of the knowledge, it is first time that the LCN volume density and canalicular volume density are reported. In addition, we also found decreasing values in each lacuno-canalicular density associated with age in the female group. In general, the lacuno-canalicular densities between the female group and the male group are in the same range. This is conflict with the founding of Mullender [Mullender *et al.* (2005)] who reported the osteocyte number density was higher in healthy females than in healthy male. The decline of lacunar number density is consistent with many previous studies [Mullender *et al.* (1996); Mori *et al.* (1997); Qiu *et al.* (2002b); Vashishth *et al.* (2005); Torres-Lagares *et al.* (2010)]. But this was not confirmed in the recent study of Carter [Carter *et al.* (2013)]. Up to now, the cause of the decline is still in debate.

In this work, both lacunar and canalicular descriptors are calculated in 3D on a series of human tibial samples. For each sample, about one hundred of lacunae and their connected canaliculi were quantified. Compared to the traditional 2D investigations on the LCN, such as the work of Beno [Beno *et al.* (2006)], our method calculates the 3D morphological parameters directly in 3D, without any model assumption. Thus, the extracted parameters are expected to be unbiased. Besides, compared to the quantification based on other imaging modalities, such as the work of Sugawara [Sugawara *et al.* (2005), (2011)] and the work of Sharma [Sharma *et al.* (2012)], our method allows to quantify a large number of lacunae and their canaliculi in a large VOI. Thus, more reliable biological representative results are also expected.

For the morphology of the lacunae, the average value of the volume of lacunae is bigger than in the previous results reported by van Hove [van Hove *et al.* (2009)]. The differences may be due to the following two reasons. First, in [van Hove *et al.* (2009)], the sample donors, all suffered from bone diseases for years. The diseases may potentially change the lacunar size due to the little daily activities of the patient. Therefore, the mechanical loading on the bone tissue, raised from the daily activities, might be less than the bone tissue of the healthy person. Second, the difference might also be due to the imaging modality. Since the worse SNR of the desktop CT image can potentially affect the segmentation of lacunae and their quantification result.

We also report the lacunar volume distribution between different aged groups (age $\leq$ 56 years (n=4) and age $\geq$84 years (n=4)). With younger group, we found a bimodal distribution,

which is in consistence with the study of Hannah [Hannah *et al.* (2010)]. However, the elder group did not show such distribution, which is also in consistence with our previous result reported on two old human femoral samples (age of 78 years and 80 years), section 6.3.3. Besides, Figure 8.18 illustrates a distribution shift between the younger group and the elder group, which has been previously reported in human femoral cortical bones [Carter *et al.* (2013)]. Although the average values of the lacunar volume standard deviation are not significantly different between the two age groups, the less variation of the lacunar volume in the elder group, might still be a reason of the different distribution patterns, Figure 8.19. In addition, the decline of the lacunar length, width and depth with respect to the age is in agreement with Carter [Carter *et al.* (2013)]. Our findings are an important characteristics to support hypothesis that the aging osteocyte may be subject to hypermineralization of its perilacunar matrix, where lacunar void fill in with mineral [Bonewald (2011)]. Our results also suggest that with aging, as the number of canaliculi decreases, the dynamics of bone fluid flow through the LCN might change dramatically, potentially influence the osteocyte function and viability.

We reported the descriptive statistical results and the distributions on the canaliculi ramification pattern. The number of canaliculi calculated at r=1.5 µm were found to decline in the female group. Besides, the distribution of Lc.NCa (r=1.5 µm) in the elder was also found to be shifted to the left, which means a relatively lower ramification in the elder group. To our knowledge, this observation has never been reported in the previous literature. The canalicular ramification on one of the specimens (M2) was calculated on both automatic segmented image and manual segmented image. With the automatic method, only less than half of the canaliculi are counted compared to the result based on the manual segmentation. Nevertheless, the reported value based on the automatic segmentation image is still consistent with previous reported values on human samples [Beno *et al.* (2006)]. Although, the numbers we reported are less than the recent study of Sharma [Sharma *et al.* (2012)], who reported about 85 primary and 387 secondary canaliculi per lacuna on rats' tibial metaphysis. Our differences in the reported numbers can be explained by the different species used and the differences in the quantification methods. In addition, despite of our underestimated ramification value, the reported values on the series of sample still reveal valuable biological meanings, which have not been reported in the existent literature.

Limitations and perspective:

Since the extracted descriptors of the LCN structure largely depend on the quality of the segmented images, it would be desirable to evaluate the segmentation process. For this purpose, we put a lot of efforts to segment manually the canaliculi architecture on a large cubic volume (512×512×512 voxels, voxel size: 300 nm), about a cubic volume with side length of 153 µm. However, this work raised many difficulties, since achieving a high quality manual segmentation of such a complex network is a goal difficult to attain. Therefore in this application the manual segmentation is certainly not the best solution to serve as a ground truth. Ideally, imaging the same sample at 300 nm and 60 nm, could be used to have a real ground truth. However, in practice, this requires to scan the sample twice which could induce radiation damage on the sample and degrade the quality of the supposedly ground truth image.

To build up the ground truth, another possibility could be to create a digital phantom. But, this operation requires the development of tools for realistic imaging simulation.

For the automatic segmentation of the canaliculi, the geodesic voting methods can only deal with the tree-like structures. Although for most of the lacunar tessellation partition, most of the canaliculi will directly converge to the centroid the lacuna, this might be a too strong assumption. Based on the experience from the manual segmentation, we observed that not all of the canaliculi "directly" converge to the center of the lacuna, some of the canaliculi make a sudden turn after they radiate from the lacunar surface. For instance this is illustrated in the very right hand canaliculi in Figure 8.13 (a). Second, the lacunar tessellation is not always ideal for dividing the territory of each lacuna, since in each tessellation domain, canaliculi which do not belong to the central lacunae can be also included. Third, since the morphological structure of canaliculi in the complex biological environment has poorly been studied, the canaliculi might suddenly stop before reaching to the lacunar tessellation border. Due to the second and third reason, each tessellation region may include some canaliculi, which do not converge to the central lacuna. It can be observed in Figure 8.13 (a), due to the existence of the cement line (the brighter line passing through the image), that this tessellation region includes other lacunar canaliculi and that the canaliculi are stopped by the cement line before reaching the tessellation border. In addition, since our manual segmentation cannot be used as a ground truth volume, the evaluation of our segmentation is performed only by a visual grading. Future works on the improvement of the manual segmented results should be pursued.

In the proposed minimal path method, a reliable segmentation comes from the high voting value on the segmented structure. However, due to the high computation cost by this method, about 30 s for one path tracing, a tradeoff was made between the number of calculated paths and the computation time. To improve the segmentation, on one hand, within acceptable calculation time, more ends points, from the neighborhood of the tessellation boarder, can be used for the calculation. One the other hand, we could further accelerate the computation time by using GPU solutions. It has been well known that the graphics processors are more capable of parallel computing, running thousands of threads simultaneously. This is simply because, while a CPU only consists of a few cores optimized for sequential serial processing, a GPU contain up to thousands of smaller but more efficient cores, designed for handling multiple tasks simultaneously.

Chapter 9

Conclusion and perspective

The aim of this thesis was to develop new three dimensional image analysis methods to obtain characteristics on bone cellular structures, providing tools dedicated to the quantitative analysis of the SR micro/nano-CT 3D images. Based on the acquired large reconstructed 3D images at multiple spatial resolutions using SR micro/nano-CT, we proposed efficient methods to characterize the bone cellular network at lacunar level and canalicular level. We have shown the feasibility of using the proposed methods to perform automatic and quantitative studies on the series of human bone data. From the acquired quantitative results, interesting and important results are explored.

We showed that the SR micro/nano-CT images with isotropic voxels at the micrometer and nanometer scale are well suited for the quantification of the bone cellular system. It overcomes the limitation of the conventional techniques in three predominant ways. First, it gives more accuracy in the assessment of the 3D structure of LCN, by providing a high quality of image in terms of high spatial resolution and high SNR. Second, it provides a larger field of view, allowing to extract more statistically representative parameters. Third, benefiting from the monochrome and coherence of the X-ray beam, it allows both the quantitative study related to the degree of mineralization of the bone tissue and the organization of micro-structure.

Two synchrotron radiation micro- and nano-CT setups at different beamlines of the ESRF in Grenoble were used for multi-scale imaging. The experimental workflow, from bone sample preparation to data acquisition, and from image reconstruction to image enhancement and elimination of artifacts, has been established on each imaging beamline. The final acquired multiple resolution images, at 1.4 μm, 300 nm and 50 nm, are well suited for the hierarchical quantitative analysis on the bone cellular network.

For the quantitative assessment of lacunae, we proposed a fast and automated method to extract 3D morphological descriptors on large data sets of osteocyte lacunae. The moment method was shown to be well suited to model the ellipsoidal shape of lacuna. New descriptors, derived from intrinsic volumes, were calculated by a fast algorithm. We also introduced the 3D local lacunar density map to visualize the lacunar density variation within the bone sample. We reported the distribution and statistics on various morphological descriptors of lacunae, such as volume, surface and lengths of the three axes, from 13 human samples. Several strong correlations between osteocyte lacunar descriptors and bone porosities were also reported for the first time in 3D quantification.

For the assessment of canaliculi, we proposed a new automatic technique to assess the number of canaliculi issued from each lacuna and quantify the ramification pattern. This method was based on mathematical morphology operators and the calculation of topological parameters. Our calculation was verified on a simple phantom and a complete lacuna with

fully interconnected canaliculi. Contrary to a method that would try to identify each node of the canalicular network, this method has the advantage to be more flexible to imperfections in segmentation which are unavoidable with the limited spatial resolution compared to the canaliculi size. This method was successfully applied to a large SR nano-CT image of the human cortical femoral sample, scanned at spatial resolution of 300nm. A whole osteon region was included in this image. The statistical results on LCN morphological descriptors, based on the 399 lacunae, were reported for the first time.

Finally, we sought to apply our developed methods on a series of human tibial samples, with a large age variation. Since the assessment of canaliculi strongly relies on the quality of image segmentation, it was necessary to put efforts to improve the canalicular segmentation. For this, we worked on a novel automatic approach to perform the segmentation of the canaliculi using the minimum path extraction based on the fast marching method and the 3D geodesic voting. While this method is attractive to improve the connectivity of the segmentation, its computing time was prohibitive. Thus, a parallel computing scheme was implemented to reduce the computation time and enable the applications of the method to volumes including more than one hundred of lacuna. We also implemented post processing steps in the aim to decrease variations along the geodesic voting paths and to enhance the canaliculi paths based on the vesselness image. After segmentation, quantitative parameters were extracted. Although limitations exist in the proposed method, the data obtained is totally original.

While the topic of this thesis was mainly oriented on the quantification of the LCN structure from binary images, the evaluation of the results on real data is inevitable. For this purpose, we put a lot efforts to segment manually the canaliculi architecture on a large cubic volume (512×512×512 voxels, voxel size: 300 nm), about a cubic volume with side length of 153 μm. However, this work raised many difficulties, since achieving a high quality manual segmentation of such a complex network is a goal difficult to attain. Therefore in this application the manual segmentation is certainly not the best solution to serve as a ground truth. Ideally, imaging the same sample at 300 nm and 60 nm, could be used to have a real ground truth. However, in practice, this requires to scan the sample twice which could induce radiation damage on the sample and degrade the quality of the supposedly ground truth image. To build up the ground truth, another possibility could be to create a digital phantom. But, this operation requires the development of tools for realistic imaging simulation.

Concerning our contribution in the characterization of the LCN, the method proposed to quantify lacunae looks quite mature and can be used in further biological studied. However, many further developments can be pursued regarding to the properties of canaliculi. Particularly, approaches based on skeletonization could be used to retrieve network parameters such as the number of nodes, the average lengths of canaliculi between nodes, and the total length of canaliculi from a single lacuna. Moreover, it would be interesting to explore the parameters extracted on the image scanned at 60 nm, using our proposed quantification methods. At 300nm, the major obstacle is the segmentation of canaliculi. For the moment, our methods only use the information from the gray-level of the image. Improvement on the segmented result could be achieved by exploiting also directional

information. A different approach for the quantification could be to perform texture analysis, working directly on the gray-level image, thus avoiding image segmentation.

From a biological point of view, this work opens up many opportunities, due to the fact that there are still very little quantitative data on the 3D lacuno-canalicular network. On one hand, our proposed quantification method, regarding the extraction of lacunar descriptors, is mature enough to be applied on series of samples, showing variations with age, diseases or anatomical sites. Regarding to the canaliculi, with the improvement of the method, new information could be derived from this little-known network. Another important application is in the field of biomechanics, since our segmented 3D LCN images could be served as realistic models to build up biomechanical simulations.

Annex 1

In this Annex, we attached the tables, which review the animal lacunar and canalicular descriptors in the literature.

Table 10.1 Animal lacunar density reported in 2D

Reference	Dim	Imaging Tech.	Species	Location	Groups	# Samples	Lc/ Ot	Value
								Density to bone matrix N.Lc/BA (#/mm^2)
[Remaggi *et al.* (1998)]	2D	LM	Frog, chick, rabbit, bovine, horse, dog and human	Parallel-fibered in shaft bone			Lc	200~1900 (human 550)
[Ferretti et al. (1999)]	2D	LM	Frog, sheep, dog, bovine, horse and human	Tibia compact bone		3	Lc	460~1050 (human 460)
[Da Costa Gómez et al. (2005)]	2D	LM	Horse	Mid-diap	Racing		Ot	589
					Non-racing		Ot	552
[Skedros et al. (2005)]	2D	SEM (BSE)	Horse	MC3 Tension '1' (D, D-L, L)		9	Lc	494.5 ± 98.8
				MC3 Tension '2' (D-L, L)		9	Lc	474.8 ± 99.0
				MC3 'C1' (P-L, P, P-M, M, D-M)		9	Lc	463.8 ± 105.5
				MC3 'C2' (P-L, P, P-M, M)		9	Lc	446.6 ± 92.6
				MC3 'C3' (P-L, P, P-M)		9	Lc	427.3 ± 91.6
				MC3 'C4' (P, P-M, M)		9	Lc	451.6 ± 92.7
			Horse	Radius Cr 'tension'		10	Lc	478.2 ± 137.3
				Radius Cd 'compression'		10	Lc	522.1 ± 152.4
				Radius M		10	Lc	512.7 ± 129.0
				Radius L		10	Lc	532.1 ± 124.9
								Density to tissue N.Lc/TA (#/mm^2)
[Ma et al. (2008)]	2D	Micro-CT	Rat	Vertebral trabeculae	SHAM		Ot	1760.8 ± 376.6
					OVX		Ot	1299.6 ± 352.8
					EST		Ot	1550.9 ± 202.2
					GEN		Ot	1550.7 ± 215.5

Table 10.2 Animal lacunar density reported in 3D

Reference	Dim	Imaging Tech.	Species	Location	Groups	# Samples	Lc/Ot	Value
								N.Lc/BV (#/mm^3)
[Sharma et al. (2012)]	3D	CLSM	Rat	Cortical bone: metaphysis	SHAM	6	Lc	67300 ± 14000
					OVX	6	Lc	77000 ± 25000
[Britz et al. (2012)]	3D	SR µCT	Rat	Tibia	Control		Lc	63,138 ± 1956
					Immobilized		Lc	49,641 ± 11,955
								N.Lc/TV (#/mm^3)
[Schneider et al. (2007)]	3D	SR CT	Mice	Femoral mid-diaphysis			Lc	49879~65865
[Tommasini et al. (2012)]	3D	SR µCT	Rat	Femoral diaphysis	Control	6	Lc	56,470 (13,710)
					OVX	6	Lc	63,670 (14,110)
					ALN	6	Lc	59,510 (9370)
					PTH	6	Lc	63,810 (9420)
								Density (category unknown) (#/mm^3)
[Fritton *et al.* (2005)]	2D+	CLSM	Rat	Tibia		6	Lc	80.600/mm^3

median (interquartile range)

Table 10.3 morphological parameters of osteocytes or lacunae in 2D

Reference	Dim	Imaging Tech.	Species	Location	Groups	# Samples	Lc/Ot	Value
								Area (μm^2)
[Shapiro (1988)]	2D	LM	Rabbit	Femoral mid-diaphysis cortical bone		17 male and 12 female rabbit	Ot	139.8±76.8
[Remaggi *et al.* (1998)]	2D	LM	Frog, chick, rabbit, bovine, horse, dog and human	Parallel-fibered in shaft bone			Lc	22~40 (human 26)
[Ferretti et al. (1999)]	2D	LM	Frog, sheep, dog, bovine, horse and human	Tibia compact bone		3	Lc	21~42 (human 25)
[Jordan et al. (2003)]	2D	LM	Human	Femur	Control		Lc	37 ± 5.4
					Coxarthrosis (coa)		Lc	49 ± 7
					Osteoporotic femoral neck fracture (FNF)		Lc	51 ± 1.1
[L Wang *et al.* (2005)]	2D	FRAP	Mice	Left tibia diaphysis		7	Lc	91 ± 18.9
								Length (μm)
[Shapiro (1988)]	2D	LM	Rabit	Femoral mid·diaphysea l cortical bone		17 male and 12 female rabbit	Ot	16.7±3.8
[Remaggi *et al.* (1998)]	2D	LM	Frog, chick, rabbit, bovine, horse, dog and human	Parallel-fibered in shaft bone			Lc	20~50 (human 25)
[L Wang *et al.* (2005)]	2D	FRAP	Mice	Left tibia diaphysis			Lc	9 ± 1.4
[Lin et al. (2011)]	2D	AFM	Bovine	Tibia cortical	Radial direction	1	Lc	10.88 ± 3.38 (5.10 ~ 16.99)
					Transverse direction	1	Lc	9.66 ± 2.82 (4.86 ~ 13.50)
								Width (μm)
[Shapiro (1988)]	2D	LM	Rabit	Femoral mid·diaphyseal cortical bone		17 male and 12 female rabbit	Ot	4.2±1.9
[Remaggi *et al.* (1998)]	2D	LM	Frog, chick, rabbit, bovine, horse, dog and human	Parallel-fibered in shaft bone			Lc	8~13 (human 10)

[L Wang *et al.* (2005)]	2D	FRAP	Mice	Left tibia diaphysis		7	Lc	3 ± 0.5
[Lin et al. (2011)]	2D	AFM	Bovine	Tibia cortical	Transverse direction	1	Lc	3.86 ± 1.02 (2.57 ~ 6.17)
					Radial direction	1	Lc	5.37± 1.71 (3.57 ~ 8.78)
								Depth (µm)
[Remaggi *et al.* (1998)]	2D	LM	Frog, chick, rabbit, bovine, horse, dog and human	Parallel-fibered in shaft bone			Lc	3~5 (human 5)
								Perimeter (µm)
[Shapiro (1988)]	2D	LM	Rabit	Femoral mid·diaphyseal cortical bone		17 male and 12 female rabbit	Ot	36.4±8.2
[L Wang *et al.* (2005)]	2D	FRAP	Mice	Left tibia diaphysis		7	Lc	41 ± 5.7
								Anisotropy
[Shapiro (1988)]	2D	LM	Rabit	Femoral mid·diaphyseal cortical bone		17 male and 12 female rabbit	Ot	4.0:1 (L1:L2)

Table 10.4 Animal morphological parameters of osteocytes or lacunae in 3D

Reference	Dim	Imaging Tech.	Species	Location	Groups	# Samples	Lc/Ot	Value
								Volume (µm^3)
[Sugawara *et al.* (2005)]	2D+	CLSM	Chick	Calvarial		?	Ot	257
[Sugawara et al. (2011)]	2D+	CLSM	Chick	Parietal bone		10	Ot	332
		CLSM	Mouse	Parietal bone		10	Ot	641
[Remaggi *et al.* (1998)]	2D->3D	LM	Frog, chick, rabbit, bovine, horse, dog and human	Parallel-fibered in shaft bone			Lc	350~850 (human (570)
[L Wang *et al.* (2005)]	2D->3D	FRAP	Mice	Left tibia diaphysis		7	Lc	421 ± 134.8
[Sharma et al. (2012)]	2D->3D	CLSM	Rat	Cortical bone: metaphysis	SHAM	6	Lc	352 ± 30
				Cortical bone: metaphysis	OVX	6	Lc	393 ± 92
[Schneider et al. (2007)]	3D	SR CT	Mice	Femoral mid-diaphyses			Lc	200 ~ 269
[Britz et al. (2012)]	3D	SR µCT	Rat	Tibia	Control		Lc	284 ± 28
					Immobilized		Lc	209 ± 72
[Tommasini et al. (2012)]	3D	SR µct	Rat	Femoral diaphysis	Control	6	Lc	266.0 (43.3)
					OVX	6	Lc	248.4 (44.9)
					ALN	6	Lc	237.0 (47.2)
					PTH	6	Lc	268.1 (18.3)
								Surface (µm^2)
[Sugawara *et al.* (2005)]	2D+	CLSM	Chick	Calvarial		?	Ot	724
[Sugawara et al. (2011)]	2D+	CLSM	Chick	Parietal bone		10	Ot	666
			Mouse	Parietal bone		10	Ot	1,067
[L Wang *et al.* (2005)]	2D->3D	FRAP	Mice	Left tibia diaphysis		7	Lc	305 ± 62.6
								Length (µm)
[Fritton *et al.* (2005)]	2D+	CLSM	Rat	Tibia		6	Lc	17.6 ± 0.3
[Vatsa *et al.* (2008)]	2D+	CLSM	Mice	Fibular		?	Ot	28.74 ± 4.67
				Calvarial		?	Ot	13.22 ± 1.47
								Width (µm)
[Fritton *et al.* (2005)]	2D+	CLSM	Rat	Tibia		6	Lc	6.1 ± 0.3
[Vatsa *et al.* (2008)]	2D+	CLSM	Mice	Fibular	Fibular	?	Ot	7.60 ± 1.15
			Mice	Calvarial	Calvarial	?	Ot	8.07 ± 0.51
								Depth (µm)
[Fritton *et al.*	2D+	CLSM	Rat	Tibia		6	Lc	4.0 ± 0.2

(2005)]								
[Vatsa *et al.* (2008)]	2D+	CLSM	Mice	Fibular		?	Ot	5.03 ± 0.80
				Calvarial		?	Ot	6.56 ± 0.64
								Anisotropy
[Vatsa *et al.* (2008)]	2D+	CLSM	Mice	Fibular		?	Ot	5.9:1.5:1 (L1:L2:L3)
				Calvarial		?	Ot	2.1:1.3:1 (L1:L2:L3)
[Vatsa *et al.* (2008)]	3D	Nano-CT	Mice	Fibular		?	Lc	3.33
				Calvarial		?	Lc	2.1
								Distance (µm)
[Sugawara et al. (2011)]	2D+	CLSM	Chick	Parietal bone		32 different regions in chicks (n = 11)	Ot	23.5 ± 6.1
			Mouse	Parietal bone		32 different regions in mice (n = 12)	Ot	39.6 ± 11.6
[Sugawara *et al.* (2005)]	2D+	CLSM	Chick	Calvarial		?	Ot	24.1 ± 2.8
[Da Costa Gómez et al. (2005)]	2D->3D	LM	Horse	Mid-diap	Racing		Ot	58
					Non-racing		Ot	60
[Skedros et al. (2005)]	2D->3D	SEM (BSE)	Horse	MC3		9	Lc	61~69
			Horse	Radius Cr ‘tension’		10	Lc	65
				Radius Cd ‘compression’		10	Lc	62
				Radius M		10	Lc	62
				Radius L		10	Lc	61
								Osteocyte span Volume (µm^3)
[Sugawara *et al.* (2005)]	2D+	CLSM	Chick	Calvarial		?	Ot	4180 ± 673
[Sugawara et al. (2011)]	2D+	CLSM	Chick	Parietal bone		10	Ot	4691 ± 935
			Mouse	Parietal bone		12	Ot	10665 ± 1510

Annex 2

In this annex, we attached the reconstructed images acquired using SR micro and nano-CT at different resolutions. For all of the sample series, images with voxel size of 3.5 µm and 300 nm are included. The former ones were acquired from beamline BM05 of ESRF, and the latter ones were acquired at beamline ID19 of ESRF. Among the samples, three of the human tibia specimens were also scanned at ID22 for imaging at ultra-resolution with voxel size of 60 nm.

In addition, we also showed the images, which were cropped from the images with voxel size of 300 nm and were used for LCN segmentation and quantification. These images include: 1) the minimum intensity projection view of 100 consecutive slices of reconstructed image, 2) the corresponded maximum intensity maps of the segmented canalicular network and 3) the corresponded maximum intensity maps of the segmented LCN in color. For the color image, a lacuna with the cold color (blue) represents a smaller volume and warm color (red) represents a larger volume. The canaliculi are rendered only in blue without any morphological meanings. The images are generated using ImageJ (NIH).

Tibia

Female

ID05: Tibia Female Age45

mqir_ID05_tib45_61604_P69_

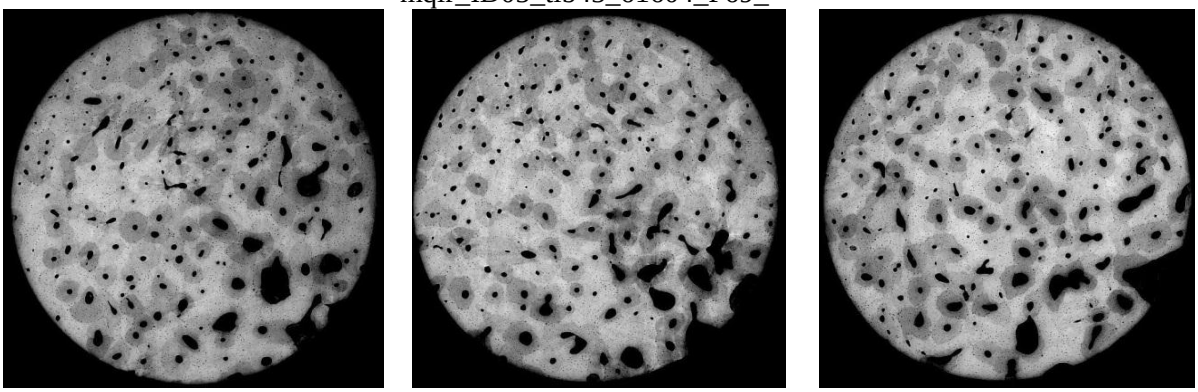

TOP MIDDLE BOTTOM

5D: mqir_tib45_61604_can05DD_dry_pag0001RC_

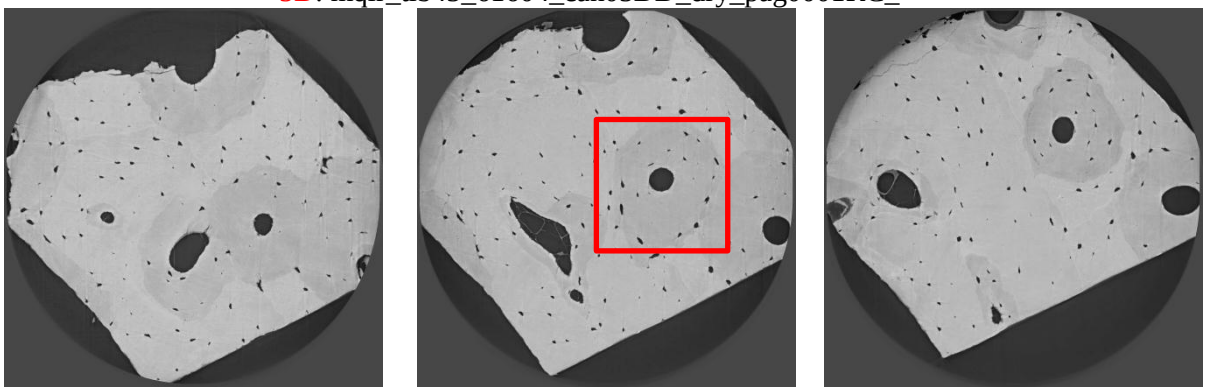

Z100 Z1000 Z2000

5D: MinIP of a crop region: 800x800x600

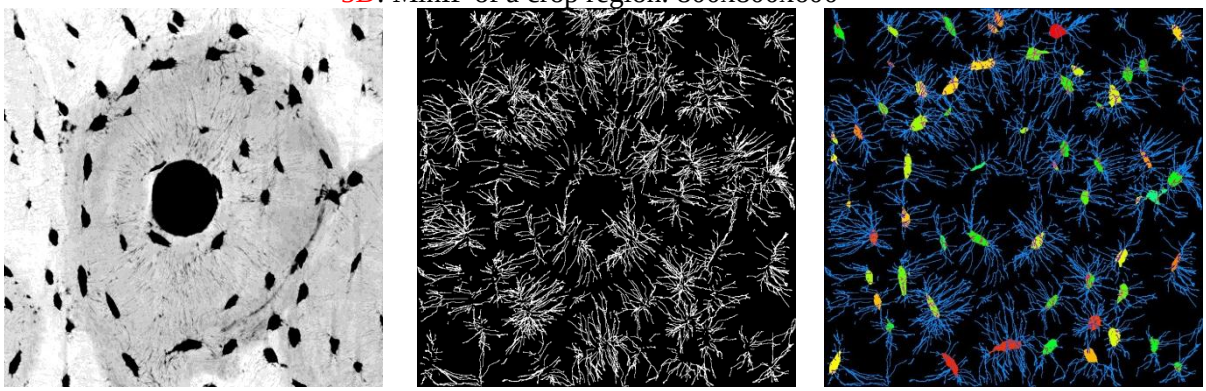

MinIP of the reconstructed image | MaxIP of the binary canaliculi image | MaxIP of the labeled LCN image

ID	Part	Units (mm)
05	A	0.6*0.6
	B	0.5*0.5
	C	0.62*0.56
	D	0.52*0.55

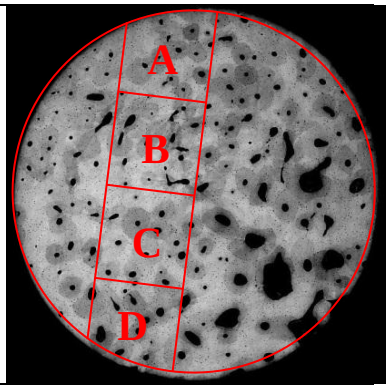

ID13: Tibia Female Age 84

mqir_ID13_tib84_59907_P69_

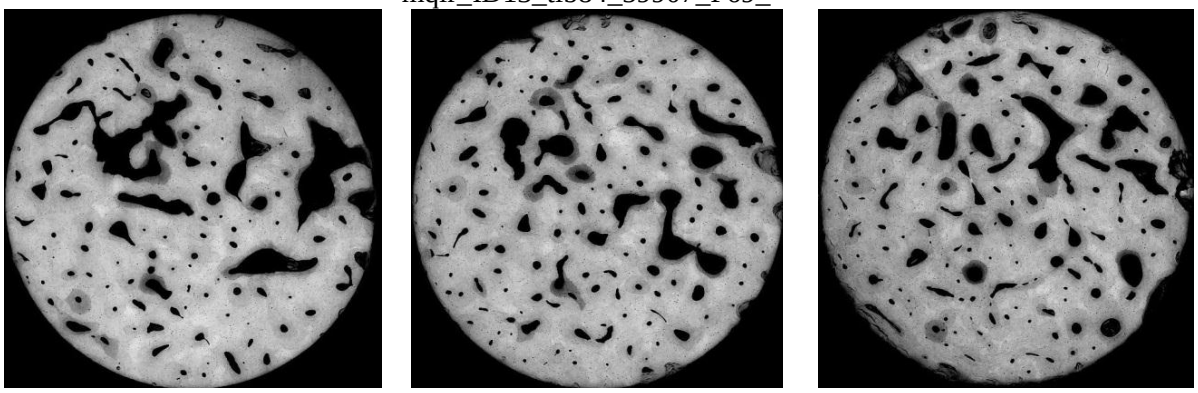

TOP MIDDLE BOTTOM

13D: mqir_tib84_59907_can13D_pag0001RC_

Z100 Z1000 Z2000

13D: MinIP of a crop region: 800x800x600

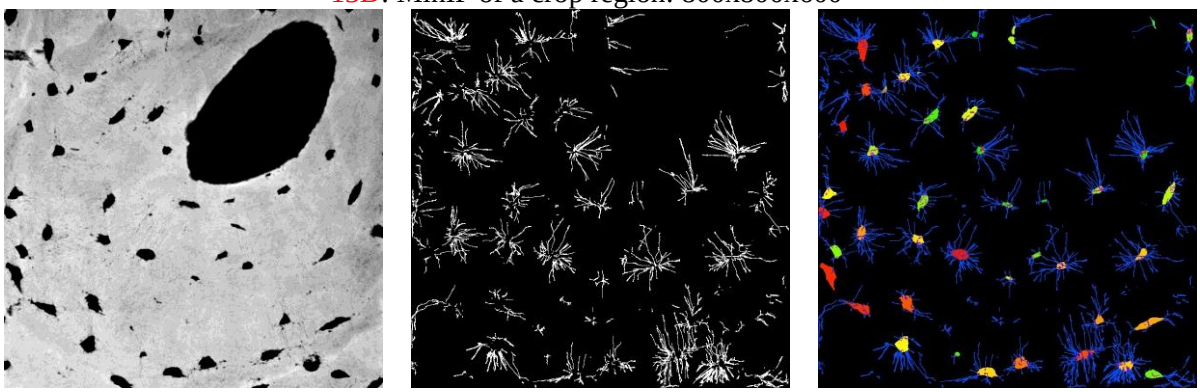

MinIP of the reconstructed image | MaxIP of the binary canaliculi image | MaxIP of the labeled LCN image

ID	Part	Units (mm)	
13	D	0.60*0.66	
	E	0.61*0.67	

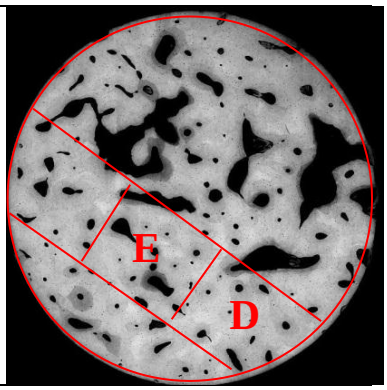

ID15: Tibia Female Age 87

mqir_ID15_tib87_59966_P69_

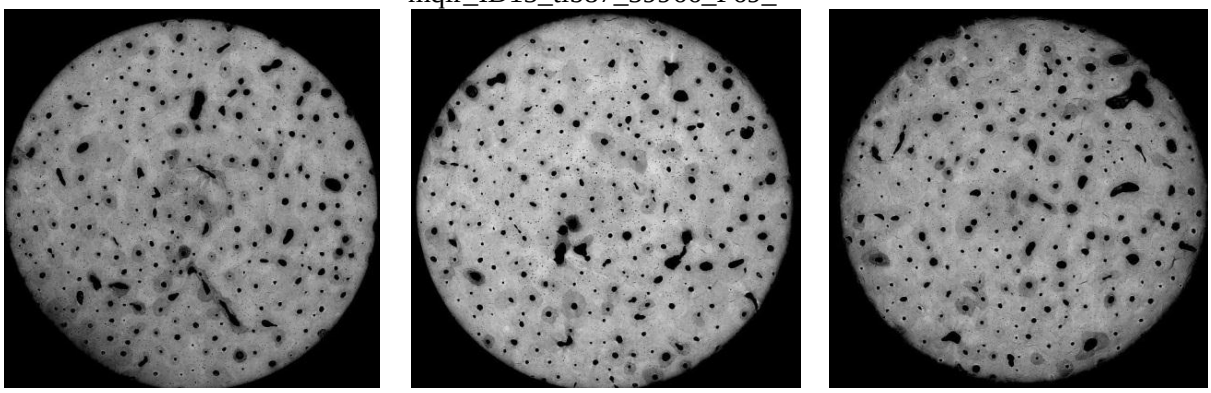

TOP MIDDLE BOTTOM

15E: mqir_tib87_59966_15E_dry_pag0001RC_

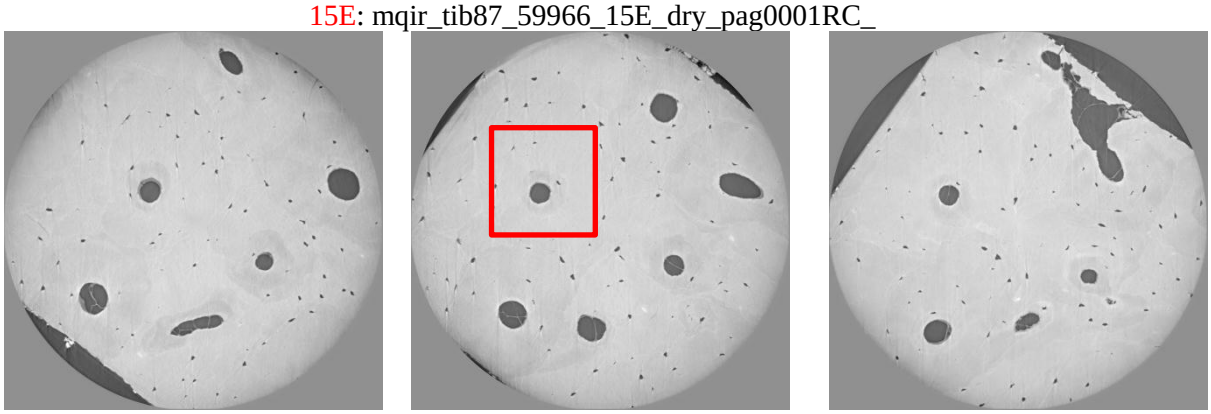

Z100 Z1000 Z2000

15E: MinIP of a crop region: 600x600x600

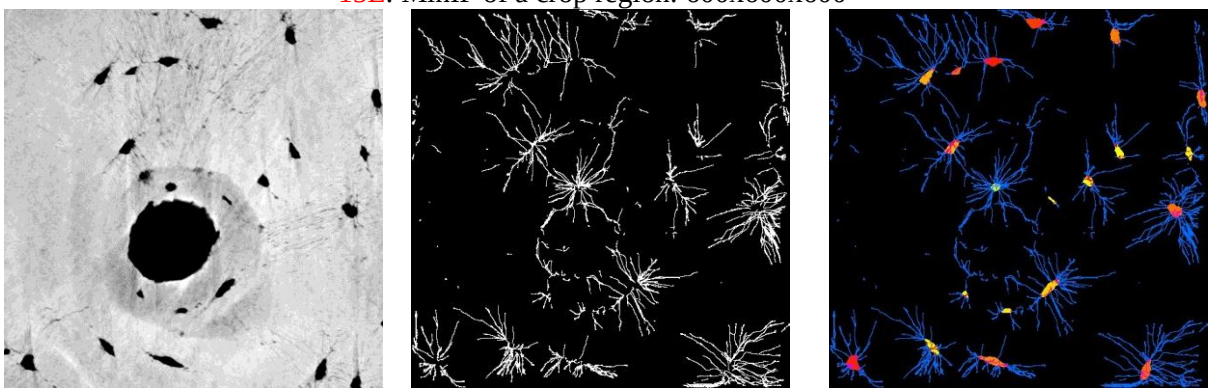

MinIP of the reconstructed image | MaxIP of the binary canaliculi image | MaxIP of the labeled LCN image

ID	Part	Units (mm)	
15	D	0.61*0.63	
	E	0.62*0.57	

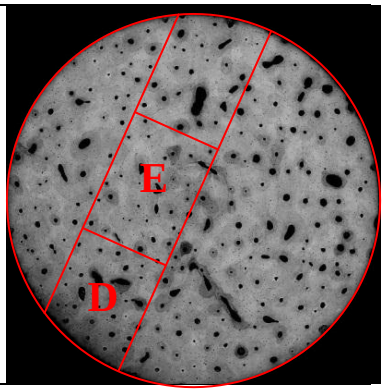

Male

ID01: Tibia Male Age 29

mqir_ID01_tib29_59869_P69_

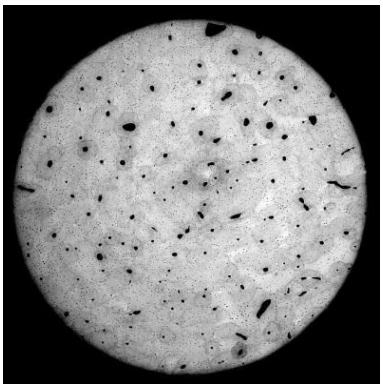
TOP

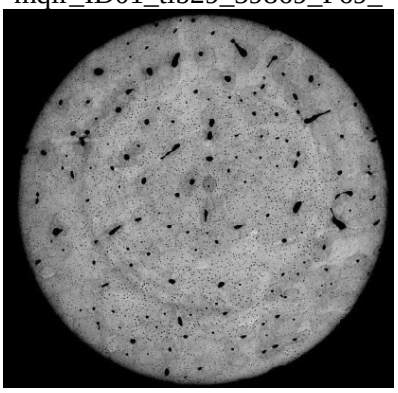
MIDDLE

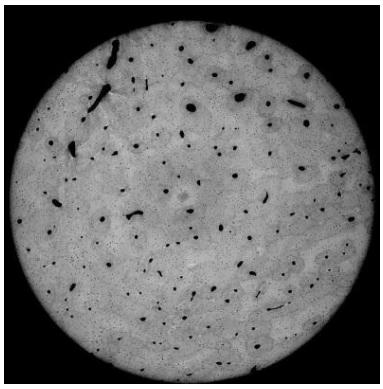
BOTTOM

1F: mqir_tib29_59869_can1F_pag0001RC_

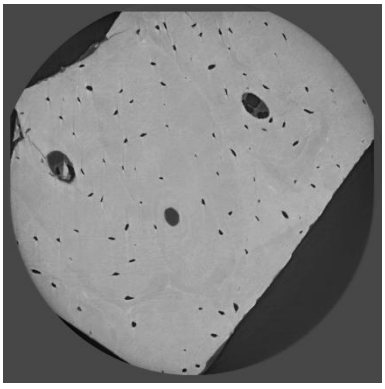
Z100

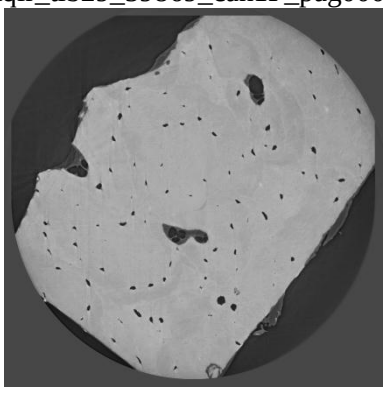
Z1000

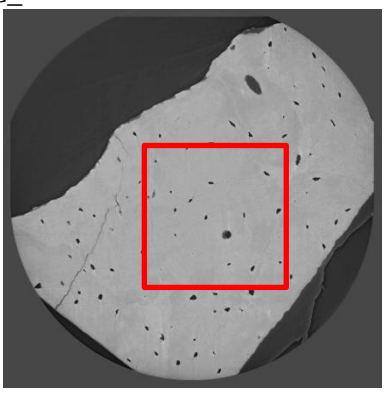
Z2000

1F: MinIP of a crop region: 800x800x600

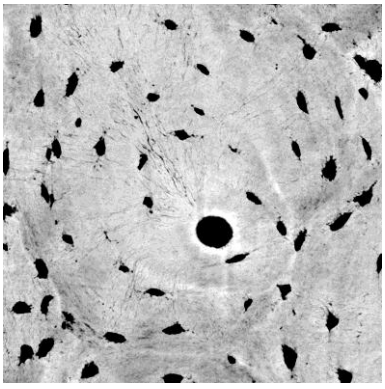
MinIP of the reconstructed image

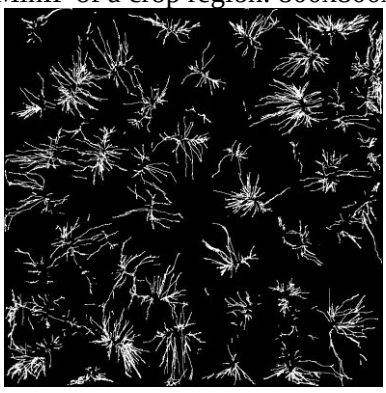
MaxIP of the binary canaliculi image

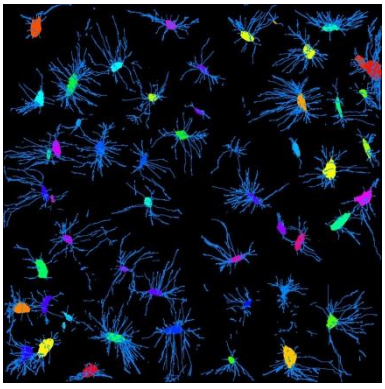
MaxIP of the labeled LCN image

1F(50 nm):mqir_tib29_59869_can1F_050_m

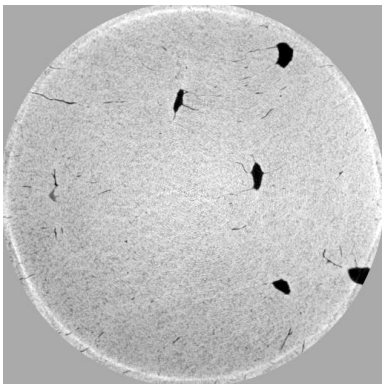

Z967

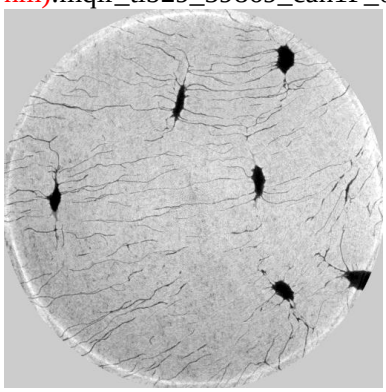

MIP Z901-1000

ID	Part	Units (mm)
01	D	0.83*0.97
	E	0.37*0.74
	E'	0.95*1.13
	F	0.44*0.44

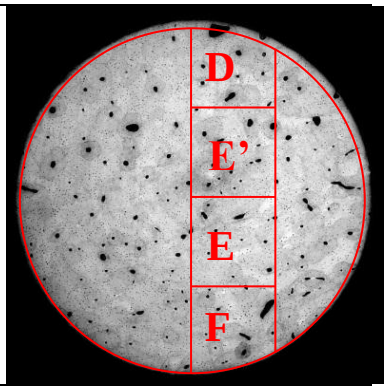

ID09: Tibia Male Age 56

mqir_ID09_tib56_59704_P69_

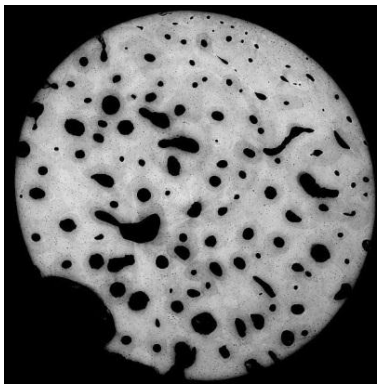

TOP

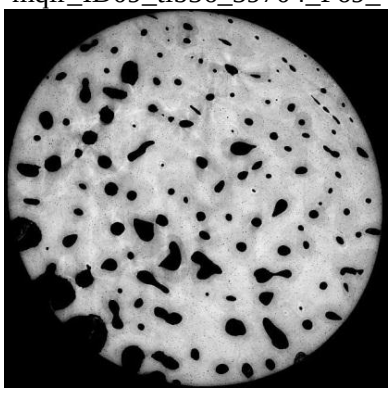

MIDDLE

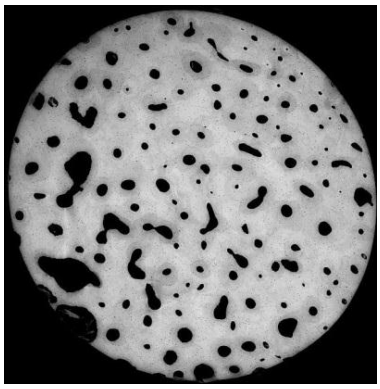

BOTTOM

9E: mqir_tib56_59704_can9D_pag0001RC_

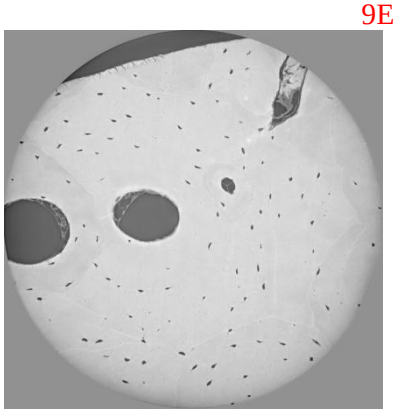

Z100

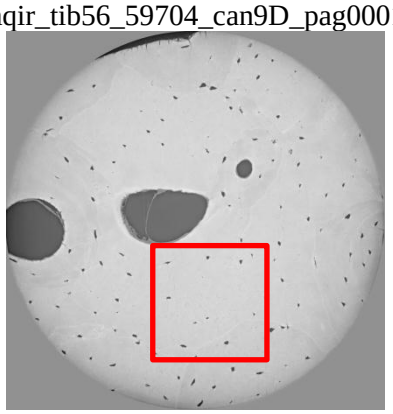

Z1000

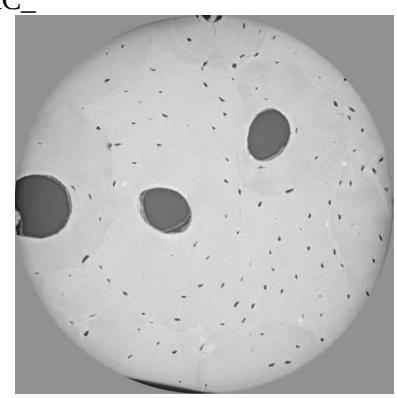

Z2000

9E: MinIP of a crop region: 512x512x512

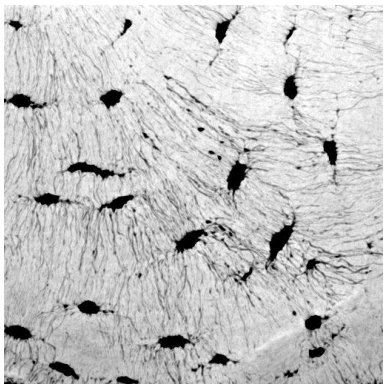

MinIP of the reconstructed image

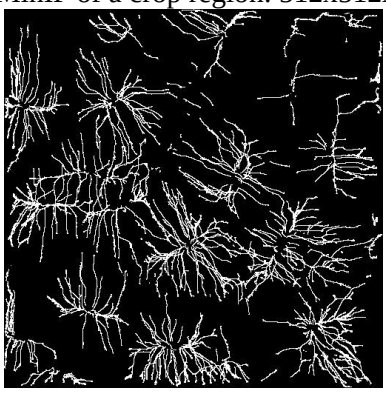

MaxIP of the binary canaliculi image

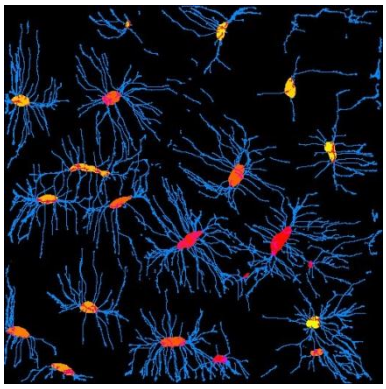

MaxIP of the labeled LCN image

9D: mqir_tib56_59704_can9DD_pag0001RC_

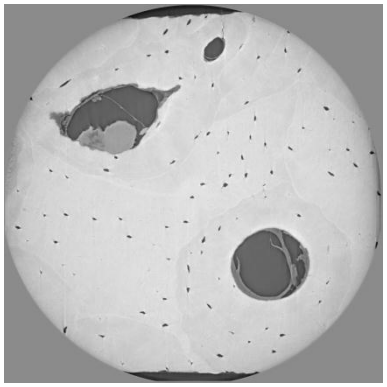
Z100

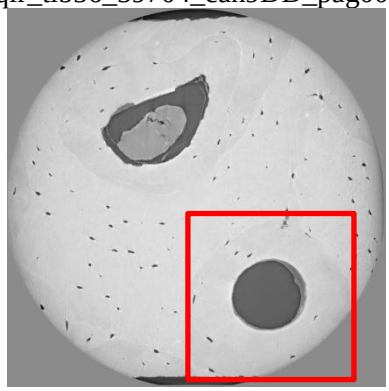
Z1000

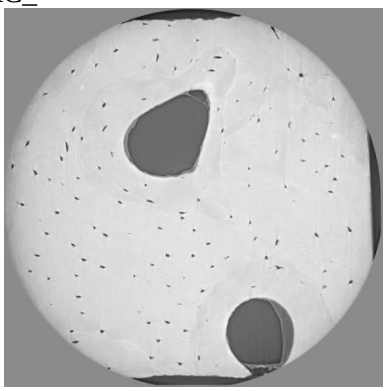
Z2000

9D: MinIP of a crop region: 900x900x600

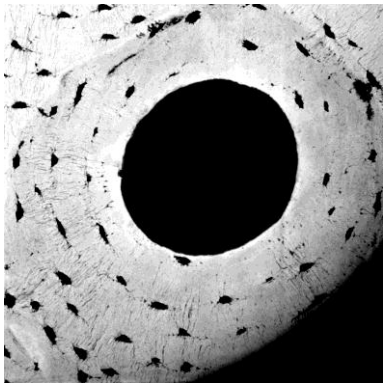
MinIP of the reconstructed image

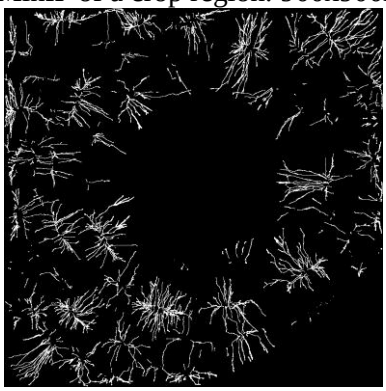
MaxIP of the binary canaliculi image

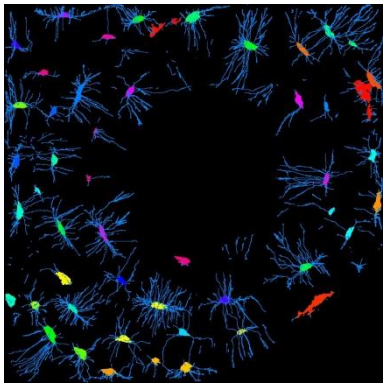
MaxIP of the labeled LCN image

9E (50 nm):: mqir_tib56_59704_can9E_050_m

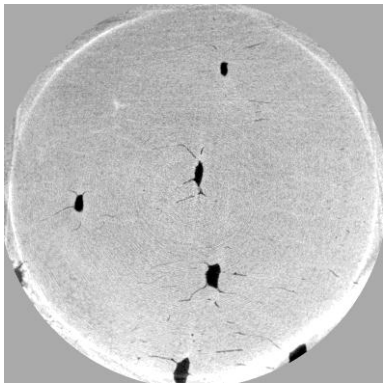
Z908

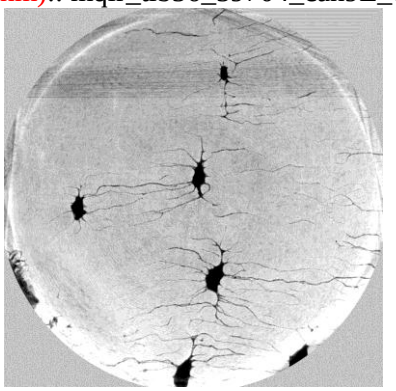
MIP Z901-1000

ID	Part	Units (mm)	
09	D	0.61*0.55	
	E	0.62*0.67	

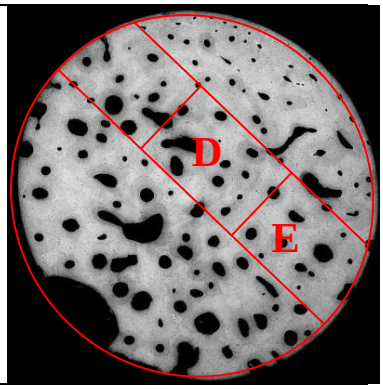

ID16: Tibia Male Age 88

mqir_ID16_tib88_60028_P69_

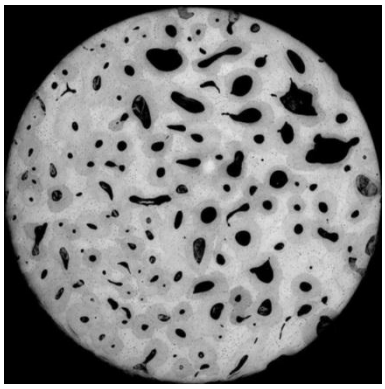

TOP

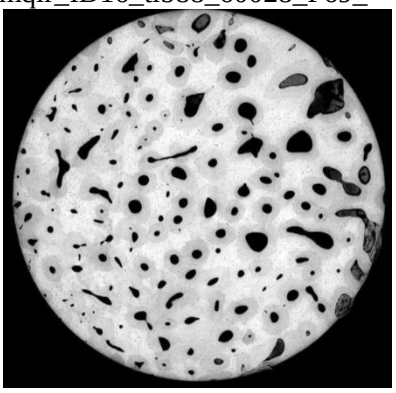

MIDDLE

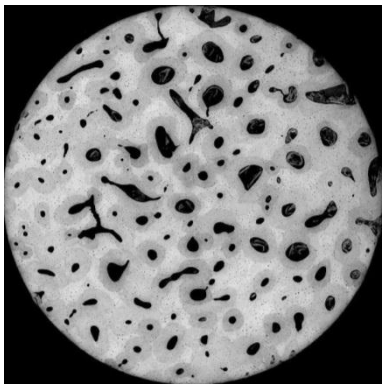

BOTTOM

16E: mqir_tib88_60028_can16E_dry_pag0001RC_

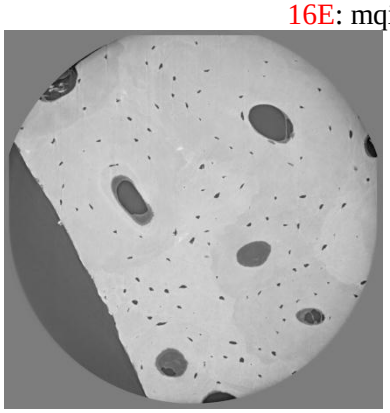

Z100

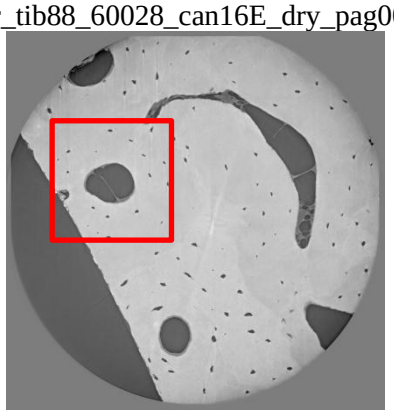

Z1000

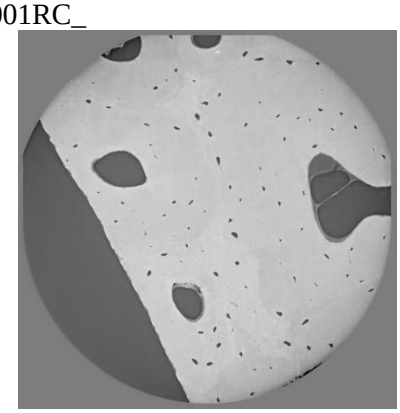

Z2000

16E: MinIP of a crop region: 700x700x500

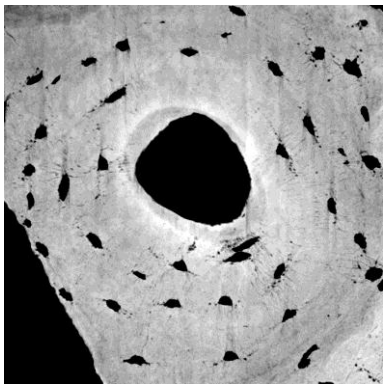

MinIP of the reconstructed image

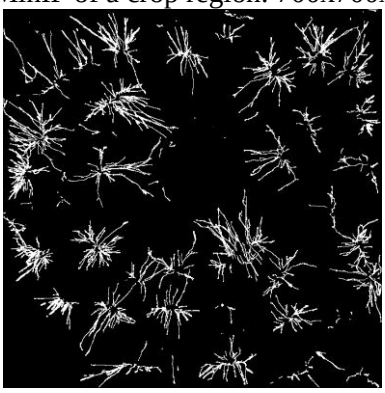

MaxIP of the binary canaliculi image

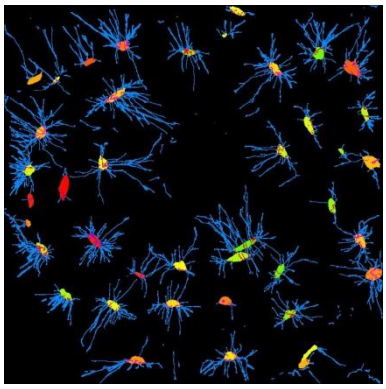

MaxIP of the labeled LCN image

16F: mqir_tib88_60028_can16F_pag0001RC_

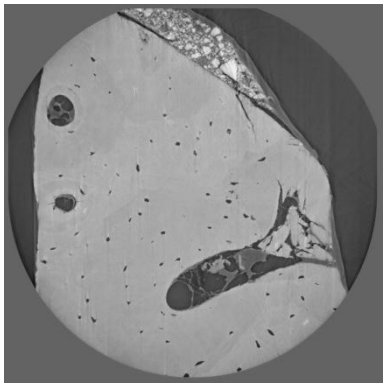
Z100

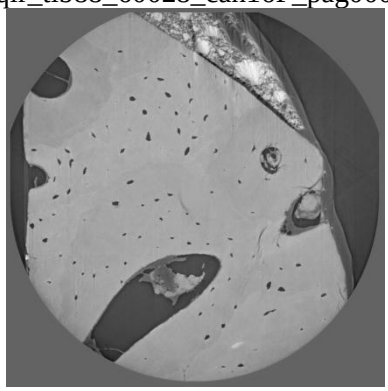
Z1000

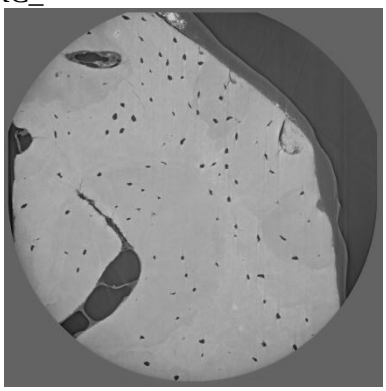
Z2000

16F (50 nm): MIN_mqir_tib88_60028_can16F_050_

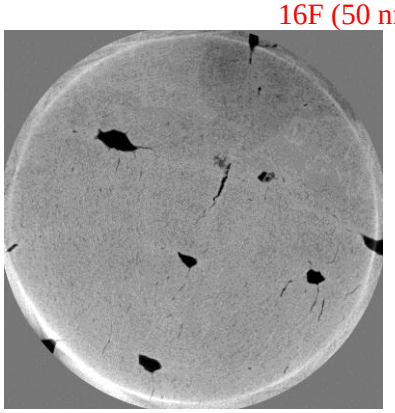
Z259

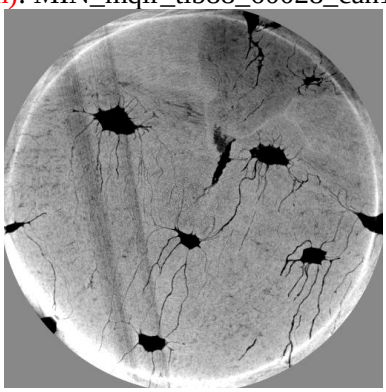
MIP Z201-300

ID	Part	Units (mm)
16	E	0.63*0.51
	F	0.73*0.64

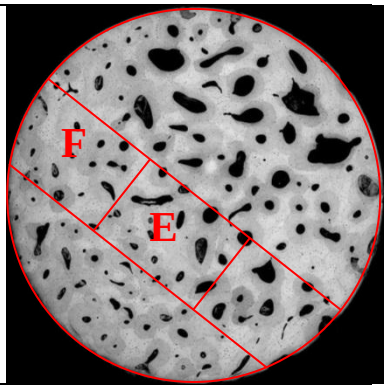

ID18: Tibia Male Age 89

mqir_ID18_tib89_59798_P69_

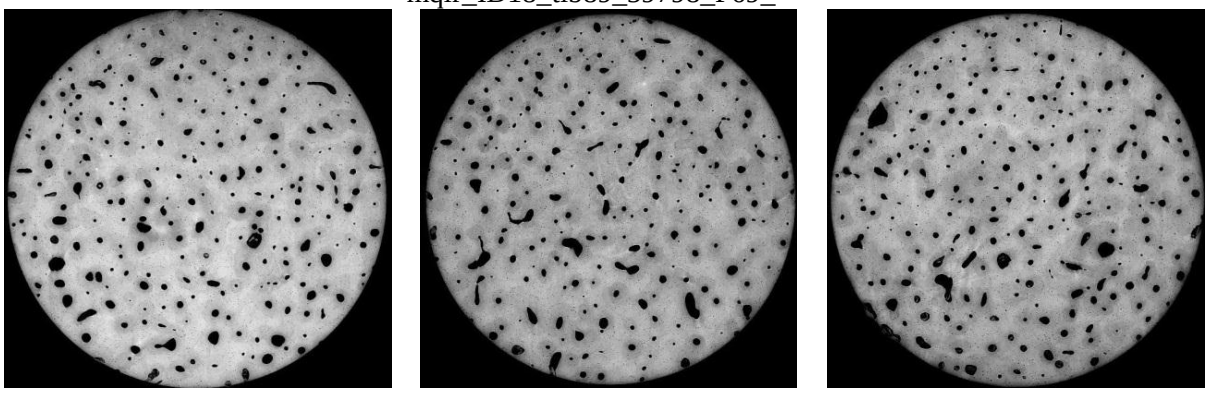

TOP MIDDLE BOTTOM

18D: mqir_tib89_59798_can18D_pag0001RC_0100

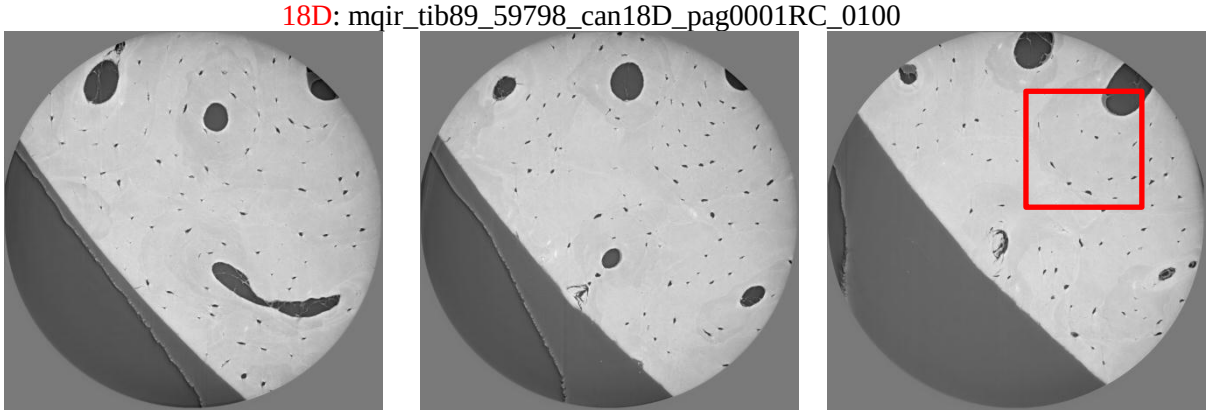

Z100 Z1000 Z2000

18E: MinIP of a crop region: 600x600x600

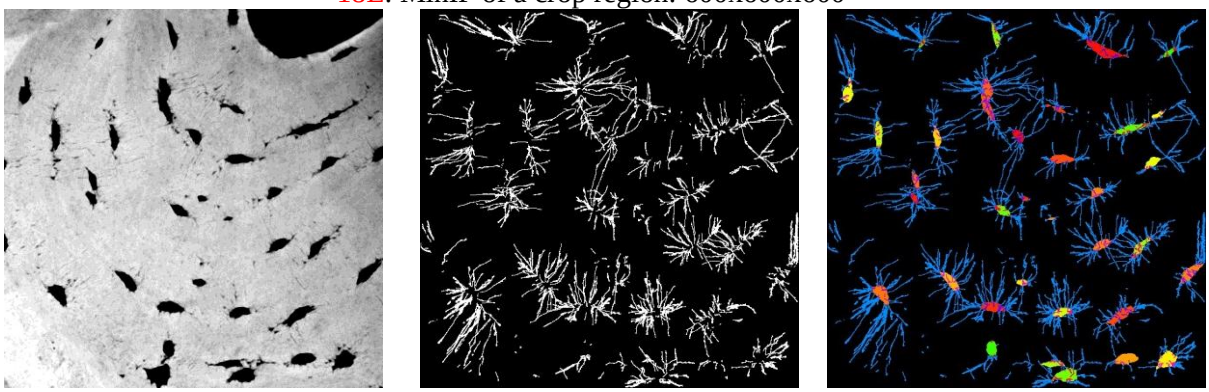

MinIP of the reconstructed image | MaxIP of the binary canaliculi image | MaxIP of the labeled LCN image

18E: mqir_tib89_can18E_pag0001RC_0100

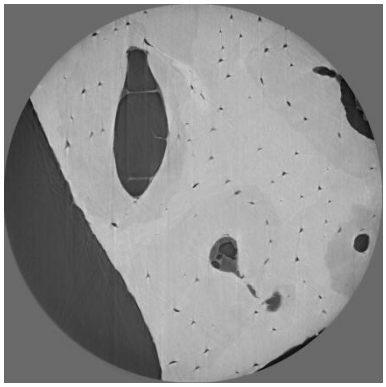

Z100

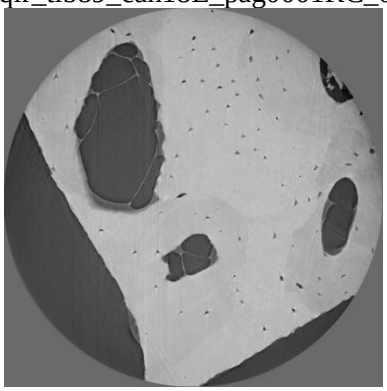

Z1000

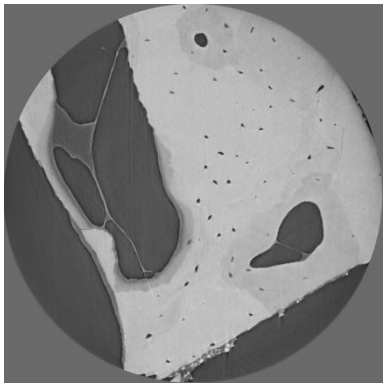

Z2000

ID	Part	Units (mm)
18	D	0.92*0.67
	E	0.67*0.71

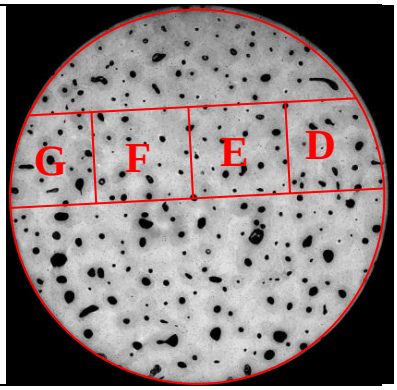

Knee

Female

ID02: Knee Female Age 37

mqir_ID02_fem37_62057_P69_

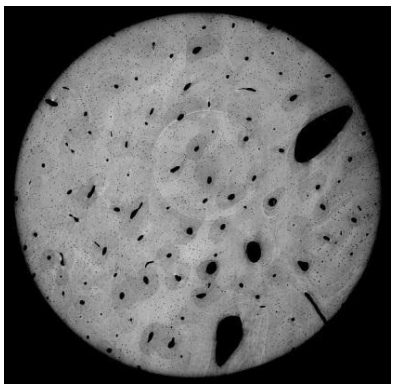
TOP

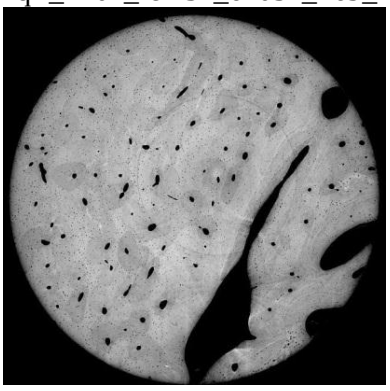
MIDDLE

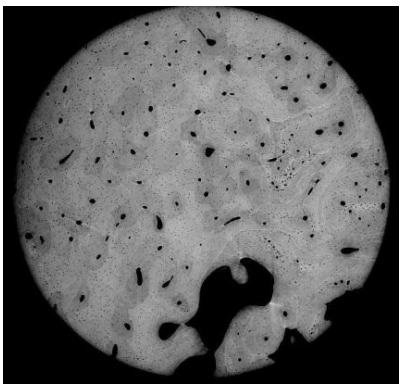
BOTTOM

2D: mqir_fem37_62057_can2D_pag0001RC_

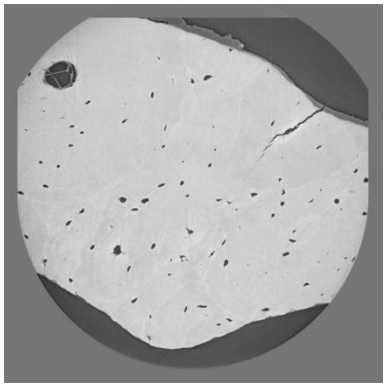
Z100

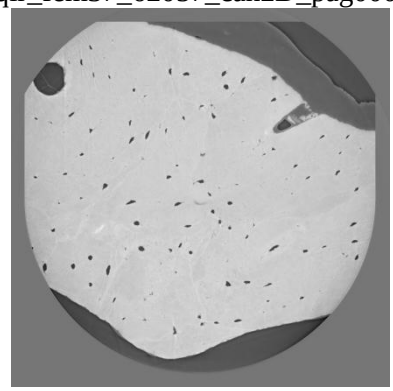
Z1000

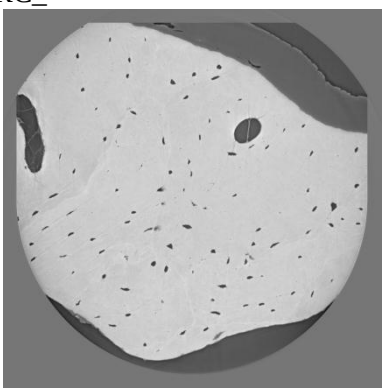
Z2000

ID	Part	Units (mm)
02	D	0.5*0.7
	E	0.55*0.55

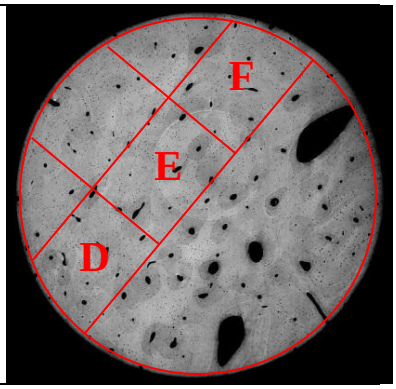

ID04: Knee Female Age 45

mqir_ID04_fem45_61604_P69_

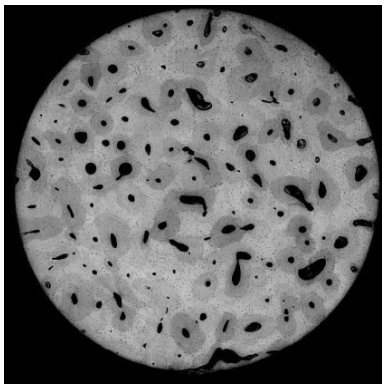
TOP

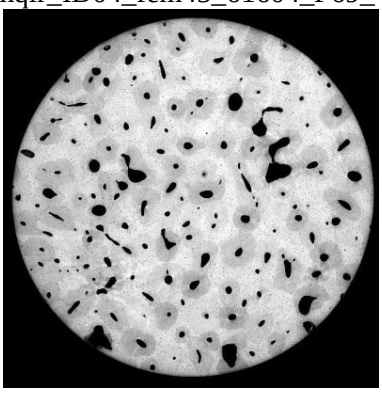
MIDDLE

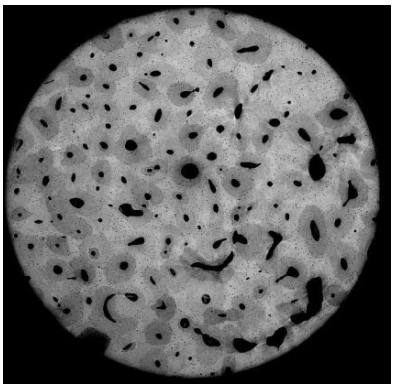
BOTTOM

4C: mqir_fem45_61604_can4C_dry_pag0001RC_

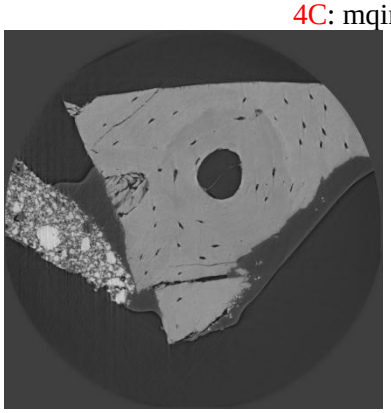
Z100

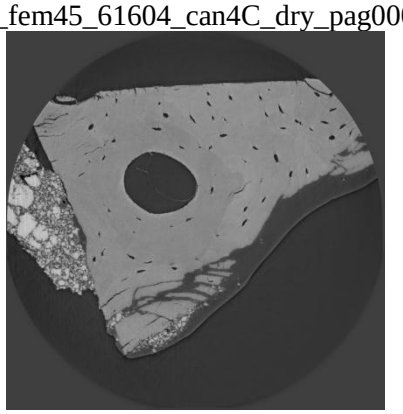
Z1000

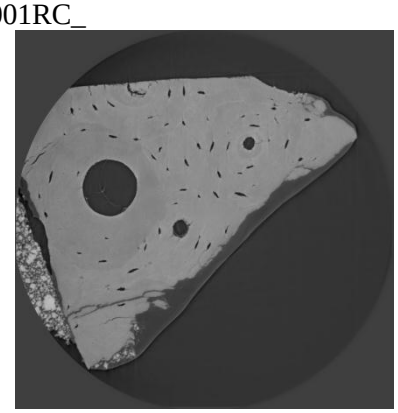
Z2000

ID	Part	Units (mm)
04	B	0.4*0.4
	C	0.4*0.4

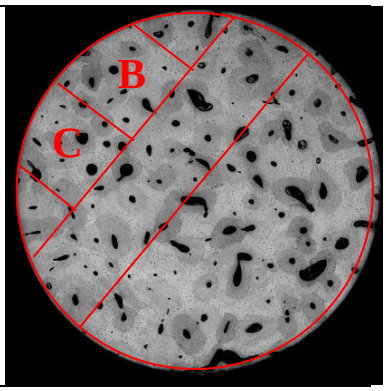

Male

ID03: Knee Male Age 43

mqir_ID03_fem43_62384_P69_

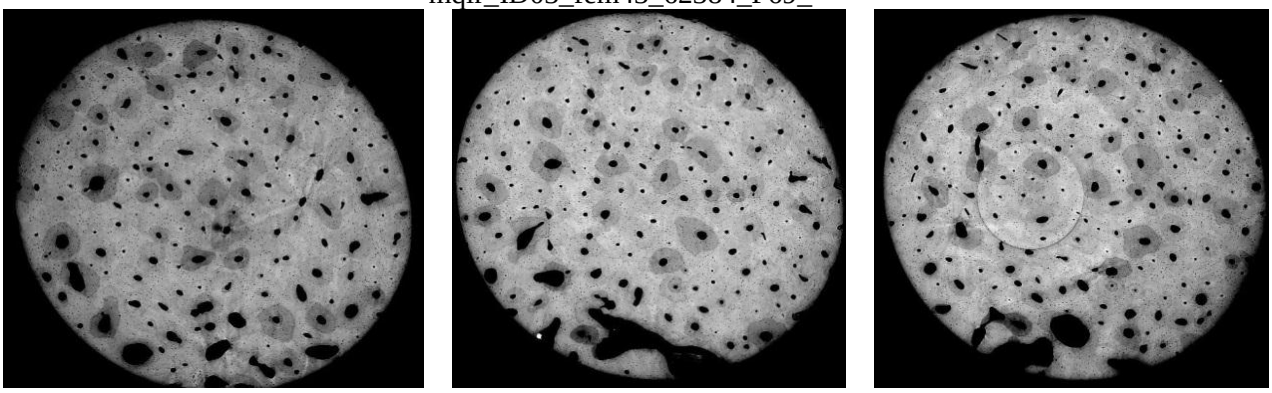

TOP MIDDLE BOTTOM

3D: mqir_fem43_62384_can3D_pag0001RC_

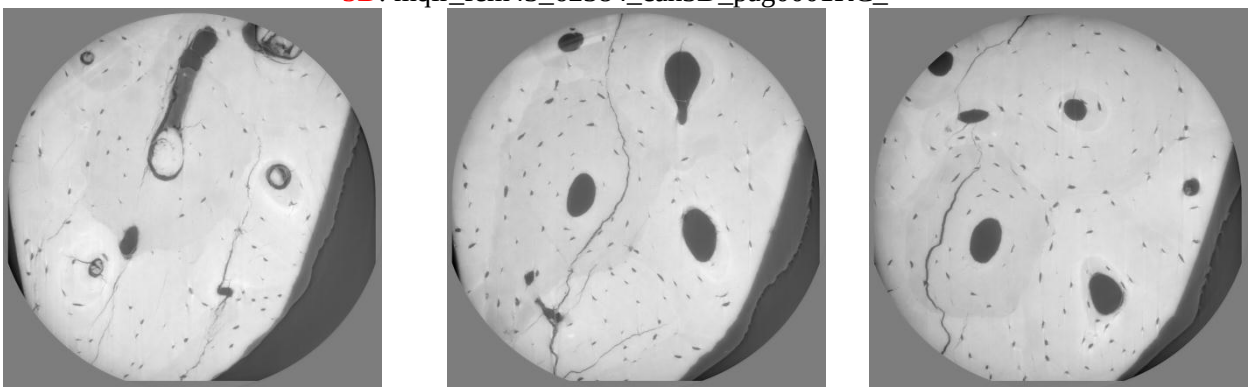

Z100 Z1000 Z2000

3E: mqir_fem43_62384_can3E_dry_pag0001RC_

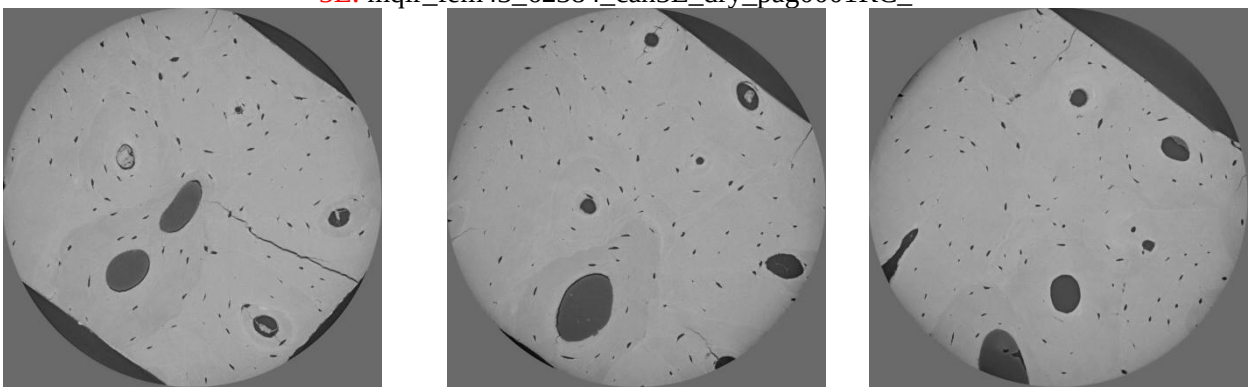

Z100 Z1000 Z2000

ID	Part	Units (mm)
03	D	0.68*0.69
	E	0.55*0.67

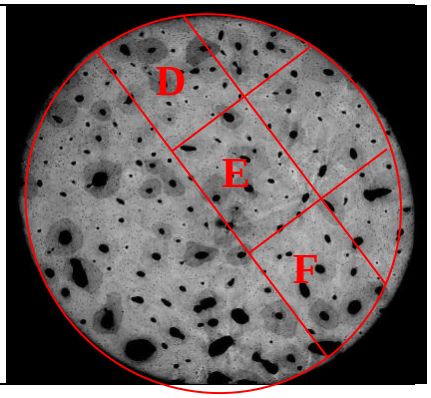

ID07: ID03: Knee Male Age 48

mqir_ID07_fem48_57323_P69_

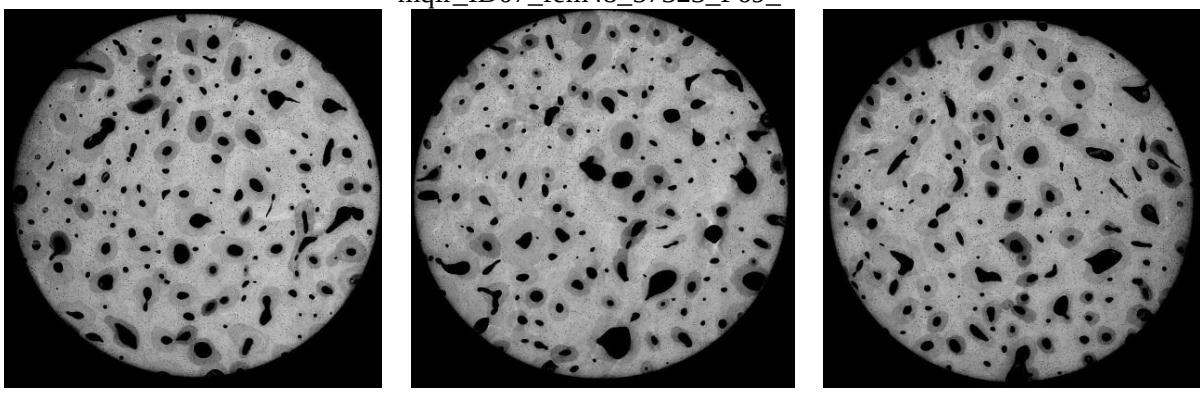

TOP MIDDLE BOTTOM

7D: mqir_fem48_57323_can7D_pag0001RC_

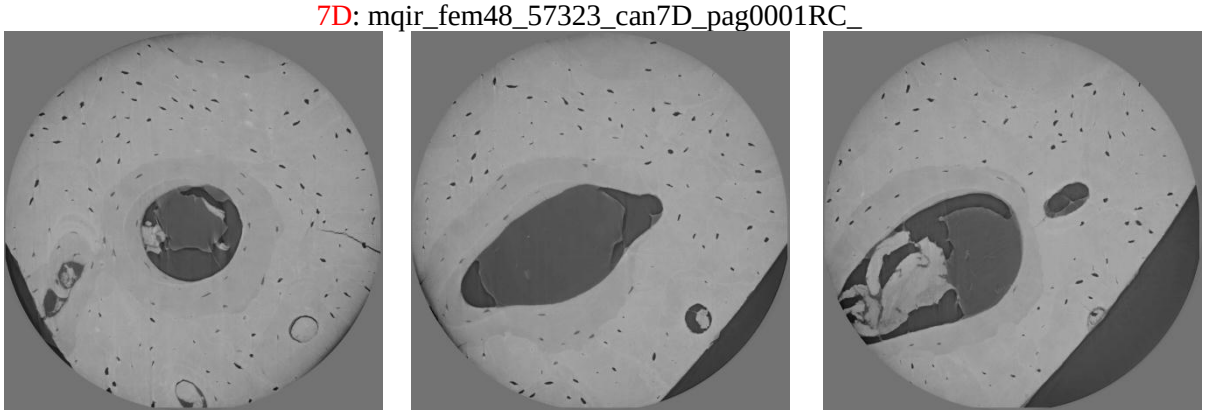

Z100 Z1000 Z2000

7E: mqir_fem48_57323_can7E_dry_pag0001RC_

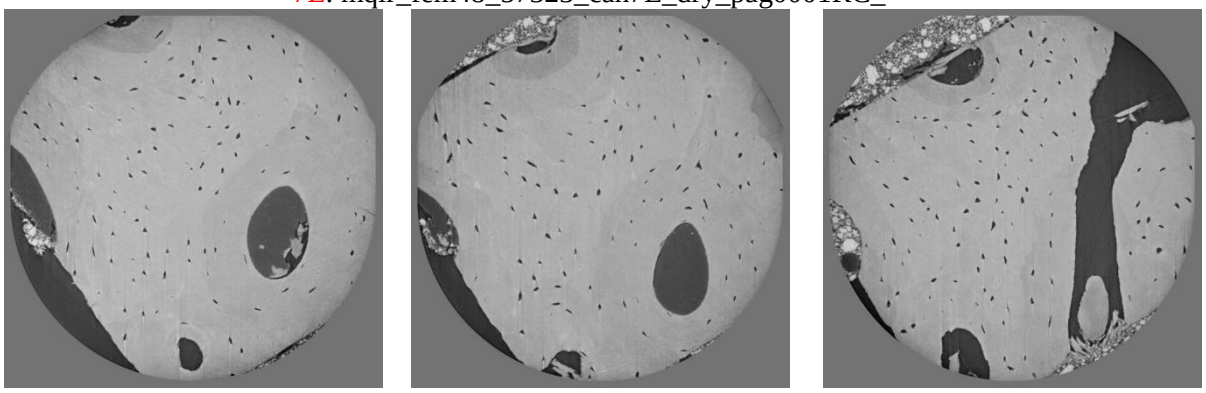

Z100 Z1000 Z2000

ID	Part	Units (mm)	
07	D	0.67*0.79	
	E	0.64*0.45	

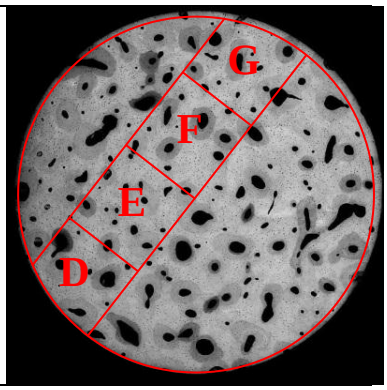

Unknown

ID11: Knee Sex unknown Age 84

mqir_ID11_fem84_57555_P69_

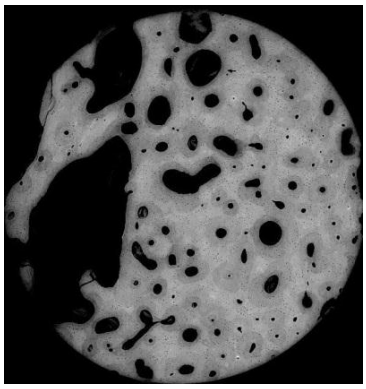

TOP

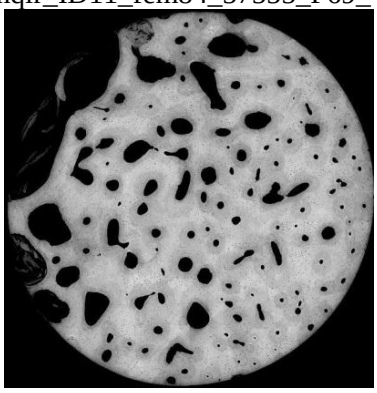

MIDDLE

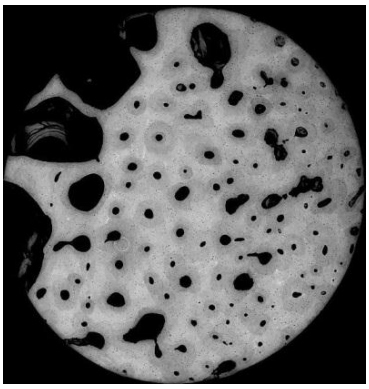

BOTTOM

11E: mqir_fem84_57555_can11E_dry_pag0001RC_

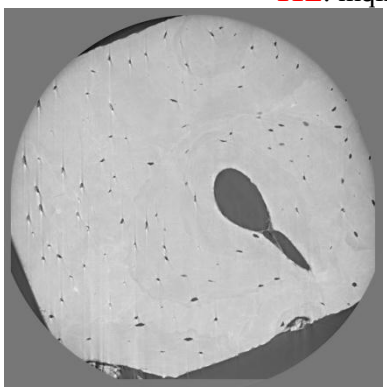

Z100

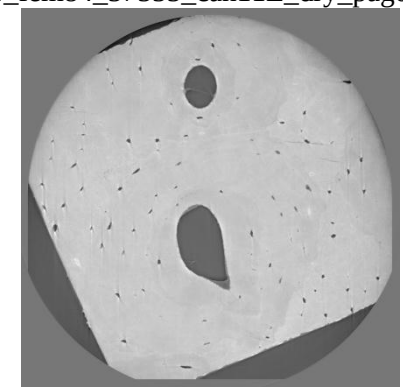

Z1000

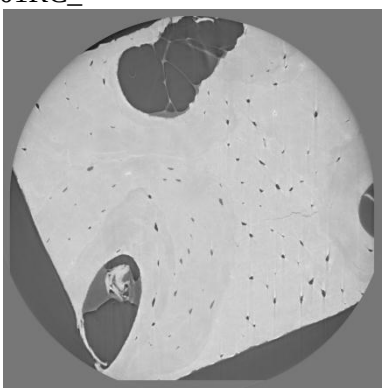

Z2000

ID	Part	Units (mm)
11	E	0.55*0.53
	F	0.61*0.85

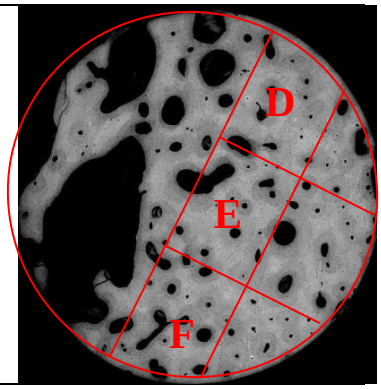

Radius

Female

ID12: Radius Female Age 84

mqir_ID12_rad84_59907_P69_

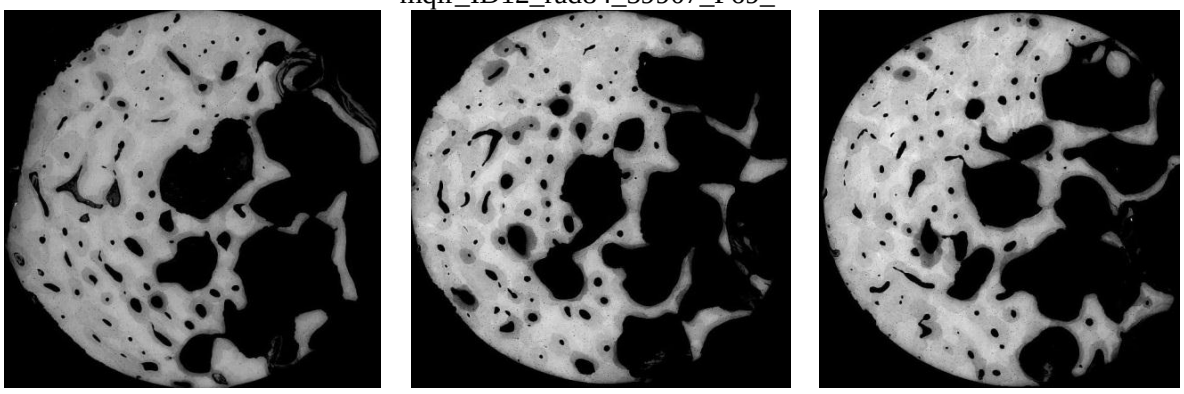

TOP MIDDLE BOTTOM

12D: mqir_rad84_59907_can12D_dry_pag0001RC_

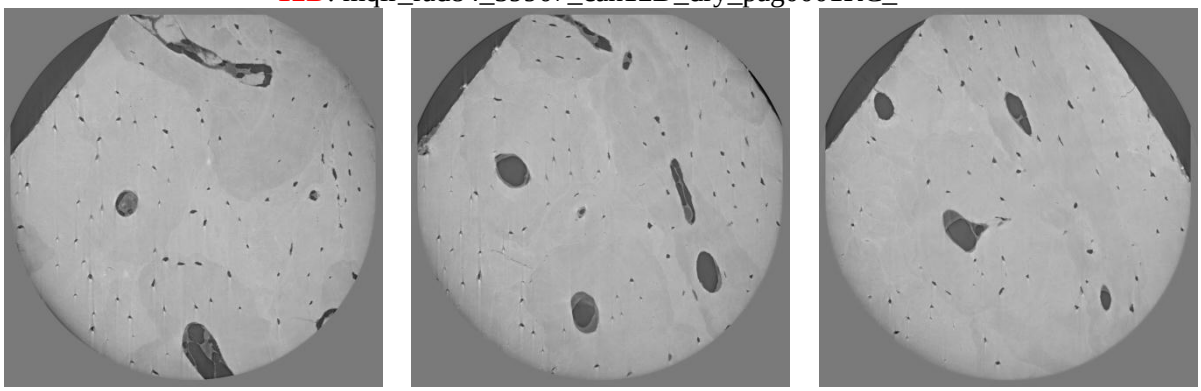

Z100 Z1000 Z2000

12F: mqir_rad84_59907_can12F_pag0001RC_

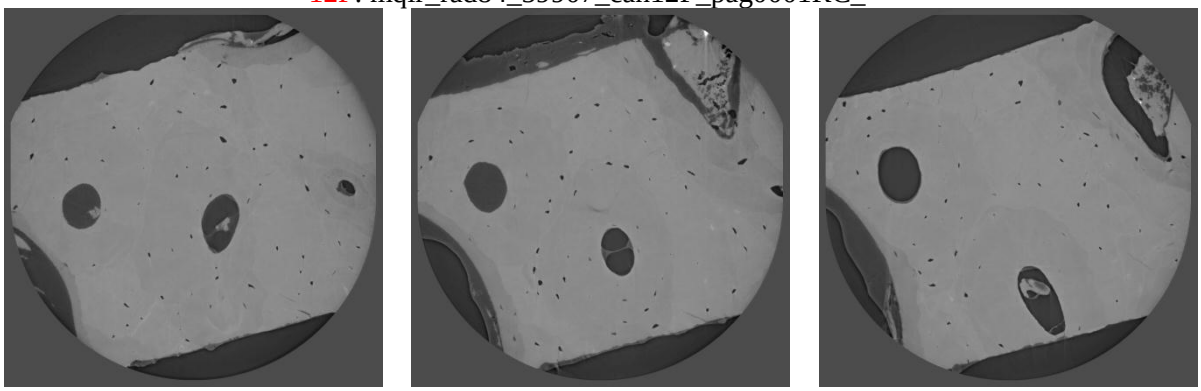

Z100 Z1000 Z2000

ID	Part	Units (mm)	
12	D	0.71*0.71	
	F	0.48*0.67	

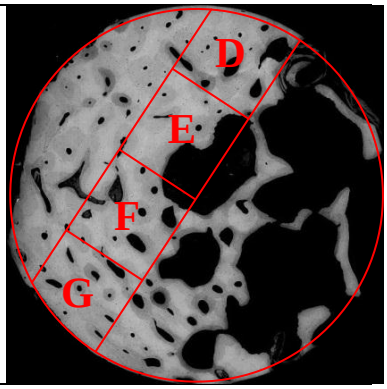

ID14: Radius Female Age 85

mqir_ID14_rad85_58641_P69_

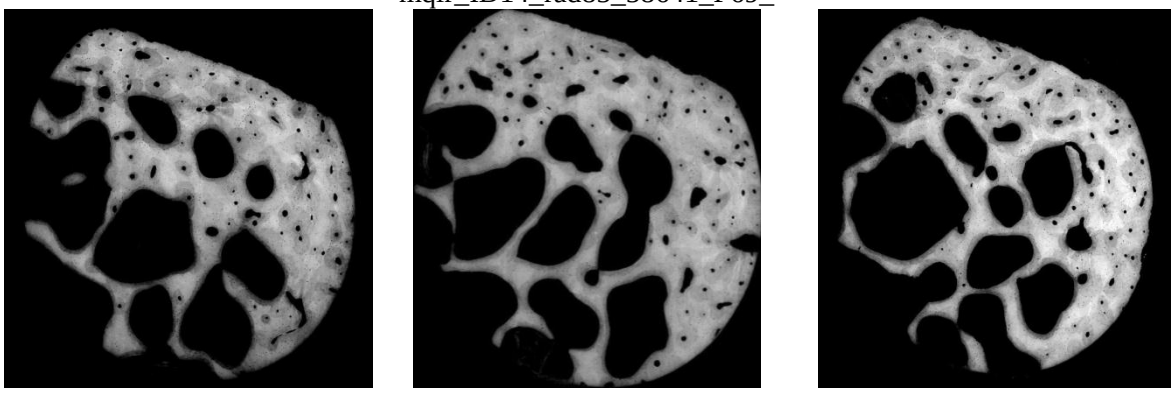

TOP MIDDLE BOTTOM

14C: mqir_rad85_58641_can14C_dry_pag0001RC_0100

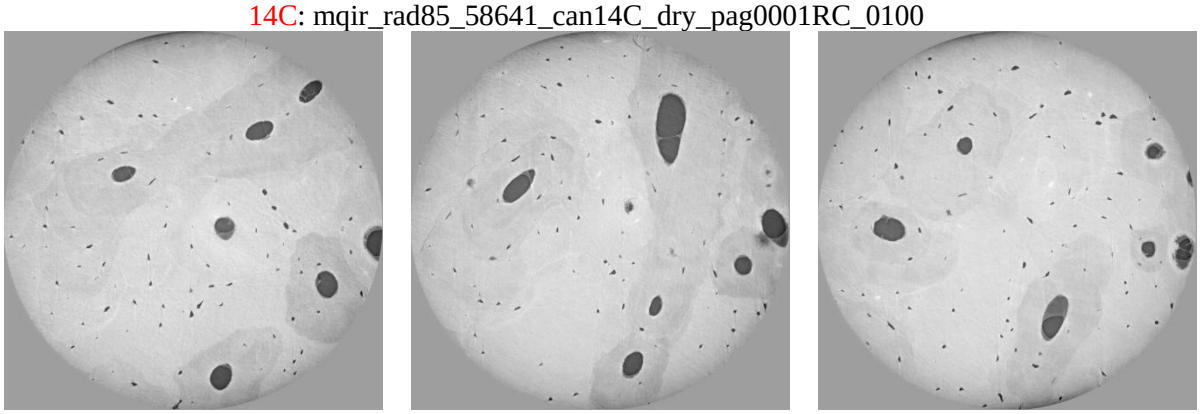

Z100 Z1000 Z2000

ID	Part	Units (mm)
14	C	0.63*0.88

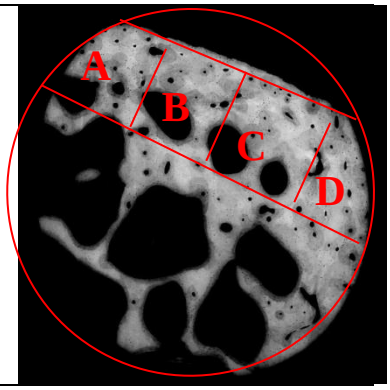

ID19: Radius Female Age 93

mqir_ID19_rad93_60024_P69_

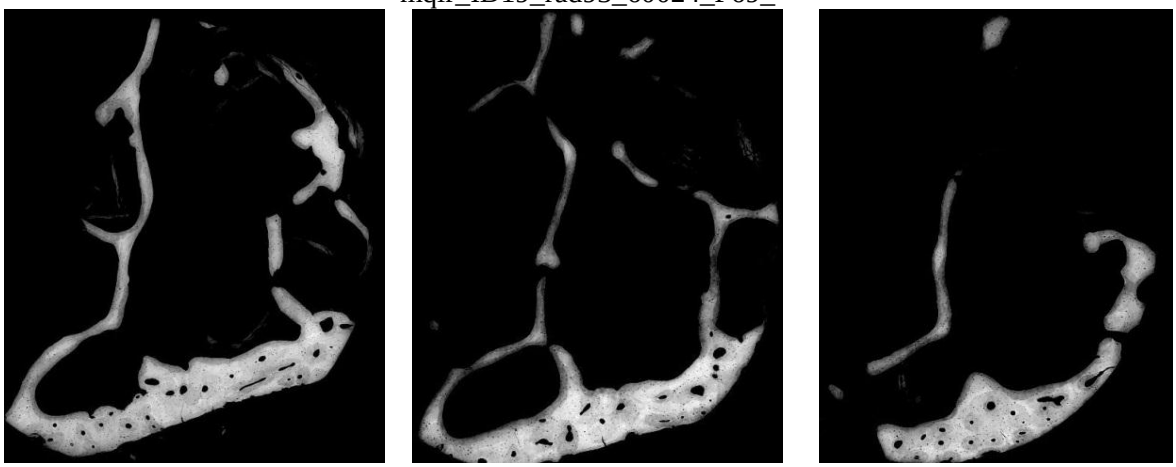

TOP MIDDLE BOTTOM

19A: mqir_rad93_60024_can19A_pag0001RC_

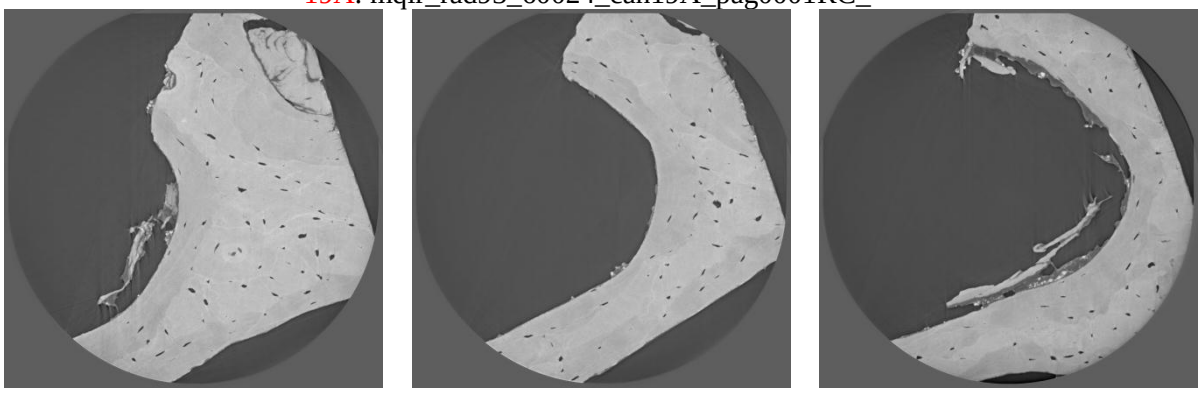

Z100 Z1000 Z2000

19B: mqir_rad93_60024_can19B_dry_pag0001RC_

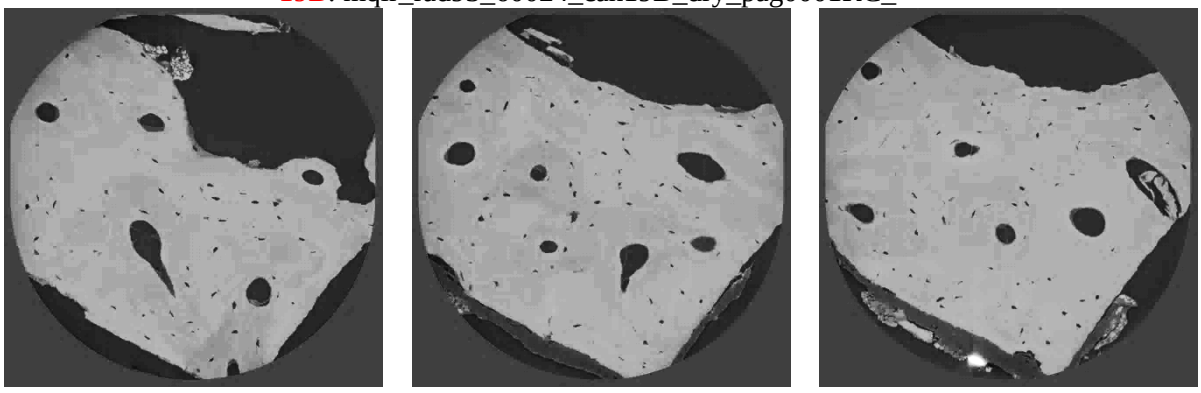

Z100 Z1000 Z2000

ID	Part	Units (mm)
19	A	0.67*0.69
	B	0.68*0.69
	C	0.22*0.9

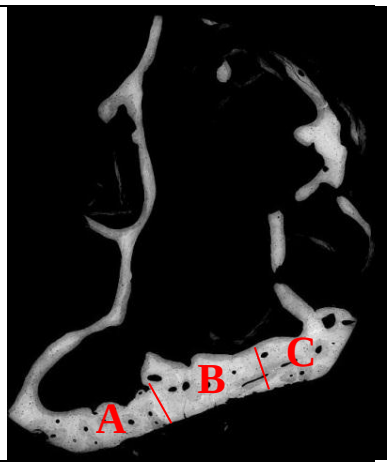

Male

ID06: Radius Male Age 47

mqir_ID06_rad47_57494_P69_

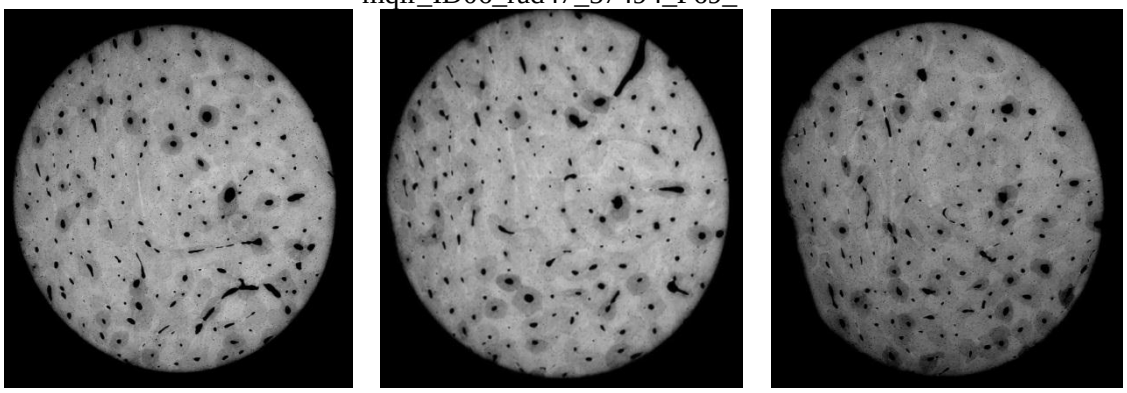

TOP MIDDLE BOTTOM

ID08: Radius Male Age 48

mqir_ID08_rad48_57323_P69_

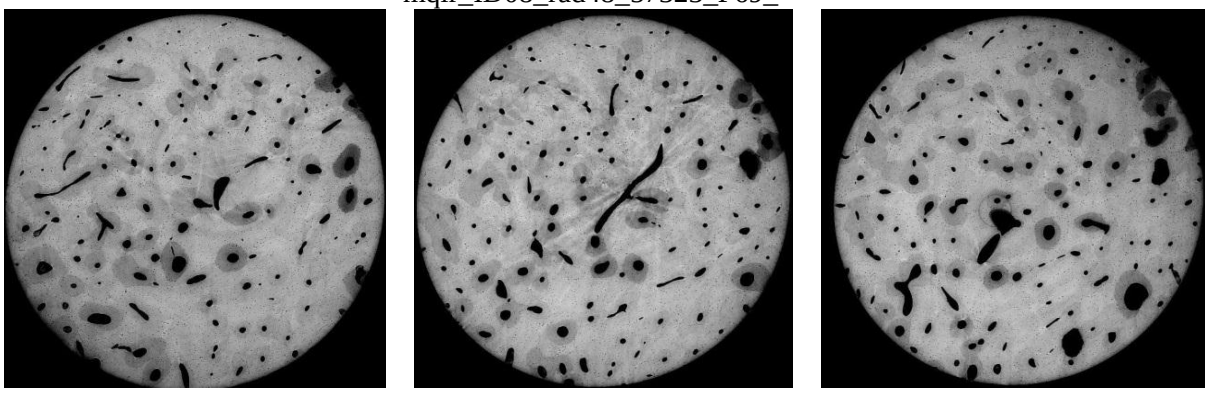

TOP MIDDLE BOTTOM

8G: mqir_rad48_57323_can8G_pag0001RC_

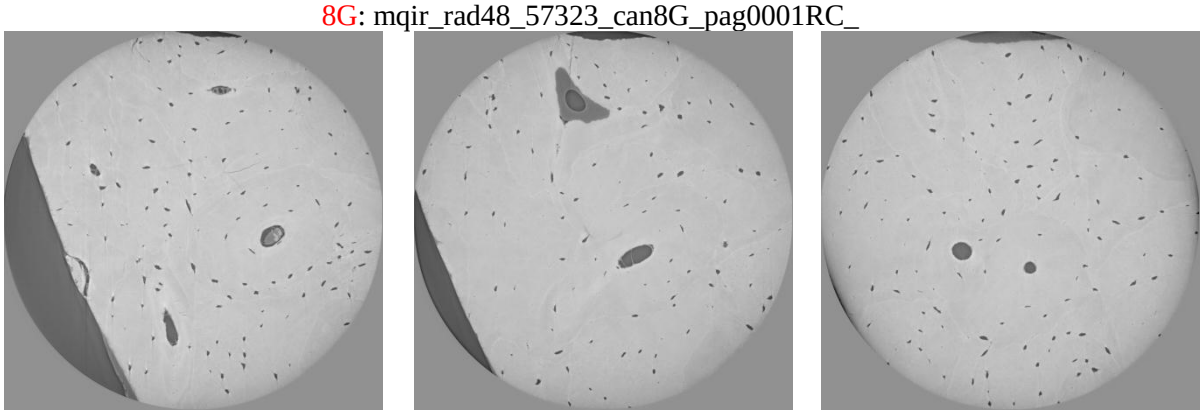

Z100 Z1000 Z2000

ID	Part	Units (mm)
08	D	1.25*0.56
	E	0.59*0.57
	F	0.59*0.6
	G	0.64*0.6

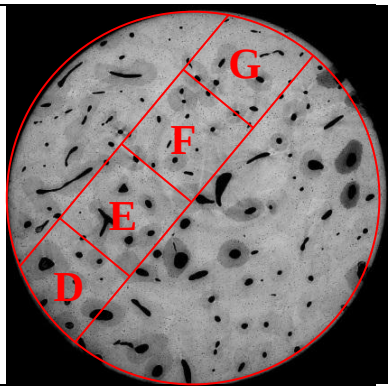

ID10: Radius Male Age 57

mqir_ID10_rad57_57495_P69_

TOP

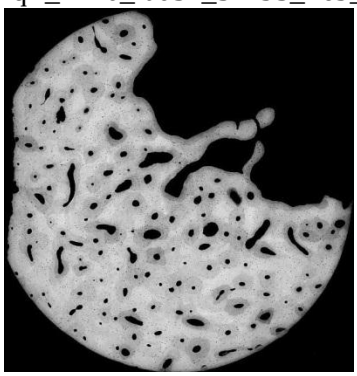

MIDDLE

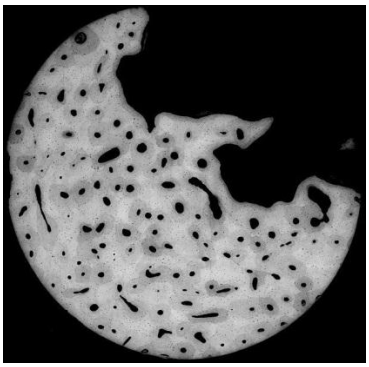

BOTTOM

ID17: Radius Male Age 88

mqir_ID17_rad88_600 m28_P69_

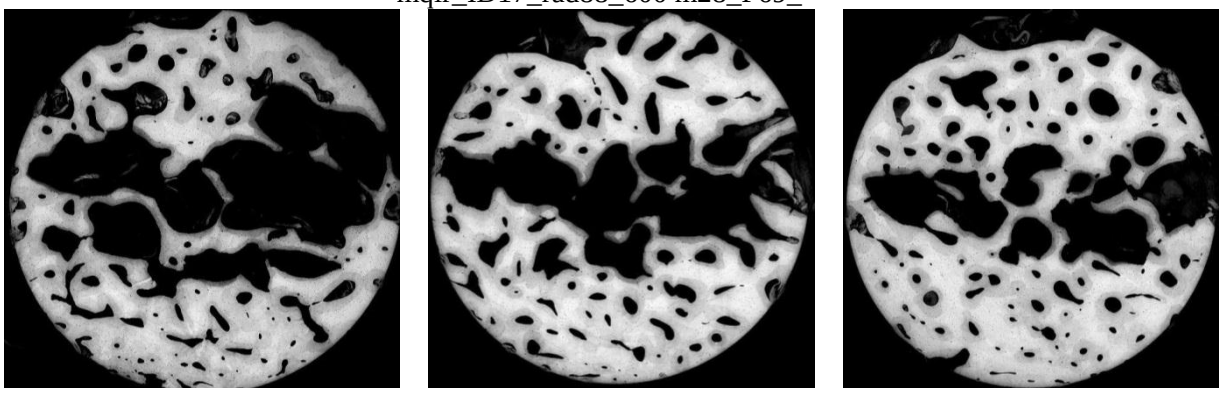

TOP MIDDLE BOTTOM

17B: mqir_rad88_60028_can17B_dry_360_pag0001RC_

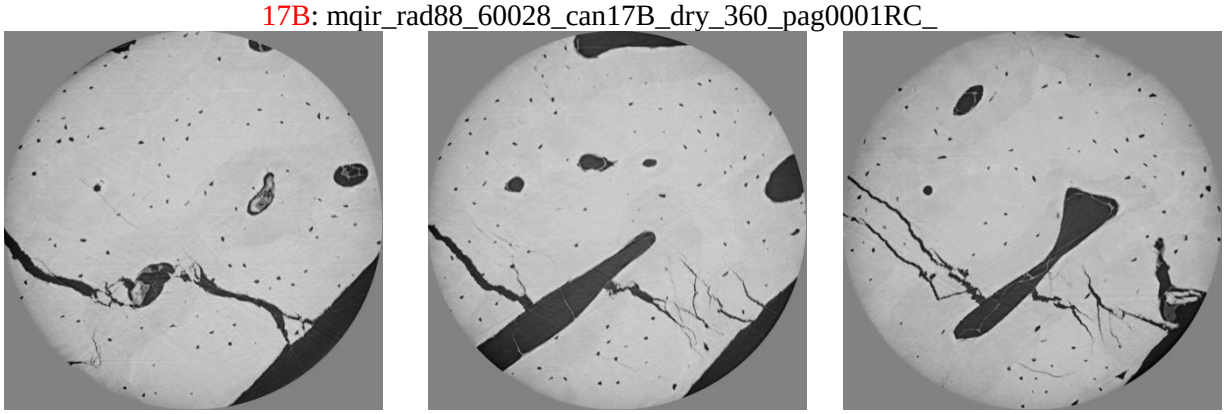

Z100 Z1000 Z2000

ID	Part	Units (mm)
17	B	0.7*0.9

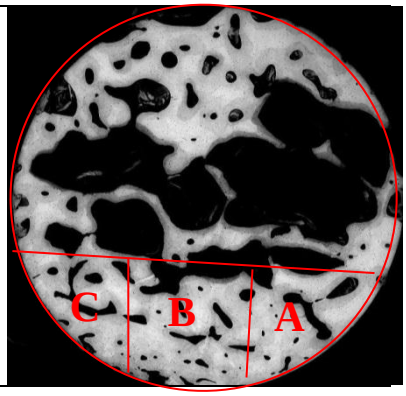

Annex 3

Since the aim of this thesis was to design automatic quantification tools for the 3D assessment of the LCN, a series of programs have been implemented in view to automatize as much as possible.

For the segmentation of the LCN network, the implementation of the workflow has been described in chapter 8. These implementations were mainly based on C++, ITK, VTK, OpenMP and shell script programming.

Besides, for the quantification of the LCN, we mainly designed two programs that allow to perform the automated lacunar descriptors extraction and the canaliculi ramification pattern analysis. The input the program is the segmented LCN image, and the output of the program is an excel file, which records all of the parameters calculated in the program.

To help in the subsequent analysis of the parameters, we also designed a program to perform the basic statistical analysis based on the outputs (excel files) of the quantification program. This program performs the statistical analysis between the data group. It calculates the mean, standard deviation, minimum and maximum of the each parameter. Besides, it also outputs the distribution and the normalized distribution of the each parameter in each data set.

These automated implementations allow a quick and efficient assessment of the 3D lacuno-canaliculi network based on the large dataset of the SR micro and nano-CT images.

PUBLICATIONS

Journal article

[1] **P. Dong**, S. Haupert, B Hesse, M Langer, P-J Gouttenoire, V Bousson, and F Peyrin, "3D osteocyte lacunar morphometric properties and distributions in human femoral cortical bone using synchrotron radiation micro-CT images", *Bone*, vol. 60, pp. 172-185, 2014.

[2] **P. Dong**, A. Pacureanu, M. A. Zuluaga, C. Olivier, G. Quentin and F Peyrin, "Quantification of The 3D Morphology of the Bone Cell Network from Synchrotron Micro-CT Images", *Image Analysis & Stereology, Accepted with minor corrections.*

[3] B. Hesse, M. Langer, P. Varga, A. Pacureanu, **P. Dong**, S. Schrof, N. Männicke, H. Suhonen, C. Olivier, P. Maurer , G. J. Kazakia, K. Raum and F. Peyrin "Investigation of the 3D structural parameters in BRONJ affected human jaw bone at cellular scale, a synchrotron µCT study", *Plos One, Accepted*.

[4] M. A. Zuluaga, M. Orkisz, , **P. Dong**, A. Pacureanu, P-J Gouttenoire and F. Peyrin, "Bone Canalicular Network Segmentation in 3D nano-CT Images through Geodesic Voting and Image Tessellation", *Physics in Medicine and Biology, Accepted with minor corrections.*

International conference paper

[5] **P. Dong,** A. Pacureanu, M. A. Zuluaga, C. Olivier, F. Frouin, G. Quentin, and F. Peyrin, "A New Quantitative Approach for Estimating Bone Cell Connections from Nano-CT Images", *IEEE EMBC*, Osaka, Japan, 2013

[6] **P. Dong**, S. Haupert, P. J. Gouttenoire, and F. Peyrin, "Efficient Extraction of 3D Bone Cells Descriptors from Micro-CT Images", *International Symposium on Biomedical Imaging (ISBI)*, San Francisco, USA, 2013

[7] **P. Dong**, A. Pacureanu, M. A. Zuluaga, P. - J. Gouttenoire, C. Olivier, and F. Peyrin, "Quantification of Bone Cell Processes from Submicrometer Synchrotron Micro-CT Images", *11th European Congress of Stereology and Image Analysis*, Kaiserslautern, Germany, 2013.

[8] **P. Dong**, A. Pacureanu, M. A. Zuluaga, F. Peyrin, "A New 3D Quantificaiton Method for Bone Cell Connections On Nano-CT Images", *Hot Topics in Molecular Imaging (TOPIM)*, Les Houches, France, 2012

[9] M. Langer, T. Frachon, L. Weber, B. Hesse, **P. Dong,** S. Rit and F. Peyrin, "Dose fractionation in X-ray In-line Phase Tomography", *International Symposium on Biomedical Imaging (ISBI)*, Beijing, China, 2014

[10] F. Peyrin, **P. Dong**, A. Pacureanu, M. ZULUAGA, C. Olivier, M. Langer, and P. Cloetens, "Synchrotron radiation CT from the micro to nanoscale for the investigation of bone tissue", *Proceedings of SPIE*, vol. 8506: SPIE Optical Engineering, Developments in X-Ray Tomography VIII, pp. 1-12, 2012.

[11] M. A. Zuluaga, **P. Dong**, A. Pacureanu, M. Orkisz, and F. Peyrin, "Minimum Cost Path Approach for the Segmentation of Bone Canalicular Network from Nano-CT Images", *IEEE Nuclear Science Symposium and Medical Imaging Conference*, Valencia, Spain, 2011.

[12] F. Peyrin., A. Pacureanu., M. A. Zuluaga, **P. Dong**, M. Langer, 3D X-ray CT imaging of the bone lacunar-canalicular network, *International Symposium on Biomedical Imaging (ISBI)*, Barcelona, Spain, 2012

National communication

[13] **P. Dong**, S. Haupert, P. - J. Gouttenoire, C. Olivier, and F. Peyrin, "3D Bone Cells Quantification From 3D Micro-CT Images ", *Imagerie du vivant*, Lyon, France, 2012

[14] A. Pacureanu, M. Langer, **P. Dong,** C. Revol-Muller, V. Buzuloiu, and F. Peyrin, "Imagerie microscopique 3D du réseau lacuno-canaliculaire dans l'os humain", GRETSI, Bordeaux, France, 2011.

BIBLIOGRAPHY

[Anderson *et al.*, (2005)] E. J. Anderson, S. Kaliyamoorthy, J. I. D. Alexander, and M. L. K. Tate. Nano-Microscale Models of Periosteocytic Flow Show Differences in Stresses Imparted to Cell Body and Processes. *Ann. Biomed. Eng.*, 2005, vol. 33, no. 1, pp. 52–62

[Anderson *et al.*, (2008)] E. J. Anderson and M. L. Knothe Tate. Idealization of Pericellular Fluid Space Geometry and Dimension Results in a Profound Underprediction of Nano-Microscale Stresses Imparted by Fluid Drag on Osteocytes. *J. Biomech.*, 2008, vol. 41, no. 8, pp. 1736–1746

[Andrews *et al.*, (2010)] J. C. Andrews, E. Almeida, M. C. H. van der Meulen, J. S. Alwood, C. Lee, Y. Liu, J. Chen, F. Meirer, M. Feser, J. Gelb, J. Rudati, A. Tkachuk, W. Yun, and P. Pianetta. Nanoscale X-Ray Microscopic Imaging of Mammalian Mineralized Tissue. *Microsc. Microanal. Off. J. Microsc. Soc. Am. Microbeam Anal. Soc. Microsc. Soc. Can.*, 2010, vol. 16, no. 3, pp. 327–336

[Ardizzoni, (2001)] A. Ardizzoni. Osteocyte Lacunar Size-Lamellar Thickness Relationships in Human Secondary Osteons. *Bone*, 2001, vol. 28, no. 2, pp. 215–219

[Arhatari *et al.*, (2011)] B. D. Arhatari, D. M. L. Cooper, C. D. L. Thomas, J. G. Clement, and A. G. Peele. Imaging the 3D Structure of Secondary Osteons in Human Cortical Bone Using Phase-Retrieval Tomography. *Phys. Med. Biol.*, 2011, vol. 56, no. 16, pp. 5265–5274

[Ascenzi *et al.*, (2008)] M.-G. Ascenzi, J. Gill, and A. Lomovtsev. Orientation of Collagen at the Osteocyte Lacunae in Human Secondary Osteons. *J. Biomech.*, 2008, vol. 41, no. 16, pp. 3426–3435

[Bacabac *et al.*, (2008)] R. G. Bacabac, D. Mizuno, C. F. Schmidt, F. C. MacKintosh, J. J. W. A. Van Loon, J. Klein-Nulend, and T. H. Smit. Round versus Flat: Bone Cell Morphology, Elasticity, and Mechanosensing. *J. Biomech.*, 2008, vol. 41, no. 7, pp. 1590–1598

[Benmansour *et al.*, (2011)] F. Benmansour and L. D. Cohen. Tubular Structure Segmentation Based on Minimal Path Method and Anisotropic Enhancement. *Int. J. Comput. Vis.*, 2011, vol. 92, no. 2, pp. 192–210

[Beno *et al.*, (2006)] T. Beno, Y.-J. Yoon, S. C. Cowin, and S. P. Fritton. Estimation of Bone Permeability Using Accurate Microstructural Measurements. *J. Biomech.*, 2006, vol. 39, no. 13, pp. 2378–2387

[Bloebaum *et al.*, (1997)] R. D. Bloebaum, J. G. Skedros, E. G. Vajda, K. N. Bachus, and B. R. Constantz. Determining Mineral Content Variations in Bone Using Backscattered Electron Imaging. *Bone*, 1997, vol. 20, no. 5, pp. 485–490

[Bonewald, (2006)] L. F. Bonewald. Mechanosensation and Transduction in Osteocytes. *BoneKEy Osteovision*, 2006, vol. 3, no. 10, pp. 7–15

[Bonewald, (2007)] L. F. Bonewald. Osteocytes as Dynamic Multifunctional Cells. *Ann. N. Y. Acad. Sci.*, 2007, vol. 1116, pp. 281–290

[Bonewald, (2011)] L. F. Bonewald. The Amazing Osteocyte. *J. Bone Miner. Res. Off. J. Am. Soc. Bone Miner. Res.*, 2011, vol. 26, no. 2, pp. 229–238

[Bonewald *et al.*, (2008)] L. F. Bonewald and M. L. Johnson. Osteocytes, Mechanosensing and Wnt Signaling. *Bone*, 2008, vol. 42, no. 4, pp. 606–615

[Bonucci, (2009)] E. Bonucci. The Osteocyte: The Underestimated Conductor of the Bone Orchestra. *Rendiconti Lincei*, 2009, vol. 20, no. 3, pp. 237–254

[Boskey *et al.*, (1999)] A. L. Boskey, T. M. Wright, and R. D. Blank. Collagen and Bone Strength. *J. Bone Miner. Res.*, 1999, vol. 14, no. 3, pp. 330–335

[Bousson *et al.*, (2004)] V. Bousson, F. Peyrin, C. Bergot, M. Hausard, A. Sautet, and J. D. Laredo. Cortical Bone of the Human Femoral Neck : Three-Dimensional Appearance and Porosity Using Synchrotron Radiation. *J Bone Min Res.*, vol. 19, no. 5, pp. 794–801

[Boyde *et al.*, (1996)] A. Boyde and S. J. Jones. Scanning Electron Microscopy of Bone: Instrument, Specimen, and Issues. *Microsc. Res. Tech.*, 1996, vol. 33, no. 2, pp. 92–120

[Bracewell *et al.*, (1967)] R. N. Bracewell and A. C. Riddle. Inversion of Fan-Beam Scans in Radio Astronomy. *Astrophys. J.*, 1967, vol. 150, p. 427

[Britz *et al.*, (2012)] H. M. Britz, Y. Carter, J. Jokihaara, O. V. Leppänen, T. L. N. Järvinen, G. Belev, and D. M. L. Cooper. Prolonged Unloading in Growing Rats Reduces Cortical Osteocyte Lacunar Density and Volume in the Distal Tibia. *Bone*, 2012, vol. 51, no. 5, pp. 913–919

[Burger *et al.*, (1999)] E. H. Burger and J. Klein-Nulend. Mechanotransduction in Bone--Role of the Lacuno-Canalicular Network. *FASEB J. Off. Publ. Fed. Am. Soc. Exp. Biol.*, 1999, vol. 13 Suppl, pp. S101–112

[Busse *et al.*, (2010)] B. Busse, D. Djonic, P. Milovanovic, M. Hahn, K. Püschel, R. O. Ritchie, M. Djuric, and M. Amling. Decrease in the Osteocyte Lacunar Density Accompanied by Hypermineralized Lacunar Occlusion Reveals Failure and Delay of Remodeling in Aged Human Bone. *Aging Cell*, 2010, vol. 9, no. 6, pp. 1065–1075

[Canny, (1986)] J. Canny. A Computational Approach to Edge Detection. *IEEE Trans. Pattern Anal. Mach. Intell.*, 1986, vol. PAMI-8, no. 6, pp. 679 –698

[Cardoso *et al.*, (2013)] L. Cardoso, S. P. Fritton, G. Gailani, M. Benalla, and S. C. Cowin. Advances in Assessment of Bone Porosity, Permeability and Interstitial Fluid Flow. *J. Biomech.*, 2013, vol. 46, no. 2, pp. 253–265

[Carter *et al.*, (2013)] Y. Carter, C. D. L. Thomas, J. G. Clement, and D. M. L. Cooper. Femoral Osteocyte Lacunar Density, Volume and Morphology in Women across the Lifespan. *J. Struct. Biol.*, 2013

[Carter *et al.*, (2012)] Y. Carter, C. D. L. Thomas, J. G. Clement, A. G. Peele, K. Hannah, and D. M. L. Cooper. Variation in Osteocyte Lacunar Morphology and Density in the Human Femur - a Synchrotron Radiation Micro-CT Study. *Bone*, 2012, vol. 52, no. 1, pp. 126–132

[Ciarelli *et al.*, (1991)] M. J. Ciarelli, S. A. Goldstein, J. L. Kuhn, D. D. Cody, and M. B. Brown. Evaluation of Orthogonal Mechanical Properties and Density of Human Trabecular Bone from the Major Metaphyseal Regions with Materials Testing and Computed Tomography. *J. Orthop. Res.*, 1991, vol. 9, no. 5, pp. 674–682

[Cloetens *et al.*, (1999)] P. Cloetens, W. Ludwig, J. Baruchel, D. Van Dyck, J. Van Landuyt, J. P. Guigay, and M. Schlenker. Holotomography: Quantitative Phase Tomography with Micrometer Resolution Using Hard Synchrotron Radiation X Rays. *Appl. Phys. Lett.*, 1999, vol. 75, no. 19, p. 2912

[Cloetens *et al.*, (1997)] P. Cloetens, M. Pateyron-Salomé, J. Y. Buffière, G. Peix, J. Baruchel, F. Peyrin, and M. Schlenker. Observation of Microstructure and Damage in Materials by Phase Sensitive Radiography and Tomography. *J. Appl. Phys.*, 1997, vol. 81, no. 9, pp. 5878–5886

[Cohen *et al.*, (2001)] L. D. Cohen and T. Deschamps. Grouping Connected Components Using Minimal Path Techniques. Application to Reconstruction of Vessels in 2D and 3D Images. *Proceedings of the 2001 IEEE Computer Society Conference on Computer Vision and Pattern Recognition, 2001. CVPR 2001*, 2001. 2001, pp. II–102 – II–109 vol.2

[Cohen *et al.*, (1997)] L. D. Cohen and R. Kimmel. Global Minimum for Active Contour Models: A Minimal Path Approach. *Int. J. Comput. Vis.*, 1997, vol. 24, no. 1, pp. 57–78

[Cooper, D.M. *et al.*, (2007)] Cooper, D.M. and Turinsky, A.; Sensen, C. & Hallgrimsson, B. Effect of Voxel Size on 3D Micro-CT Analysis of Cortical Bone Porosity. *Calcif Tissue Int*, 2007, vol. 80, no. 3, pp. 211–219

[Currey, (2002)] J. D. Currey. Bones: Structure and Mechanics. Princeton University Press, 2002, ISBN 0691090963

[Currey, (2003a)] J. D. Currey. The Many Adaptations of Bone. *J. Biomech.*, 2003, vol. 36, no. 10, pp. 1487–1495

[Currey, (2003b)] J. D. Currey. The Many Adaptations of Bone. *J. Biomech.*, 2003, vol. 36, no. 10, pp. 1487–1495

[Currey *et al.*, (2013)] J. D. Currey and R. Shahar. Cavities in the Compact Bone in Tetrapods and Fish and Their Effect on Mechanical Properties. *J. Struct. Biol.*, 2013, vol. 183, no. 2, pp. 107–122

[Da Costa Gómez *et al.*, (2005)] T. M. Da Costa Gómez, J. G. Barrett, S. J. Sample, C. L. Radtke, V. L. Kalscheur, Y. Lu, M. D. Markel, E. M. Santschi, M. C. Scollay, and P. Muir. Up-Regulation of Site-Specific Remodeling without Accumulation of Microcracking and Loss of Osteocytes. *Bone*, 2005, vol. 37, no. 1, pp. 16–24

[Deligianni *et al.*, (2008)] D. D. Deligianni and C. A. Apostolopoulos. Multilevel Finite Element Modeling for the Prediction of Local Cellular Deformation in Bone. *Biomech. Model. Mechanobiol.*, 2008, vol. 7, no. 2, pp. 151–159

[Deng *et al.*, (2005)] H. Deng, Y. Liu, and C.-Y. Guo. Current Topics in Bone Biology. World Scientific, 2005, ISBN 9789812562098

[Dice, (1945)] L. R. Dice. Measures of the Amount of Ecologic Association Between Species. *Ecology*, 1945, vol. 26, no. 3, p. 297

[Dierolf *et al.*, (2010)] M. Dierolf, A. Menzel, P. Thibault, P. Schneider, C. M. Kewish, R. Wepf, O. Bunk, and F. Pfeiffer. Ptychographic X-Ray Computed Tomography at the Nanoscale. *Nature*, 2010, vol. 467, no. 7314, pp. 436–439

[Dong *et al.*, (2014)] P. Dong, S. Haupert, B. Hesse, M. Langer, P.-J. Gouttenoire, V. Bousson, and F. Peyrin. 3D Osteocyte Lacunar Morphometric Properties and Distributions in Human Femoral Cortical Bone Using Synchrotron Radiation Micro-CT Images. *Bone*, 2014, vol. 60, pp. 172–185

[Douissard *et al.*, (2010)] P. A. Douissard, A. Cecilia, T. Martin, V. Chevalier, M. Couchaud, T. Baumbach, K. Dupré, M. Kühbacher, and A. Rack. A Novel Epitaxially Grown LSO-Based Thin-Film Scintillator for Micro-Imaging Using Hard Synchrotron Radiation. *J. Synchrotron Radiat.*, 2010, vol. 17, no. 5, pp. 571–583

[Engelke *et al.*, (1993)] K. Engelke, W. Graeff, L. Meiss, M. Hahn, and G. Delling. High Spatial Resolution Imaging of Bone Mineral Using Computed Microtomography. Comparison with Microradiography and Undecalcified Histologic Sections. *Invest. Radiol.*, 1993, vol. 28, no. 4, pp. 341–349

[Erni *et al.*, (2009)] R. Erni, M. D. Rossell, C. Kisielowski, and U. Dahmen. Atomic-Resolution Imaging with a Sub-50-Pm Electron Probe. *Phys. Rev. Lett.*, 2009, vol. 102, no. 9, p. 096101

[Ferretti *et al.*, (1999)] M. Ferretti, M. A. Muglia, F. Remaggi, V. Canè, and C. Palumbo. Histomorphometric Study on the Osteocyte Lacuno-Canalicular Network in Animals of Different Species. II. Parallel-Fibered and Lamellar Bones. *Ital. J. Anat. Embryol. Arch. Ital. Anat. Ed Embriologia*, 1999, vol. 104, no. 3, pp. 121–131

[Flannery *et al.*, (1987)] B. P. Flannery, H. W. Deckman, W. G. Roberge, and K. L. D'Amico. Three-Dimensional X-Ray Microtomography. *Science*, 1987, vol. 237, no. 4821, pp. 1439–1444

[Frangi *et al.*, (1998)] A. F. Frangi, W. J. Niessen, K. L. Vincken, and M. A. Viergever. Multiscale Vessel Enhancement Filtering, in *Medical Image Computing and Computer-Assisted Interventation — MICCAI'98*, WELLS, COLCHESTER Alan, DELP Scott Springer Berlin Heidelberg, 1998, pp. 130–137

[Fritton *et al.*, (2005)] S. P. Fritton, T. Beno, C. Ciani, and S. B. Doty. Osteocyte Lacunar and Canalicular Structure. presented at the Seventh International Bone Fluid Flow Workshop. 2005

[FROST, (1960)] H. M. FROST. Micropetrosis. *J. Bone Joint Surg. Am.*, 1960, vol. 42-A, pp. 144–150

[Gentleman *et al.*, (2010)] E. Gentleman, Y. C. Fredholm, G. Jell, N. Lotfibakhshaiesh, M. D. O'Donnell, R. G. Hill, and M. M. Stevens. The Effects of Strontium-Substituted Bioactive Glasses on Osteoblasts and Osteoclasts in Vitro. *Biomaterials*, 2010, vol. 31, no. 14, pp. 3949–3956

[Granke *et al.*, (2011)] M. Granke, Q. Grimal, A. Saïed, P. Nauleau, F. Peyrin, and P. Laugier. Change in Porosity Is the Major Determinant of the Variation of Cortical Bone Elasticity at the Millimeter Scale in Aged Women. *Bone*, 2011, vol. 49, no. 5, pp. 1020–1026

[Grötz *et al.*, (1999)] K. A. Grötz, B. Piepkorn, B. Al-Nawas, H. Duschner, F. Bittinger, P. Kann, J. Beyer, and W. Wagner. Confocal Laser Scanning Microscopy: A Nondestructive Subsurface Histotomography of Healthy Human Bone. *Calcif. Tissue Int.*, 1999, vol. 65, no. 1, pp. 8–10

[Gu *et al.*, (2007)] G. Gu, K. Kurata, Z. Chen, and K. H. VÄÄNÄNEN. Osteocyte: A Cellular Basis for Mechanotransduction in Bone. *J. Biomech. Sci. Eng.*, 2007, vol. 2, no. 4, pp. 150–165

[Guigay *et al.*, (2007)] J. P. Guigay, M. Langer, R. Boistel, and P. Cloetens. Mixed Transfer Function and Transport of Intensity Approach for Phase Retrieval in the Fresnel Region. *Opt. Lett.*, 2007, vol. 32, no. 12, pp. 1617–1619

[Han *et al.*, (2004)] Y. Han, S. C. Cowin, M. B. Schaffler, and S. Weinbaum. Mechanotransduction and Strain Amplification in Osteocyte Cell Processes. *Proc. Natl. Acad. Sci. U. S. A.*, 2004, vol. 101, no. 47, pp. 16689–16694

[Hannah *et al.*, (2010)] K. M. Hannah, C. D. L. Thomas, J. G. Clement, F. De Carlo, and A. G. Peele. Bimodal Distribution of Osteocyte Lacunar Size in the Human Femoral Cortex as Revealed by Micro-CT. *Bone*, 2010, vol. 47, no. 5, pp. 866–871

[Hazenberg *et al.*, (2006)] J. G. Hazenberg, M. Freeley, E. Foran, T. C. Lee, and D. Taylor. Microdamage: A Cell Transducing Mechanism Based on Ruptured Osteocyte Processes. *J. Biomech.*, 2006, vol. 39, no. 11, pp. 2096–2103

[Hengsberger *et al.*, (2003)] S. Hengsberger, J. Enstroem, F. Peyrin, and P. Zysset. How Is the Indentation Modulus of Bone Tissue Related to Its Macroscopic Elastic Response? A Validation Study. *J. Biomech.*, 2003, vol. 36, no. 10, pp. 1503–1509

[Hildebrand *et al.*, (1997)] T. Hildebrand and P. Rüegsegger. Quantification of Bone Microarchitecture with the Structure Model Index. *Comput. Methods Biomech. Biomed. Engin.*, 1997, vol. 1, no. 1, pp. 15–23

[Hirose *et al.*, (2007)] S. Hirose, M. Li, T. Kojima, P. H. L. de Freitas, S. Ubaidus, K. Oda, C. Saito, and N. Amizuka. A Histological Assessment on the Distribution of the Osteocytic Lacunar Canalicular System Using Silver Staining. *J. Bone Miner. Metab.*, 2007, vol. 25, no. 6, pp. 374–382

[Holmbeck *et al.*, (2005)] K. Holmbeck, P. Bianco, I. Pidoux, S. Inoue, R. C. Billinghurst, W. Wu, K. Chrysovergis, S. Yamada, H. Birkedal-Hansen, and A. R. Poole. The Metalloproteinase MT1-MMP Is Required for Normal Development and Maintenance of Osteocyte Processes in Bone. *J. Cell Sci.*, 2005, vol. 118, no. Pt 1, pp. 147–156

[Hoshen *et al.*, (1976)] J. Hoshen and R. Kopelman. Percolation and Cluster Distribution. I. Cluster Multiple Labeling Technique and Critical Concentration Algorithm. *Phys. Rev. B*, 1976, vol. 14, no. 8, pp. 3438–3445

[J.Hoshen *et al.*, (1976)] J.Hoshen and R.Kopelman. Percolation and Cluster Distibution. I. Cluster Multiple Labeling Technique and Critical Concentration Algorithm.pdf. 1976

[Jones *et al.*, (2005)] C. W. Jones, D. Smolinski, A. Keogh, T. B. Kirk, and M. H. Zheng. Confocal Laser Scanning Microscopy in Orthopaedic Research. *Prog. Histochem. Cytochem.*, 2005, vol. 40, no. 1, pp. 1–71

[Jordan *et al.*, (2003)] G. R. Jordan, N. Loveridge, J. Power, M. T. Clarke, M. Parker, and J. Reeve. The Ratio of Osteocytic Incorporation to Bone Matrix Formation in Femoral Neck Cancellous Bone: An Enhanced Osteoblast Work Rate in the Vicinity of Hip Osteoarthritis. *Calcif. Tissue Int.*, 2003, vol. 72, no. 3, pp. 190–196

[Kamioka *et al.*, (2001)] H. Kamioka, T. Honjo, and T. Takano-Yamamoto. A Three-Dimensional Distribution of Osteocyte Processes Revealed by the Combination of Confocal Laser Scanning Microscopy and Differential Interference Contrast Microscopy. *Bone*, 2001, vol. 28, no. 2, pp. 145–149

[Kamioka *et al.*, (2009)] H. Kamioka, S. A. Murshid, Y. Ishihara, N. Kajimura, T. Hasegawa, R. Ando, Y. Sugawara, T. Yamashiro, A. Takaoka, and T. Takano-Yamamoto. A Method for Observing Silver-Stained Osteocytes In Situ in 3-Mm Sections Using Ultra-High Voltage Electron Microscopy Tomography. *Microsc. Microanal.*, 2009, vol. 15, no. 05, pp. 377–383

[Kerschnitzki *et al.*, (2013)] M. Kerschnitzki, P. Kollmannsberger, M. Burghammer, G. N. Duda, R. Weinkamer, W. Wagermaier, and P. Fratzl. Architecture of the Osteocyte Network Correlates with Bone Material Quality. *J. Bone Miner. Res. Off. J. Am. Soc. Bone Miner. Res.*, 2013

[Kingsmill *et al.*, (1998)] V. J. Kingsmill and A. Boyde. Mineralisation Density of Human Mandibular Bone: Quantitative Backscattered Electron Image Analysis. *J. Anat.*, 1998, vol. 192, no. Pt 2, pp. 245–256

[Klein-Nulend *et al.*, (2005)] J. Klein-Nulend, R. G. Bacabac, and M. G. Mullender. Mechanobiology of Bone Tissue. *Pathol. Biol.*, 2005, vol. 53, no. 10, pp. 576–580

[Kubek *et al.*, (2010)] D. J. Kubek, V. H. Gattone 2nd, and M. R. Allen. Methodological Assessment of Acid-Etching for Visualizing the Osteocyte Lacunar-Canalicular Networks Using Scanning Electron Microscopy. *Microsc. Res. Tech.*, 2010, vol. 73, no. 3, pp. 182–186

[Labiche *et al.*, (2007)] J.-C. Labiche, O. Mathon, S. Pascarelli, M. A. Newton, G. G. Ferre, C. Curfs, G. Vaughan, A. Homs, and D. F. Carreiras. Invited Article: The Fast Readout Low Noise Camera as a Versatile X-Ray Detector for Time Resolved Dispersive Extended X-Ray Absorption Fine Structure and Diffraction Studies of Dynamic Problems in Materials Science, Chemistry, and Catalysis. *Rev. Sci. Instrum.*, 2007, vol. 78, no. 9, p. 091301

[Landis *et al.*, (1996)] W. J. Landis, K. J. Hodgens, J. Arena, M. J. Song, and B. F. McEwen. Structural Relations between Collagen and Mineral in Bone as Determined by High Voltage Electron Microscopic Tomography. *Microsc. Res. Tech.*, 1996, vol. 33, no. 2, pp. 192–202

[Langer *et al.*, (2010)] M. Langer, P. Cloetens, and F. Peyrin. Regularization of Phase Retrieval with Phase-Attenuation Duality Prior for 3D Holotomography. *IEEE Trans Image Proces*, 2010, vol. 19, pp. 2428 – 2436

[Langer *et al.*, (2012)] M. Langer, A. Pacureanu, H. Suhonen, Q. Grimal, P. Cloetens, and F. Peyrin. X-Ray Phase Nanotomography Resolves the 3D Human Bone Ultrastructure. *PLoS ONE*, 2012, vol. 7, no. 8, p. e35691

[Larrue *et al.*, (2011)] A. Larrue, A. Rattner, Z.-A. Peter, C. Olivier, N. Laroche, L. Vico, and F. Peyrin. Synchrotron Radiation Micro-CT at the Micrometer Scale for the Analysis of the Three-

Dimensional Morphology of Microcracks in Human Trabecular Bone. *PloS One*, vol. 6, no. 7, p. e21297

[Li *et al.*, (2007)] H. Li and A. Yezzi. Vessels as 4-D Curves: Global Minimal 4-D Paths to Extract 3-D Tubular Surfaces and Centerlines. *IEEE Trans. Med. Imaging*, 2007, vol. 26, no. 9, pp. 1213–1223

[Lin *et al.*, (2011)] Y. Lin and S. Xu. AFM Analysis of the Lacunar-Canalicular Network in Demineralized Compact Bone. *J. Microsc.*, 2011, vol. 241, no. 3, pp. 291–302

[Ma *et al.*, (2008)] Y.-L. Ma, R.-C. Dai, Z.-F. Sheng, Y. Jin, Y.-H. Zhang, L.-N. Fang, H.-J. Fan, and E.-Y. Liao. Quantitative Associations between Osteocyte Density and Biomechanics, Microcrack and Microstructure in OVX Rats Vertebral Trabeculae. *J. Biomech.*, 2008, vol. 41, no. 6, pp. 1324–1332

[Mader *et al.*, (2013)] K. S. Mader, P. Schneider, R. Müller, and M. Stampanoni. A Quantitative Framework for the 3D Characterization of the Osteocyte Lacunar System. *Bone*, 2013, vol. 57, no. 1, pp. 142–154

[Marotti, (1979)] G. Marotti. Osteocyte Orientation in Human Lamellar Bone and Its Relevance to the Morphometry of Periosteocytic Lacunae. *Metab. Bone Dis. Relat. Res.*, 1979, vol. 1, no. 4, pp. 325–333

[Marotti, (1993)] G. Marotti. A New Theory of Bone Lamellation. *Calcif. Tissue Int.*, 1993, vol. 53 Suppl 1, pp. S47–55; discussion S56

[Marotti *et al.*, (1995)] G. Marotti, M. Ferretti, F. Remaggi, and C. Palumbo. Quantitative Evaluation on Osteocyte Canalicular Density in Human Secondary Osteons. *Bone*, 1995, vol. 16, no. 1, pp. 125–128

[Martin *et al.*, (1998)] R. B. Martin, D. B. Burr, and N. A. Sharkey. Skeletal Tissue Mechanics. New York: Springer, 1998, ISBN 0387984747 9780387984742 0387984747 9780387984742 1441931287 9781441931283

[Martin-Badosa *et al.*, (2003)] E. Martin-Badosa, A. Elmoutaouakkil, S. Nuzzo, D. Amblard, L. Vico, and F. Peyrin. A Method for the Automatic Characterization of Bone Architecture in 3D Mice Microtomographic Images. *Comput Med Imag Grap*, vol. 27, no. 6, pp. 447–458

[Martínez-Criado *et al.*, (2012)] G. Martínez-Criado, R. Tucoulou, P. Cloetens, P. Bleuet, S. Bohic, J. Cauzid, I. Kieffer, E. Kosior, S. Labouré, S. Petitgirard, A. Rack, J. A. Sans, J. Segura-Ruiz, H. Suhonen, J. Susini, and J. Villanova. Status of the Hard X-Ray Microprobe Beamline ID22 of the European Synchrotron Radiation Facility. *J. Synchrotron Radiat.*, 2012, vol. 19, no. Pt 1, pp. 10–18

[Maurer, C.R. *et al.*, (2003)] J. Maurer, C.R., R. Qi, and V. Raghavan. A Linear Time Algorithm for Computing Exact Euclidean Distance Transforms of Binary Images in Arbitrary Dimensions. *IEEE Trans. Pattern Anal. Mach. Intell.*, 2003, vol. 25, no. 2, pp. 265–270

[McCreadie *et al.*, (2004)] B. R. McCreadie, S. J. Hollister, M. B. Schaffler, and S. A. Goldstein. Osteocyte Lacuna Size and Shape in Women with and without Osteoporotic Fracture. *J. Biomech.*, 2004, vol. 37, no. 4, pp. 563–572

[Mori *et al.*, (1997)] S. Mori, R. Harruff, W. Ambrosius, and D. B. Burr. Trabecular Bone Volume and Microdamage Accumulation in the Femoral Heads of Women with and without Femoral Neck Fractures. *Bone*, 1997, vol. 21, no. 6, pp. 521–526

[Müller, (2009)] R. Müller. Hierarchical Microimaging of Bone Structure and Function. *Nat. Rev. Rheumatol.*, 2009, vol. 5, no. 7, pp. 373–381

[Mullender *et al.*, (2005)] M. G. Mullender, S. D. Tan, L. Vico, C. Alexandre, and J. Klein-Nulend. Differences in Osteocyte Density and Bone Histomorphometry between Men and Women and between Healthy and Osteoporotic Subjects. *Calcif. Tissue Int.*, 2005, vol. 77, no. 5, pp. 291–296

[Mullender *et al.*, (1996)] M. G. Mullender, D. D. van der Meer, R. Huiskes, and P. Lips. Osteocyte Density Changes in Aging and Osteoporosis. *Bone*, 1996, vol. 18, no. 2, pp. 109–113

[Mullins *et al.*, (2007)] L. P. Mullins, J. P. McGarry, M. S. Bruzzi, and P. E. McHugh. Micromechanical Modelling of Cortical Bone. *Comput. Methods Biomech. Biomed. Engin.*, 2007, vol. 10, no. 3, pp. 159–169

[Nalla *et al.*, (2006)] R. K. Nalla, J. J. Kruzic, J. H. Kinney, M. Balooch, J. W. Ager III, and R. O. Ritchie. Role of Microstructure in the Aging-Related Deterioration of the Toughness of Human Cortical Bone. *Mater. Sci. Eng. C*, 2006, vol. 26, no. 8, pp. 1251–1260

[Nuzzo *et al.*, (2002a)] S. Nuzzo, M. H. Lafage-Proust, E. Martin-Badosa, G. Boivin, T. Thomas, C. Alexandre, and F. Peyrin. Synchrotron Radiation Microtomography Allows the Analysis of Three-Dimensional Micro-Architecture and Degree of Mineralization of Human Iliac Crest Biopsies : Effects of Etidronate Treatment. *J Bone Min Res.*, 2002, vol. 17, no. 8, pp. 1372–1382

[Nuzzo *et al.*, (2002b)] S. Nuzzo, F. Peyrin, P. Cloetens, J. Baruchel, and G. Boivin. Quantification of the Degree of Mineralization of Bone in Three Dimension Using Synchrotron Radiation Microtomography. *Med Phys*, vol. 19, no. 11, pp. 2672–2681

[Odgaard, (1997)] A. Odgaard. Three-Dimensional Methods for Quantification of Cancellous Bone Architecture. *Bone*, 1997, vol. 20, no. 4, pp. 315–328

[Ohser *et al.*, (2009a)] J. Ohser and S. Katja. 3D Images of Materials Structures: Processing and Analysis. 2009,

[Ohser *et al.*, (2000)] J. Ohser and F. Mücklich. Statistical Analysis of Microstructures in Materials Science. John Wiley, 2000, 381 p.

[Ohser *et al.*, (2009b)] J. Ohser, W. Nagel, and K. Schladitz. MILES FORMULAE FOR BOOLEAN MODELS OBSERVED ON LATTICES. *Image Anal. Stereol.*, 2009, vol. 28, no. 2, pp. 77–92

[Okada *et al.*, (2002)] S. Okada, S. Yoshida, S. H. Ashrafi, and D. E. Schraufnagel. The Canalicular Structure of Compact Bone in the Rat at Different Ages. *Microsc. Microanal. Off. J. Microsc. Soc. Am. Microbeam Anal. Soc. Microsc. Soc. Can.*, 2002, vol. 8, no. 2, pp. 104–115

[Pacureanu *et al.*, (2012)] A. Pacureanu, M. Langer, E. Boller, P. Tafforeau, and F. Peyrin. Nanoscale Imaging of the Bone Cell Network with Synchrotron X-Ray Tomography: Optimization of Acquisition Setup. *Med. Phys.*, 2012, vol. 39, no. 4, pp. 2229–2238

[Pacureanu *et al.*, (2013)] A. Pacureanu, A. Larrue, M. Langer, C. Olivier, C. Muller, M.-H. Lafage-Proust, and F. Peyrin. Adaptive Filtering for Enhancement of the Osteocyte Cell Network in 3D Microtomography Images. *IRBM*, 2013, vol. 34, no. 1, pp. 48–52

[Pacureanu *et al.*, (2009)] A. Pacureanu, A. Larrue, Z. Peter, and F. Peyrin. 3D Non-Linear Enhancement of Tubular Microscopic Bone Porosities. *2009 IEEE International Symposium on Biomedical Imaging: From Nano to Macro*, Jun.2009, Boston, MA, USA. 2009, pp. 602–605

[Pacureanu *et al.*, (2010)] A. Pacureanu, C. Revol-Muller, J. Rose, M. S. Ruiz, and F. Peyrin. Vesselness-Guided Variational Segmentation of Cellular Networks from 3D Micro-CT. *2010 IEEE International Symposium on Biomedical Imaging: From Nano to Macro*, Apr.2010. 2010, pp. 912 – 915

[Pacureanu *et al.*, (2011)] A. Pacureanu, J. Rollet, C. Revol-Muller, V. Buzuloiu, M. Langer, and F. Peyrin. Segmentation of 3D Celluar Networks from SR-MICRO-CT Images. *2011 IEEE International Symposium on Biomedical Imaging: From Nano to Macro*, 2011, Chicago, USA. 2011, pp. 1970–1973

[Paganin *et al.*, (2002)] D. Paganin, S. C. Mayo, T. E. Gureyev, P. R. Miller, and S. W. Wilkins. Simultaneous Phase and Amplitude Extraction from a Single Defocused Image of a Homogeneous Object. *J. Microsc.*, 2002, vol. 206, no. Pt 1, pp. 33–40

[Paglieroni, (1992)] D. W. Paglieroni. Distance Transforms: Properties and Machine Vision Applications. *CVGIP Graph. Models Image Process.*, 1992, vol. 54, no. 1, pp. 56–74

[Palumbo *et al.*, (1990)] C. Palumbo, S. Palazzini, and G. Marotti. Morphological Study of Intercellular Junctions during Osteocyte Differentiation. *Bone*, 1990, vol. 11, no. 6, pp. 401–406

[Pazzaglia *et al.*, (2012)] U. E. Pazzaglia, T. Congiu, M. Marchese, G. Zarattini, and C. Dell'Orbo. The Canalicular System and the Osteoblast Domain in Human Secondary Osteons. *Anat. Histol. Embryol.*, 2012, vol. 41, no. 6, pp. 410–418

[Peyrin *et al.*, (1998)] F. Peyrin, M. Salome, P. Cloetens, A. M. Laval-Jeantet, E. Ritman, and P. Rüegsegger. Micro-CT Examinations of Trabecular Bone Samples at Different Resolutions: 14, 7 and 2 Micron Level. *Technol. Health Care Off. J. Eur. Soc. Eng. Med.*, 1998, vol. 6, no. 5–6, pp. 391–401

[Peyrin *et al.*, (2000)] F. Peyrin, M. Salome-Pateyron, S. Nuzzo, P. Cloetens, A. M. Laval-Jeantet, and J. Baruchel. Perspectives in Three-Dimensional Analysis of Bone Samples Using Synchrotron Radiation Microtomography. *Cell Mol Biol*, 2000, vol. 46, no. 6, pp. 1089–1102

[Power *et al.*, (2012)] J. Power, M. Doube, R. L. van Bezooijen, N. Loveridge, and J. Reeve. Osteocyte Recruitment Declines as the Osteon Fills in: Interacting Effects of Osteocytic Sclerostin and Previous Hip Fracture on the Size of Cortical Canals in the Femoral Neck. *Bone*, 2012, vol. 50, no. 5, pp. 1107–1114

[Power *et al.*, (2001)] J. Power, B. S. Noble, N. Loveridge, K. L. Bell, N. Rushton, and J. Reeve. Osteocyte Lacunar Occupancy in the Femoral Neck Cortex: An Association with Cortical Remodeling in Hip Fracture Cases and Controls. *Calcif. Tissue Int.*, 2001, vol. 69, no. 1, pp. 13–19

[Qing *et al.*, (2012)] H. Qing, L. Ardeshirpour, P. D. Pajevic, V. Dusevich, K. Jähn, S. Kato, J. Wysolmerski, and L. F. Bonewald. Demonstration of Osteocytic Perilacunar/canalicular Remodeling in Mice during Lactation. *J. Bone Miner. Res. Off. J. Am. Soc. Bone Miner. Res.*, 2012, vol. 27, no. 5, pp. 1018–1029

[Qiu *et al.*, (2003a)] S. Qiu, D. P. Fyhrie, S. Palnitkar, and D. S. Rao. Histomorphometric Assessment of Haversian Canal and Osteocyte Lacunae in Different-Sized Osteons in Human Rib. *Anat. Rec. A. Discov. Mol. Cell. Evol. Biol.*, 2003, vol. 272, no. 2, pp. 520–525

[Qiu *et al.*, (2002a)] S. Qiu, D. . Rao, S. Palnitkar, and A. . Parfitt. Relationships between Osteocyte Density and Bone Formation Rate in Human Cancellous Bone. *Bone*, 2002, vol. 31, no. 6, pp. 709–711

[Qiu *et al.*, (2002b)] S. Qiu, D. S. Rao, S. Palnitkar, and A. M. Parfitt. Age and Distance from the Surface but Not Menopause Reduce Osteocyte Density in Human Cancellous Bone. *Bone*, 2002, vol. 31, no. 2, pp. 313–318

[Qiu *et al.*, (2003b)] S. Qiu, D. S. Rao, S. Palnitkar, and A. M. Parfitt. Reduced Iliac Cancellous Osteocyte Density in Patients with Osteoporotic Vertebral Fracture. *J. Bone Miner. Res. Off. J. Am. Soc. Bone Miner. Res.*, 2003, vol. 18, no. 9, pp. 1657–1663

[Qiu *et al.*, (2006)] S. Qiu, D. S. Rao, S. Palnitkar, and A. M. Parfitt. Differences in Osteocyte and Lacunar Density between Black and White American Women. *Bone*, 2006, vol. 38, no. 1, pp. 130–135

[Remaggi *et al.*, (1998)] F. Remaggi, V. Canè, C. Palumbo, and M. Ferretti. Histomorphometric Study on the Osteocyte Lacuno-Canalicular Network in Animals of Different Species. I. Woven-Fibered and Parallel-Fibered Bones. *Ital. J. Anat. Embryol. Arch. Ital. Anat. Ed Embriologia*, 1998, vol. 103, no. 4, pp. 145–155

[Rey *et al.*, (2009)] C. Rey, C. Combes, C. Drouet, and M. J. Glimcher. Bone Mineral: Update on Chemical Composition and Structure. *Osteoporos. Int. J. Establ. Result Coop. Eur. Found. Osteoporos. Natl. Osteoporos. Found. USA*, 2009, vol. 20, no. 6, pp. 1013–1021

[Rho *et al.*, (1998)] J. Y. Rho, L. Kuhn-Spearing, and P. Zioupos. Mechanical Properties and the Hierarchical Structure of Bone. *Med. Eng. Phys.*, 1998, vol. 20, no. 2, pp. 92–102

[Roach, (1994)] H. I. Roach. Why Does Bone Matrix Contain Non-Collagenous Proteins? The Possible Roles of Osteocalcin, Osteonectin, Osteopontin and Bone Sialoprotein in Bone Mineralisation and Resorption. *Cell Biol. Int.*, 1994, vol. 18, no. 6, pp. 617–628

[Roschger *et al.*, (1995)] P. Roschger, H. Plenk Jr, K. Klaushofer, and J. Eschberger. A New Scanning Electron Microscopy Approach to the Quantification of Bone Mineral Distribution: Backscattered Electron Image Grey-Levels Correlated to Calcium K Alpha-Line Intensities. *Scanning Microsc.*, 1995, vol. 9, no. 1, pp. 75–86; discussion 86–88

[Rosenfeld *et al.*, (1966)] A. Rosenfeld and J. L. Pfaltz. Sequential Operations in Digital Picture Processing. *J ACM*, 1966, vol. 13, no. 4, pp. 471–494

[Rouchdy *et al.*, (2008)] Y. Rouchdy and L. D. Cohen. Image Segmentation by Geodesic Voting. Application to the Extraction of Tree Structures from Confocal Microscope Images. *19th International Conference on Pattern Recognition, 2008. ICPR 2008*, 2008. 2008, pp. 1–5

[Rouchdy *et al.*, (2009)] Y. Rouchdy and L. D. Cohen. The Shading Zone Problem in Geodesic Voting and Its Solutions for the Segmentation of Tree Structures. Application to the Segmentation of Microglia Extensions. *IEEE Computer Society Conference on Computer Vision and Pattern Recognition Workshops, 2009. CVPR Workshops 2009*, 2009. 2009, pp. 66–71

[Rouchdy *et al.*, (2011)] Y. Rouchdy and L. D. Cohen. A Geodesic Voting Method for the Segmentation of Tubular Tree and Centerlines. *2011 IEEE International Symposium on Biomedical Imaging: From Nano to Macro*, 2011. 2011, pp. 979–983

[Rouchdy *et al.*, (2013)] Y. Rouchdy and L. D. Cohen. Geodesic Voting Methods: Overview, Extensions and Application to Blood Vessel Segmentation. *Comput. Methods Biomech. Biomed. Eng. Imaging Vis.*, 2013, vol. 1, no. 2, pp. 79–88

[Rubin *et al.*, (2005)] M. A. Rubin and I. Jasiuk. The TEM Characterization of the Lamellar Structure of Osteoporotic Human Trabecular Bone. *Micron Oxf. Engl. 1993*, 2005, vol. 36, no. 7–8, pp. 653–664

[Rubin *et al.*, (2004)] M. A. Rubin, J. Rubin, and I. Jasiuk. SEM and TEM Study of the Hierarchical Structure of C57BL/6J and C3H/HeJ Mice Trabecular Bone. *Bone*, 2004, vol. 35, no. 1, pp. 11–20

[Sahar *et al.*, (2005)] N. D. Sahar, S.-I. Hong, and D. H. Kohn. Micro- and Nano-Structural Analyses of Damage in Bone. *Micron Oxf. Engl. 1993*, 2005, vol. 36, no. 7–8, pp. 617–629

[Saito *et al.*, (1994)] T. Saito and J.-I. Toriwaki. New Algorithms for Euclidean Distance Transformation of an N-Dimensional Digitized Picture with Applications. *Pattern Recognit.*, 1994, vol. 27, no. 11, pp. 1551–1565

[Salomé *et al.*, (1999)] M. Salomé, F. Peyrin, P. Cloetens, C. Odet, A. M. Laval-Jeantet, J. Baruchel, and P. Spanne. A Synchrotron Radiation Microtomography System for the Analysis of Trabecular Bone Samples. *Med. Phys.*, 1999, vol. 26, no. 10, pp. 2194–2204

[Sasaki *et al.*, (1989)] N. Sasaki, N. Matsushima, T. Ikawa, H. Yamamura, and A. Fukuda. Orientation of Bone Mineral and Its Role in the Anisotropic Mechanical Properties of Bone--Transverse Anisotropy. *J. Biomech.*, 1989, vol. 22, no. 2, pp. 157–164

[Sato *et al.*, (1998)] Y. Sato, S. Nakajima, N. Shiraga, H. Atsumi, S. Yoshida, T. Koller, G. Gerig, and R. Kikinis. Three-Dimensional Multi-Scale Line Filter for Segmentation and

Visualization of Curvilinear Structures in Medical Images. *Med. Image Anal.*, 1998, vol. 2, no. 2, pp. 143–168

[Schneider *et al.*, (2010)] P. Schneider, M. Meier, R. Wepf, and R. Müller. Towards Quantitative 3D Imaging of the Osteocyte Lacuno-Canalicular Network. *Bone*, 2010, vol. 47, no. 5, pp. 848–858

[Schneider *et al.*, (2011)] P. Schneider, M. Meier, R. Wepf, and R. Müller. Serial FIB/SEM Imaging for Quantitative 3D Assessment of the Osteocyte Lacuno-Canalicular Network. *Bone*, 2011

[Schneider *et al.*, (2007)] P. Schneider, M. Stauber, R. Voide, M. Stampanoni, L. R. Donahue, and R. Müller. Ultrastructural Properties in Cortical Bone Vary Greatly in Two Inbred Strains of Mice as Assessed by Synchrotron Light Based Micro- and Nano-CT. *J. Bone Miner. Res. Off. J. Am. Soc. Bone Miner. Res.*, 2007, vol. 22, no. 10, pp. 1557–1570

[Seeman *et al.*, (2006)] E. Seeman and P. D. Delmas. Bone Quality--the Material and Structural Basis of Bone Strength and Fragility. *N. Engl. J. Med.*, 2006, vol. 354, no. 21, pp. 2250–2261

[Serra, (1982)] J. Serra. Image Analysis and Mathematical Morphology. Academic Press, 1982, ISBN 9780126372427

[Sethian, (1996)] J. A. Sethian. A Fast Marching Level Set Method for Monotonically Advancing Fronts. *Proc. Natl. Acad. Sci.*, 1996, vol. 93, no. 4, pp. 1591–1595

[Shahar *et al.*, (2011)] R. Shahar, C. Lukas, S. Papo, J. W. C. Dunlop, and R. Weinkamer. Characterization of the Spatial Arrangement of Secondary Osteons in the Diaphysis of Equine and Canine Long Bones. *Anat. Rec. Hoboken NJ 2007*, 2011, vol. 294, no. 7, pp. 1093–1102

[Shainberg *et al.*, (2012)] A. P. M. Shainberg, P. Valério, A. Zonari, F. N. Oktar, L. S. Ozyegin, M. P. F. Graça, M. F. Leite and A. M. Goes. Attachment and Proliferation of Osteoblasts on Lithium-Hydroxyapatite Composites. *Adv. Mater. Sci. Eng.*, 2012, vol. 2012

[Shapiro, (1988)] F. Shapiro. Cortical Bone Repair. The Relationship of the Lacunar-Canalicular System and Intercellular Gap Junctions to the Repair Process. *J. Bone Joint Surg. Am.*, 1988, vol. 70, no. 7, pp. 1067–1081

[Sharma *et al.*, (2012)] D. Sharma, C. Ciani, P. A. R. Marin, J. D. Levy, S. B. Doty, and S. P. Fritton. Alterations in the Osteocyte Lacunar-Canalicular Microenvironment due to Estrogen Deficiency. *Bone*, 2012, vol. 51, no. 3, pp. 488–497

[Skedros *et al.*, (2005)] J. G. Skedros, T. R. Grunander, and M. W. Hamrick. Spatial Distribution of Osteocyte Lacunae in Equine Radii and Third Metacarpals: Considerations for Cellular Communication, Microdamage Detection and Metabolism. *Cells Tissues Organs*, 2005, vol. 180, no. 4, pp. 215–236

[Stokes *et al.*, (2005)] D. J. Stokes, J. R. Tong, J. Juhasz, P. A. Midgley, and S. M. Best. Characterisation and 3D Visualisation of Biomaterials and Tissues Using Focused Ion Beam (E)SEM. *Microsc. Microanal.*, 2005, vol. 11, no. Supplement S02, pp. 1260–1261

[Sugawara *et al.*, (2011)] Y. Sugawara, R. Ando, H. Kamioka, Y. Ishihara, T. Honjo, N. Kawanabe, H. Kurosaka, T. Takano-Yamamoto, and T. Yamashiro. The Three-Dimensional Morphometry and Cell-Cell Communication of the Osteocyte Network in Chick and Mouse Embryonic Calvaria. *Calcif. Tissue Int.*, 2011, vol. 88, no. 5, pp. 416–424

[Sugawara *et al.*, (2005)] Y. Sugawara, H. Kamioka, T. Honjo, K. Tezuka, and T. Takano-Yamamoto. Three-Dimensional Reconstruction of Chick Calvarial Osteocytes and Their Cell Processes Using Confocal Microscopy. *Bone*, 2005, vol. 36, no. 5, pp. 877–883

[Taylor *et al.*, (2007)] D. Taylor, J. G. Hazenberg, and T. C. Lee. Living with Cracks: Damage and Repair in Human Bone. *Nat. Mater.*, 2007, vol. 6, no. 4, pp. 263–268

[Teague, (1982)] M. R. Teague. Irradiance Moments: Their Propagation and Use for Unique Retrieval of Phase. *J. Opt. Soc. Am.*, 1982, vol. 72, no. 9, pp. 1199–1209

[Teti *et al.*, (2009)] A. Teti and A. Zallone. Do Osteocytes Contribute to Bone Mineral Homeostasis? Osteocytic Osteolysis Revisited. *Bone*, 2009, vol. 44, no. 1, pp. 11–16

[Tommasini *et al.*, (2012)] S. M. Tommasini, A. Trinward, A. S. Acerbo, F. De Carlo, L. M. Miller, and S. Judex. Changes in Intracortical Microporosities Induced by Pharmaceutical Treatment of Osteoporosis as Detected by High Resolution Micro-CT. *Bone*, 2012, vol. 50, no. 3, pp. 596–604

[Toriwaki *et al.*, (2002)] J. Toriwaki and T. Yonekura. Euler Number and Connectivity Indexes of a Three Dimensional Digital Picture. *Forma*, 2002, vol. 17, pp. 183–209

[Torres-Lagares *et al.*, (2010)] D. Torres-Lagares, J.-F. Tulasne, C. Pouget, A. Llorens, J.-L. Saffar, and P. Lesclous. Structure and Remodelling of the Human Parietal Bone: An Age and Gender Histomorphometric Study. *J. Cranio-Maxillo-Fac. Surg. Off. Publ. Eur. Assoc. Cranio-Maxillo-Fac. Surg.*, 2010, vol. 38, no. 5, pp. 325–330

[Van Hove *et al.*, (2009)] R. P. van Hove, P. A. Nolte, A. Vatsa, C. M. Semeins, P. L. Salmon, T. H. Smit, and J. Klein-Nulend. Osteocyte Morphology in Human Tibiae of Different Bone Pathologies with Different Bone Mineral Density--Is There a Role for Mechanosensing? *Bone*, 2009, vol. 45, no. 2, pp. 321–329

[Vashishth *et al.*, (2005)] D. Vashishth, G. J. Gibson, and D. P. Fyhrie. Sexual Dimorphism and Age Dependence of Osteocyte Lacunar Density for Human Vertebral Cancellous Bone. *Anat. Rec. A. Discov. Mol. Cell. Evol. Biol.*, 2005, vol. 282, no. 2, pp. 157–162

[Vashishth *et al.*, (2002)] D. Vashishth, G. Gibson, J. Kimura, M. B. Schaffler, and D. P. Fyhrie. Determination of Bone Volume by Osteocyte Population. *Anat. Rec.*, 2002, vol. 267, no. 4, pp. 292–295

[Vashishth *et al.*, (2000)] D. Vashishth, O. Verborgt, G. Divine, M. B. Schaffler, and D. P. Fyhrie. Decline in Osteocyte Lacunar Density in Human Cortical Bone Is Associated with Accumulation of Microcracks with Age. *Bone*, 2000, vol. 26, no. 4, pp. 375–380

[Vatsa *et al.*, (2008)] A. Vatsa, R. G. Breuls, C. M. Semeins, P. L. Salmon, T. H. Smit, and J. Klein-Nulend. Osteocyte Morphology in Fibula and Calvaria --- Is There a Role for Mechanosensing? *Bone*, 2008, vol. 43, no. 3, pp. 452–458

[Viguet-Carrin *et al.*, (2006)] S. Viguet-Carrin, P. Garnero, and P. D. Delmas. The Role of Collagen in Bone Strength. *Osteoporos. Int. J. Establ. Result Coop. Eur. Found. Osteoporos. Natl. Osteoporos. Found. USA*, 2006, vol. 17, no. 3, pp. 319–336

[L Wang *et al.*, (2005)] L. Wang, Y. Wang, Y. Han, S. C. Henderson, R. J. Majeska, S. Weinbaum, and M. B. Schaffler. In Situ Measurement of Solute Transport in the Bone Lacunar-Canalicular System. *Proc. Natl. Acad. Sci. U. S. A.*, 2005, vol. 102, no. 33, pp. 11911–11916

[X Wang *et al.*, (2010)] X. Wang, J. S. Nyman, X. Dong, H. Leng, and M. Reyes. Fundamental Biomechanics in Bone Tissue Engineering. 2010,

[Wassermann *et al.*, (1965)] F. Wassermann and J. A. Yaeger. Fine Structure of the Osteocyte Capsule and of the Wall of the Lacunae in Bone. *Z. Für Zellforsch. Mikrosk. Anat.*, 1965, vol. 67, no. 5, pp. 636–652

[Weinbaum *et al.*, (1994)] S. Weinbaum, S. C. Cowin, and Y. Zeng. A Model for the Excitation of Osteocytes by Mechanical Loading-Induced Bone Fluid Shear Stresses. *J. Biomech.*, 1994, vol. 27, no. 3, pp. 339–360

[Weiner *et al.*, (1999)] S. Weiner, W. Traub, and H. D. Wagner. Lamellar Bone: Structure-Function Relations. *J. Struct. Biol.*, 1999, vol. 126, no. 3, pp. 241–255

[Weitkamp *et al.*, (2011)] T. Weitkamp, D. Haas, D. Wegrzynek, and A. Rack. ANKAphase: Software for Single-Distance Phase Retrieval from Inline X-Ray Phase-Contrast Radiographs. *J. Synchrotron Radiat.*, 2011, vol. 18, no. Pt 4, pp. 617–629

[Westbroek *et al.*, (2002)] I. Westbroek, K. E. De Rooij, and P. J. Nijweide. Osteocyte-Specific Monoclonal Antibody MAb OB7.3 Is Directed against Phex Protein. *J. Bone Miner. Res. Off. J. Am. Soc. Bone Miner. Res.*, 2002, vol. 17, no. 5, pp. 845–853

[Withers, (2007)] P. J. Withers. X-Ray Nanotomography. *Mater. Today*, 2007, vol. 10, no. 12, pp. 26–34

[Wright *et al.*, (1978)] P. H. Wright, J. O. Jowsey, and R. A. Robb. Osteocyte Lacunar Area in Normal Bone, Hyperparathyroidism, Renal Disease, and Osteoporosis. *Surg. Forum*, 1978, vol. 29, pp. 558–559

[LD You *et al.*, (2004)] L. D. You, S. Weinbaum, S. C. Cowin, and M. B. Schaffler. Ultrastructure of the Osteocyte Process and Its Pericellular Matrix. *Anat. Rec. A. Discov. Mol. Cell. Evol. Biol.*, 2004, vol. 278, no. 2, pp. 505–513

[L You *et al.*, (2004)] L. You, S. Weinbaum, S. C. Cowin, and M. B. Schaffler. Ultrastructure of the Osteocyte Process and Its Pericellular Matrix. *Anat. Rec. A. Discov. Mol. Cell. Evol. Biol.*, 2004, vol. 278A, no. 2, pp. 505–513

[Zebaze *et al.*, (2010)] R. M. D. Zebaze, A. Ghasem-Zadeh, A. Bohte, S. Iuliano-Burns, M. Mirams, R. I. Price, E. J. Mackie, and E. Seeman. Intracortical Remodelling and Porosity in the Distal Radius and Post-Mortem Femurs of Women: A Cross-Sectional Study. *Lancet*, 2010, vol. 375, no. 9727, pp. 1729–1736

[Zhang *et al.*, (2006)] K. Zhang, C. Barragan-Adjemian, L. Ye, S. Kotha, M. Dallas, Y. Lu, S. Zhao, M. Harris, S. E. Harris, J. Q. Feng, and L. F. Bonewald. E11/gp38 Selective Expression in Osteocytes: Regulation by Mechanical Strain and Role in Dendrite Elongation. *Mol. Cell. Biol.*, 2006, vol. 26, no. 12, pp. 4539–4552

[Zuluaga *et al.*, (2011)] M. A. Zuluaga, P. Dong, A. Pacureanu, M. Orkisz, and F. Peyrin. Minimum Cost Path Approach for the Segmentation of Bone Canalicular Network from Nano-CT Images. presented at the IEEE Nuclear Science Symposium and Medical Imaging Conference. 2011

[Zuluaga *et al.*, (accepted)] M. A. Zuluaga, M. Orkisz, P. Dong, A. Pacureanu, P.-J. Gouttenoire, and F. Peyrin. Bone Canalicular Network Segmentation in 3D Nano-CT Images through Geodesic Voting and Image Tessellation. *Phys. Med. Biol.*, accepted

[Zuluaga *et al.*, (2014)] M. A. Zuluaga, M. Orkisz, P. Dong, A. Pacureanu, P.-J. Gouttenoire, and F. Peyrin. Bone Canalicular Network Segmentation in 3D Nano-CT Images through Geodesic Voting and Image Tessellation. *Phys. Med. Biol.*, 2014, vol. 59, no. 9, p. 2155

FOLIO ADMINISTRATIF

THESE SOUTENUE DEVANT L'INSTITUT NATIONAL DES SCIENCES APPLIQUEES DE LYON

NOM : DONG **DATE de SOUTENANCE** : 21/02/2014

Prénoms : Pei

TITRE : Three-dimensional analysis of bone cellular tissue from SR CT Imaging

NATURE : Doctorat **Numéro d'ordre** : 2014-ISAL-0022

Ecole doctorale : Electronique, Electrotechnique, Automatique

Spécialité :

RESUME :

The osteocyte system has raised increasing interest in the recent years, since it is hypothesized to play an important role in orchestrating bone adaptation through mechanosensation and bone mechanotransduction mechanism. The osteocytes are deeply buried within the bone matrix, where their bodies are encysted in cavities called lacunae and their stellular processes are enclosed in tunnels called canaliculi. Together, they formed the lacuno-canalicular network (LCN). The geometry of the LCN is of importance since it is supposed to potentially affect and reflect the viability of the osteocyte and is supposed to be related to biomechanical constraints at the cell level. However, studying the LCN is quite challenging, due to limitations in an ideal imaging modality and the lack of quantitative analysis tools. In this thesis, we propose computational efficient and automated methods to quantify the 3D morphological properties of the lacuno-canalicular network from large 3D synchrotron radiation (SR) micro and nano-CT images.

For image acquisition, we used the SR micro/nano-CT setups installed on beamlines ID19 and ID22 at ESRF. A series of human cortical samples were imaged with spatial resolutions ranging from 3.5 µm to 50 nm. For the 3D assessment of the lacunae, we used an image moment-based approach to calculate the volume, length, width, height and anisotropy of each osteocyte lacuna. We employed a fast algorithm to further efficiently calculate the surface area, the Euler number and the structure model index of each lacuna. The segmentation was refined by eliminating artifacts according to some descriptors. Validation of segmentation and experimental results on thirteen bone samples are presented. We also introduced the 3D lacunar density map to directly visualize the lacunar density variation over a large field of view. For the 3D assessment of canaliculi, we propose a method to quantify the ramification of canaliculi around each lacuna. After segmentation, our method first separates and labels each lacuna from the LCN. Then, a signature of the numbers of canaliculi at different distances from the lacunar surface is estimated through the calculation of topological parameters. Validation of this method and statistical results a large 3D SR micro-CT image of a human femoral bone sample are reported.

The last contribution of this work was to improve the segmentation of the canaliculi network and to illustrate the feasibility of using this method for the automated quantification on a series of bone specimens. We investigated a segmentation approach based on minimum cost paths and geodesic voting method. A parallel computation scheme was implemented to overcome the prohibitive computational cost. The quantification of the LCN was later performed by using the methods proposed in the previous chapters. Besides, we introduced the parameters quantified based on the Voronoi tessellation. Statistical results are reported on 8 large 3D micro-CT images, including about over a hundred of lacunae with their connected canaliculi.

Future works need to concern the improvement of canaliculi segmentation from images at 300 nm. The segmentation evaluation remains a challenging work. In terms of quantification, further works have also to be performed to extract additional descriptors from SR CT images at both 300 nm and 50 nm. Nevertheless, this work opens many perspectives for a better knowledge of the physiopathology of bone at the cellular scale.

MOTS-CLES : Lacuno-canalicular network, Synchrotron radiation micro/nano-CT, 3D image analysis, LCN descriptors Cortical bone

Laboratoire (s) de recherche : Centre de Recherche en Acquisition et Traitement de l'Image pour la Santé (CREATIS) CNRS UMR 5220 ; INSERM U1044 ; Université Lyon 1 ; INSA Lyon

Directeur de thèse: Françoise PEYRIN, Directeur de recherche INSERM

Président de jury : Maciej ORKISZ

Composition du jury : Françoise PEYRIN (Directeur de thèse), Valérie BOUSSON (Rapporteur), Jean Marc Chassery (Rapporteur), Joachim OHSER (Examinateur), Maciej ORKISZ (Examinateur)